

# **DEVELOPMENT OF GRAPHENE NANOSTRUCTURES FOR USE IN ANTI-CANCER NANOMEDICINE**

**Submitted by**

**Tanveer Ahmad Tabish**

**to the University of Exeter as a thesis for the degree of Doctor of Philosophy  
(PhD) in Engineering in February 2018.**

This thesis is available for Library use on the understanding that it is copyright material and that no quotation from the thesis may be published without proper acknowledgement.

I certify that all material in this thesis which is not my work has been identified and that no material is included for which a degree has previously been conferred upon me.

.....  
Tanveer A. Tabish

## Table of contents

<b>Table of contents.....</b>	<b>2</b>
<b>Abstract .....</b>	<b>6</b>
<b>Acknowledgement.....</b>	<b>8</b>
<b>List of publications .....</b>	<b>11</b>
<b>List of abbreviations .....</b>	<b>14</b>
<b>List of Schemes .....</b>	<b>15</b>
<b>List of Figures .....</b>	<b>16</b>
<b>List of Tables.....</b>	<b>22</b>
<b>Chapter 1      Introduction and Overview of the Thesis.....</b>	<b>23</b>
1.1      Background.....	23
1.2      Specific aims and overview of the thesis.....	23
1.3      Structure of the thesis.....	27
1.4      Significance of the thesis.....	28
References.....	30
<b>Chapter 2      Literature Review.....</b>	<b>32</b>
2.1      Structure and properties of graphene nanostructure .....	32
2.2      Methods for graphene preparation.....	36
2.2.1      Modified Hummer’s method.....	36
2.2.2      Chemical reduction of graphene.....	37
2.2.3      Heat treatment of reduced graphene oxide.....	37
2.2.4      Bottom-up approach.....	38
2.2.5      CVD method.....	38
2.2      Toxic potential of graphene family nanomaterials.....	39
2.3      Graphene in enzyme engineering and cancer treatment.....	42
2.4      Summary.....	47
Reference.....	48
<b>Chapter 3      Analysis Techniques and Raw Materials.....</b>	<b>55</b>
3.1      Raw materials.....	55
3.2      Scanning electron microscopy.....	55
3.3      Transmission electron microscopy.....	56
3.4      Ultraviolet/Visible (UV/Vis) spectroscopy.....	57
3.5      Raman spectroscopy.....	58

3.6	Fourier Transform Infrared (FT-IR) spectroscopy.....	59
3.7	X-Ray diffraction (XRD).....	60
3.8	Photoluminescence spectroscopy.....	61
3.9	BET surface area analyser.....	61
3.10	Contact angle goniometer.....	62
3.11	Zeta potential probe.....	62
3.12	Cell Viability evaluation and flow cytometry analysis .....	63
3.13	<i>In vivo</i> studies.....	63
3.14	Statistical analysis.....	64
3.15	Regression analysis.....	64
3.16	Adsorption kinetic model.....	65
	References .....	66
<b>Chapter 4</b>	<b>Graphene Oxide based Targeting Extracellular Cathepsin D and Cathepsin L in Novel Anti-Metastatic Enzyme Cancer Therapy.....</b>	<b>67</b>
4.1	Introduction.....	67
4.2	Materials and methods.....	72
	4.2.1 Synthesis and characterization.....	72
	4.2.2 Cell viability.....	73
	4.2.3 Regression model.....	73
	4.2.4 Water contact angle and surface energy calculations.....	74
	4.2.5 CathD proteolytic activities pH experiment .....	75
	4.2.6 CathL proteolytic activities pH experiment .....	76
	4.2.7 Enzyme interaction with GO.....	77
	4.2.8 Statistical analysis.....	78
4.3	Results.....	78
	4.3.1 Synthesis and <i>In vitro</i> toxic effects of GO on lung cancer cells.....	78
	4.3.2 Basic characterization of enzymes.....	83
	4.3.3 Enzyme interaction with GO.....	86
4.4	Discussion.....	94
4.5	Conclusion.....	96
4.5	Supplementary information.....	96

	References.....	103
<b>Chapter 5</b>	<b><i>In Vitro</i> Toxic Effects of Reduced Graphene Oxide Nanosheets on Lung Cancer Cells.....</b>	<b>108</b>
5.1	Introduction.....	108
5.2	Materials and methods.....	110
5.2.1	Synthesis and characterization.....	110
5.2.2	Cell viability.....	111
5.2.3	Regression model.....	111
5.3	Results and discussion.....	111
5.4	Conclusion.....	119
	References.....	120
<b>Chapter 6</b>	<b>Investigation into the Toxic Effects of Graphene Nanopores on Lung Cancer Cells and Biological Tissues.....</b>	<b>122</b>
6.1	Introduction.....	123
6.2	Materials and methods.....	127
6.2.1	Synthesis of graphene nanopores.....	127
6.2.2	Cell viability.....	127
6.2.3	Regression model analysis.....	128
6.2.4	Cell apoptosis and necrosis.....	128
6.2.5	Animals.....	128
6.2.6	Complete blood count and clinical biochemistry panel analysis.....	129
6.2.7	Liver and kidney function analysis.....	129
6.2.8	Histological analysis.....	130
6.2.9	Oxidative stress biomarkers.....	130
6.2.10	Statistical analysis.....	130
6.3	Results.....	131
6.3.1	Basic Characterization.....	131
6.3.2	<i>In Vitro</i> toxic effects of GNPs on lung cancer cells.....	134
6.3.3	Effects of GNPs on body and relative organ weights.....	138
6.3.4	Effects of GNPs on complete blood count in the rat.....	138
6.3.5	Liver and kidney function analysis.....	140
6.3.6	Histological changes.....	141



	6.3.7 Biomarkers of oxidative stress.....	146
6.4	Discussion.....	147
6.5	Conclusion.....	150
6.6	Supplementary information.....	152
	References.....	157
<b>Chapter 7</b>	<b>Influence of Luminescent Graphene Quantum Dots on Trypsin Activity.....</b>	<b>161</b>
7.1	Introduction.....	161
7.2	Materials and methods.....	163
	7.2.1 Synthesis and basic characterization.....	163
	7.2.2 Trypsin proteolytic activity on substrates and GQDs.....	164
7.3	Results and discussion.....	165
	7.3.1 Basic characterization.....	165
	7.3.2 Trypsin activity with substrate and GQDs.....	166
7.4	Conclusion.....	176
7.5	Supplementary information.....	177
	References.....	180
<b>Chapter 8</b>	<b>Tracing the Bioavailability of Three-Dimensional Graphene Foam in Biological Tissues.....</b>	<b>182</b>
8.1	Introduction.....	182
8.2	Materials and methods.....	184
	8.2.1 Fabrication and characterization of GF.....	184
	8.2.2 Cell viability and fluorescence imaging.....	184
	8.2.3 Procedure for <i>in vivo</i> toxicity.....	185
	8.2.4 Measurement of enzymatic activities and other biochemical parameters.....	186
8.3	Results and discussion.....	186
8.4	Conclusion.....	199
8.5	Supplementary information.....	200
	References.....	206
<b>Chapter 9</b>	<b>Conclusion and Future Work.....</b>	<b>209</b>
12.1	Conclusion.....	209
12.2	Future work.....	212

## Abstract

Nanomedicine utilises biocompatible nanomaterials for therapeutic as well as imaging purposes, for the treatment of various diseases including cancer, neurological disorders and wound infections. Graphene, a material composed of a single layer of carbon atoms, has recently shown great potential to improve diagnostics and therapeutics, owing to its small size, large surface-area-to-volume ratio and unique physicochemical properties. However, the limited fabrication, *in vitro* and *in vivo* functionalities published in the literature indicate inconsistencies regarding the factors affecting metabolic fate, biodistribution as well as toxicity patterns of graphene. This thesis focuses on the biological effects of graphene-based materials, including graphene oxide (GO), reduced graphene oxide (rGO), graphene nanopores (GNPs), graphene quantum dots (GQDs) and three-dimensional graphene foam (GF). These can be used to closely mimic therapeutic functions and thereby open up new pathways to anticancer nanomedicine. In this work, a biocompatible GO-based anti-metastatic enzyme cancer therapy approach has been introduced for the first time to target the extracellular pro-metastatic and pro-tumourigenic enzymes of cathepsin D and cathepsin L, which are typically overexpressed in ovarian and breast cancers. Definitive binding and modulation of cathepsin- D and -L with GO has revealed that both of the enzymes were adsorbed onto the surface of GO through its cationic and hydrophilic residues under the biologically relevant condition of acidic pH. It has been demonstrated that low concentrations of rGO were shown to significantly produce late apoptosis and necrosis rather than early apoptotic events in lung cancer cells (A549 and SKMES-1), suggesting that it was able to disintegrate the cellular membranes in a dose-dependent manner. GNPs at lower concentrations (250µg/ml) induce upregulation of phosphatidylserine on cell surface membrane (*i.e.* early apoptotic event), which does not significantly disintegrate the cell membrane in the aforementioned lung cancer cells, while higher concentrations of GNPs (5 and 15 mg/kg) in rats (when intraperitoneally injected) exhibited sub-chronic toxicity in a period of 27 days. The interaction of GQDs and trypsin has revealed the strong bonding capacity of GQDs with trypsin, owing to their surface charge and surface functionalities evidencing the high bioavailability of GQDs in enzyme engineering. Finally, 3D GF was developed to probe the role of graphene-based scaffold cues in the field of regenerative medicine revealing their cell attachment to *in vitro* cell cultures. Furthermore, GF was shown to

maintain remarkable biocompatibility with *in vitro* and *in vivo* toxicity screening models when exposed for 7 days at doses of 5, 10 and 15 mg/l. Taken together, graphene and its modified structures developed in this thesis promise to revolutionise clinical settings across the board in nanomedicine which include, but are not limited to, ultra-high sensitive enzyme adsorbents, high throughput biosensors, enzyme modulators and smart scaffolds for tissue regeneration.

## **Acknowledgement**

The most salient and instant impetus for my choice of doing this PhD was the outcome of a scientific inquiry grew out of the field of biomedical engineering when I was doing my masters research in the development of cardiovascular stents. The findings presented here are the aftermath of unflagging pleasure, untold nightmares, and strong experiences of a 3-years journey. After a gradual and confounded start, I realised that PhD should not be tagged as a professional or academic training, but should be a life experience which should stay with us until 'the sun grows cold'. Very soon I started dealing with the common fears of 'doctoral condition' in a more existential fashion, which helped me realize a sense of awareness of my abilities as a researcher and of my shortcomings as a person. This dream could only be revealed with the support, encouragement and love of my parents and brother; therefore, this thesis is partly theirs. Their unconditional love and inspiration are the asset of my life; it feels so boundless that the true extent of it cannot be realistically conveyed by words alone.

It is traditional, of course, to thank your supervisor for his support during these years. Special thanks goes to Prof. Shaowei Zhang: you showed me what skills I needed to be a good scientist, so for that I am eternally grateful. It has been an honour to be your student and I hope I can make you proud to have been my supervisor. Your constant encouragement, enormous trust, suggestions, ideas, and appreciation paid to the excellence of the work accomplished. You are really an influential person who always prompts me to think harder and write simpler. I much acknowledge your patience and quick replies to my queries even on the weekends and the days of your vacation. I am also grateful for the contribution and advices of my second supervisor Dr. Yongde Xia and my mentor Prof. Alastair Hibbins during the high tides of this work. I would like to extend my thanks to Engineering and Physical Sciences Research Council (EPSRC), UK for their funding, without which this project would not exist. I am also very grateful to EPSRC CDT in Metamaterials for their support.

A big thanks also goes to Prof. Paul Winyard (University of Exeter Medical School). Paul, your ability to ask such questions that make me realise I know nothing should not be underestimated! The way you approached to understand a new problem was

inspirational. Your genuine appraisal of my current progress was really adoring and motivational. Definitely, I could not think of my best scientific thoughts but in his possession, which contributed to enrich my intellectual thrill and passions during this period. I would like to acknowledge my collaborators Dr. Chris Scotton and Dr. Jacqueline Whatmore (University of Exeter Medical School), Dr. David Horsell (School of Physics, University of Exeter) and Prof. Muhammad Ali and Prof. Farhat Jabeen (Government College University, Faisalabad, Pakistan) for their constant support and the permission to doing some experimental work of this thesis in their labs. This project has led to a research visit to Italy. Special thanks to Prof. Lorenza Draghi (Tissue Engineering and Regenerative Medicine Research Group, Politecnico di Milano, Italy), who warmly welcomed me in her research group. This visit was an amazing opportunity for me to undertake research in an exciting and active research environment, and allowed me to develop a range of new research skills.

Above all, my deepest debt is to lab colleagues, Dr. Liangxu Lin, Dr. Yan Wen, Dr. Ke Bao and Cheng Liu. Also thanks to my friends Dr. Sakineh Chabi, Dr. Binling Chen, Dr. Zahid Pranjol, Laicong Deng and Dr. Hasan Hayat. Special thanks to Victoria Richards, I also valued her motivational 'interventions' during the write-up of this thesis. Happily I accepted her advices and suggestions.

Tanveer

January 23, 2018

**To my beloved parents Bashir Ahmad Tahir, Sultana Bashir and my  
brother Dr. Naseem Abbas Ahmar**  
for their unflagging support and unconditional love

## List of publications

### Book chapter

(1) **Tanveer A. Tabish** and Shaowei Zhang “Graphene quantum dots: syntheses, properties, and biological applications”, In: Saleem Hashmi (editor-in-chief). *Reference Module in Materials Science and Materials Engineering*, Oxford: Elsevier; 2016. pp. 1-21.

### Review paper

(2) **Tanveer A. Tabish**, Shaowei Zhang, Paul G. Winyard, Developing the next generation of graphene-based cancer therapeutic platforms: the potential role of reactive oxygen species, *Redox Biology* (2018) 15, 34-40.

### Journal papers

(3) **Tanveer A. Tabish**, Md Zahidul I. Pranjol, Hasan Hayat, Alma A. M. Rahat, Trefa M. Abdullah, Jacqueline L. Whatmore, and Shaowei Zhang, *In vitro* toxic effects of reduced graphene oxide nanosheets on lung cancer cells, *Nanotechnology*, (2017) 28, 505001-505008.

(4) **Tanveer A. Tabish**, Liangxu Lin, Muhammad Ali, Farhat Jabeen, Muhammad Ali, Rehana Iqbal, David W. Horsell, Paul G. Winyard, and Shaowei Zhang, Investigating the bioavailability of graphene quantum dots in lung tissues via Fourier transform infrared spectroscopy, *Journal of Royal Society Interface Focus*, (2018) 8(3), 20170054-20170058.

(5) **Tanveer A. Tabish**, Md Zahidul I. Pranjol, Ilayda Karadag, David W. Horsell, Jacqueline L. Whatmore, and Shaowei Zhang, Influence of luminescent graphene quantum dots on trypsin activity, *International Journal of Nanomedicine*, (2018) 13, 1525-1538.

(6) **Tanveer A. Tabish**, Fayyaz Memon , Diego Gomez , David Horsell, and Shaowei Zhang, A facile synthesis of porous graphene for efficient water and wastewater treatment, *Scientific Reports*, (2018) 8(1), 1817-1820.

(7) **Tanveer A. Tabish**, Sakineh Chabi, Muhammad Ali, Yongde Xia, Farhat Jabeen, and Shaowei Zhang, Tracing the bioavailability of three-dimensional graphene foam in biological tissues. *Materials*, (2017) 10(4), 336-339.

(8) **Tanveer A. Tabish**, Chris J. Scotton, Daniel C. Ferguson, Liangxu Lin, Anienke van der Veen, Sophie Lowry, Muhammad Ali, Farhat Jabeen, M. Ali, Paul G. Winyard and Shaowei Zhang, Biocompatibility and toxicity of graphene quantum dots for potential application in photodynamic therapy, (Accepted) *Nanomedicine, Future medicine*.

#### **Submitted/under preparation papers**

(9) **Tanveer A. Tabish**, Shaowei Zhang, L. Draghi, and Chris J. Scotton, 'Three dimensional graphene foam in regenerative neural stem cell culture" (Invited paper to be submitted to '*Materials Today*').

(10) **Tanveer A. Tabish**, Md Zahidul I. Pranjol, F. Jabeen, Hasan Hayat, Trefa Abdulla, Alma A. M. Rahat, M. Ali, Paul G. Winyard, Jacqueline L. Whatmore, Shaowei Zhang, Investigation into the toxic effects of graphene nanopores on lung cancer cells and biological tissues (Under review).

(11) **Tanveer A. Tabish**, Md Zahidul I. Pranjol, Hasan Hayat, Alma A. M. Rahat, David W. Horsell, Jacqueline L. Whatmore, Paul G. Winyard, Shaowei Zhang, Graphene oxide based targeting extracellular cathepsin D and cathepsin L in novel anti-metastatic enzyme cancer therapy (In preparation).

#### **Conferences**

(1) 'Fabrication of graphene nanopres for application in marine biology' (Oral presentation) 'Workshop on Offshore Wind and Wave Energy for Turkey' Ankara, Turkey 11-15<sup>th</sup> of September, 2017 at Middle East Technical University, Ankara. Organized by British Council and Royal Society of Chemistry.

(2) Development of three-dimensional graphene network for use in regenerative Alzheimer's stem cell culture, Oral presentation, SPIE Biophotonics Conference, University of St. Andrews, 2-5 November, 2016.

(3) Bio-imaging of lung diseases using luminescent graphene nanocrystals, Oral presentation, 11<sup>th</sup> IEEE Nanotechnology Materials and Devices Conference (NMDC 2016), 9-12 October 2016, Toulouse France, IEEE proceedings (NMDC), 2016 (pp. 1-2). IEEE.



- (4) 'Porous graphene for effective drinking water decontamination' in "Indo-UK Workshop: Clean Water through Advanced and Affordable Materials. Chennai, India 8-10 August 2016." Organized by British Council and Royal Society of Chemistry.
- (5) Can luminescent graphene quantum dots help us diagnose skin cancer? Postgraduate Research Showcase 2016, University of Exeter, 25-27 April, 2016.
- (6) Luminescent graphene quantum dots as a cancer theranostic agent, The Exeter Imaging Network (EIN), University of Exeter, UK, 1<sup>st</sup> February 2016.
- (7) Biocompatibility of graphene quantum dots intraperitoneally administrated in rabbits—effects of dose and exposure protocols, The 21<sup>st</sup> International Biomedical Science and Technology Symposium Antalya, Turkey 22-24th October, 2015, Organized by European Society of Biomaterials.
- (8) *In Vivo* toxicity and biodistribution of water soluble self-passivated graphene quantum dots, Oral presentation at The 22<sup>nd</sup> CSCST-SCI conference Renewable Energy and Novel Materials for sustainable future, Birmingham, 19th September, 2015.
- (9) Synthesise and characterization of water soluble self-passivated graphene quantum dots, The 9<sup>th</sup> International Congress on Advanced Electromagnetic Materials in Microwaves and Optics, 7-10 September 2015. University of Oxford, UK, IEEE proceedings.

## List of abbreviations

<b>2D</b>	Two dimensional	<b>LPCR</b>	large platelet concentration ration
<b>3D</b>	Three dimensional	<b>LYM</b>	Lymphocytosis
<b>Å</b>	Angstrom, 10 <sup>-10</sup> m	<b>mAb</b>	Monoclonal antibody
<b>ALB</b>	Albumin	<b>MCH</b>	Mean corpuscular haemoglobin
<b>ALP</b>	Alkaline phosphatase	<b>MCHC</b>	Mean corpuscular hemoglobin concentration
<b>ALT</b>	Alanine transaminase	<b>MCV</b>	Mean corpuscular haemoglobin
<b>AP-1</b>	Activator protein-1	<b>MDA</b>	Malondialdehyde
<b>Ar</b>	Argon	<b>MID</b>	Mid-range absolute count
<b>AST</b>	Aspartate transaminase	<b>ml</b>	Millilitre, 10 <sup>-6</sup> L
<b>BET</b>	Brunauer, Emmett and Teller method	<b>MPC</b>	Mean platelet component
<b>BUN</b>	Blood urea nitrogen	<b>µg</b>	Microgram
<b>CAT</b>	Catalase	<b>nm</b>	Nanometer
<b>CSI</b>	Cardio-somatic index	<b>N<sub>2</sub></b>	Nitrogen gas
<b>CVD</b>	Chemical vapour deposition	<b>NaNO<sub>3</sub></b>	Sodium nitrate
<b>Cath D</b>	Cathepsin D	<b>NaCl</b>	Sodium chloride
<b>Cath L</b>	Cathepsin L	<b>NF-κB- NF kappa B</b>	Nuclear factor kappa-light-chain-enhancer of activated B cells
<b>CRE</b>	Creatinine	<b>NH<sub>3</sub></b>	Ammonia
<b>DMSO</b>	Dimethyl sulfoxide	<b>Nrf2</b>	Nuclear factor erythroid-derived 2-like 2
<b>EDS</b>	Energy dispersive X-ray spectrometer	<b>PBS</b>	Phosphate buffered saline
<b>et al.</b>	<i>et alia</i> ; and others	<b>PDT</b>	Pphotodynamic therapy
<b>FT-IR</b>	Fourier Transform Infrared	<b>PI</b>	Propidium iodide
<b>GF</b>	Graphene foam	<b>PL</b>	Photoluminescence
<b>GGT</b>	γ-glutamyltransferase	<b>PLT</b>	Platelet count
<b>GLU</b>	Glucose	<b>PPa</b>	Pyropheophorbide-a
<b>GO</b>	Graphene oxide	<b>PTEN</b>	Phosphatase and tensin homolog deleted on chromosome 10
<b>GOT</b>	Glutamic oxaloacetic transaminase	<b>Rb</b>	Retinoblastoma
<b>GP</b>	Gaussian process	<b>RBC</b>	Red blood cell count
<b>GQDs</b>	Reduced graphene oxide	<b>RDW</b>	Red cell distribution width
<b>GRA</b>	Total % of granulocytes	<b>ROS</b>	Reactive oxygen species
<b>GSH</b>	Glutathione	<b>RONs</b>	Reactive oxygen and nitrogen species
<b>GSI</b>	Gonado-somatic Index	<b>rGO</b>	Reduced graphene oxide
<b>GST</b>	Glutathione-S-transferase	<b>RSI</b>	Renato-somatic Index
<b>HBGL</b>	Hemoglobin	<b>SEM</b>	Scanning electron microscopy
<b>HCT</b>	Haematocrit	<b>SOD</b>	Superoxide dismutase
<b>H &amp; E</b>	Haemotoxylene-eosin	<b>SISI</b>	Small intestine somatic index
<b>Hh</b>	Hedgehog	<b>Sp1</b>	Specificity protein 1
<b>HIF-1α</b>	Hypoxia-inducible factor-1 alpha	<b>SSI</b>	Spleeno-somatic Index
<b>H<sub>2</sub>O</b>	Water	<b>STAT3</b>	Signal transducer and activator of transcription 3
<b>HRTEM</b>	High resolution transmission electron microscopy	<b>TBIL</b>	Total bilirubin
<b>HSI</b>	Hepato-somatic index	<b>TEM</b>	Transmission electron microscopy
<b>H<sub>2</sub>O<sub>2</sub></b>	Hydrogen peroxide	<b>TCHO</b>	Total cholesterol
<b>H<sub>2</sub>SO<sub>4</sub></b>	Sulfuric acid	<b>UV/Vis</b>	Ultraviolet/Visible
<b>KMnO<sub>4</sub></b>	Potassium permanganate	<b>WBC</b>	White blood cell count
<b>L</b>	Litre	<b>XRD</b>	X-ray diffraction

## List of Schemes

<b>Scheme 1.1:</b> A schematic illustration of the biological applications of graphene-based materials, the potential mechanism of toxicity and graphene-mediated reactive oxygen and nitrogen species (RONS) generation.....	24
<b>Scheme 2.1:</b> Schematic representation of a typical theranostic platform for the combined use of a range of imaging and therapeutic approaches.....	34
<b>Scheme 2.2:</b> Summary of structural models of various derivatives of graphene. (a) Graphene, (b) graphene oxide (GO), (c) reduced graphene oxide, (d) porous graphene, (e) graphene quantum dots and (f) three-dimensional graphene foam.....	35
<b>Scheme 2.3:</b> Schematic illustration of the potential mechanisms by which reactive oxygen species (ROS) are associated with the cellular toxicity of graphene.....	41
<b>Scheme 2.4:</b> Cell signaling and molecular targets of ROS in cancer.....	43
<b>Scheme 2.5:</b> Schematic representations of the mechanism involved in singlet oxygen production and their synergistic effects in programmed cell death induced by combined photodynamic and photothermal therapies using a graphene nanocomposite as a photosensitizer.....	46
<b>Scheme 3.1:</b> Schematic diagram of a SEM.....	56
<b>Scheme 3.2:</b> Illustration of TEM system.....	57
<b>Scheme 3.3:</b> Schematic layout of UV/Vis spectrometer.....	58
<b>Scheme 3.4:</b> Energy diagrams for light scattering: Rayleigh (elastic) vs. Raman (inelastic).....	59
<b>Scheme 3.5:</b> A schematic of an interferometer used in a Fourier Transfer Infrared Spectrometer (FTIR).....	60
<b>Scheme 6.1:</b> Schematic illustration of the potential mechanisms of action of graphene nanopores (GNPs).....	126

## List of Figures

<b>Figure 4.1:</b> Proposed mechanism of cathepsin function in cancer metastasis and use of graphene oxide as an adsorbent to remove cathepsin from a living system.....	71
<b>Figure 4.2:</b> The percentage of living and dying A549 and SKMES-1 lung carcinoma cells before and after graphene oxide treatment.....	81
<b>Figure 4.3:</b> Characterization of cathepsin D (CathD) and cathepsin L (CathL).....	85
<b>Figure 4.4:</b> Effect of different concentrations of GO on CathD and CathL activities..	88
<b>Figure 4.5:</b> Kinetic models fitting to the data for CathD and CathL using piecewise linear regression analysis of the adsorption experiments of CathD and CathL on GO.....	89
<b>Figure 4.6:</b> (A-B) FT-IR spectra of CathD/CathL-linked graphene oxide (GO) at 50, 500, and 1000 $\mu\text{g/ml}$ concentrations of GO. (C-D) Raman spectra of CathD/CathL-linked GO at 50, 500, and 1000 $\mu\text{g/ml}$ GO concentrations (E-F) Contact angle profiles of CathD/CathL-linked GO interfaces at 50, 500 and 1000 $\mu\text{g/ml}$ concentrations of GO. Diiodomethane contact angle was measured to calculate the surface energy of enzymes, GO and their interfaces. (G-H) Surface energy profile of GO- CathD/CathL interfaces which have three segments of total surface energy, dispersive surface energy and polar surface energy of 50, 500 and 1000 $\mu\text{g/ml}$ concentration of GO treated with CathD and CathL .....	93
<b>SI Figure 4.1:</b> Transmission electron microscopy image of graphene oxide.....	97
<b>SI Figure 4.2:</b> Raman spectrum of the graphene oxide sample shows intense D ( $1358\text{ cm}^{-1}$ ) and G peaks ( $1595\text{ cm}^{-1}$ ) of defects and the in-plane stretching motion of pairs of $\text{sp}^2$ atoms, respectively.....	97
<b>SI Figure 4.3:</b> BET surface area of graphene oxide measured by nitrogen sorption isotherms measured at $-196\text{ }^{\circ}\text{C}$ . The BET surface area value obtained for this sample using the BET method is $25\text{ m}^2/\text{g}$ .....	98
<b>SI Figure 4.4:</b> Representative zeta potential of graphene oxide over a range of different pH values. ....	98
<b>SI Figure 4.5:</b> Fourier transformer infrared (FTIR) spectrum of graphene oxide shows vibrations of functional groups of C-O-C ( $\sim 1000\text{ cm}^{-1}$ ), C-O ( $1230\text{ cm}^{-1}$ ), C=C ( $\sim 1620\text{ cm}^{-1}$ ), C=O ( $1740\text{--}1720\text{ cm}^{-1}$ ) bonds and O-H ( $3600\text{--}3300\text{ cm}^{-1}$ ).....	99

<b>SI Figure 4.6:</b> (A) UV/Vis absorption spectra of graphene oxide solutions with different concentrations (from 0.039-10 mg/ml) show the main peak around 232 nm. (B) The plot of the absorbance ( $\lambda_{\text{ex}} = 232 \text{ nm}$ ) divided by the cell length, versus the concentration, given by the Lambert–Beer law ( $A = \alpha/C$ ), which determined the absorption coefficient ( $\alpha$ ) related to the absorbance per unit path length $A/l$ . This linear relationship fits well with the Lambert-Beer Law, indicating the good water solubility of the GO product. ....	99
<b>SI Figure 4.7:</b> XRD pattern recorded for graphene oxide shows a (001) peak at $2\theta$ of $13.7^\circ$ . ....	100
<b>SI Figure 4.8:</b> Gaussian process (GP) regression models for cell survival rates of A549 ( <i>left</i> ) and SKMES-1 ( <i>right</i> ) cells interacted with various concentrations of reduced Graphene Oxide (rGO). The green solid lines show the mean GP prediction, while the light green areas around the mean show the uncertainty (one standard deviation) in prediction. The models are trained with the data indicated by the red crosses. ....	101
<b>SI Figure 4.9:</b> Effect of different concentrations of GO on CathD and CathL fluorescence activities. GO at different concentrations (50, 500, and 1000 $\mu\text{g/ml}$ ) were incubated with CathD(A, B) and CathL (C, D) in 96 well plates at different time-points (2, 5, 10, 15, and 20 mins) as shown. Data (symbols) are shown together with guides to the eye (connecting lines). Fluorescence signals were determined using plate reader at Ex/Em: 355/460nm. ....	103
<b>Figure 5.1:</b> (A)- TEM and (B) HRTEM images of as-prepared exfoliated rGO sheets. ....	112
<b>Figure 5.2:</b> (A)- XRD pattern, (B)- Raman spectrum, (C) FTIR spectrum, and (D) Zeta potential-pH curve of as-prepared rGO. ....	113
<b>Figure 5.3:</b> Bar graphs quantifying the percentage of dead, living, early-stage apoptotic, and late-stage apoptotic cells in response to different concentrations of reduced graphene oxide (rGO). Flow cytometry for A549 and SKMES-1 lung carcinoma cells stained with annexin V (apoptosis) and propidium iodide (PI; late apoptosis and necrosis) following 24 h of treatment with various concentrations of rGO (0–1000 $\mu\text{g/ml}$ ). (A) graphic representation of percentage of living cells (B) early apoptosis (C) necrosis, (D) late apoptosis (flow cytometry) in response to rGO. Data were represented as mean $\pm$ SD, n.s., * $p < 0.05$ vs control (0 $\mu\text{g/ml}$ ). ....	114

<b>Figure 5.4:</b> Gaussian process (GP) regression models for cell survival rates of A549 ( <i>left</i> ) and SKMES-1 ( <i>right</i> ) cells interacted with various concentrations of reduced Graphene Oxide (rGO). The green solid lines show the mean GP prediction, while the light green areas around the mean show the uncertainty (one standard deviation) in prediction. The models are trained with the data indicated by the red crosses.....	115
<b>Figure 5.5:</b> Representative FACS images and analysis of one experiment. Data were presented as percentage of the cell population. Cell viability of A549 (upper panel) and SKMES-1 (lower panel) at selected concentrations. Experiments were performed and interpreted as follows: Annexin V <sup>-ve</sup> /PI <sup>-ve</sup> cells (lower left quadrant), AnnV <sup>+ve</sup> /PI <sup>-ve</sup> cells (lower right quadrant), AnnV <sup>+ve</sup> /PI <sup>+ve</sup> (upper right quadrant) and AnnV <sup>-ve</sup> /PI <sup>+ve</sup> (upper left quadrant) were considered as living, early apoptotic, late apoptotic, and necrotic cells respectively .	116
<b>Figure 6.1:</b> Basic characterization of as-prepared GNPs.....	133
<b>Figure 6.2.</b> Bar graph quantifying the percentage of dead, living, early-stage apoptotic, and late-stage apoptotic cells in response to different concentrations of porous graphene (GNPS) .....	135
<b>Figure 6.3:</b> Representation of FACS images and analysis of one experiment. Data are presented as percentage of the cell population. ....	137
<b>Figure 6.4:</b> Daily body weight (g) of control groups and treated groups exposed to GNPs along with intraperitoneal injection of rats for 27 days.....	138
<b>Figure 6.5:</b> (A-O) Complete blood count in rats after 27 days of GNPs administration. Rats (n=8 per group) were intraperitoneally injected with single doses of 5 mg/kg body weight and 15 mg/kg body weight and multiple doses of 5 mg/kg body weight and 15 mg/kg body weight of rats .....	139
<b>Figure 6.6:</b> Liver and kidney enzyme functions results in rats after 27 day post GNPs administration. Rats (n=8 per group) were intraperitoneally injected with single doses of 5 mg/kg body weight (group 1), 15 mg/kg body weight (group 2) and multiple doses of 5 mg/kg body weight (group 3) and 15 mg/kg body weight (group 4). Values are expressed as mean $\pm$ standard deviation, for: A) Alanine transaminase (ALT), B) Aspartate transaminase (AST), C) alkaline phosphatase (ALP) and D) creatinine.....	141

**Figure 6.7:** Representative histopathological changes of the liver, kidney and heart of the GNPs-exposed and control rats in the haemotoxyline-eosin (H&E) stained sections after 27 days. The doses of GNPs were 5 and 15 mg/kg for the single-dose exposure and 5 and 15 mg/kg (every other day, in total fourteen injections) for the multiple-dose exposure ..... 143

**Figure 6.8:** Representative histopathological changes of the brain, testis and lung of the GNPs-exposed and control rat in the haemotoxyline-eosin (H&E) stained sections after 27 days. The doses of GNPs were 5 and 15 mg/kg for the single-dose exposure and 5 and 15 mg/kg (every other day, in total fourteen injections) for the multiple-dose exposure..... 145

**Figure 6.9:** Biomarkers of oxidative stress results in rats after 27 days of GNPs administration. Rats (n=8 per group) were intraperitoneally injected with single doses of 5 mg/kg body weight (group 1), 15 mg/kg body weight (group 2) and multiple doses of 5 mg/kg body weight (group 3) and 15 mg/kg body weight (group 4). Values are expressed as mean  $\pm$  standard deviation, for: A) MDA, B) hydroperoxide, C) GSH, and D) catalase..... 147

**SI Figure 6.1:** Exposure schedule of graphene nanopores (GNPs) administration in rats. Rats were intraperitoneally injected with GNPs in a period of 27 days to test at single and multiple doses of GNPs (5 and 15 mg/kg) to analyse blood biochemistry, organo-somatic index, liver and kidney enzymes functions analysis, oxidative stress biomarkers and histological examinations. All of these testing has been carried out at day 27..... 152

**SI Figure 6.2:** Organosomatic indices of organs in different groups of rats at 14 days after intravenous administration. All treated groups showed statistically no significant differences from the control group..... 153

**SI Figure 6.3:** Representative histopathological changes of the liver, kidney and heart of the GNPs-exposed and control rat in the haemotoxyline-eosin (H&E) section after 14 days. The doses of GNPs were 5 and 15 mg/kg for the single-dose exposure and 5 and 15 mg/kg (every other day, in total fourteen injections) for the multiple-dose exposure..... 154

**SI Figure 6.4:** Representative histopathological changes of the brain, testis and lung of the GNPs-exposed and control rat in the haemotoxyline-eosin (H&E) section after 14 days. The doses of GNPs were 5 and 15 mg/kg for the single-dose exposure and 5

and 15 mg/kg (every other day, in total fourteen injections) for the multiple-dose exposure.....	156
<b>Figure 7.1:</b> Water solubility, wetting transparency and surface energy of GQDs.....	166
<b>Figure 7.2:</b> Fluorescence intensity of trypsin, substrate and trypsin+substrate as a function of time and substrate concentration.....	167
<b>Figure 7.3:</b> Effect of different concentrations of GQDs on trypsin activity. GQDs at different concentrations (150, 125, 100, 75, 50 and 25 µg/ml) were incubated with 1 % trypsin in 96 well plates at different time-points (2, 5, 10, 15, 30 and 60mins) as shown.....	169
<b>Figure 7.4:</b> FT-IR spectra of trypsin-linked GQDs. (A) 25, (B) 50, (C) 75, (D) 100, (E) 125, and (F) 150 µg/ml GQDs concentration .....	171
<b>Figure 7.5:</b> Raman spectra of trypsin-linked GQDs. (A) 25 and (B) 150 µg/ml.....	172
<b>Figure 7.6:</b> Contact angle profiles of trypsin-GQDs interfaces at 25 and 150 µg/ml concentrations of GQDs. (A) water contact angle of interface from 5 to 60 mins. (B) DIIO contact angle of interface from 5 to 60 mins. ....	174
<b>Figure 7.7:</b> Water contact angle and surface energy profile of GQDs-trypsin interfaces from 0 to 60 mins. (A) water contact angle (B) total surface energy (C) dispersive surface energy and (D) polar surface energy of 25 µg/ml, 50 µg/ml, 75 µg/ml, 100 µg/ml, 125 µg/ml and 150 µg/ml concentration of GQDs treated with trypsin.....	175
<b>SI Figure 7.1:</b> Basic characterization of GQDs. (A) Transmission electron microscopy image of GQDs showing their regular diameter, round shape and spatial distribution. Scale bar: 200 nm. (B) FTIR spectrum of the GQDs showing vibrations of different functional groups. (C) Raman spectrum of the GQDs showing the D ( $1355\text{cm}^{-1}$ ) and G peaks ( $1580\text{ cm}^{-1}$ ). (D) Photoluminescence spectrum of the GQDs.....	177
<b>SI Figure 7.2:</b> Luminescence property and emission diagram of GQDs. PL spectra of GQDs at the excitation wavelength of 340, 350, 360, 370 and 380 nm. The strongest photoluminescence emission occurs at 460 nm.....	178
<b>SI Figure 7.3:</b> FTIR of 1% trypsin showing vibrations of C=N at $1629\text{ cm}^{-1}$ , stretching modes of O–H and C–O–C at $1100\text{-}1200\text{ cm}^{-1}$ , and stretching vibration of C–H at $3300\text{-}3550\text{ cm}^{-1}$ .....	179
<b>SI Figure 7.4:</b> Trypsin contact angle measurements with water (left, $45^\circ$ ) and DIIO (right, $42^\circ$ ) .....	179



<b>Figure 8.1:</b> Basic characterization of as prepared graphene foam (GF) (A, B) Scanning electron microscopy (SEM) images of GF representing its porous network, (C) a photograph of a piece of GF .....	188
<b>Figure 8.2:</b> (A) Raman spectroscopy and (B) XRD of GF with Cu-Ka radiation ( $\lambda$ 0.154 nm) operated at 40 kV and 40 mA .....	188
<b>Figure 8.3:</b> Cytotoxicity and fluorescence imaging of 3D graphene foam. (A) Alamar Blue™ cell viability assay test on U87 seeded on GF and polystyrene samples over 28 days, (B) SEM images of cells cultured on GF-based scaffold and (C, D) immunofluorescence image of U87 cells seeded on 3D GF for 21 days at magnifications of 200 and 100 $\mu$ m .....	190
<b>Figure 8.4 (A,B):</b> Blood analysis of common carp exposed to GF as a function of dose level after 7 days. These results showed mean and standard deviations of ALB: albumin (d/dL), BUN: blood urea nitrogen (mg/dL), CRE: creatinine (mg/dL), TBIL: total bilirubin (mg/dL) and B: NH <sub>3</sub> : ammonia ( $\mu$ g/dL), GLU: glucose (mg/dL), TCHO: total cholesterol (mg/dL), ALP: alkaline phosphates ( $\mu$ L), GOT/AST: glutamic oxaloacetic transaminase/Aspartate Aminotransferase ( $\mu$ L), GPT/ALT: alanine aminotransferase ( $\mu$ L) and GGT: $\gamma$ -glutamyltransferase ( $\mu$ L). Data are presented as mean $\pm$ SE ( $n = 3$ ).....	191
<b>Figure 8.5:</b> Glutathione-S-transferase (GST) activity in different organs of the common carp exposed to various concentrations of GF for different times: (A) 24 h (B) 48 h (C) 96 h (D) 7 days. Data are presented as mean $\pm$ SE ( $n = 3$ ).....	193
<b>Figure 8.6:</b> Catalase (CAT), activity in different organs of the common carp exposed to various concentrations of GF for different times: (A) 24 h (B) 48 h (C) 96 h (D) 7 days. Data are presented as mean $\pm$ SE ( $n = 3$ ).....	194
<b>Figure 8.7:</b> Superoxide dismutase (SOD) activity in different organs of the common carp exposed to GF for different times: (A) 24 h (B) 48 h (C) 96 h (D) 7 days. Data are presented as mean $\pm$ SE ( $n = 3$ ).....	195
<b>Figure 8.8:</b> H & E stained light micrographs of <i>Cyprinus carpio</i> {heart (a–d), kidney (e–h) and liver tissues (i–l)} treated with GF in a dose dependent manner.....	197
<b>SI Figure 8.1:</b> Mean and standard deviations of body weight of common carp treated with GF show no statistically substantial changes over a period of 7 days. Data are presented as mean $\pm$ SE ( $n = 3$ ) .....	200
<b>SI Figure 8.3:</b> H & E stained light micrographs of <i>Cyprinus carpio</i> {heart (A-D), kidney (E-H) and liver tissues (I-L)} treated with GF in dose dependant manner after 5 days.	

Figures A,B, E,F and I,J show normal histology of heart, kidney and liver. Figures C,D, G-H and K-L show histological alterations in dose dependent manner in selected tissues. Details of histological alterations are given in Table S2. All the images were taken at 50µm scale bar ..... 203

## List of Tables

<b>SI Table 4.1:</b> Characteristic IR bands of the protein linkages.....	102
<b>SI Table 4.2:</b> Kinetic parameters obtained for CathD and CathL for GO using intraparticle diffusion model .....	102
<b>SI Table 8.1:</b> Histological changes in fish after treatment with GF for 7 days. Histological changes were observed in both control and treated groups and indicated by '+' and '-' (where + means this is found in particular tissue, '++' means this is highly noted in particular tissue, and '-' means it is not found in the tissue).....	203
<b>SI Table 8.2:</b> Histological changes in fish after treatment with GF for 5 days. Histological changes were observed in both control and treated groups and indicated by '+' and '-' (where '+' means this is found in particular tissue, '++' means this is highly noted in particular tissue, and '-' means it is not found in the tissue).....	205

# Chapter 1

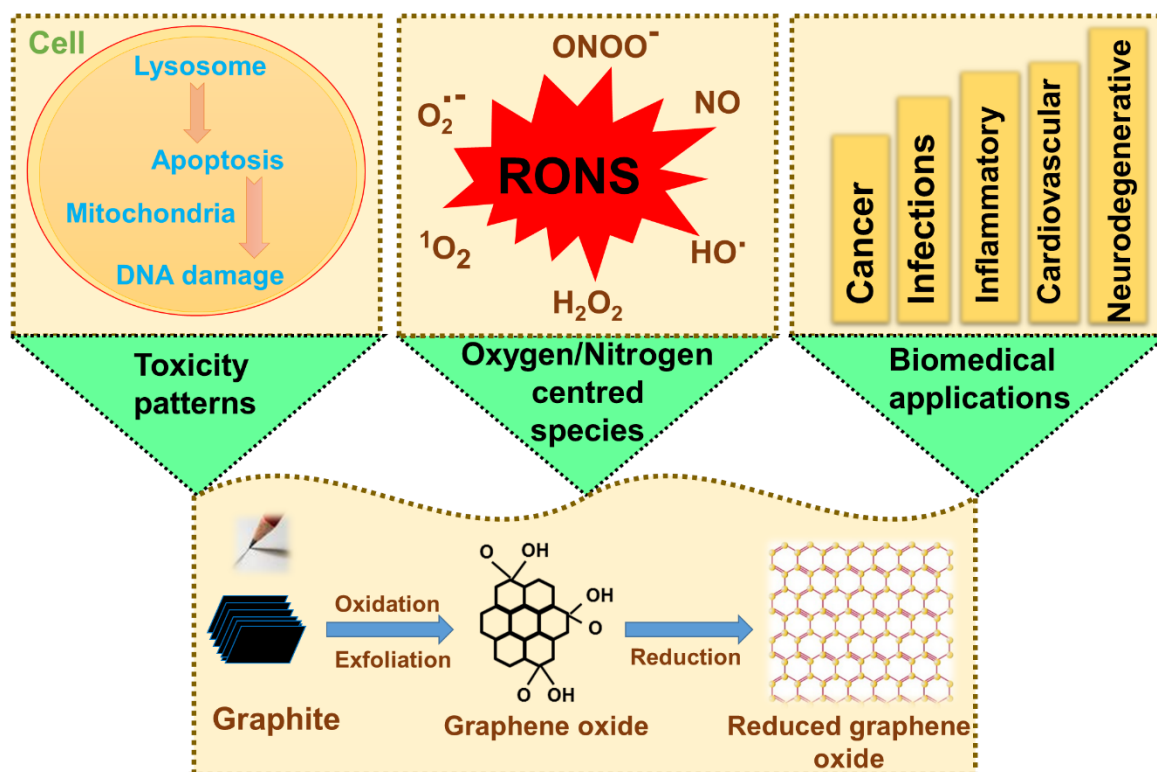
## Introduction

---

### 1.1 Background

The use of graphene is becoming well established in the fields of photonics and electronics, but it is only now, with the technologies maturing, that it is branching out into new areas such as nanomedicine and synthetic biology. Its use promises to revolutionise clinical settings across the board in areas including, but not limited to, drug delivery systems for theranostics, high throughput biosensors and bioassay, smart scaffolds for tissue regeneration, and ultra-high sensitivity biomarkers [1-3]. Graphene is the archetypal monolayer framework of carbon atoms, forming the basis of carbon nanotubes, fullerenes, and graphite [4]. Graphite is composed of stacked graphene layers, each layer being one atom thick and composed of  $sp^2$  hybridised carbon atoms packed in a hexagonal lattice [5]. The unique and tunable features of different derivatives of graphene (including pristine graphene, graphene oxide, reduced graphene oxide, graphene quantum dots, nanoribbons and nanoplatelets, three dimensional graphene foam, and many others) promises many new approaches in medical interventions, where its high specific surface area, exceptional electrical and thermal characteristics, and high strength could be a boon for drug delivery techniques [6-8] (**See scheme 1.1**). Their lateral dimensions and thickness can be tuned between nano- to milli-metres and mono- to few-layers, respectively. In addition, their two-dimensional nature can be modified to zero, one and three-dimensional assemblies [9]. Graphene-based materials are perhaps the first systems that allow us to take advantage of such a tunability approach, improving the accumulation of drug vehicles and contrast agents at specific target sites in different diseases. Applications of graphene in the biomedical field are currently in their early stages, and over the past decade, the use of nanostructured graphene in cancer diagnosis and therapy along with their potential toxic effects have become increasingly important. The continuous and widespread exposure of graphene-based materials raises urgent occupational, environmental and health concerns to living organisms. The first study on graphene in drug delivery was reported by the Hongjie Dai group in 2008,

demonstrating that doxorubicin, a widely utilised anticancer drug, can be loaded to nano-graphene oxide (tagged with antibody) for *in vitro* targeting of tumors [10]. Since then, many significant studies on graphene-based materials for drug delivery systems, bio-imaging, and biosensors have been reported [11,12].



**Scheme 1.1:** A schematic diagram of the biological applications of graphene-based materials, the potential mechanism of toxicity and graphene-mediated reactive oxygen and nitrogen species (RONS) generation. The lower panel represents the preparation and structures of graphene oxide and reduced graphene oxide. Chemical preparation of graphene is generally carried out by oxidation and exfoliation of graphite flakes while reduced graphene oxide is prepared by reduction of graphene oxide using a variety of reducing agents, such as sulphur, hydrazine and nitrogen, which helps eliminate the functional groups existing on the surface of graphene. The upper right panel refers to the applications of graphene in the biomedical field such as cancer, infectious, inflammatory, and cardiovascular and neurodegenerative diseases and the middle panel represents the oxygen and nitrogen centred radicals such as hydroxyl radical ( $\cdot\text{OH}$ ), hydrogen peroxide ( $\text{H}_2\text{O}_2$ ), superoxide ( $\cdot\text{O}-2$ ), singlet oxygen ( $^1\text{O}_2$ ),  $\text{ONOO}^-$  (peroxynitrite), nitric oxide ( $\text{NO}$ ). The left panel shows the potential toxic pathways of graphene within a cell such as cell cycle arrest, apoptosis, damage to the cell membrane, mitochondrial and DNA damages.

Nanomedicine refers to the application of nanotechnology to healthcare management, which aims to develop and implement new mechanisms, platforms, and treatment options for the diagnosis and treatment of human diseases. This paradigm has widely been benefited by cancer research and care in recent years [13]. The preparation of graphene nanostructures is at the forefront of anticancer nanomedicine. Graphene-based materials have extensively been exploited for standard treatment options, including surgical resection, alongside therapeutic strategies (such as chemotherapy, radiotherapy, and photodynamic therapy) [14-16]. The graphene nanostructures designed and reported so far in the literature reveal remarkable efficacy for their *in vitro* and *in vivo* applicability against several malignant tumors and cell lines; nevertheless, the physiochemical interaction of graphene nanostructures with cells and biological tissues needs to be explored to better achieve their bio functionality and reduced side effects [17-19]. Some of these studies have reported higher toxicity levels of graphene compared to other nanoparticles [20]. Although recent studies have demonstrated their *in vitro* and *in vivo* anti-cancer applicability in nanomedicine, there still exists a critical need to explore the potential health benefits and risks of these materials in living models [21,22]. *In vivo* toxicity findings for acute, sub-chronic and chronic circulation, biodistribution, and clearance of nanomedicines are not fully understood. Furthermore, the influence of surface chemistry of graphene-based materials for protein adsorption has not been studied [23].

It has become evident that the protein adsorption is vital in biomedical engineering to determine the hemo- and biocompatibility and biological relevant properties of nanomaterials [24]. The high adsorption capacities of such nanomaterials could make them an ideal candidate for progressive loading of high molecular weight drugs and their control release at targeted sites. Similarly, high specific adsorption of pro-metastatic enzymes can be a promising strategy to remove and clear out such enzymes in various cancers. For example, cathepsin D and cathepsin L are overexpressed extracellular enzymes in several human cancers [25]. Each enzyme plays an important role in directing cancer development, proliferation, and metastasis within the tumor microenvironment [26, 27]. Therefore, it is important to discover novel therapeutic treatment strategies to target such pro-metastatic enzymes to impede metastasis. With further discoveries on innovative biocompatible adsorbent interactions with enzymes

and advances in adsorbent delivery to tumor microenvironments, the class of graphene nanostructures could prove to be important vehicles to deliver, deactivate and clear out pro-metastatic enzymes used as novel therapies for disease management. Taken together, the current challenges in developing the next generation of graphene-based platform for cancer therapeutics are: 1) toxic effect of graphene nanostructures on cancer cells and biological tissues; 2) Interaction of the most abundant proteins with graphene; and 3) adsorption of extracellularly found pro-metastatic enzymes by graphene-based materials for their selective and targeted clearance for the point-of-care management and treatment of cancer. This thesis takes these challenges into account to contribute to the contemporary anticancer nanomedicine research.

## **1.2 Specific aims and overview of the thesis**

The translation of current advances in graphene-based anticancer nanomedicine have the potential to address important unmet needs and to transform healthcare. To make it happen *via* this project, it is hypothesised that the development of graphene structures could play an important role in cancer treatment.

**Sub-hypotheses:** (i) Graphene oxide could target and adsorb extracellular cathepsin D and cathepsin L in anti-metastatic enzyme cancer therapy; (ii) reduced graphene oxide could cause toxic effects on cancer cells by inducing programmed cell death; (iii) graphene nanopores could affect biological tissues at sub-chronic levels, affirming the limited biosafety of such nanopores which are not bioavailable for healthcare management; (iv) the interaction of graphene quantum dots and trypsin (the most abundant digestive protein) could lead to the formation of protein coronas and nano-bio-interfaces, which in turn could determine the ultimate fate of graphene quantum dots in enzyme engineering; (v) the bioavailability of three-dimensional graphene foam based scaffolds in biological tissues could allow cells to attach and regrow in a 3D microenvironment, as well as facilitate the development of novel regenerative medical treatments to help restore and strengthen lost functionality.

The primary research component of this thesis is focused on testing these hypotheses to achieve the aims of the project. The following were the set aims:

**Aim 1:** To demonstrate selective targeting of biocompatible graphene oxide for anti-metastatic enzyme cancer therapy, by assessing the adsorption capacity of graphene oxide to target and remove extracellular pro-metastatic and -tumourigenic enzymes cathepsin D and cathepsin L when exposed under different acidic conditions. This aim is to test sub-hypothesis (i).

**Aim 2:** To investigate the mechanism of cell death induced by reduced graphene oxide in lung cancer cells. This aim is to test sub-hypothesis (ii).

**Aim 3:** To develop a facile and scalable route for graphene nanopores preparation and to correlate targeting, intracellular destination, and local dissolution of as-prepared graphene nanopores with their toxicity mechanism in lung cancer cells and biological tissues. This aim is to test sub-hypothesis (iii).

**Aim 4:** To assess the integrative physiochemical interaction between trypsin and graphene quantum dots to determine their potential biological identity in enzyme engineering at different conditions of enzyme activity and concentration of quantum dots, as well as nature of their binding. This aim is to test sub-hypothesis (iv).

**Aim 5:** To investigate the *in vitro* and *in vivo* bioavailability of 3D graphene foam based scaffolds, and to address the role of physicochemical properties of graphene scaffolds in cell attachment and regrowth to reduce the side effects associated with cell regeneration, leading to potential effectiveness of stem cell therapy. This aim is to test sub-hypothesis (v).

### 1.3 Structure of the thesis

This thesis is divided into 9 chapters. **Chapter 1** presents an overview of this thesis and defines the hypothesis, aims and significance of the work. **Chapter 2** will describe the features, development, toxicity mechanism and application of graphene-based materials in cancer treatment. **Chapter 3** will present the various analysis techniques used in this thesis. **Chapter 4** is the first experimental chapter. It will discuss the

development of highly adaptable and straightforward GO-based strategies for the rapid and facile removal of pro-metastasis enzymes that could effectively rescue the disease. **Chapter 5** will present the *in vitro* toxic effects and limited bioavailability of unmodified reduced graphene oxide on lung cancer cells. **Chapter 6** will present the novel synthesis of graphene nanopores and further *in vitro* and *in vivo* investigations into the toxicity and biocompatibility of graphene nanopores on lung cancer cells and organs of rats. This is to elucidate the toxicity mechanism by analysing the oxidative stress and subsequent programmed cell death in time and dose dependent manner. **Chapter 7** will describe the interactions of graphene quantum dots with trypsin to elucidate the general fate of these dots in biological systems as a potential substrate for efficient enzyme immobilisation, separation, and purification approaches. **Chapter 8** will focus on the fabrication and biocompatibility of three-dimensional porous graphene foam-based scaffolds to investigate cell viability, attachment and growth within 3D microenvironments promoting their potential biostability, survival, integration, enhanced differentiation, and synergistic cell control signals. **Chapter 9** will summarise the key findings, their impact, and future directions of this work for the progress of nanomedicine and biomedical engineering fields.

## 1.4 Significance of the thesis

The overall goal of this research work is to contribute to the fundamental understanding of graphene nanostructures in anticancer nanomedicine, enabling a biomedical research market that would allow these translational technologies to solve real-world clinical problems. Current state-of-the-art methodologies based on graphene nanostructures are limited primarily through pre-clinical constraints as outlined earlier, such as non-specific targeting of malignant tumors alongside side effects on normal cells, as well as cost effectiveness of such materials [28]. This thesis involves zero to three-dimensional sized structures of graphene. The research work will contribute in four broad and valuable ways to expanding the knowledge of anticancer nanomedicine. Firstly, this work has revealed that graphene oxide, with its variable zeta potential, variety of functional groups and very large (and in principle fully accessible) surface area, is an ideal candidate for the adsorption and inhibition of cathepsin D and cathepsin L, which in turn could enhance the anti-metastatic



challenges faced in breast and ovarian cancers. Given the therapeutic challenges posed by secreted cathepsin D and L in breast and ovarian cancers, a fuller clearance of these proteins before their involvement in secondary tumour formation may aid development of new treatment modalities. Additionally, graphene oxide nanostructures are easy to manufacture and are stable, which simplifies long-term storage and correspondingly reduces the cost. Secondly, this work demonstrates the toxicological effects of reduced graphene oxide and graphene nanopores to look at their biosafety profile for clinical applications. Furthermore, the novel, facile and scalable synthesis of graphene nanopores was carried out *via* thermal treatment of reduced graphene oxide. Graphene nanopores are also promising candidates for DNA sequencing, but their toxicological implications have not been studied before. *In vivo* toxicity findings for long term acute, sub-chronic and chronic circulation, biodistribution, specific targeting within diseased cells and clearance of nanomedicines have not been fully understood. Thirdly, for the first time, the interaction of graphene quantum dots with trypsin and the impact of graphene quantum dots on the adsorption of enzymes was evaluated. Investigation into such interactions could play an increasingly important role in bionanotechnology and enzyme engineering to assess the biocompatibility of such biomaterials in applications of blood purification, biocatalysis, and in drug delivery as a vehicle for loading of high molecular weight drugs and metabolites. Lastly, a biocompatible 3D graphene-based scaffold was designed to be used in cell regeneration and growth. Currently, there is no *in vivo* and *in vitro* toxicity study available for the side effects of this type of scaffold on biological tissues for potential applications in stem cell and regenerative therapies.

In summary, this work is a key step in the roadmap for the progressive integration of graphene nanostructures to be practical in a clinical setting. With further discoveries arising from the interplay between nanostructured graphene and biological systems, and advances in the delivery of graphene-based materials to tumor microenvironments, the class of graphene nanostructures described here will prove to be important vehicles to deliver nanodrugs and clear out pro-metastatic enzymes in the point-of-care management and treatment of cancer.

## References:

- [1] Kostarelos, K., & Novoselov, K. S. (2014). Exploring the interface of graphene and biology. *Science*, 344(6181), 261-263.
- [2] Ferrari, A. C., Bonaccorso, F., Fal'Ko, V., Novoselov, K. S., Roche, S., Bøggild, P., & Garrido, J. A. (2015). Science and technology roadmap for graphene, related two-dimensional crystals, and hybrid systems. *Nanoscale*, 7(11), 4598-4810.
- [3] Bitounis, D., Ali-Boucetta, H., Hong, B. H., Min, D. H., & Kostarelos, K. (2013). Prospects and challenges of graphene in biomedical applications. *Adv. Mater.* 25(16), 2258-2268.
- [4] Kostarelos, K., & Novoselov, K. S. (2014). Graphene devices for life. *Nat. Nanotechnol.* 9(10), 744-745.
- [5] Allen, M. J., Tung, V. C., & Kaner, R. B. (2009). Honeycomb carbon: a review of graphene. *Chem. Rev.* 110(1), 132-145.
- [6] Liu, J., Cui, L., & Losic, D. (2013). Graphene and graphene oxide as new nanocarriers for drug delivery applications. *Acta Biomater.*, 9(12), 9243-9257.
- [7] Sun, X., Liu, Z., Welsher, K., Robinson, J. T., Goodwin, A., Zaric, S., & Dai, H. (2008). Nano-graphene oxide for cellular imaging and drug delivery. *Nano Res.* 1(3), 203-212.
- [8] Mei, K. C., Rubio, N., Costa, P. M., Kafa, H., Abbate, V., Festy, F., & Al-Jamal, K. T. (2015). Synthesis of double-clickable functionalised graphene oxide for biological applications. *Chem. Commun.* 51(81), 14981-14984.
- [9] Tiwari, J. N., Tiwari, R. N., & Kim, K. S. (2012). Zero-dimensional, one-dimensional, two-dimensional and three-dimensional nanostructured materials for advanced electrochemical energy devices. *Prog. Mater. Sci.* 57(4), 724-803.
- [10] Sun, X., Liu, Z., Welsher, K., Robinson, J. T., Goodwin, A., Zaric, S., & Dai, H. (2008). Nano-graphene oxide for cellular imaging and drug delivery. *Nano Res.* 1(3), 203-212.
- [11] Bitounis, D., Ali-Boucetta, H., Hong, B. H., Min, D. H., & Kostarelos, K. (2013). Prospects and challenges of graphene in biomedical applications. *Adv. Mater.* 25(16), 2258-2268.
- [12] Tabish, T. A., Pranjol, Z., Hayat, H., Rahat, A., Abdullah, T. M., Whatmore, J., & Zhang, S. (2017). In vitro toxic effects of reduced graphene oxide nanosheets on lung cancer cells. *Nanotechnology*, 28(50), 504001-504008.
- [13] Yang, K., Feng, L., Shi, X., & Liu, Z. (2013). Nano-graphene in biomedicine: theranostic applications. *Chem. Soc. Rev.* 42(2), 530-547.
- [14] Feng, L., Wu, L., & Qu, X. (2013). New horizons for diagnostics and therapeutic applications of graphene and graphene oxide. *Adv. Mater.* 25(2), 168-186.
- [15] Tian, B., Wang, C., Zhang, S., Feng, L., & Liu, Z. (2011). Photothermally enhanced photodynamic therapy delivered by nano-graphene oxide. *ACS Nano*, 5(9), 7000-7009.

- [16] Goenka, S., Sant, V., & Sant, S. (2014). Graphene-based nanomaterials for drug delivery and tissue engineering. *J. Controlled Release*, 173, 75-88.
- [17] Yang, K., Zhang, S., Zhang, G., Sun, X., Lee, S. T., & Liu, Z. (2010). Graphene in mice: ultrahigh in vivo tumor uptake and efficient photothermal therapy. *Nano Lett.* 10(9), 3318-3323.
- [18] Markovic, Z. M., Harhaji-Trajkovic, L. M., Todorovic-Markovic, B. M., Kepić, D. P., Arsić, K. M., Jovanović, S. P., & Trajkovic, V. S. (2011). In vitro comparison of the photothermal anticancer activity of graphene nanoparticles and carbon nanotubes. *Biomaterials*, 32(4), 1121-1129.
- [19] Bussy, C., Jasim, D., Lozano, N., Terry, D., & Kostarelos, K. (2015). The current graphene safety landscape—a literature mining exercise. *Nanoscale*, 7(15), 6432-6435.
- [20] Seabra, A. B., Paula, A. J., de Lima, R., Alves, O. L., & Durán, N. (2014). Nanotoxicity of graphene and graphene oxide. *Chem. Res. Toxicol.* 27(2), 159-168.
- [21] Zhou, L., Wang, W., Tang, J., Zhou, J. H., Jiang, H. J., & Shen, J. (2011). Graphene oxide noncovalent photosensitizer and its anticancer activity in vitro. *Chem-Eu J.* 17(43), 12084-12091.
- [22] Liu, G., Shen, H., Mao, J., Zhang, L., Jiang, Z., Sun, T., & Zhang, Z. (2013). Transferrin modified graphene oxide for glioma-targeted drug delivery: in vitro and in vivo evaluations. *ACS Appl. Mater. Inter.* 5(15), 6909-6914.
- [23] Seredych, M., Mikhalovska, L., Mikhalovsky, S., & Gogotsi, Y. (2018). Adsorption of Bovine Serum Albumin on Carbon-Based Materials. *C*, 4(1), 1-14.
- [24] Roach, P., Farrar, D., & Perry, C. C. (2005). Interpretation of protein adsorption: surface-induced conformational changes. *J. Amer. Chem. Soc.* 127(22), 8168-8173.
- [25] Pranjol, M. Z. I., Gutowski, N., Hannemann, M., & Whatmore, J. (2015). The potential role of the proteases cathepsin D and cathepsin L in the progression and metastasis of epithelial ovarian cancer. *Biomolecules*, 5(4), 3260-3279.
- [26] Tandon, A. K., Clark, G. M., Chamness, G. C., Chirgwin, J. M., & McGuire, W. L. (1990). Cathepsin D and prognosis in breast cancer. *New Eng. J. Med.* 322(5), 297-302.
- [27] Chauhan, S. S., Goldstein, L. J., & Gottesman, M. M. (1991). Expression of cathepsin L in human tumors. *Cancer Res.* 51(5), 1478-1481.
- [28] Tabish, T. A., Zhang, S., & Winyard, P. G. (2018). Developing the next generation of graphene-based platforms for cancer therapeutics: The potential role of reactive oxygen species. *Redox Biol.* 15, 34-40

## Chapter 2

### Literature Review

---

Graphene has a promising future in applications such as disease diagnosis, cancer therapy, and drug/gene delivery, bio-imaging and antibacterial approaches owing to graphene's unique physiochemical and mechanical features alongside minimal toxicity, and photo-stability. However, these unique features and bioavailability of graphene are fraught with uncertainties and concerns for environmental and occupational exposure. Changes in the physicochemical properties of graphene affect biological responses including reactive oxygen species (ROS) production. Lower production of ROS by currently available theranostic agents, *e.g.* magnetic nanoparticles, carbon nanotubes, gold nanostructures or polymeric nanoparticles, restricts their clinical application. Oxidative stress induced by graphene accumulated in living organs is due to acellular factors which may affect physiological interactions between graphene and target biological tissues and cells. Acellular factors include particle size, shape, surface charge, surface containing functional groups, and light activation. Cellular responses such as mitochondrial respiration, graphene-cell interactions and pH of the medium are also determinants of ROS production. The mechanism of toxicity for nanostructured graphene is poorly understood. This chapter describes the structures, properties, preparation methods, mechanism of toxicity and biomedical applications of graphene.

#### **2.1 Structures and properties of graphene nanostructures**

Cancer is one of the leading causes of morbidity and mortality worldwide, with more than 14 million new cases and 8.8 million deaths in 2012 [1]. Globally, cancer accounts for nearly one of every six deaths. Cancer elicits a significant economic cost. The total annual economic cost of cancer in 2010 was estimated at approximately US\$ 1.16 trillion [2]. Conventional therapeutic options including chemotherapy and radiation therapy are most commonly used in the treatment of cancer. However, these modalities yield low success rates and have profound adverse side effects on patients'

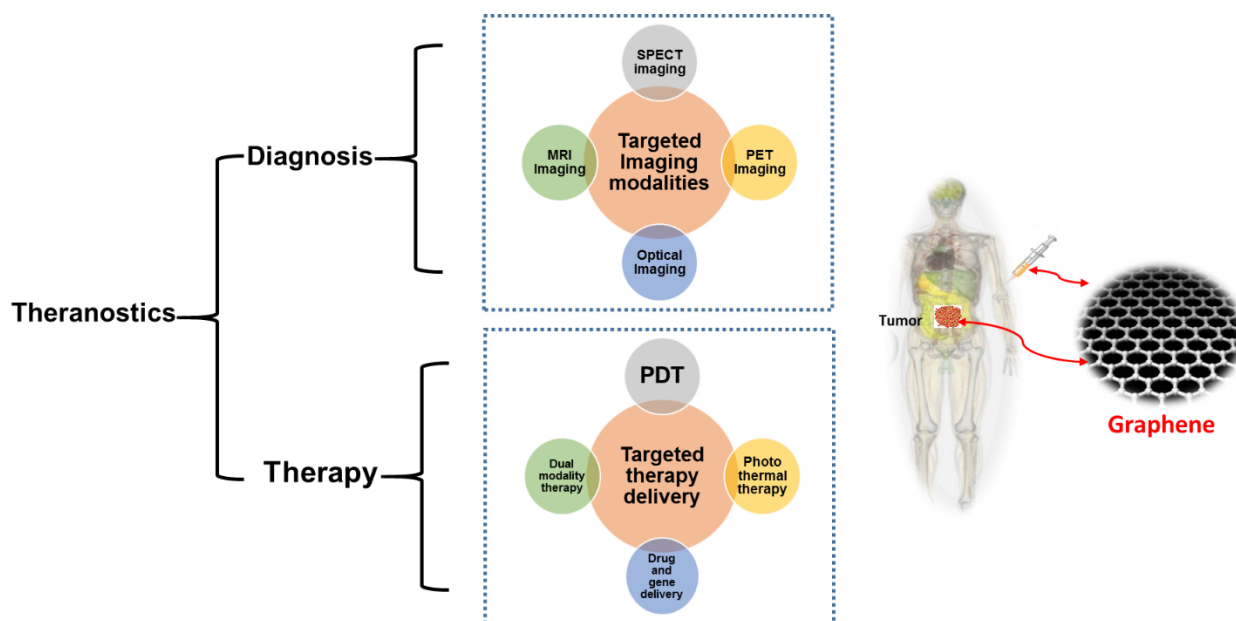
physical and mental health [3]. Therefore less invasive, and more effectively targeted, treatments need to be developed for palliative care and improvement of quality of life. Novel regimes for simultaneous diagnosis and therapy, known as theranostics, have changed the cancer treatment algorithm by the combination of bio-imaging with site-specific and site-selective targeting of tumors, without damaging normal cells [4]. A schematic representation of the components of a typical theranostic platform is given in **Figure 2.1**.

The two key components of this theranostic platform are: first, targeted diagnostic imaging modalities and, secondly, targeted delivery of therapies such as photodynamic therapy (PDT). An excellent review of targeted diagnostic imaging has recently been contributed by Cope et al (2016) [5]. PDT has evolved into a practical, effective and systematic theranostic option comprising of the multiple-exposure, guided, non-invasive, treatment of tumors in combination with real-time detection and tracking of malignant tissue by fluorescence imaging. The basis of PDT is that light is utilised to trigger a photosensitizer, leading to the generation and localization of highly toxic reactive oxygen species (ROS) at the targeted site of cancerous tissue. PDT offers several advantages over traditional treatment options, typically including low toxicity of the photosensitizer in the absence of light interaction/irradiation, better efficacy, low side effects, selective and specific accumulation, and deep penetration of photosensitizer into the tumors [6]. Nevertheless, the mechanism of the selective and specific killing of tumor cells by ROS remains unclear. A better understanding of this phenomenon will empower patients and clinicians with a greater confidence in this treatment option.

A key feature of PDT is to exploit the light source for selective activation of the photosensitizer within the tumor cells. A light source of appropriate wavelength (visible or near-infrared) is utilised to activate a photosensitizer that generates and releases ROS, for the selective killing of tumors [7]. The photo-activation of the photosensitizer initially enables its excitation to a triplet state through a short-lived intermediate called the 'singlet state'. The electron and energy transfer to the surrounding free oxygen produces ROS, such as singlet oxygen, the superoxide anion radical, the hydroxyl

species, and hydrogen peroxide. Highly toxic ROS cause tumor cell death by oxidative stress.

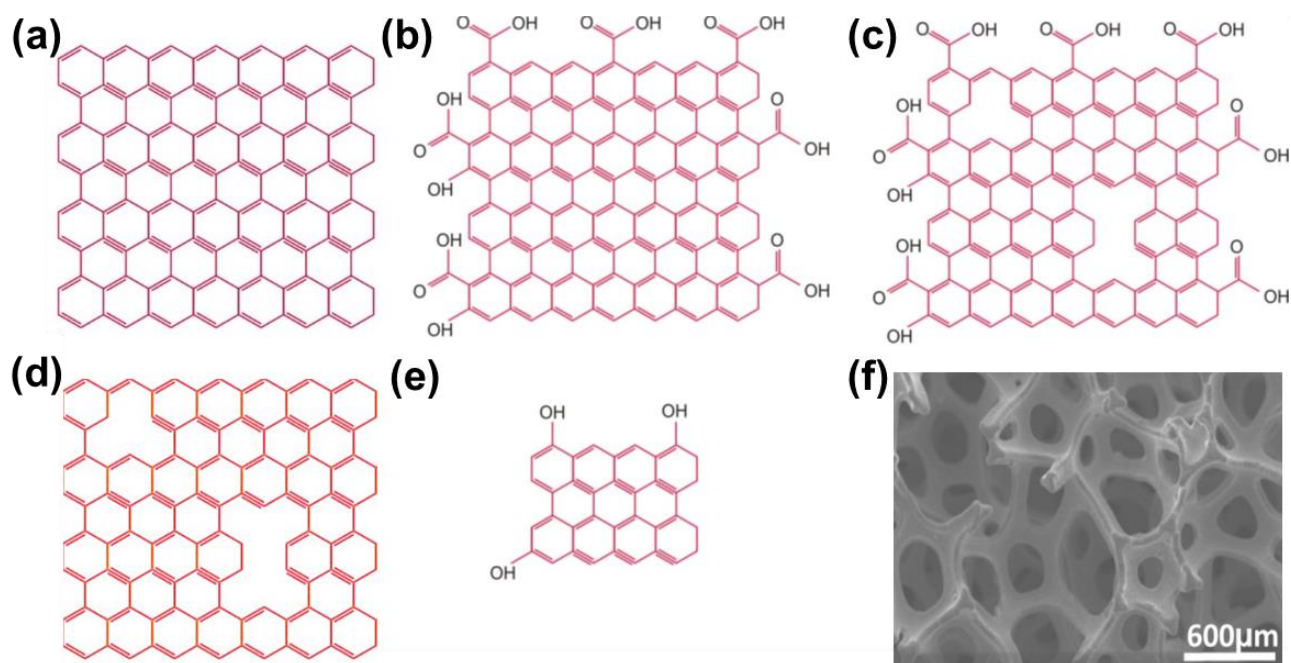
Historically, the development of photosensitizers has resulted in three eminent generations of photosensitizer types. The first generation was porphyrins [8]. The clinical limitations of porphyrins are poor selectivity, poor photosensitivity, a low clearance rate, and a low light penetration within tumors. The second generation of photosensitizers - including chlorins, porphyrinoids and transition metal complexes - also have several problems such as: high hydrophobicity, poor tumor selectivity, complex surface chemistry, and aggregation in aqueous media. The third generation includes biomolecule conjugates and covalently attached peptides [8]. The selection of biomolecules is critical for their clinical efficacy because of the selective targeting capability, the structural and photochemical properties of these conjugates, and the degree of receptor expression in the targeted tumors.



**Scheme 2.1: Schematic representation of a typical theranostic platform for the combined use of a range of imaging and therapeutic approaches.** Imaging modalities include: ultrasonography, positron electron tomography, fluorescence imaging, magnetic resonance imaging and single-photon emission computed tomography. Therapeutic approaches include: drug delivery, photothermal therapy, photodynamic therapy, or a combination of two therapies. Based on its unique properties, graphene can be employed as a theranostic agent that combines the capabilities of diverse imaging and therapeutic modalities to target tumors.

Recently, novel photosensitizers have been fabricated to improve the selective tissue penetration of incident light, and to improve the clinical efficacy of PDT. Among

such novel developments, graphene has also recently been fabricated and utilised as a photosensitizer and theranostic agent [9]. Graphene is a two-dimensional single-layer-thin material with  $sp^2$ -bonded carbon atoms composed in a honeycomb lattice. This material has gained significant attention in many disciplines of life science, owing to its electronic, optical and structural properties. Graphene has been applied as a drug vehicle in chemotherapy, and as a photosensitizer for photothermal therapy and PDT. A graphene nanohybrid showed improved anticancer PDT effects compared with the conventional photosensitizers [10]. Graphene has significant potential for use in theranostic agents owing to its unique characteristics, including a high surface area, appropriate energy and/or electron transfer features, a high fluorescence quantum yield,  $\pi$ - $\pi$  stacking, good water dispersibility, good biocompatibility, enhanced drug-loading efficiency, selective tumor uptake, minimal side effects and a high yield of ROS production. Graphene has a variety of derivatives including graphene oxide (GO), reduced graphene oxide, graphene quantum dots, graphene nanoribbons, three dimensional graphene foam and graphene nanopores. The structural models of several graphene derivatives are shown in **Figure 2.2**. GO is a highly efficient long-range quencher for various fluorescence processes [11].



**Scheme 2.2 Summary of structural models of various derivatives of graphene.** (a) Graphene, (b) graphene oxide (GO), (c) reduced graphene oxide, (d) porous graphene, (e) graphene quantum dots and (f) three dimensional graphene foam. Graphene is a  $sp^2$  hybridized model of carbon atoms in a repeated manner, forming a regular lattice structure (as shown in panel a), while GO and reduced

GO have functional groups and defects in their basal planes (panels b and c). The physicochemical properties and structures of different graphene variants depend on the fabrication method and conditions. The presence of both defects and functional groups provides potential advantages for the efficient utilisation of graphene variants in the production of ROS. The chemical exfoliation method is thought to be an efficient route for synthesizing graphene on a large scale and at low cost. Porous graphene is a graphene sheet that is missing carbon atoms from its plane. The various forms of porous graphene provides fascinating materials for biological applications owing to their high specific surface areas, hydrophobic nature and biocompatibility. Graphene nanopores usually have pore sizes of 1-30 nm. Pores and vacancies can clearly be seen in the porous graphene sheet, as shown in panel (d). Graphene quantum dots are luminescent nanocrystals having a size less than 50 nm. These have attractive properties and potential applications in cancer diagnosis and treatment. Water soluble graphene quantum dots, shown in panel (e), have functional groups (C–OH, C=O, C–O–C, C–H) on their surface. Three-dimensional graphene networks in the form of a foam, sponge or aerogel have recently been assembled from individual graphene sheets using chemical vapour deposition templated methods, which also preserve the unique properties of individual graphene sheets. [Panel f is adapted from [12], with permission of MDPI Publishing Group, Copyright 2015.]

The therapeutic responses of different derivatives of graphene such as GO and graphene quantum dots revealed them as promising treatment agents and showed the possibility of exploiting ROS in cancer treatment. A better understanding of the role of ROS in the therapeutic mode of action of graphene, in cancer treatment, will facilitate the development of improved graphene-based theranostic platforms.

## **2.2 Methods for graphene preparation**

The methods of preparing graphene-based materials mainly include mechanical exfoliation [13,14], chemical exfoliation [15,16], chemical reduction [17,18], bottom up and top-down approaches [19,20], unzipping of carbon nanotubes [21,22], chemical vapour deposition (CVD) methods [23-26], and epitaxial growth of graphene [27-29]. The methods employed for the production of graphene nanostructures (used in this work) are as follows:

### **2.2.1 Modified Hummer's Method**

There are several methods reported for the preparation of GO. In 1958, Hummer and his colleagues developed a method for preparing graphite oxide by the oxidation process of graphite flakes with the addition of sulfuric acid, sodium nitrate and potassium permanganate maintained below 45 °C for 2 h [31]. A combination of concentrated sulfuric acid, sodium nitrate and potassium permanganate lead to the formation of a highly oxidized product. The product was termed as graphite oxide, which was obtained after washing and centrifuging the oxidised product. This method



is also considered as a green route to prepare GO by exfoliation of graphite oxide to graphene oxide since 2004 [32]. The chemical exfoliation of GO is commonly carried out by using graphite flakes in  $\text{H}_2\text{SO}_4$  and  $\text{NaNO}_3$  to oxidize graphite flakes into graphite oxide. The chemical reaction for this step is:  $2 \text{NaNO}_3 + \text{H}_2\text{SO}_4 = 2 \text{HNO}_3 + \text{Na}_2\text{SO}_4$ . Oxidation by  $\text{HNO}_3$  may liberate gaseous  $\text{NO}_2$  and/or  $\text{N}_2\text{O}_4$ . The addition of  $\text{NaNO}_3$  increases the interlayer distance marginally, with improved basal planes oxidation of graphite. As a result, graphite flakes are broken into the smallest sheets (single or few layers) with the maximum functionalization on the basal planes. However, many modifications have recently been carried out to this technique to enhance the product yield and to increase the reproducibility of properties of single or few layered graphene [33].

### **2.2.2 Chemical reduction of graphene oxide**

Chemical reduction of GO is considered as one of the most promising and extensively used method to prepare reduced graphene oxide, owing to its scalability and relative ease of reduction flexibility [34, 35]. After the exfoliation of GO, several reducing agents have been employed to reduce the functional groups and achieve 'graphene' such as sodium borohydride [36], oxygen-containing reducing agents [37], ascorbic acid [38], hydrohalic acid [39] and sulfur [40]. However, technical drawbacks related to these reduction methods, such as insufficient reducing capability, agglomeration and poor wetting properties of graphene, have been reported in literature [41]. Hydrazine is the commonly used reducing agent to reduce the functional groups and also to enhance surface area and porosity [42, 43]. In this thesis, hydrazine has been used to prepare reduced GO.

### **2.2.3 Heat treatment of reduced graphene oxide**

Recent developments in the preparation of porous graphene and graphene nanopores (GNPs) offer new opportunities to design advanced materials with enhanced adsorption capacities and improved sequencing of DNA [44-46]. Available routes to prepare GNPs include electron beam irradiation [47], ion bombardment [48], doping [49], chemical etching [50], chemical methods [51] and solution deposition method [52]. Unfortunately, these methods are very expensive and not viable for practical

applications due to non-uniform amounts of porous nanostructured graphene. In this thesis, GNPs have been developed by a facile and scalable conversion of reduced GO into porous reduced graphene oxide via thermal treatment. Theoretically, graphene has a surface area of  $2630 \text{ m}^2 \text{ g}^{-1}$ . However, experimentally determined values for porous rGO are generally less than  $200 \text{ m}^2 \text{ g}^{-1}$  [53-57]. This method includes the oxidation of graphite flakes to form graphite oxide and further exfoliation for 2 h in an ultrasonic bath to attain GO, followed by reduction using hydrazine as a reducing agent. To obtain GNPs, the filtered product was oven-dried in a vacuum overnight and then thermally treated at  $200^\circ\text{C}$  in Ar for 12 h. Additionally, the temperature range involved in this treatment process was ( $190\text{--}200^\circ\text{C}$ ), which was lower than that previously reported for the synthesis of porous rGO ( $800^\circ\text{C}$ ) [54-56].

#### **2.2.4 Bottom-up approach**

Currently, the methods to prepare GQDs include bottom-up and top-down approaches [58, 59], hydrothermal processes [60], lithography [61] and electrochemical routes [62, 63]. Many of these methods suffer from low product yield, high number of layers and agglomerated dots and cost-effectiveness, and the problems associated with the separation and purification of the condensed amorphous carbon phase from low crystalline carbon blacks and fibres [64-66]. The resultant product of this partial separation and purification is an oxidized graphite framework and graphene oxide QDs rather than GQDs [67]. In this thesis we have used a bottom-up approach to prepare GQDs by tuning the carbonization degree of citric acid, which is a commonly used organic precursor. This process involved heating citric acid to  $200^\circ\text{C}$ , using a heating mantle, for 30 mins to obtain a GQDs solution. In this method, citric acid can be carbonized to form water soluble photo luminescent GQDs which contain small  $\text{sp}^2$  clusters in a uniform size and excitation-dependent photoluminescence features [68].

#### **2.2.5 CVD method**

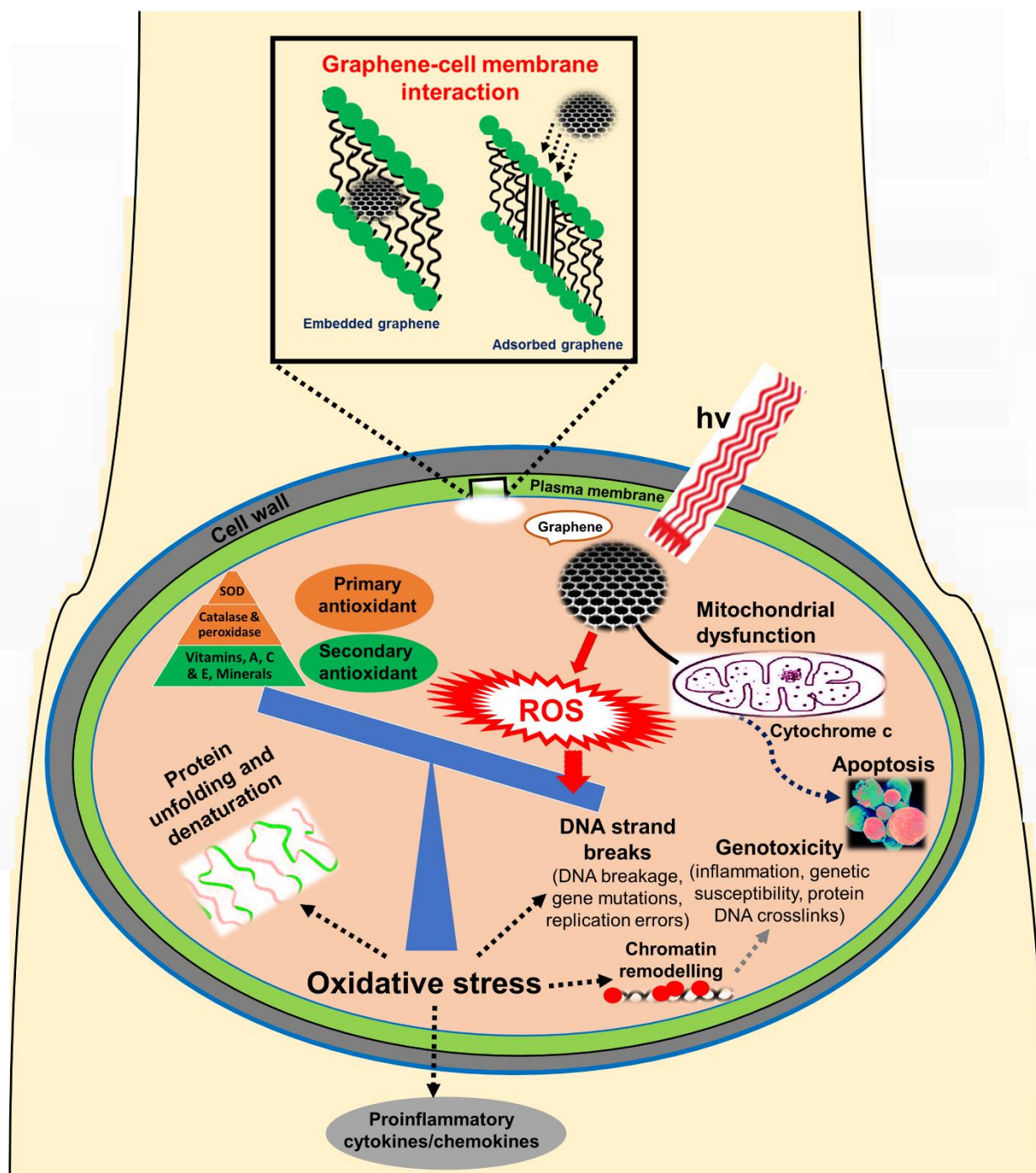
It is evident that CVD is an efficient route to prepare high quality graphene on a substrate, making efficient growth possible using a carbon source as precursor on a substrate under high temperature conditions [69-72]. The CVD preparation of graphene has several advantages over other methods, such as the large size and high

quality of the graphene [73]. The only drawback of this kind of method is that this is only suitable for experimental purposes because of its low production along with high cost [74]. This is an effective approach to prepare 3D graphene foam [75-77]. In this work, we have used the CVD method to prepare graphene foam. This method involves heating and stabilizing Cu film, following by introducing a carbon precursor, cooling down the duration and etching in a solution. The last step involves the transference of prepared graphene to an appropriate substrate [78].

### **2.3 Toxic potential of graphene family nanomaterials**

ROS generation by nanoparticles has been considered as the primary source of their toxicity [79]. Potential adverse effects of ROS include the downregulation of defensive systems to disrupt the structure and function of normal cells. ROS cause damage to cellular components such as proteins, DNA and lipids, resulting in the release of inflammatory cytokines and chemokines. ROS generation by graphene is dependent on several factors that strongly define the extent of graphene-induced toxicity, such as: size and shape, particle surface, surface charges, surface-associated chemical groups, solubility and dispersion, ions released from graphene, photo-activation, aggregation, mode of interaction with cells, the presence of inflammation in tissues, and the pH of the system. In addition, the conditions of experiments in which graphene is administered, either *in vivo* or *in vitro*, affect the interactions between graphene and targeted biological tissues and cells. Such conditions include the time of exposure, dose, and (in the case of *in vitro* experiments) the cell type and the criterion used for examining cell viability. For *in vivo* models, the method of administration is also of course crucial [9]. Graphene can cause an inflammatory response that produces relatively large amounts of free radicals such as hydroxyl radicals [80]. GO at a low concentration (< 4 µg/ml) resulted in a perturbation of mitochondrial structure and function in Hep G2 cells, as measured by a decrease in the mitochondrial membrane potential and the dysregulation of mitochondrial Ca<sup>2+</sup> homeostasis, while higher concentrations of graphene quantum dots (< 200 µg/ml) also caused decreases in the mitochondrial membrane potential by increased ROS generation, in association with apoptotic and autophagic cell deaths, with an increase in the expression caspase 3, caspase 9, beclin 1, and microtubule-associated protein 1A/1B-light chain 3 [81, 82].

Apoptosis and autophagy are two key modes of cancer cell death, in addition to necrosis. Apoptosis is a widely studied form of cell death and mainly originates through the activation of death receptors (extrinsic pathway) or through mitochondrial permeabilization (intrinsic pathway). ROS play a key role in both the extrinsic and intrinsic pathways of apoptosis, as initiators and in enabling signaling events. The apoptosis-inducing ligand, Fas, produces ROS in the extrinsic pathway of the apoptotic process [83]. Activation of the extrinsic pathway requires an inflammatory response to tissue injury and may cause a delay in intrinsic pathway initiation that responds immediately to calcium and ROS. Oxidative stress may be associated with the intracellular accumulation of ROS. Moreover, increased intracellular ROS levels, with associated increases in apoptosis, were detected in murine RAW 264.7 macrophages exposed to graphene (20-100  $\mu\text{g/ml}$ ) [84]. Chang et al reported a concentration-dependent toxicity of GO on A549 cells *in vitro*, a concentration of 200  $\mu\text{g/ml}$  causing a dose-dependent oxidative stress in cells and inducing a loss of cell viability [85]. However it was also found that a low concentration of GO (10  $\mu\text{g/ml}$ ) did not enter A549 cells and had no obvious toxicity. The higher concentration of GO (200  $\mu\text{g/ml}$ ) caused oxidative stress and induced a slight loss of cell viability. Oxidative stress as a result of graphene-cell interactions may cause cell mutagenesis, carcinogenesis and ageing [86]. Graphene may cause mitochondrial toxicity that includes changes in mitochondrial calcium levels and depletion of the mitochondrial membrane potential. Graphene subsequently triggers apoptosis by the activation of mitochondrial pathways, namely the mitogen-activated protein kinase (MAPKs) and transforming growth factor- $\beta$  (TGF- $\beta$ )-related signaling pathways. Graphene has the potential to adsorb aromatic amino acids by  $\pi$ - $\pi$  stacking [87]. Recent *in vivo* and *in vitro* studies have shown the role of ROS in mediating the toxicity of graphene [12, 80-86, 88, 89]. A schematic illustration of the potential ROS-mediated mechanisms manifested by graphene in the cell is shown in **Figure 2.3**.



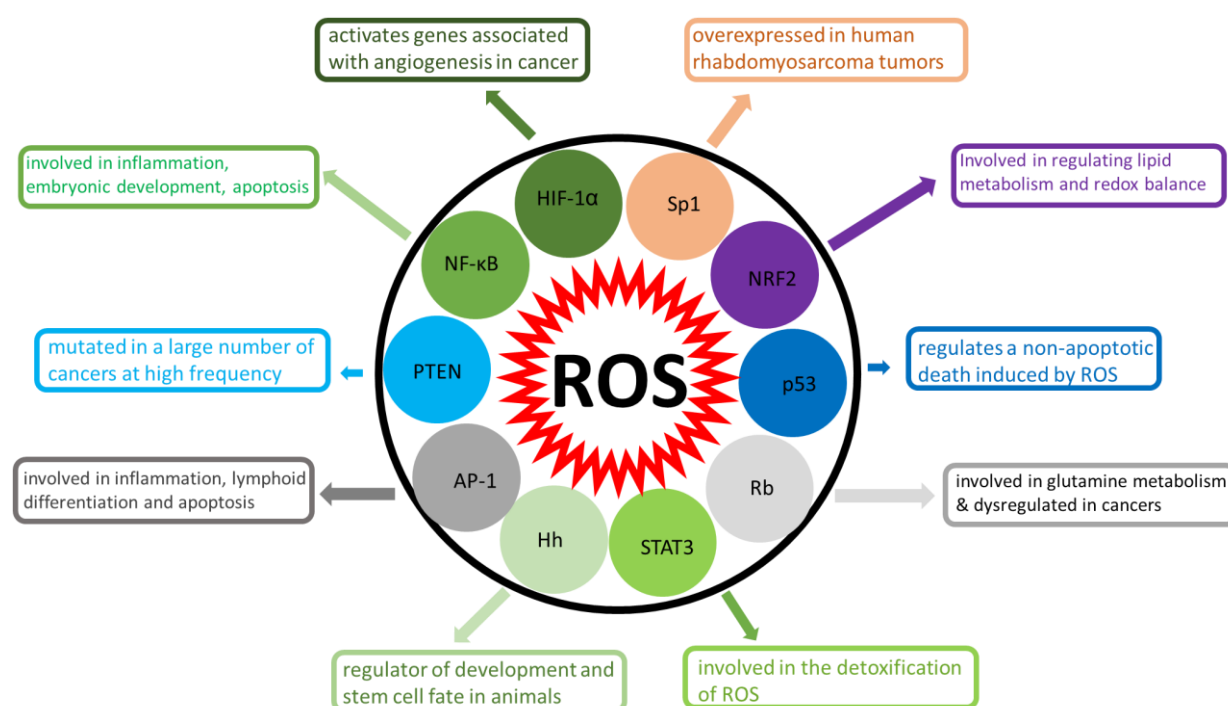
**Scheme 2.3** Schematic illustration of the potential mechanisms by which reactive oxygen species (ROS) are associated with the cellular toxicity of graphene. Graphene may affect biological behaviour at the cellular, subcellular, protein and gene levels. The toxicity of graphene depends on its physicochemical interactions and its accumulation in specific organs. Uptake of graphene into specific organs also affects cell function as a result of cellular changes within the organs. The deposition, distribution and clearance of graphene after entering into a living system is a major knowledge gap in understanding the toxicity of graphene. Graphene circulating in the bloodstream is internalized into cells through the plasma membrane. The plasma membrane is a selectively permeable membrane that transfers materials such as ions and nano-sized

proteins. Graphene (depending on its size, shape, and surface chemistry) enters the cell via different pathways such as clathrin/caveolar-mediated endocytosis, phagocytosis, macropinocytosis, and pinocytosis and exits the cell via the pathways of lysosome secretion, vesicle-related secretion, and non-vesicle-related secretion. The nature of plasma membrane interaction with graphene determines the fate of graphene in a wide range of potential applications with high biocompatibility, including drug- and gene-delivery, photothermal and photodynamic therapy. This interaction may lead to the possibility of events such as adsorption or incorporation of graphene onto the surfaces of cells. Furthermore, the entrapped biomolecules on the surface of graphene, when graphene is present within the extracellular matrix, may influence the tertiary structure of a protein - resulting in the formation of a protein-graphene interface and malfunction. The extracellular mechanisms causing the accumulation of graphene in the extracellular matrix and the subsequent effects of graphene on the extracellular matrix remain undefined. Graphene-induced ROS may cause oxidative stress, loss of cell function, mitochondrial damage, initiation of lipid peroxidation, covalent chemical modifications of nucleic acids, DNA-strand breaks, induction of gene expression via the activation of transcription factors, and modulation of inflammation via signal transduction, leading to toxicity, cell death and genotoxicity. The specific minerals in the secondary antioxidants are being referred to selenium, zinc, molybdenum, iron and copper. The antioxidant defence system is overwhelmed by high levels of ROS, leading to oxidative stress, inflammation and toxicity. One potential way to minimize the toxicity of graphene is to functionalize the graphene with biodegradable agents.

## **2.4 Graphene in enzyme engineering and cancer treatment**

Interaction of nanomaterials with proteins plays a critical role in investigating their biocompatibility for enzyme purification and wound healing applications. Recent developments in nanostructured graphene reveal promising approaches to bind and adsorb proteins which in turn influences their extracellular toxic potential. Pristine graphene, GO and rGO have recently been reported to show their interactions with enzymes [90-94]. Recent studies in this area reveal the binding capacity of graphene to influence the chemical changes and breakdown in the structures of enzymes by making protein coronas and nano-biointerfaces. Surface functionalities of GO make them an ideal candidate for enzyme adsorption. The electrostatic binding capacity,  $\pi$ - $\pi$  stacking and ionic/covalent bonding have been reported as main factors influencing their interactions with enzymes. High adsorption of enzymes onto the surface of graphene can lead to the adsorption of high molecular weight carrying drugs and biomarkers. Therefore, investigations into these interactions is of critical importance for practical applications of graphene in biomarkers, biosensing and medical devices.

The proof-of-concept investigations of graphene in cancer theranostics are still at a preclinical stage. An early report on GO as theranostic agent was published by Cho and his group [95]. They synthesized a GO-based photosensitizer with a redox-responsive disulfide linker which was activated by glutathione. This photosensitizer exhibited a remarkable fluorescence emission and singlet oxygen generation in the presence of glutathione as a reducing agent. There was efficient cellular internalization and preferential accumulation of the photosensitizer inside cancer cells, and glutathione was then able to cleave the disulfide linkers. Cho et al demonstrated *in vitro* cellular uptake and fluorescence activation of the photosensitizer, but they did not report the role of ROS in phototoxicity towards A549 cells. As mentioned earlier, ascertaining the type of ROS produced, the nature of intracellular ROS signaling, ROS localization, and cancer cell-specific ROS-sensing mechanisms are the most important challenges in relation to understanding the role of the ROS in cell killing by graphene. The molecular targets of ROS in cancer are shown in **Figure 2.4**. ROS may induce both transcription factors/activators and genes associated with tumor suppression [96].



**Scheme 2.4:** Cell signaling and molecular targets of ROS in cancer. ROS may induce both transcriptional factors/activators and genes associated with tumor suppression: HIF-1α (hypoxia-inducible factor-1 alpha); NF-κB (nuclear factor kappa-light-chain-enhancer of activated B cells); PTEN (phosphatase and tensin homolog deleted on chromosome 10); AP-1 (activator protein-1); Hh (hedgehog protein); STAT3 (signal

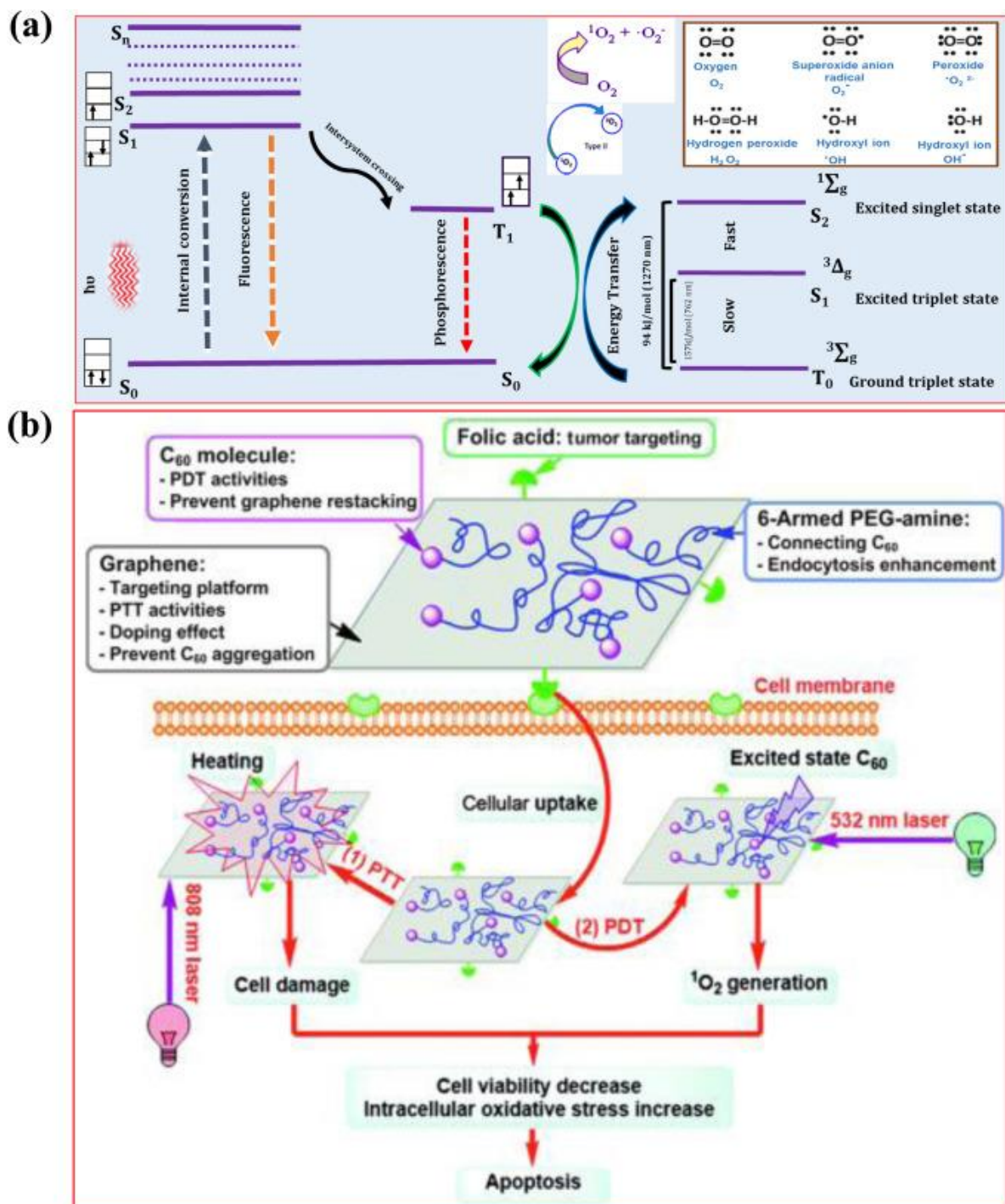
transducer and activator of transcription 3); Rb (retinoblastoma protein); Nrf2 (nuclear factor (erythroid-derived 2)-like 2); Sp1 (specificity protein 1). NF- $\kappa$ B and AP-1 are transcription factors that play key roles in the expression of many genes involved in inflammation as well as many other significant events such as embryonic development, lymphoid differentiation and apoptosis. HIF-1 $\alpha$  plays an essential role in embryonic vascularization and tumor angiogenesis. Nrf2, a redox-sensitive transcription factor, regulates genes which bind antioxidant response elements in DNA. PTEN is a tumor suppressor gene, which is deleted or mutated at high frequency in a large number of cancers. Rb protein is a tumor suppressor gene which controls cell cycle progression. Sp1 is a transcription factor which contributes to overexpression of MDM2 in rhabdomyosarcoma tumors. Stat 3 is a transcription factor which plays an important role in cell growth and apoptosis. ROS-mediated signaling through activation of these transcription factors controls the expression of genes involved in inflammation, metastasis, cell proliferation and tumor angiogenesis, as well as tumor cell death or survival.

Cancer cells possess an inherent nature of survival and re-growth [97]. Thus, the effectiveness of a therapy depends on the selective and specific targeting of tumors without producing chronic, severe, harm to vital organs and normal cells. Caspase activation by the intrinsic pathway leads to the release of: cytochrome c, a family of proteins known as “inhibitors of apoptosis proteins”, and endonuclease G. Release of these factors leads to the disintegration of mitochondrial membrane to form mitochondrial permeability transition pore complex. Cao et al prepared a multifunctional theranostic agent based on porphyrin-conjugated polyethylene glycol-functionalized graphene quantum dots [98]. These functionalized graphene quantum dots demonstrated a clear discrimination (as observed by the use of a cell imaging label and intracellular micro RNA detection) of cancer cells from somatic cells. The functionalized graphene quantum dots also exhibited a high production of singlet oxygen (quantum yield  $\leq 1.08$ ) with 28.58% photothermal conversion efficiency. Apoptotic events and cell membrane destruction were observed in A549 cells exposed to these porphyrin-conjugated polyethylene glycol-functionalized graphene quantum dots. However, porphyrin-based functionalized graphene quantum dots revealed a slightly slower  $^1\text{O}_2$  production rate compared with porphyrin alone. Wei et al prepared a nanodrug pyropheophorbide-a-nano GO-monoclonal antibody conjugate, within which the monoclonal antibody was directed against integrin  $\alpha_v\beta_3$  as a mechanism for tumor targeting [99]. The authors demonstrated that the phototoxicity of GO-bound pyropheophorbide can be switched on and off in both organic and aqueous



environments after the conjugation of pyropheophorbide with polyethylene-glycol. The functionalized GO efficiently targets the cancer cells' surface ligand (i.e. integrin  $\alpha_v\beta_3$ ). Once endocytosed by the cells, and having then escaped from lysosomes, the functionalized GO subsequently moves to the mitochondria. The two-fold on/off switching of this functionalized GO considerably increases the intrinsic pathway of apoptosis.

H<sub>2</sub>O<sub>2</sub>-induced apoptosis usually occurs in lymphoma cells via activation of cysteine proteases such as caspase-3 [100]. H<sub>2</sub>O<sub>2</sub> is a precursor of highly reactive hydroxyl radicals, while H<sub>2</sub>O<sub>2</sub> itself has relatively low reactivity. H<sub>2</sub>O<sub>2</sub> produced by nanoparticles has shown great potential to initiate apoptosis in the cells of osteosarcoma, breast, bladder, and lung cancer cells. He et al reported a nanoagent based on iron hydroxide/oxide-modified GO and showed a higher generation of superoxide anion radicals under near-infrared light irradiation, compared with GO alone [101]. In respect of this composite, it was proved that near-infrared light irradiation promoted electron transfer from GO to Fe(III) (endogenously present within the cells) and accelerated the formation of superoxide radicals. H<sub>2</sub>O<sub>2</sub> then reacted with Fe(II) and gave an improved yield of hydroxyl radicals. Excessive generation of ROS may contribute to necrotic cell death by inducing degradation of biomolecules and resulting in mitochondrial membrane permeabilization [102]. ROS may also cause both apoptosis and necrosis in tumors. Qu et al described GO-induced macrophagic cell death through programmed necrosis in J774A.1 cells and showed that GO toxicity is facilitated by activation of toll-like receptor 4 (TLR4) signalling [103]. Macrophage cell death linked to GO exposure was attributed to programmed necrosis mediated by a receptor-relating protein kinase 1 and 3 complex, downstream of TNF- $\alpha$  induction. A schematic illustration of the mechanisms by which photosensitizers generate <sup>1</sup>O<sub>2</sub>, and the mechanism by which the hybrid of folic acid polyethylene glycol and C<sub>60</sub> (a spherical fullerene molecule with the formula C<sub>60</sub> called buckminsterfullerene) conjugated onto GO (FA-GO-PEG/C<sub>60</sub>) achieves the combined synergistic effects of photothermal therapy and PDT are shown in **Figure 2.5 a & b**.



**Scheme 2.5:** Schematic representations of the mechanism involved in singlet oxygen production and their synergistic effects in programmed cell death induced by combined photodynamic and photothermal therapies using a graphene nanocomposite as a photosensitizer. Panel (a) shows a schematic illustration of the mechanisms of singlet oxygen ( $^1O_2$ ) generation by a photosensitizer, in the form of a Jablonski diagram representing the electronic states of a photosensitizer after light absorption, followed by energy transfer to an oxygen molecule to generate  $^1O_2$ . The photosensitizer displays intersystem crossing to the triplet state when the photosensitizer is excited to the singlet state. The electronic states are shown in the diagram. **Internal conversion:** transitions between states of similar electronic spin, where the electronic states are

singlet and triplet. **Fluorescence:** The emitted photon has energy resembling the energy difference between the initial and final states of the non-toxic photosensitizer. The emitting and final states have similar electronic spin states, either singlet or triplet. **Intersystem crossing:** the change of electronic spin in the excited state, from singlet to triplet. **Phosphorescence:** the emitted photon has energy resembling the energy difference between the initial and final states of the photosensitizer. The emitting and final states have different electronic spin states, such as one in the singlet state and the other in the triplet state. Panel **(b)** is a schematic illustration of the mechanism of cancer cell killing induced by a functionalized hybrid of folic acid (FA), polyethylene glycol (PEG) and C<sub>60</sub> (a spherical fullerene molecule with the formula C<sub>60</sub> called buckminsterfullerene) non-covalently conjugated to GO for synergistic combined photothermal therapy and photodynamic therapy. Thus, the functionalized hybrid consists of FA-GO-PEG/C<sub>60</sub> [FA (cancer targeting moiety) and C<sub>60</sub> (photosensitizer) conjugated to PEGylated graphene oxide]. Functionalized GO was exposed to near infrared light (808 nm) for enhanced cellular uptake of C<sub>60</sub> in cancer cells. The GO nanocomposite showed effective cell apoptosis and death and exhibited a synergistic effect of combined photodynamic and photothermal therapies. [Panel (b) is adapted from [10], with permission of the Royal Society of Chemistry, Inc., Copyright 2015].

## 2.5 Summary

In summary, recent studies underpin the potential of graphene in the theranostic field. Many groups have utilised graphene in PDT, photothermal therapy and fluorescent imaging for cancer treatment. The combination of imaging and therapy could produce synergistic effects to increase the targeted killing with minimal side effects and with the maintenance of biocompatibility. The scope for functionalization and conjugation of graphene can potentially generate a promising array of theranostic agents. Further *in vivo* studies are obligatory to better understand the real-world applications of nanostructured graphene. Moreover, the ROS generation, toxicity and potential cancer theranostic approaches for other derivatives of graphene such as graphene nanoribbons, graphene nanoplatelets, three dimensional graphene foams, and graphene nanopores need to be studied. Oxidative stress induced by graphene accumulated in living organs is due to acellular factors including particle size, particle shape, surface charge, surface functional groups, and light activation, while cellular responses such as mitochondrial respiration, and immune cell activation, pH of the medium and physiological redox-regulated functions are critical determinants affecting the production of ROS. To date, the mechanisms and roles of ROS production by most

forms of graphene in relation to cancer treatment, are not understood. A basic understanding of graphene-cell interactions, as well as the optimal conditions for their proper use, will provide new theranostic platforms in the future.

## 2.6 References

- [1] Ferlay, J., Soerjomataram, I., Ervik, M., Dikshit, R., Eser, S., Mathers, C., & Bray, F. (2013). Cancer Incidence and Mortality Worldwide: IARC CancerBase No. 11. Lyon, France: International Agency for Research on Cancer. GLOBOCAN 2012 v1. 0, 2013.
- [2] Stewart, B. W. K. P., & Wild, C. P. (2014). World cancer report 2014.
- [3] Johnstone, R. W., Ruefli, A. A., & Lowe, S. W. (2002). Apoptosis: a link between cancer genetics and chemotherapy. *Cell*, 108(2), 153-164.
- [4] Muthu, M. S., Leong, D. T., Mei, L., & Feng, S. S. (2014). Nanotheranostics-application and further development of nanomedicine strategies for advanced theranostics. *Theranostics*, 4(6), 660-677.
- [5] Cope, F. O., Abbruzzese, B., Sanders, J., Metz, W., Sturms, K., Ralph, D., & Behr, S. (2016). The inextricable axis of targeted diagnostic imaging and therapy: An immunological natural history approach. *Nucl. Med. Biol.* 43(3), 215-225.
- [6] Dolmans, D. E., Fukumura, D., & Jain, R. K. (2003). Photodynamic therapy for cancer. *Nat. Rev. Cancer* 3(5), 380-387.
- [7] Pye, A., Dogra, Y., Tyrrell, J., Winyard, P. G., & Curnow, A. (2009). Photodynamic Therapy with Aminolevulinic Acid and Iron Chelators: A Clinical Example of Redox Signaling. *Redox Signaling and Regulation in Biology and Medicine*, 351-372.
- [8] Gomer, C. J. (1991). Preclinical examination of first and second generation photosensitizers used in photodynamic therapy. *Photochem. Photobiol.* 54(6), 1093-1107.
- [9] Chen, D., Dougherty, C. A., Zhu, K., & Hong, H. (2015). Theranostic applications of carbon nanomaterials in cancer: Focus on imaging and cargo delivery. *J. Controlled Release*, 210, 230-245.
- [10] Hu, Z., Li, J., Huang, Y., Chen, L., & Li, Z. (2015). Functionalized graphene/C 60 nanohybrid for targeting photothermally enhanced photodynamic therapy. *RSC Adv.* 5(1), 654-664
- [11] Zhou, L., Wang, W., Tang, J., Zhou, J. H., Jiang, H. J., & Shen, J. (2011). Graphene oxide noncovalent photosensitizer and its anticancer activity in vitro. *Chem.-Eu. J.* 17(43), 12084-12091.
- [12] Tabish, T. A., Chabi, S., Ali, M., Xia, Y., Jabeen, F., & Zhang, S. (2017). Tracing the Bioavailability of Three-Dimensional Graphene Foam in Biological Tissues. *Materials*, 10(4), 1-13.
- [13] Yi, M., & Shen, Z. (2015). A review on mechanical exfoliation for the scalable production of graphene. *J. Mater. Chem. A* 3(22), 11700-11715.

- [14] Martinez, A., Fuse, K., & Yamashita, S. (2011). Mechanical exfoliation of graphene for the passive mode-locking of fiber lasers. *Appl. Phys. Lett.* 99(12), 121107-121110.
- [15] Hernandez, Y., Nicolosi, V., Lotya, M., Blighe, F. M., Sun, Z., De, S., & Boland, J. J. (2008). High-yield production of graphene by liquid-phase exfoliation of graphite. *Nat. Nanotechnol.* 3(9), 563-568.
- [16] Zhang, L., Liang, J., Huang, Y., Ma, Y., Wang, Y., & Chen, Y. (2009). Size-controlled synthesis of graphene oxide sheets on a large scale using chemical exfoliation. *Carbon*, 47(14), 3365-3368.
- [17] Abdolhosseinzadeh, S., Asgharzadeh, H., & Kim, H. S. (2015). Fast and fully-scalable synthesis of reduced graphene oxide. *Sci. Rep.* 5, 1-7.
- [18] Guex, L. G., Sacchi, B., Peuvot, K., Andersson, R. L., Pourrahimi, A. M., Strom, V., & Olsson, R. T. (2017). Experimental review: Chemical reduction of graphene oxide (GO) to reduced graphene oxide (rGO) by aqueous chemistry. *Nanoscale*, 9(27), 9562-9571.
- [19] Tour, J. M. (2013). Top-down versus bottom-up fabrication of graphene-based electronics. *Chem. Mater.* 26(1), 163-171.
- [20] Zhi, L., & Müllen, K. (2008). A bottom-up approach from molecular nanographenes to unconventional carbon materials. *J. Mater. Chem.* 18(13), 1472-1484.
- [21] Kosynkin, D. V., Higginbotham, A. L., Sinitskii, A., Lomeda, J. R., Dimiev, A., Price, B. K., & Tour, J. M. (2009). Longitudinal unzipping of carbon nanotubes to form graphene nanoribbons. *Nature* 458(7240), 872-876.
- [22] Shinde, D. B., Debgupta, J., Kushwaha, A., Aslam, M., & Pillai, V. K. (2011). Electrochemical unzipping of multi-walled carbon nanotubes for facile synthesis of high-quality graphene nanoribbons. *J. Amer. Chem. Soc.* 133(12), 4168-4171.
- [23] Reina, A., Jia, X., Ho, J., Nezich, D., Son, H., Bulovic, V., & Kong, J. (2008). Large area, few-layer graphene films on arbitrary substrates by chemical vapor deposition. *Nano Lett.* 9(1), 30-35.
- [24] Li, X., Cai, W., An, J., Kim, S., Nah, J., Yang, D., & Banerjee, S. K. (2009). Large-area synthesis of high-quality and uniform graphene films on copper foils. *Science* 324(5932), 1312-1314.
- [25] Yu, Q., Jauregui, L. A., Wu, W., Colby, R., Tian, J., Su, Z., & Chung, T. F. (2011). Control and characterization of individual grains and grain boundaries in graphene grown by chemical vapour deposition. *Nat. Mater.* 10(6), 443-449.
- [26] Malesevic, A., Vitchev, R., Schouteden, K., Volodin, A., Zhang, L., Van Tendeloo, G., & Van Haesendonck, C. (2008). Synthesis of few-layer graphene via microwave plasma-enhanced chemical vapour deposition. *Nanotechnology*, 19(30), 305604.
- [27] Yang, W., Chen, G., Shi, Z., Liu, C. C., Zhang, L., Xie, G., & Watanabe, K. (2013). Epitaxial growth of single-domain graphene on hexagonal boron nitride. *Nat. Mater.* 12(9), 792-797.
- [28] Borovikov, V., & Zangwill, A. (2009). Step-edge instability during epitaxial growth of graphene from SiC (0001). *Phys Rev. B* 80(12), 121406-121409.

- [29] Gao, M., Pan, Y., Huang, L., Hu, H., Zhang, L. Z., Guo, H. M., & Gao, H. J. (2011). Epitaxial growth and structural property of graphene on Pt (111). *Appl. Phys. Lett.* 98(3), 033101-033109.
- [30] Chung, C., Kim, Y. K., Shin, D., Ryoo, S. R., Hong, B. H., & Min, D. H. (2013). Biomedical applications of graphene and graphene oxide. *Accounts Chem. Res.* 46(10), 2211-2224.
- [31] Hummers Jr, W. S., & Offeman, R. E. (1958). Preparation of graphitic oxide. *J. Amer. Chem. Soc.* 80(6), 1339-1339.
- [32] Park, S., & Ruoff, R. S. (2009). Chemical methods for the production of graphenes. *Nat. Nanotechnol.* 4(4), 217-224.
- [33] Marcano, D. C., Kosynkin, D. V., Berlin, J. M., Sinitskii, A., Sun, Z., Slesarev, A., & Tour, J. M. (2010). Improved synthesis of graphene oxide. *ACS Nano* 4 (8), 4806–4814
- [34] Chen, D., Feng, H., & Li, J. (2012). Graphene oxide: preparation, functionalization, and electrochemical applications. *Chem. Rev.* 112(11), 6027-6053.
- [35] Dreyer, D. R., Park, S., Bielawski, C. W., & Ruoff, R. S. (2010). The chemistry of graphene oxide. *Chem. Soc. Rev.* 39(1), 228-240.
- [36] Shin, H. J., Kim, K. K., Benayad, A., Yoon, S. M., Park, H. K., Jung, I. S., & Lee, Y. H. (2009). Efficient reduction of graphite oxide by sodium borohydride and its effect on electrical conductance. *Adv. Funct. Mater.* 19(12), 1987-1992.
- [37] Chua, C. K., & Pumera, M. (2014). Chemical reduction of graphene oxide: a synthetic chemistry viewpoint. *Chem. Soc. Rev.* 43(1), 291-312.
- [38] Emiru, T. F., & Ayele, D. W. (2017). Controlled synthesis, characterization and reduction of graphene oxide: A convenient method for large scale production. *Egypt. J. Bas. Appl. Sci.* 4(1), 74-79.
- [39] Pei, S., Zhao, J., Du, J., Ren, W., & Cheng, H. M. (2010). Direct reduction of graphene oxide films into highly conductive and flexible graphene films by hydrohalic acids. *Carbon*, 48(15), 4466-4474.
- [40] Chen, W., Yan, L., & Bangal, P. R. (2010). Chemical reduction of graphene oxide to graphene by sulfur-containing compounds. *J. Phys. Chem. C* 114(47), 19885-19890.
- [41] Pei, S., & Cheng, H. M. (2012). The reduction of graphene oxide. *Carbon*, 50(9), 3210-3228.
- [42] Park, S., An, J., Potts, J. R., Velamakanni, A., Murali, S., & Ruoff, R. S. (2011). Hydrazine-reduction of graphite-and graphene oxide. *Carbon*, 49(9), 3019-3023.
- [43] Gao, X., Jang, J., & Nagase, S. (2009). Hydrazine and thermal reduction of graphene oxide: reaction mechanisms, product structures, and reaction design. *J. Phys. Chem. C* 114(2), 832-842.
- [44] Cohen-Tanugi, D., & Grossman, J. C. (2012). Water desalination across nanoporous graphene. *Nano Lett.* 12(7), 3602-3608.
- [45] Zhao, J., Ren, W., & Cheng, H. M. (2012). Graphene sponge for efficient and repeatable adsorption and desorption of water contaminations. *J. Mater. Chem.* 22(38), 20197-20202.

- [46] Schneider, G. F., Kowalczyk, S. W., Calado, V. E., Pandraud, G., Zandbergen, H. W., Vandersypen, L. M., & Dekker, C. (2010). DNA translocation through graphene nanopores. *Nano Lett.* 10(8), 3163-3167.
- [47] Russo, C. J., & Golovchenko, J. A. (2012). Atom-by-atom nucleation and growth of graphene nanopores. *P. Nat. Acad. Sci. USA* 109(16), 5953-5957.
- [48] Surwade, S. P., Smirnov, S. N., Vlassiuk, I. V., Unocic, R. R., Veith, G. M., Dai, S., & Mahurin, S. M. (2015). Water desalination using nanoporous single-layer graphene. *Nat. Nanotechnol.* 10(5), 459-464.
- [49] Huang, X., Qian, K., Yang, J., Zhang, J., Li, L., Yu, C., & Zhao, D. (2012). Functional nanoporous graphene foams with controlled pore sizes. *Adv. Mater.* 24(32), 4419-4423.
- [50] Liu, S., Zhao, Q., Xu, J., Yan, K., Peng, H., Yang, F., & Yu, D. (2012). Fast and controllable fabrication of suspended graphene nanopore devices. *Nanotechnology*, 23(8), 085301-085306.
- [51] Fan, Z., Zhao, Q., Li, T., Yan, J., Ren, Y., Feng, J., & Wei, T. (2012). Easy synthesis of porous graphene nanosheets and their use in supercapacitors. *Carbon*, 50(4), 1699-1703.
- [52] Fang, Y., Lv, Y., Che, R., Wu, H., Zhang, X., Gu, D., & Zhao, D. (2013). Two-dimensional mesoporous carbon nanosheets and their derived graphene nanosheets: synthesis and efficient lithium ion storage. *J. Amer. Chem. Soc.* 135(4), 1524-1530.
- [53] Alazmi, A., El Tall, O., Rasul, S., Hedhili, M. N., Patole, S. P., & Costa, P. M. (2016). A process to enhance the specific surface area and capacitance of hydrothermally reduced graphene oxide. *Nanoscale*, 8(41), 17782-17787.
- [54] Du, M., Sun, J., Chang, J., Yang, F., Shi, L., & Gao, L. (2014). Synthesis of nitrogen-doped reduced graphene oxide directly from nitrogen-doped graphene oxide as a high-performance lithium ion battery anode. *RSC Adv.*, 4(80), 42412-42417.
- [55] Vermisoglou, E. C., Giannakopoulou, T., Romanos, G., Giannouri, M., Boukos, N., Lei, C., & Trapalis, C. (2015). Effect of hydrothermal reaction time and alkaline conditions on the electrochemical properties of reduced graphene oxide. *Appl. Surf. Sci.*, 358, 100-109.
- [56] Zhang, L. L., Zhao, X., Stoller, M. D., Zhu, Y., Ji, H., Murali, S., & Ruoff, R. S. (2012). Highly conductive and porous activated reduced graphene oxide films for high-power supercapacitors. *Nano Lett.*, 12(4), 1806-1812.
- [57] Singh, S. K., Dhavale, V. M., Boukherroub, R., Kurungot, S., & Szunerits, S. (2017). N-doped porous reduced graphene oxide as an efficient electrode material for high performance flexible solid-state supercapacitor. *Appl. Mat. Today*, 8, 141-149.
- [58] Liu, R., Wu, D., Feng, X., & Müllen, K. (2011). Bottom-up fabrication of photoluminescent graphene quantum dots with uniform morphology. *J. Amer. Chem. Soc.* 133(39), 15221-15223.
- [59] Li, L. L., Ji, J., Fei, R., Wang, C. Z., Lu, Q., Zhang, J. R., & Zhu, J. J. (2012). A Facile Microwave Avenue to Electrochemiluminescent Two-Color Graphene Quantum Dots. *Adv. Funct. Mater.* 22(14), 2971-2979.

- [60] Pan, D., Zhang, J., Li, Z., & Wu, M. (2010). Hydrothermal route for cutting graphene sheets into blue-luminescent graphene quantum dots. *Adv. Mater.* 22(6), 734-738.
- [61] Li, L., Wu, G., Yang, G., Peng, J., Zhao, J., & Zhu, J. J. (2013). Focusing on luminescent graphene quantum dots: current status and future perspectives. *Nanoscale*, 5(10), 4015-4039.
- [62] Shinde, D. B., & Pillai, V. K. (2012). Electrochemical preparation of luminescent graphene quantum dots from multiwalled carbon nanotubes. *Chem.-Eu. J.* 18(39), 12522-12528.
- [63] Li, Y., Hu, Y., Zhao, Y., Shi, G., Deng, L., Hou, Y., & Qu, L. (2011). An electrochemical avenue to green-luminescent graphene quantum dots as potential electron-acceptors for photovoltaics. *Adv. Mater.* 23(6), 776-780.
- [64] Lin, L. & Zhang, S. (2012) Creating high yield water soluble luminescent graphene quantum dots via exfoliating and disintegrating carbon nanotubes and graphite flakes. *Chem. Commun.* 48, 10177-10179.
- [65] T. A. Tabish & S. Zhang, "Graphene Quantum Dots: Syntheses, Properties, and Biological Applications", In: Saleem Hashmi (editor-in-chief). *Reference Module in Materials Science and Materials Engineering*. Oxford: Elsevier. 1-21 (2016)
- [66] Shen, J., Zhu, Y., Yang, X., & Li, C. (2012) Graphene quantum dots: emergent nanolights for bioimaging, sensors, catalysis and photovoltaic devices. *Chem. Commun.* 48, 3686-3699.
- [67] Liu, R., Wu, D., Feng, X., & Müllen, K. (2011) Bottom-up fabrication of photoluminescent graphene quantum dots with uniform morphology. *J. Am. Chem. Soc.* 133, 15221-15223.
- [68] Dong, Y., Shao, J., Chen, C., Li, H., Wang, R., Chi, Y., & Chen, G. (2012). Blue luminescent graphene quantum dots and graphene oxide prepared by tuning the carbonization degree of citric acid. *Carbon*, 50(12), 4738-4743.
- [69] Mattevi, C., Kim, H., & Chhowalla, M. (2011). A review of chemical vapour deposition of graphene on copper. *J. Mater. Chem.* 21(10), 3324-3334.
- [70] Kim, K. S., Zhao, Y., Jang, H., Lee, S. Y., Kim, J. M., Kim, K. S., & Hong, B. H. (2009). Large-scale pattern growth of graphene films for stretchable transparent electrodes. *Nature*, 457(7230), 706-710.
- [71] Malesevic, A., Vitchev, R., Schouteden, K., Volodin, A., Zhang, L., Van Tendeloo, G., & Van Haesendonck, C. (2008). Synthesis of few-layer graphene via microwave plasma-enhanced chemical vapour deposition. *Nanotechnology*, 19(30), 305604-305613.
- [72] Yu, Q., Jauregui, L. A., Wu, W., Colby, R., Tian, J., Su, Z., & Chung, T. F. (2011). Control and characterization of individual grains and grain boundaries in graphene grown by chemical vapour deposition. *Nat. Mater.* 10(6), 443-449.
- [73] Novoselov, K. S., Fal, V. I., Colombo, L., Gellert, P. R., Schwab, M. G., & Kim, K. (2012). A roadmap for graphene. *Nature*, 490(7419), 192-200.
- [74] Brownson, D. A., & Banks, C. E. (2012). The electrochemistry of CVD graphene: progress and prospects. *Phys. Chem. Chem. Phys.* 14(23), 8264-8281.



- [75] Chen, Z., Ren, W., Gao, L., Liu, B., Pei, S., & Cheng, H. M. (2011). Three-dimensional flexible and conductive interconnected graphene networks grown by chemical vapour deposition. *Nat. Mater.* 10(6), 424-428.
- [76] Yang, Z., Yan, C., Liu, J., Chabi, S., Xia, Y., & Zhu, Y. (2015). Designing 3D graphene networks via a 3D-printed Ni template. *RSC Adv.* 5(37), 29397-29400.
- [77] Yang, Z., Chabi, S., Xia, Y., & Zhu, Y. (2015). Preparation of 3D graphene-based architectures and their applications in supercapacitors. *Prog. Nat. Sci.-Mater.* 25(6), 554-562.
- [78] Chabi, S., Peng, C., Yang, Z., Xia, Y., & Zhu, Y. (2015). Three dimensional (3D) flexible graphene foam/polypyrrole composite: towards highly efficient supercapacitors. *RSC Adv.* 5(6), 3999-4008.
- [79] Fu, P. P., Xia, Q., Hwang, H. M., Ray, P. C., & Yu, H. (2014). Mechanisms of nanotoxicity: generation of reactive oxygen species. *J. Food Drug Anal.* 22(1), 64-75.
- [80] Zhang, B., Wei, P., Zhou, Z., & Wei, T. (2016). Interactions of graphene with mammalian cells: Molecular mechanisms and biomedical insights. *Adv. Drug Deliver. Rev.* 105, 145-162.
- [81] Lammel, T., Boisseaux, P., Fernández-Cruz, M. L., & Navas, J. M. (2013). Internalization and cytotoxicity of graphene oxide and carboxyl graphene nanoplatelets in the human hepatocellular carcinoma cell line Hep G2. *Part. Fibre Toxicol.* 10(1), 27.
- [82] Qin, Y., Zhou, Z. W., Pan, S. T., He, Z. X., Zhang, X., Qiu, J. X., & Zhou, S. F. (2015). Graphene quantum dots induce apoptosis, autophagy, and inflammatory response via p38 mitogen-activated protein kinase and nuclear factor- $\kappa$ B mediated signaling pathways in activated THP-1 macrophages. *Toxicology*, 327, 62-76.
- [83] Fumarola, C., & Guidotti, G. G. (2004). Stress-induced apoptosis: toward a symmetry with receptor-mediated cell death. *Apoptosis*, 9(1), 77-82.
- [84] Li, Y., Liu, Y., Fu, Y., Wei, T., Le Guyader, L., Gao, G., & Chen, C. (2012). The triggering of apoptosis in macrophages by pristine graphene through the MAPK and TGF-beta signaling pathways. *Biomaterials*, 33(2), 402-411.
- [85] Chang, Y., Yang, S. T., Liu, J. H., Dong, E., Wang, Y., Cao, A., & Wang, H. (2011). In vitro toxicity evaluation of graphene oxide on A549 cells. *Toxicol Lett.* 200(3):201–210.
- [86] Ou, L., Song, B., Liang, H., Liu, J., Feng, X., Deng, B., & Shao, L. (2016). Toxicity of graphene-family nanoparticles: a general review of the origins and mechanisms. *Part. Fibre Toxicol.* 13(1), 57.
- [87] Singla, P., Riyaz, M., Singhal, S., & Goel, N. (2016). Theoretical study of adsorption of amino acids on graphene and BN sheet in gas and aqueous phase with empirical DFT dispersion correction. *Phys. Chem. Chem. Phys.* 18(7), 5597-5604.
- [88] Chong, Y., Ma, Y., Shen, H., Tu, X., Zhou, X., Xu, J., & Zhang, Z. (2014). The in vitro and in vivo toxicity of graphene quantum dots. *Biomaterials*, 35(19), 5041-5048.
- [89] Park, E. J., Lee, G. H., Han, B. S., Lee, B. S., Lee, S., Cho, M. H., & Kim, D. W. (2015). Toxic response of graphene nanoplatelets in vivo and in vitro. *Arch. Toxicol.* 89(9), 1557-1568.

- [90] Jin, L., Yang, K., Yao, K., Zhang, S., Tao, H., Lee, S. T., & Peng, R. (2012). Functionalized graphene oxide in enzyme engineering: a selective modulator for enzyme activity and thermostability. *ACS Nano*, 6(6), 4864-4875.
- [91] Hernández-Cancel, G., Suazo-Dávila, D., Ojeda-Cruzado, A. J., García-Torres, D., Cabrera, C. R., & Griebenow, K. (2015). Graphene oxide as a protein matrix: influence on protein biophysical properties. *J. Nanobiotechnol.*, 13, 1-12.
- [92] De, M., Chou, S. S., & Dravid, V. P. (2011). Graphene oxide as an enzyme inhibitor: modulation of activity of  $\alpha$ -chymotrypsin. *J. Amer. Chem. Soc.* 133(44), 17524-17527.
- [93] Zhu, Z., Wang, Y., Kang, Y., Zhang, H., Zhang, Z., Fei, Z., & Cao, J. (2017). Graphene oxide destabilizes myoglobin and alters its conformation. *Carbon*, 114, 449-456.
- [94] Huang, W., Hao, Q., Lei, W., Wu, L., & Xia, X. (2014). Polypyrrole-hemin-reduce graphene oxide: rapid synthesis and enhanced electrocatalytic activity towards the reduction of hydrogen peroxide. *Mater. Res. Express*, 1(4), 045601-045619.
- [95] Cho, Y., & Choi, Y. (2012). Graphene oxide–photosensitizer conjugate as a redox-responsive theranostic agent. *Chem. Commun.* 48(79), 9912-9914.
- [96] Thannickal, V. J., & Fanburg, B. L. (2000). Reactive oxygen species in cell signaling. *Am. J. Physiol-Lung C.* 279(6), L1005-L1028.
- [97] Fidler, I. J. (2003). The pathogenesis of cancer metastasis: the 'seed and soil' hypothesis revisited. *Nat. Rev. Cancer* 3(6), 453-458.
- [98] Cao, Y., Dong, H., Yang, Z., Zhong, X., Chen, Y., Dai, W., & Zhang, X. (2017). Aptamer-Conjugated Graphene Quantum Dots/Porphyrin Derivative Theranostic Agent for Intracellular Cancer-Related MicroRNA Detection and Fluorescence-Guided Photothermal/Photodynamic Synergetic Therapy. *ACS Appl. Mater. Interf.* 9 (1), 159–166.
- [99] Wei, Y., Zhou, F., Zhang, D., Chen, Q., & Xing, D. (2016). A graphene oxide based smart drug delivery system for tumor mitochondria-targeting photodynamic therapy. *Nanoscale*, 8(6), 3530-3538.
- [100] Hampton, M. B., & Orrenius, S. (1997). Dual regulation of caspase activity by hydrogen peroxide: implications for apoptosis. *FEBS Lett.* 414(3), 552-556.
- [101] He, Y., Del Valle, A., Qian, Y., & Huang, Y. F. (2017). Near infrared light-mediated enhancement of reactive oxygen species generation through electron transfer from graphene oxide to iron hydroxide/oxide. *Nanoscale* 9(4), 1559-1566.
- [102] Kroemer, G., & Reed, J. C. (2000). Mitochondrial control of cell death. *Nat. Med.* 6(5), 513-519.
- [103] Qu, G., Liu, S., Zhang, S., Wang, L., Wang, X., Sun, B., & Jiang, G. B. (2013). Graphene oxide induces toll-like receptor 4 (TLR4)-dependent necrosis in macrophages. *ACS Nano*, 7(7), 5732-5745.

## Chapter 3

# Raw Materials and Analysis Techniques

---

The generic experimental methodology and procedures applied for this research will be presented in this chapter.

### 3.1 Raw materials

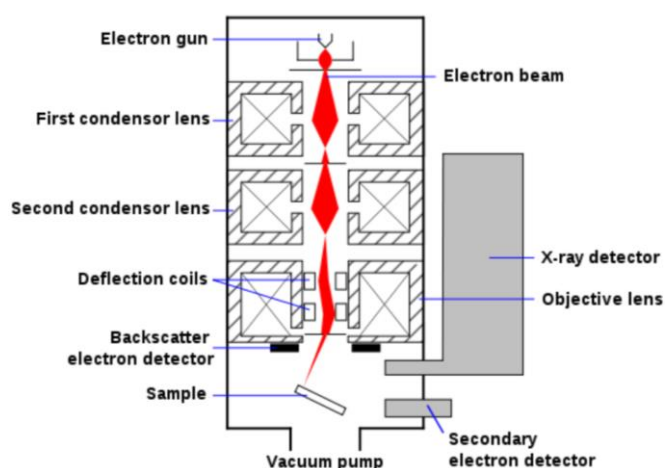
The reagents used throughout this thesis were of analytical grade and purchased from indicated sources. H<sub>2</sub>SO<sub>4</sub> (95.0-98.0%, Product No. 320501), KMnO<sub>4</sub> (Product No. 223468), NaNO<sub>3</sub> (product no. S5506), H<sub>2</sub>O<sub>2</sub> (30 wt%, Product No. 216763), hydrazine (35 wt%, product No. 309400), potassium nitrate salt (product No.: 542040), 0.1 M Tris-HCl buffer (product No. 07066), Diiodomethane (product number 158429), potassium bromide (product number P0838), disodium hydrogen phosphate (product no. 7558-79-4) and styrene (product no. 100-42-5) were purchased from Sigma-Aldrich. HCl (36 wt%, product No.: 7647-01-0), was purchased from Acros. Graphite flake (GFs, product No.17346-25) and 0.2 micron membrane filter were purchased from Thermo and Fisher Scientific suppliers. Reagent kits for measuring the concentrations of enzymes were purchased from Chemelex, S.A., Canovelles, Spain. Citric acid was purchased from Alfa Aesar. Trypsin (1%), Boc-Gln-Ala-Arg-AMC fluorogenic substrate for trypsin ( $k_{cat}/K_m=2.0 \times 10^7 \text{ M}^{-1}\text{sec}^{-1}$ ;  $K_m=6.0 \mu\text{M}$ ), cathepsin L fluorogenic substrate Z-Val-Val-Arg-AMC (ZVA) and cathepsin D fluorogenic substrate were obtained from Enzo Life Sciences (UK) Ltd and was stored at -20 °C. Ni foam was purchased from Inco. Ltd, Canada. Annexin binding buffer and propidium iodide were purchased from BioLegend, UK and Sigma-Aldrich, UK respectively. AlamarBlue® cell viability assay was purchased from Thermofisher Scientific, Italy.

### 3.2 Scanning electron microscopy

Scanning Electron Microscopes (SEM) makes this form of microscopy an appropriate tool for characterizing surface morphology. In standard SEM, a filament produces an

electron stream which is then directed at the sample using a positive electron potential – this thin, monochromatic beam is focused by metal apertures and lenses, as shown in **Scheme 3.1** [1]. Secondary electrons (SE) and X-rays are produced when these interact with the specimen; the secondary electrons are produced only from the top layer of the sample (10 nm), so the images produced by these can provide topographic details of the specimen surface.

In this work, SEM images of the samples were taken on a Philips XL-30 SEM under high vacuum conditions with accelerating voltage 20 kV. Both the powder samples and liquid samples were mounted onto carbon sticky tape, with the latter first dried before mounting.

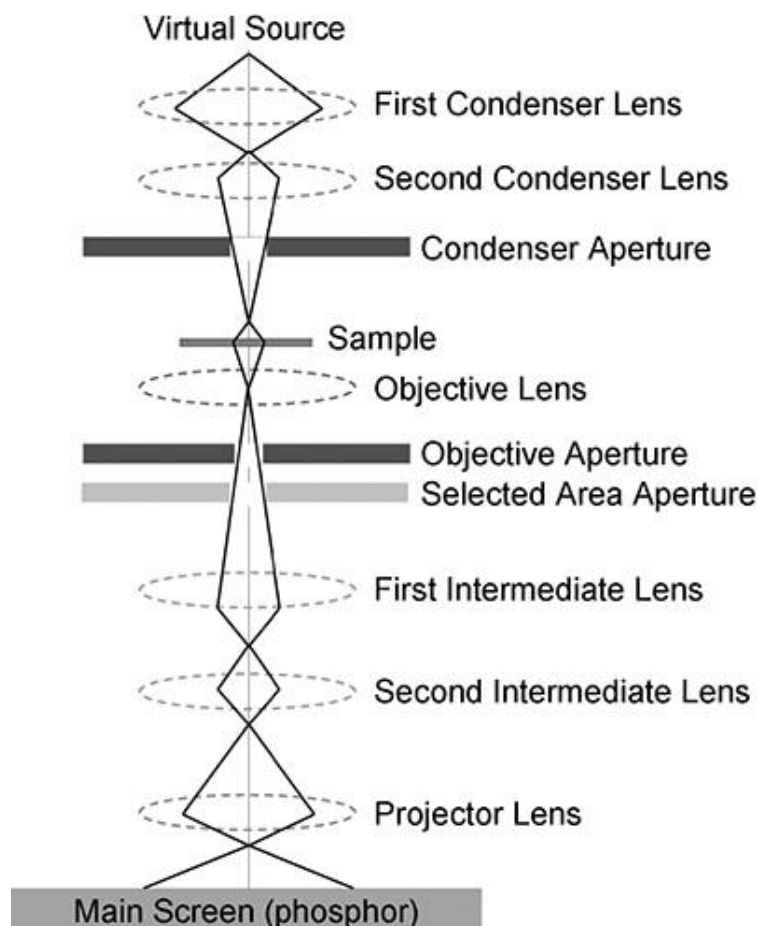


**Scheme 3.1:** Schematic diagram of a SEM [1].

### 3.3 Transmission electron microscopy

Transmission Electron Microscopy (TEM) has an ultra-high resolution down to 0.2 nm, making it an efficient technique for obtaining highly detailed images. Unlike SEM, where electrons only hit the specimen surface, the electrons beams utilised in TEM travel through the entire sample and can provide information on internal structures of materials. STEM bright field (BF) and dark field (DF) imaging and Elemental Mapping are all possible using TEM; **Scheme 3.2** illustrates the TEM system. Electron diffraction can be used to analyze the crystal structures of samples, making this method of microscopy indispensable in nanomaterial analysis; some researchers have even used TEM to observe adatoms (atoms which lie on a crystal surface), which is an important

advancement in this field [2]. In this work high resolution microstructural images were also taken, on a JEOL-2100 TEM operating at a voltage of 200 kV. The powder sample was dispersed in acetone, after which the sample was dropped on the centre of a carbon Cu grid using a micro pipet.

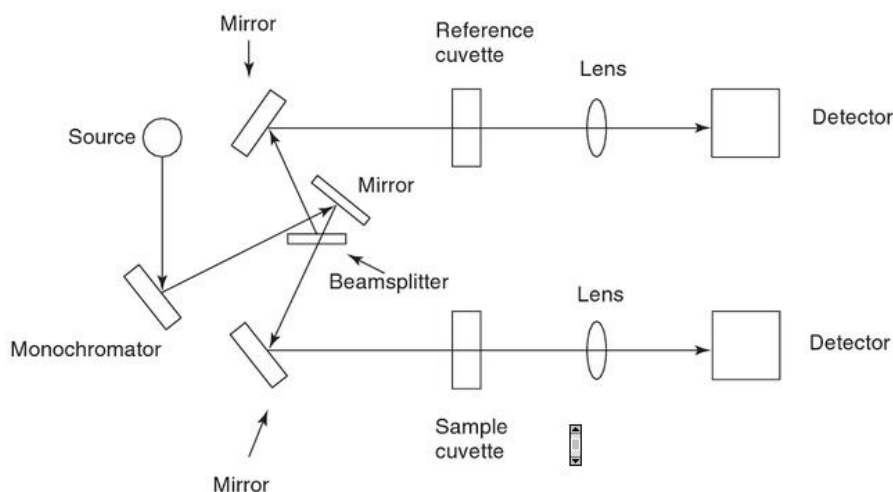


**Scheme 3.2:** Illustration of TEM system [2].

### 3.4 Ultraviolet/Visible (UV/Vis) spectroscopy

Ultraviolet–visible spectroscopy (UV-Vis) is a spectroscopic tool that uses an ultraviolet-visible beam to analyse a samples chemical composition. As the electronic transition energy of the molecules move from ground state to the excited state, the UV-visible beam is absorbed (**Scheme 3.3**) [3]. By analysing the absorption peaks, chemical composition of the sample can be determined; the instrument used for this is a UV-visible spectrophotometer. It gives the measurement of the intensity of light going through a sepecimen ( $I$ ), and associates this to the lights intensity before passing through the specimen ( $I_0$ ), typically light from the visible and adjacent ranges.

In this work, UV–Vis absorbance were obtained by using a Jenway 6715 UV/Vis spectrophotometer. Most of the samples used in this thesis were in liquid form, while powder samples were dispersed in water before using this machine.

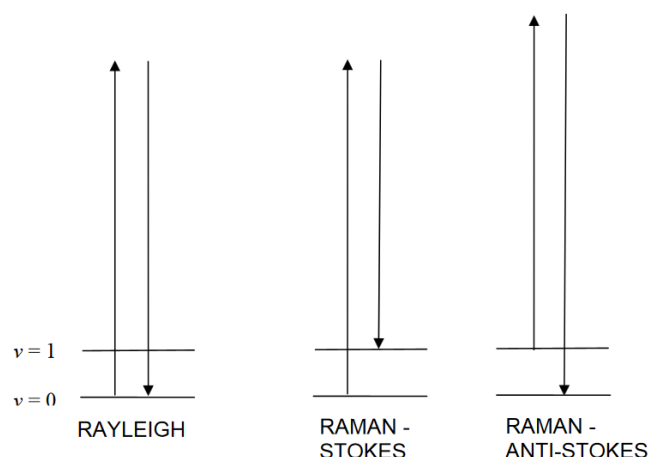


**Scheme 3.3:** Schematic layout of UV/Vis spectrometer [3].

### 3.5 Raman spectroscopy

Raman Spectroscopy is a spectroscopic tool used to analyse the chemical composition of a sample. It uses lasers to do this – lasers with different ranges, typically visible, near infrared and near ultraviolet, are emitted to interact with molecular vibrations. This leads to the generation of up or down shifts of the energy of laser photons (**Scheme 3.4**); these shifts are analysed to measure the vibration modes of a sample. Each molecule has a different set of vibrational energy levels, so when the lasers are focused on a particular molecule, the photon can be scattered either elastically or inelastically. Only a small amount of scattered light is inelastically scattered – about 1 in every 30 million photons. The vast majority is therefore the same as the excitation source, so shows no Raman effect (Rayleigh). Raman spectroscopy is also an effective technique to characterise graphene intensity and number of its layers [4].

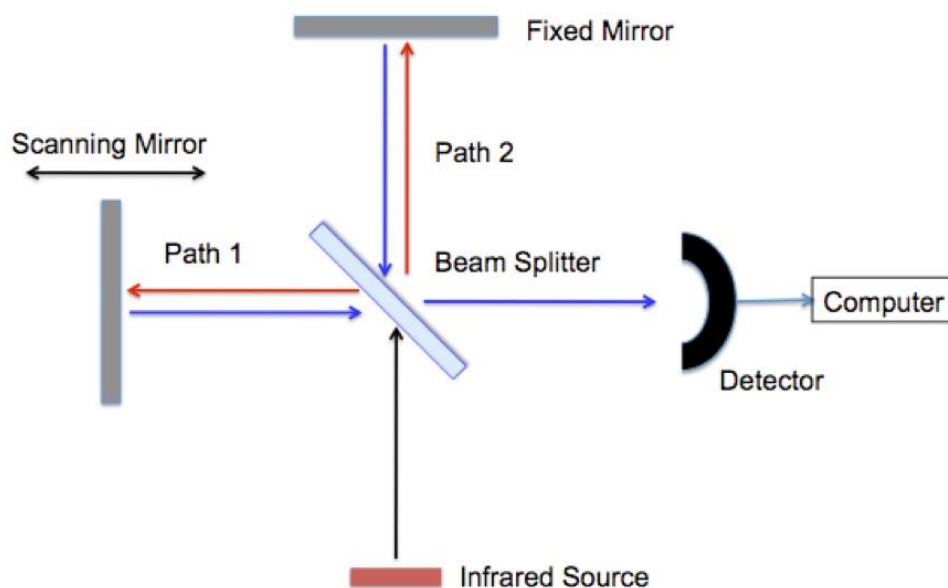
In this work, the Raman spectra were collected using a 532 nm laser excitation operating at 6 mW power. The power of the laser was kept at 6 mW. The 2D and quantum dots samples were prepared by dropping their solution on a glass slide while the 3D sample was prepared by grinding them into fine powder.



**Scheme 3.4:** Energy diagrams for light scattering: Rayleigh (elastic) vs. Raman (inelastic) [4].

### 3.6 Fourier Transform Infrared (FT-IR) spectroscopy

Fourier transform infrared spectroscopy (FTIR) is often utilised to acquire an infrared spectrum by absorption or transmission through a solid, liquid, or gas. When infrared (IR) radiation passes through a sample, some electromagnetic radiation is absorbed and some transmitted, resulting an infrared spectrum characteristic of the specific sample. The FTIR and assisting computer software can then measure and decode all infrared frequencies, generating the spectral information of the sample in question (**Scheme 3.5**). It also shows the molecular finger-print of the sample [5]. In our experiment, FTIR spectra were obtained using an Alpha Bruker system. The samples were measured in the wavenumber range of 4000–450  $\text{cm}^{-1}$ . Samples used in this thesis were prepared by mixing the original samples with KBr.



**Scheme 3.5:** A schematic of an interferometer used in a Fourier Transfer Infrared Spectrometer (FTIR) [6].

### 3.7 X-Ray diffraction (XRD)

X-ray Diffraction (XRD) is a powerful tool utilised for the identification of phases of a crystalline material, providing key evidences on a variety of characteristics, such as unit cell dimensions, crystal perfection, lattice spacing,  $d$ , grain size, and texture. XRD is typically based on the productive interfering of monochromatic X-rays and a crystalline specimen [7]. These X-rays are produced by a cathode tube, which is filtered to generate monochromatic radiation, and focused toward the specimen. The crystallite features of samples can be identified from the XRD peaks. An interference formed by the interaction of the incident beam with the specimen, and thus following the Bragg's Law which is given as below [8]:

$$n\lambda = 2d \sin\theta \quad \dots\dots\dots (3.1)$$

In this work, X-ray diffraction (XRD) analysis was performed using Cu K $\alpha$  radiation (at 40 kV and –40 mA). Powdered samples were prepared for XRD analysis. As prepared sample, was inserted into the sample holder and scanned from 10 - 80° 2 $\theta$  with a step size of 0.02°, and 1 s step time.



### 3.8 Photoluminescence spectroscopy

Photoluminescence (PL) Spectroscopy is an efficient technique for analysing the electronic structure of nanostructured materials [9]. Light is focused onto the specimen and directs excessive energy into the samples, causing electrons within the materials to reach an excited state. (It can be noted that this is like the process of UV-visible spectrometry, as described in section 3.3.) When the excited electrons return back to their equilibrium positions, excessive energy is emitted in form of light (radiative process) or thermal energy (non-radiative process) [9]. If it is the former, the process is photoluminescence; the energy of this is reliant on the energy difference between the excited and equilibrium states of the electrons. This process of absorption and emission can be clarified using a Jablonski diagram (**Scheme 2.5 a**). In this schematic representation, S<sub>0</sub>, S<sub>1</sub> and S<sub>2</sub> show the singlet ground, first and second electronic states, respectively.

In this work, PL features were obtained by using an Edinburgh Instruments Spectrofluorometer FS5 at 350 nm of excitation wavelength. The sample used for PL was in liquid form.

### 3.9 BET Surface area analyser

The Brunauer-Emmett-Teller method (BET) is a technique used to determine the physical adsorption of gases in solid materials that have complicated shapes, e.g. porous materials. Adsorption and desorption isotherms are used to find the number of gas molecules adsorbed on the material [10]. The BET equation describes an adsorption where the adsorbate contains multiple layers. It has several main assumptions: (1) The adsorbed molecules are fixed in the material; (2) The enthalpy of adsorption of all the layers is the same; (3) The energy of adsorption for all layers is the same, except for the first layer; (4) A new layer can start before the one before has finished.

In this work surface area was calculated by using Brunauer–Emmett–Teller (BET) theory method. The total pore volume ( $V_t$ ) was measured from the amount of adsorbed nitrogen (at  $P/P_o = ca. 0.99$ ).

### **3.10 Contact angle goniometer**

The measurements of contact angle and surface energy of materials are of critical importance in surface science [11]. The most popular approach to measure the contact angle is direct measurement of the shape of liquid drop on a flat surface [12]. It involves straightforward measurement of a sessile drop profile. The equipment contains a stage to hold sample, a pipette to form a liquid drop profile, a light source, and a digital camera to record the image of drop profile.

In this work, the wettability of samples was determined using a contact angle goniometer. A digital camera was used to record the images and the contact angle was calculated (using PolyPro). The surface of the sample was prepared for wetting by gently drop casting it onto a glass slide. The surface energy was determined by measuring the contact angle of a 10  $\mu$ l drop of diiodomethane (DIO) on the surface. The equations used in the surface energy calculations are given in chapter 4.

### **3.11 Zeta potential probe**

Zeta potential is used to investigate the nature of the electrostatic potential on the surface of a material. Suspended particles generally carry a surface charge which is typically negative or positive. Functional groups existing on the surface of any sheet of particle can also cause to produce a surface charge. Surface charge is a critical feature in graphene to investigating the adsorption capacity and nature of interactions with proteins, cells and biological tissues.

In this work, zeta potential measurements were carried out using a colloidal dynamics zeta probe to identify the surface charge of rGO as a function of pH, balanced in the acidic–basic ranges using  $10^{-4}$ M HCl and KOH solutions, respectively.

### **3.12 Cell Viability evaluation and flow cytometry analysis**

A549 and SKMES-1 lung cancer cells were seeded in 6 well plates at a density of 350,000 per well. After overnight incubation, cells were treated with or without 5, 50, 250, 500 and 1000 µg/ml of GO for 24 h. Then, cells were trypsinised and centrifuged at 200 g for 5 min. Cell pellets were then re-suspended in 100µl of annexin binding buffer containing annexin (BioLegend, UK) and propidium iodide (PI) (Sigma-Aldrich, UK), and incubated for 15 min in the dark. Flow cytometry was performed using a Guava flow cytometer. The data were analysed using Guava 3.1.1 software. The early and late apoptotic populations of the cells were analysed by flow cytometer Alexa Fluor647 Annexin V (apoptosis) – F2, Propidium iodide necrosis –F3 YEL. The criteria for early and late apoptotic cells are Annexin V-positive, PI-negative and Annexin V-positive, and PI-positive, respectively. Signals were detected using Alexa Fluor® 647, a bright far-red–fluorescent dye with excitation ideally suited for the 594 nm or 633 nm laser lines. PI is yellow-fluorescent dye with excitation ideally suited to the 532 nm laser line. Toxicity assays were repeated 3 times.

In cell attachment experiment, cytotoxicity was determined using AlamarBlue® cell viability assay (Thermofisher Scientific, Italy) following the guideline provided by manufacturer [13]. The cell culture medium was changed with fresh medium which contains 10% of AlamarBlue® reagent. Then, fluorescence ( $\lambda_{\text{ex}} = 540 \text{ nm}$ ;  $\lambda_{\text{em}} = 595 \text{ nm}$ ) was measured by using plate reader after 2 h of incubation at 37 °C. Experiments were repeated for 3 times and cell viability was presented as percentage of control cells. A fluorescence microscope (Olympus MODEL BX51WIF) was employed for imaging assessment of cell attachment to 3D graphene foam.

### **3.13 *In Vivo* studies**

All animal experiments were carried out following the regulations of the institutional ethics committee on animal welfare (Animal Care and Use Program Guidelines of Government College University, Faisalabad, Pakistan), and with their prior approval for using the animal models. Sprague-Dawley adult male rats (average age of 6-7 weeks, 230-250g weight) were obtained from the animal house of institution, and

housed in groups in ventilated cages under standard lighting conditions and natural day/night cycle after approval from the ethical committee of the institution. Common carp (*Cyprinus carpio*) ( $50 \pm 2$  g weight and  $29 \pm 0.9$  cm in length) was procured from the Fish Hatchery Satiana Road Faisalabad Punjab, Pakistan and held there for two weeks in a stock aquarium with flowing aerated dechlorinated tap water. They were given free access to water and food and the surrounding humidity and temperature ( $25\text{ }^{\circ}\text{C} \pm 2\text{ }^{\circ}\text{C}$ ) was controlled. After a period of acclimatization for 7 days, the animals of similar mean initial body weights were divided into five groups,  $n=8$  per group. The body weights of the control group and all the experimental groups were observed and recorded weekly to note changes in body weights. The body weight and behaviour were also noted every day after graphene exposure. Blood samples were collected at the start and end of the experiments and used for the analysis of complete blood count (CBC), selected serum biochemical parameters, haematology and oxidative stress enzymes.

### **3.14 Statistical Analysis**

The data of cell viability were analysed in GraphPad Prism 5.04, and expressed as % cell count  $\pm$  standard deviation, Mann Whitney. The *in vivo* data was statistically analysed in GraphPad Prism 5.04 to determine the GNPs treatment effects on various parameters of cell count, body weight, liver and kidney function tests, complete blood count and oxidative stress biomarkers.  $P < 0.05$  was considered as statistically significant. Results have been shown as the mean  $\pm$  standard deviation (SD).

### **3.15 Regression analysis**

We investigated the relationship between concentration of graphene sample and cell death rate, so that the most appropriate concentration levels could be determined for biological applications. Standard non-linear regression methods will only capture the general trend without taking into account the uncertainties in measurements and predictions. Therefore, we used a Gaussian process (GP) to model the relationships and readily incorporate the uncertainties in measurements to produce a Bayesian posterior predictive distribution [14, 15]. A GP is essentially a collection of random

variables, and any finite number of these have joint Gaussian distribution. Given a dataset  $D = \{(x_i, y_i)\}_{i=1}^n$  with  $n$  data points, where  $x_i$  is the  $i$ th graphene sample concentration and  $y_i$  is the associated cell count, the posterior predictive distribution is  $P(y_{n+1}|x_{n+1}, D, \theta) \sim \mathcal{N}(y_{n+1}|\mu(x_{n+1}), \sigma(x_{n+1}))$ . Here, the mean prediction  $\mu(\cdot)$  and the standard deviation  $\sigma(\cdot)$  are functions of the covariance matrix. The covariance matrix captures the covariance between observed concentrations, which is governed by the specific covariance function and the set of hyper-parameters  $\theta$ . In this study, we used the Matern52 covariance function. The hyper-parameters are set by maximising the likelihood of the data.

### 3.16 Adsorption kinetic model

Adsorption kinetic models are typically employed to study and better understand the kinetics of the adsorption mechanism. Such models are useful to determine the performance and capacity of an adsorbent. In this study, we have used intraparticle model to better understand the adsorption mechanism of graphene oxide. Fick's second law was used to reveal if intraparticle diffusion is adsorption controlling phenomena involved in our study, which is given below [16,17]:

$$q_t = k_{id}\sqrt{t} + I,$$

where  $I$  represents the boundary layer effect and  $k_{id}$  shows the intraparticle rate constant.

Intraparticle plot indicates a multi-linear trend, representing two or more shapes. The first segment typically shows the instantaneous surface adsorption [18,19]. The second part of the plot represents the slow adsorption step. The third segment shows the final equilibrium stage where intraparticle diffusion gradually becomes slow due to the less available sites of adsorbate.

## References

- [1]  
[http://piyushcharan.yolasite.com/resources/NANO\\_NOTES/Scanning%20Electron%20Microscope.pdf](http://piyushcharan.yolasite.com/resources/NANO_NOTES/Scanning%20Electron%20Microscope.pdf) Consulted on 29<sup>th</sup> of December, 2017.
- [2]  
[https://www.researchgate.net/publication/233753570\\_Nanotechnologies\\_for\\_the\\_Life\\_Sciences/figures?lo=1](https://www.researchgate.net/publication/233753570_Nanotechnologies_for_the_Life_Sciences/figures?lo=1) Visited on 29<sup>th</sup> of December, 2017

- [3] Stuart, B. H. (2007). *Analytical techniques in materials conservation*. John Wiley & Sons.
- [4] <http://www.eng.uc.edu/~beaucag/Classes/Characterization/RamanCALTECH.pdf>  
Consulted on 29<sup>th</sup> of December, 2017.
- [5] Berthomieu, C., & Hienerwadel, R. (2009). Fourier transform infrared (FTIR) spectroscopy. *Photosynth Res.* 101(2-3), 157-170.
- [6] [https://chem.libretexts.org/LibreTexts/Howard\\_University/Howard%3A\\_Physical\\_Chemistry\\_Laboratory/14.\\_Fourier\\_Transform\\_Infrared\\_Spectroscopy\\_\(FTIR\)](https://chem.libretexts.org/LibreTexts/Howard_University/Howard%3A_Physical_Chemistry_Laboratory/14._Fourier_Transform_Infrared_Spectroscopy_(FTIR))  
Consulted on 29<sup>th</sup> of December, 2017.
- [7] Bunaciu, A. A., Udrişţoiu, E. G., & Aboul-Enein, H. Y. (2015). X-ray diffraction: instrumentation and applications. *Cr Rev. Anal. Chem.* 45(4), 289-299.
- [8] Whittig, L. D., & Allardice, W. R. (1986). X-ray diffraction techniques. *Methods of Soil Analysis: Part 1—Physical and Mineralogical Methods*, (methodsofsoilan1), 331-362.
- [9] J. R. Lakowica, *Principle of Fluorescence Spectroscopy* (3rd Ed.). **2006**, Springer.
- [10] Brunauer, S., & Copeland, L. (1963, January). Physical adsorption of gases and vapors on solids. In *Symposium on Properties of Surfaces*. ASTM International.
- [11] Van Oss, C. J., Good, R. J., & Chaudhury, M. K. (1988). Additive and nonadditive surface tension components and the interpretation of contact angles. *Langmuir*, 4(4), 884-891.
- [12] Good, R. J. (1992). Contact angle, wetting, and adhesion: a critical review. *J. Adhes. Sci. Tech.* 6(12), 1269-1302.
- [13] Melone, L., Tarsini, P., Candiani, G., & Punta, C. (2016). N-Hydroxyphthalimide catalysts as bioactive pro-oxidants. *RSC Adv.* 6(26), 21749-21755.
- [14] Tabish, T. A., Pranjol, M. Z. I., Hayat, H., Rahat, A. A., Abdullah, T. M., Whatmore, J. L., & Zhang, S. (2017). In vitro toxic effects of reduced graphene oxide nanosheets on lung cancer cells. *Nanotechnology*, 28(50), 504001.
- [15] Rasmussen, C. E., & Williams, C. K. (2006). *Gaussian processes for machine learning* (Vol. 1). Cambridge: MIT press.
- [16] Malana, M. A., Qureshi, R. B., & Ashiq, M. N. (2011) Adsorption studies of arsenic on nano aluminium doped manganese copper ferrite polymer (MA, VA, AA) composite: kinetics and mechanism. *Chem. Eng. J.* 172, 721-727.
- [17]. Alkan, M., Demirbaş, Ö., Celikcapa, S., & Doğan, M. (2004) Sorption of acid red 57 from aqueous solution onto sepiolite. *J. Hazard. Mater.* 116, 135-145.
- [18]. Altenor S., Carene B., Emmanuel E., Lambert J., Ehrhardt J. J. et al. (2009) Adsorption studies of methylene blue and phenol onto vetiver roots activated carbon prepared by chemical activation. *J. Hazard. Mater.* 165, 1029-1039.
- [19]. Qi L., and Xu Z. (2004) Lead sorption from aqueous solutions on chitosan nanoparticles. *Colloids and Surfaces A: Physicochemical and Engineering Aspects* 251: 183-190.

## **Chapter 4**

# **Graphene Oxide Based Targeting Extracellular Cathepsin D and Cathepsin L in Novel Anti-Metastatic Enzyme Cancer Therapy**

---

Overexpression and secretion of the enzymes cathepsin D (CathD) and cathepsin L (CathL) is associated with metastasis in several human cancers. As a superfamily, extracellularly, these proteins may act within the tumor microenvironment to drive cancer progression, proliferation, invasion and metastasis. Therefore, it is important to discover novel therapeutic treatment strategies to target CathD and CathL and impede metastasis. Graphene oxide (GO) could form the basis of such a strategy by acting as an adsorbent for pro-metastatic enzymes. In this chapter, we have conducted research into the potential of anti-metastatic target therapy using GO to adsorb these pro-tumourigenic enzymes. Definitive binding and modulation of CathD/L-GO revealed that CathD/L were adsorbed onto the surface of GO through its cationic and hydrophilic residues. The work described in this chapter could provide a roadmap for the rational integration of CathD/L-targeting agents into clinical settings.

### **4.1 Introduction**

Every year more than 2.28 million new cases of breast and ovarian cancers are diagnosed, principally in developed countries and 807,440 women die of these worldwide, with these cancers representing the first and fifth most common cause of female malignancies, respectively [1-5]. Although these diseases have different pathologies they share a common set of molecular mechanisms such as the misfolding/aggregation, overexpression and hypersecretion of specific proteins typically involved in degrading cross-linked, abnormal, short-lived self- and foreign-proteins in lysosomes and phagocytosis. The intracellular and extracellular responses of the tumor microenvironment tend to be more prominent in response to conditions such as acidic pH [6], the enhanced permeability and retention effect [7], the enzyme abundance in the tumor extracellular matrix, [8] and overexpression of particular cell

membrane receptors [9]. Typically, this emanates from the misfolding-prone proteins forming potentially pathogenic aggregates, either because they lose their ability to execute their physiological functions efficiently in certain regions of their sequence or because they form harmful oligomeric and/or cytotoxic species in the molecular etiology of these diseases [10]. The upregulated activity of lysosomal proteases such as cathepsin D (CathD) and cathepsin L (CathL) have long been known for their intracellular protein-degrading activities usually regulated within acidic endosomal/lysosomes compartments. However, in tumor invasion and development, these enzymes play a significant role extracellularly influencing cell proliferation, differentiation, apoptosis, angiogenesis, inflammation and extracellular tissue remodelling [11, 12].

Elevated levels of CathL and CathD are reported to be associated with an increased risk of metastasis [13]. For example, CathL is considered to be involved in tumor invasion and metastasis, by degrading subunits of extracellular matrix such as proteoglycans, elastin, laminin, fibronectin, perlecan and interstitial and basement-membrane collagens. Recently, we showed a significant expression of CathL in the omentum hosting metastatic ovarian high-grade serous carcinoma compared with omentum from control patients with benign ovarian cystadenoma, and that exogenous CathL induced pro-angiogenic effects on omental microvascular endothelial cells which may aid metastasis [14, 15]. Recent immunohistochemical studies have demonstrated that enhanced CathD expression is an indicator of potential malignancy in serous ovarian cancer [13], for example Losch et al. demonstrated that CathD was detected in more than 70% of invasive ovarian cancers [16]. Secreted CathD from breast cancer cells and its proteolytic role in degrading extracellular matrix (ECM) proteins and subsequently releasing growth factors such as bFGF, have also been reported, which are important steps for cancer cells to invade surrounding tissue [17]. Misfolding, overexpression and hypersecretion of CathD and CathL have now been demonstrated in numerous cancer types including ovarian, breast, endometrial, lung and prostate, as well as malignant glioma and melanoma and are recognized as critical players in cancer biology by regulating diverse proteolytic functions in fuelling the breakdown of the extracellular matrix and facilitating tumor invasion [18-21]. Adsorption of these enzymes to two-dimensional materials opens a window of opportunity to develop a wide range of new approaches in the prevention of cancer.



Nanotechnology and its underpinning sciences have significantly contributed to the improvement of nanodrug bioavailability and therapeutic index in cancer therapy [22]. Recently, graphene oxide (GO) formulations have been developed into adaptable nanoscale platforms for medical interventions as one of the most sophisticated and minimally toxic tools [23] that permit direct contact and manipulation of the intracellular environment. This could offer a potential therapeutic tool by adsorbing the pro-metastatic enzymes, which are cancer associated stimuli. GO has a large interfacial area and spatial constraints for biological interaction, ideally suited to constructing a robust and cost-effective extracellular tumor-specific enzyme binding method [24]. This capability of GO to bind and track an active enzyme could open the door to new clinical algorithms based on 'enzyme-targeted therapy'. GO nanoformulations that uptake these enzymes could be key enablers of novel anti-metastatic enzyme therapy by breaking down the functional and structural integrity of extracellular enzymes. These GO nanoplatfoms offer a simple, safe and robust strategy in boosting the concept of 'anti-metastatic enzyme targeted therapy', a neologism coined to indicate an innovative and revolutionary approach useful to adsorb and treat 'pro-tumourigenic' with a number of outcomes, notably the clearance of these enzymes, their structural breakdown, their digestion to active site-directed specific adsorbents and deregulation. It is generally understood that the biocompatibility of graphene-based materials is limited by their sharp edges and 2D monolayered structures, which is evident from concentration-dependent toxic effects in numerous cell lines. Notable exceptions however need to be taken into account to find an appropriate biocompatible concentration whose adsorption efficiency is not the outcome of obvious toxic alterations. Targeting and therapeutic adsorption of CathD and CathL in cancer treatment are currently unknown and undefined. The process of enzyme adsorption, and its therapeutic efficacy are effected by several factors such as the properties of proteins and concentration in solution, pH, ionic strength, temperature of the medium, pH-dependent adsorption performance, structural stability of proteins, the selection and nature of adsorbent, porous sites/vacancies in adsorbents to uptake the proteins and strength/stability of adsorbate-adsorbent interface. The mechanistic aspects of protein adsorption and/or protein corona formation as a result of their interaction with graphene may be via electrostatic and hydrophobic interactions [25]. The intrinsic stability of adsorbent matrix structure, which can be revealed by undergoing structural rearrangements, and

conformational alteration resulting protein denaturation and/or loss of functional activities and change in surface energy allows a wide range of chemical changes in functional groups and wettabilities. The established method of fluorescence quenching and absorbance, together with vibrational spectrometry, wetting transparency, adsorption kinetics, and regression analysis can be used to reveal the fundamental aspects of the enzyme-graphene interaction and to address a variety of pre-clinical unknowns in the same theranostic session.

Given the therapeutic challenges posed by secreted CathD and CathL in breast and ovarian cancers, a fuller clearance of these proteins before their involvement in secondary tumour formation may aid development of treatment modalities. We have previously published expression and secretion of CathL and CathD in the omentum and ascites of ovarian malignant patients, as well as in the tumour conditioned media of ovarian cancer cells [14]. In this chapter, we use GO to investigate whether CathD and CathL might be cleared out through an adsorption process. To help visualize the role that GO plays, we use cost-effective and scalable batch adsorption approach, where complementary information is channelled via multimodal kinetic and regression models as an analogy of a multiplexed toxicity-dependent clearance of pro-metastasis enzymes. This chapter reveals that inhibition of CathD and CathL could indeed enhance the therapeutic challenges faced in breast and ovarian cancers. The idea of enzyme targeting therapy is illustrated in **Figure 4.1**.

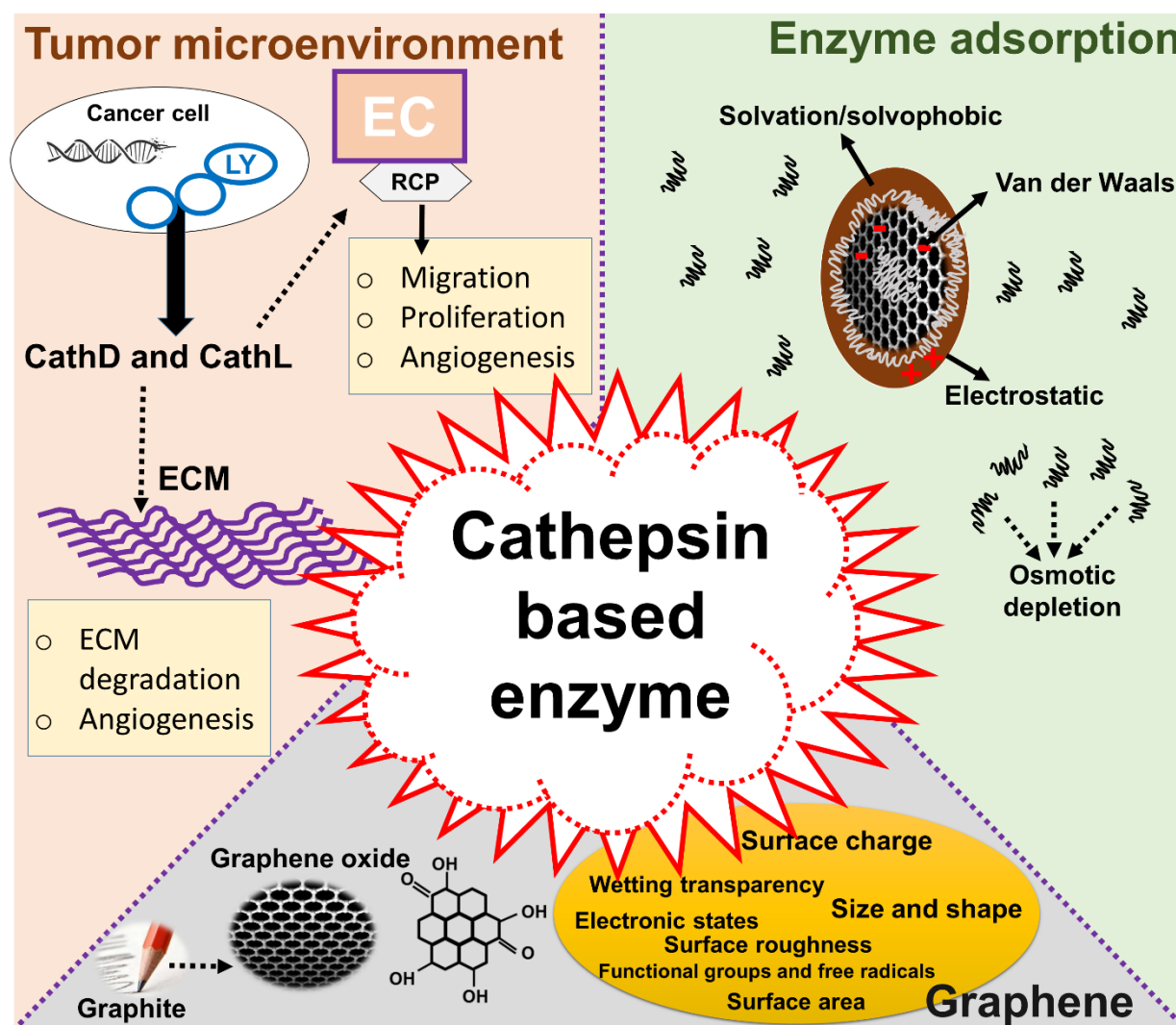


**Figure 4.1: Proposed mechanism of cathepsin function in cancer metastasis and use of graphene oxide (GO) as an adsorbent to remove cathepsin from a living system.** There are three panels in this diagram: (1) role of cathepsins in cancer progression: (2) structure of graphene oxide and its parameters relevant to the adsorption of cathepsins: and (3) the mechanism of adsorption. The left panel (1) illustrates the potential roles of tumor cell-secreted cathepsin D (CathD) and cathepsin L (CathL) on extracellular matrix (ECM), tumor, fibroblast and endothelial cells (EC) in the tumor microenvironment. CathD is synthesized and processed in the rough endoplasmic reticulum (rER) and Golgi bodies (G), and subsequently transported to lysosomes (LY). Overexpressed CathD/CathL is secreted into the extracellular space by tumor cells. Mature cathepsin cleaves ECM and releases basic fibroblast growth factor that may induce angiogenesis. Both CathD and CathL induce tumor cell

proliferation, and hence invasion. CathD induces proliferation of fibroblasts and migration of endothelial cells. RCP represents the Rab-coupling protein in the scheme which, together with EC, is involved in inducing proliferative effects. The bottom panel (2) shows the structure of graphene oxide. This is prepared from graphite using the modified Hummer's method [26, 27, 28]. GO has good properties to adsorb these enzymes such as surface charge, surface area, functional groups, electronic and chemical properties. The right panel (3) shows the potential mechanism involved in particle internalization, their interaction to CathD/CathL and their further breakdown which may lead to cathepsin removal. Electrostatic and van der Waals forces, osmotic depletion and solvophobicity play a pivotal role in adsorption of such enzymes.

## **4.2 Materials and methods**

### **4.2.1 Synthesis and characterization**

Exfoliated graphene oxide (GO) flakes were prepared following the modified Hummer's method previously reported by us [27-29]. 2 g graphite flake, 1.5 g NaNO<sub>3</sub> and 150 ml H<sub>2</sub>SO<sub>4</sub> (98%) were added in an 800 ml flask and mixed under magnetic stirring. The flask was immersed in an oil bath which was warmed to 35 °C, before 9 g KMnO<sub>4</sub> had been added into the flask. The mixture was continuously stirred for 24 h, followed by further addition of 280 ml H<sub>2</sub>SO<sub>4</sub> (5%) and increasing the temperature to 85-95 °C. After 2 h further stirring, the bath was removed and the flask was allowed to cool down to around 60 °C before further addition of 15 ml H<sub>2</sub>O<sub>2</sub> (30 wt%) into it. After another 2 h stirring, the solid product in the suspension was collected, and washed repeatedly with diluted HCl (3 wt%) and distilled water to remove any residual Mn<sup>4+</sup> and other impurities. The resultant GO was dispersed in water under stirring to the concentration of 0.25 mg ml<sup>-1</sup>. The resultant GO was then used for further characterization. High resolution microstructural images were taken on a JEOL-2100 transmission electron microscope (TEM) operating at an accelerating voltage of 200 kV. TEM samples were prepared by dropping onto a holey carbon Cu grid using a micropipette. X-ray diffraction (XRD) analysis was performed using Cu K $\alpha$  radiation (at 40 kV and 40 mA). Spectra were collected with a step size of 0.02° (2 $\theta$ ) and a step time of 1 s. Fourier-transform infrared (FTIR) spectra were recorded in the wavenumber range of 4000–500 cm<sup>-1</sup> using a Bruker Optics Tensor-27 FTIR spectrometer. Samples used in this

case were prepared by mixing the original sample powders with KBr. Raman spectra were recorded using a 532 nm laser excitation operating at 6 mW power. Zeta potential measurements were carried out using a colloidal dynamics zeta probe to identify the surface charge of GO as a function of pH, balanced in the acidic–basic ranges using  $10^{-1}$ M HCl and KOH solutions, respectively. A Jenway 6715 UV/Vis spectrophotometer was used to obtain the UV–Vis diffuse reflectance spectra.

#### **4.2.2 Cell viability**

A549 and SKMES-1 lung cancer cells were seeded in 6 well plates at a density of 350,000 per well. After overnight incubation, cells were treated with or without 5, 50, 250 and 500  $\mu$ g/ml of GO for 24 h. Then, cells were trypsinised and centrifuged at 200 g for 5 min. Cell pellets were then re-suspended in 100  $\mu$ l of annexin binding buffer containing annexin (BioLegend, UK) and propidium iodide (PI) (Sigma-Aldrich, UK), and incubated for 15 min in the dark. Flow cytometry was performed using a Guava flow cytometer. The data were analysed using Guava 3.1.1 software. The early and late apoptotic populations of the cells were analysed by flow cytometer Alexa Fluor647 Annexin V (apoptosis) – F2, Propidium iodide necrosis –F3 YEL. The criteria for early and late apoptotic cells are Annexin V-positive, PI-negative and Annexin V-positive, and PI-positive, respectively. Signals were detected using Alexa Fluor® 647, a bright far-red–fluorescent dye with excitation ideally suited for the 594 nm or 633 nm laser lines. PI is yellow-fluorescent dye with excitation ideally suited to the 532 nm laser line. Toxicity assays were repeated 3 times. The data were analysed in GraphPad Prism 5.04, and expressed as % cell count  $\pm$  SD, Mann Whitney.  $P < 0.05$  was considered statistically significant.

#### **4.2.3 Regression model**

We investigated the relationship between concentration of GO and cell death rate, so that the most appropriate concentration levels could be determined for biological applications. Standard non-linear regression methods will only capture the general trend without taking into account the uncertainties in measurements and predictions. Therefore, we used a Gaussian process (GP) to model the relationships and readily incorporate the uncertainties in measurements to produce a Bayesian posterior

predictive distribution [29, 30]. A GP is essentially a collection of random variables, and any finite number of these have joint Gaussian distribution. Given a dataset  $D = \{(x_i, y_i)\}_{i=1}^n$  with  $n$  data points, where  $x_i$  is the  $i$ th GO concentration and  $y_i$  is the associated cell count, the posterior predictive distribution is  $P(y_{n+1}|x_{n+1}, D, \theta) \sim \mathcal{N}(y_{n+1}|\mu(x_{n+1}), \sigma(x_{n+1}))$ . Here, the mean prediction  $\mu(\cdot)$  and the standard deviation  $\sigma(\cdot)$  are functions of the covariance matrix. The covariance matrix captures the covariance between observed concentrations, which is governed by the specific covariance function and the set of hyper-parameters  $\theta$ . In this study, we used the Matern52 covariance function. The hyper-parameters are set by maximising the likelihood of the data.

#### 4.2.4 Water contact angle measurements and surface energy calculations

The wettability of GO, CathD and CathL were determined using a contact angle goniometer. A digital camera was used to record the images and the contact angle was calculated (using PolyPro). The surface of the sample was prepared for wetting by gently drop casting it onto a glass slide. The surface energy was determined by measuring the contact angle of a 10  $\mu$ l drop of diiodomethane (DIIO) on the surface.

From Young's equation, the surface free energy of a solid (S),

$$\sigma_S = \sigma_{SL} + \sigma_L \cos \theta, \quad (1)$$

where  $\sigma_L$  is the surface tension of the liquid (L),  $\sigma_{SL}$  is the interfacial tension between the liquid and the solid (SL), and  $\theta$  is the contact angle formed by the liquid drop on the surface of the solid. Our aim is to determine  $\sigma_S$  using known  $\sigma_L$  and unknown  $\sigma_{SL}$ .

Following the Fowkes method [45], the interfacial tension

$$\sigma_{SL} = \sigma_L + \sigma_S - 2( (\sigma_L^D \sigma_S^D)^{1/2} + (\sigma_L^P \sigma_S^P)^{1/2} ), \quad (2)$$

where the surface energies are composed of dispersive (D) and polar (P) components.

We can use this to eliminate the unknown in equation 1.

For diiodomethane (DIIO), the liquid polar component is zero, so

$$\sigma_S^D = \sigma_L(\cos \theta + 1)^2/4, \quad (3)$$

where  $\sigma_L = \sigma_L^D = 50.8$  mN/m. From this, we directly find the dispersive component of the surface free energy of the solid from a measurement of the contact angle.

Water has both a polar and dispersive component:  $\sigma_L^D = 26.4$  mN/m and  $\sigma_L^P = 46.4$  mN/m. By rearranging equations 1 and 2 we can determine the polar component of the surface energy of the solid:

$$\sigma_S^P = ( \sigma_L(\cos\theta+1)/2 - (\sigma_L^D\sigma_S^D)^{1/2} )^2/\sigma_L^P, \quad (4)$$

Once we know the dispersive and polar components, the total surface energy of the solid

$$\sigma_S = \sigma_S^D + \sigma_S^P.$$

On pure samples of GO, DIIO formed a contact angle of 33.4° and water 20°. This gives surface energies of 42.8, 29.6 and 72.4 mN/m for the dispersive component, polar component and total, respectively [31]. The other surface energies were calculated in the same manner.

#### 4.2.5 CathD proteolytic activities pH experiment

Citric acid monohydrate and Na<sub>2</sub>HPO<sub>4</sub> pH buffer solutions were prepared ranging between 3, 5.6 and 7. Their composition is given in **SI note 3**. The final volume of each pH buffer was 50 ml containing 0.005% Tween 20 (2.5 µl, sigma). CathD fluorogenic substrate (Enzo Life Sciences) 1 mg was reconstituted in 570 µl DMSO to produce 10 mM stock concentration. 3 µl of this stock was diluted with 2.997 µl of dH<sub>2</sub>O to produce 10 µM working solution (3 ml). This 10 µM solution was further diluted into 100 nM (final concentration) by adding 50 µl (10 µM) to 4.950 µl individual pH buffer. Substrate and substrate-pH buffer solution were kept away from light. Pepstatin A 5 mg was reconstituted in 363.5 µl DMSO, producing a stock solution of 20 mM (stored at -20 °C). A working solution (20 µM) was made by diluting the stock (2 µl) with 1.998 ml dH<sub>2</sub>O. The final concentration was 1 µM (110 µl of 20 µM in 2 ml of each substrate+pH buffer) which was recommended by the supplier (Calbiochem, Millipore) to be the effective concentration. Pepstatin A was added to substrate+buffer solution to produce the final concentration 1 µM. A final concentration of 50 ng/ml CathD was prepared from the stock solution (50 µg/ml). Firstly, 28 µl stock was diluted 10 times in 252 µl dH<sub>2</sub>O to produce 5 µg/ml intermediate stock. This was further diluted to 300 ng/ml. 20 µl of 300 ng was dispensed into test wells containing 100 µl buffer (+substrate, +-pepstatin A) to give a final concentration 50 ng/ml. The experiment was carried out in 4, 96 well black opaque plates (greiner bio-one): 2 plates were for CD+substrate and 2 for CathD+Substrate+pepA. Therefore, in the former 2 plates, substrate+buffer

solution (100 nM) was dispensed in each well, and in the latter 2, 100 µl of pepstatin+substrate pH buffer solution was dispensed per well. Each condition was run in quadruplets per plate. Next, 20 µl of corresponding pH buffer (only) was dispensed in the control wells. Finally, 20 µl of corresponding buffer was added to control wells and 20 µl enzyme solution was added to test wells. Plates were read immediately and up to 10 mins of incubation at room temperature on bench top. Plates were read at Ex/Em: 320/393 and the data normalised to control and represented as a percentage of the control.

#### 4.2.6 CathL proteolytic activities pH experiment

Citric acid monohydrate and Na<sub>2</sub>HPO<sub>4</sub> pH buffer solutions were prepared ranging between 5.6 and 7. Their composition is given in **SI note 3**. CathL fluorogenic substrate Z-Val-Val-Arg-AMC (ZVA) 10mg was reconstituted in 150.6 µl DMSO to produce 100 mM stock solution. An intermediate solution (100 µM) was made by adding 2 µl (100 mM) stock to 1.998 ml pH buffer 5.5. This was further diluted to produce final concentration of 5µM substrate solution in individual pH buffer (100 µl substrate + 1900 µl pH buffer) to make 2 ml. CathL inhibitor Z-Phe-Tyr-CHO (FY-CHO) 2 mg was reconstituted in 45 µl to produce a stock solution of 100 mM. The stock solution was diluted further to make 1 mM working solution by adding 5 µl to 450 µl pH 5.5 buffer. Final concentration was 10 µM in substrate pH solution. CathL 274 µg/ml (pH 5.5, Sigma) was diluted 10 times to produce 27.4 µg/ml intermediate solution in 5.5 pH buffer. Further dilution was made to produce 300 ng/ml concentration in individual pH buffer before dispensing in to the test wells (100 µl/well), to give final concentration of 50 ng/ml (120 µl). The experiment was carried out in 4, 96 well black opaque plates (greiner bio-one). Two of these plates were used to test CathL proteolytic activity in the presence of ZVA. The inhibitory effect of FY-CHO was tested in the other two plates. Firstly, 100 µl of substrate pH buffer solution was dispensed in each corresponding well (both control and test wells) of the former 2 plates. The latter 2, contained substrate + FY-CHO buffer solution (100 µl-both control and test wells). Each condition was run in quadruplets per plate. Finally, 20 µl of corresponding pH buffer was added to each control well and 20 µl of enzyme solution (300 ng/ml) was added to all test wells. Plates were read immediately and up to 10 min of incubation at room



temperature on bench top. Plates were read at Ex/Em: 365/440 using Matt's plate reader.

#### 4.2.7 Enzyme interaction with GO

An interaction between CathD or CathL (50ng/ml) and GO (50, 500 and 1000 µg/ml) was tested in pH buffers (pHs 3.6 and 7 for CathD, and pHs 5.5 and 7 for CathL). pHs values of 3.6 and 5.5 are optimum for CathD and CathL activity, respectively. CathD and/or CathL was incubated with GO at different concentrations for 2, 5, 10, 15 and 20 min. The experiment was carried out in x4 96 well black opaque plates (greiner bio-one). Plates were read at the aforementioned time points of incubation at room temperature to measure absorbance at 280 nm for CathD and CathL using a SpectraMAX plate reader. Plates were read at Ex/Em: 485/530 nm and 490/520 nm to measure fluorescence intensity of CathD and CathL respectively and the data normalised to the control (and represented as a percentage of this control). The fluorescence intensity of the GO hydrolysis was detected kinetically using a SpectraMax plate reader. The same procedure was repeated ( $n=4$ ) with CathL at various concentrations (50, 500 and 1000 µg/ml). The control wells contained GO only (dispersed in distilled water). FTIR, Raman spectroscopy, water contact angle and diiodomethane contact angles were measured in the same way as described in the previous section.

To verify the adsorption of CathD and CathL, an intra-particle diffusion model with the experimental data of this study was used.

Fick's second law was used to find out if intraparticle diffusion is a rate-controlling step during the adsorption experiment [32,33]:

$$q_t = k_{id}\sqrt{t} + I,$$

where  $I$  represents the boundary layer effect (a large value corresponds to a larger boundary layer thickness) and  $k_{id}$  is the intraparticle rate constant. Such plots may present a multi-linearity [34,35], indicating that two or more steps take place. The first, sharper portion is the external surface adsorption or instantaneous adsorption stage. The second portion is the gradual adsorption stage, where intraparticle diffusion is rate-controlled and from it  $K_{int}$  is obtained. The third portion is the final equilibrium stage

where intraparticle diffusion starts to slow down due to extremely low adsorbate concentrations in the solution.

#### 4.2.8 Statistical analysis

Statistical analysis was performed between two groups by an unpaired Student's t-test, and between multiple treatment groups by one-way analysis of variance (ANOVA) with Tukey post-hoc testing or two-way ANOVA with Bonferroni post-hoc test, using Graphpad Prism 5 software. Results are presented as mean  $\pm$  s.d, unless otherwise indicated. The value of  $p < 0.05$  was considered significant.

### 4.3 Results

#### 4.3.1 Synthesis and *in vitro* toxic effects of GO on lung cancer cells

Similar to our previously reported work, exfoliated GO has been synthesized following the modified Hummer's method [26-28]. The basic characterization is given in **Supplementary note 2** and **SI Figures 4.1-4.7**. The TEM image showed the flake-like shapes of GO (**SI Figure 4.1**). The Raman spectrum of GO (**SI Figure 4.2**) exhibited a D band at  $1358\text{ cm}^{-1}$  and a G band at  $1595\text{ cm}^{-1}$ , highlighting the presence of defects and the in-plane stretching motion of pairs of  $\text{sp}^2$  atoms, respectively [36,37]. The surface area of the GO was measured by the  $\text{N}_2$  absorption Brunauer–Emmett–Teller (BET) method and found to be  $25\text{ m}^2/\text{g}$  with a pore volume of  $0.07\text{ cm}^3/\text{g}$  (**SI Figure 4.3**). The zeta potential of the GO sheet was determined as a function of pH to evaluate the effect of GO sheet concentration on the surface charge of the samples. The GO sheets are highly negatively charged when dispersed in water due to the deprotonation of surface carboxylic acid and phenolic hydroxyl groups (**SI Figure 4.4**). GO exhibited the lowest zeta potential value ( $-63.54\text{ mV}$ ) due to the presence of a significant amount of free carboxylic groups. Furthermore, the FTIR spectrum of GO (**SI Figure 4.5**) shows the following characteristic functional groups of GO: C–O–C ( $\sim 1000\text{ cm}^{-1}$ ), C–O ( $1230\text{ cm}^{-1}$ ), C=C ( $\sim 1620\text{ cm}^{-1}$ ) and C=O ( $1740\text{--}1720\text{ cm}^{-1}$ ) bonds. The O–H stretching vibrations in the region of  $3600\text{--}3300\text{ cm}^{-1}$  are attributed to the hydroxyl and carboxyl groups of GO and residual water between the GO sheets [37]. The dispersibility of GO was examined from the linear relationship

between the absorbance ( $A$ ) and the concentration ( $C$ ) of a compound in a solution, given by the Lambert–Beer law. A calibration line was constructed by measuring the absorbance at 232 nm of nine different concentrations of the GO (0.039-10 mg/ml) solution which has given good water dispersibility of GO (**SI figure 4.6**) [39]. The XRD pattern of as-prepared GO gives a (001) reflection peak at  $2\theta = 13.7^\circ$  (**SI Figure 4.7**), corresponding to a d-space of 0.75 nm, indicating an increased interlayer distance compared to that (3.34 Å) ( $2\theta \approx 26.7^\circ$ ) in the graphite structure [40] and complete disintegration of graphite structure to form GO under ultra-sonic vibration.

*In vitro* toxic effects of GO were determined by measuring cell viability, early and late apoptosis, and necrosis in two cell lung cancer cell lines at different concentrations of GO (5-500 µg/ml). Early apoptosis is defined by an increase in phosphatidylserine (PS) expression on an intact cell membrane (detected by annexin V). In late apoptosis, however the membrane loses its integrity and PI permeates into the cells and flags these cells as late apoptotic/necrotic. **Figure 4.2A** demonstrates that after 24-h exposure to GO, the cell viability of both A549 and SKMES cells exhibited a slight but significant ( $p < 0.05$ ) reduction at concentrations of 250 and 500 µg/ml, compared to control (0 µg/ml). Significant early apoptosis was also detected (**Figure 4.2B**), in A549 cells at 500 µg/ml ( $p < 0.05$ ) compared to control (0 µg/ml), and in SKMES-1 cells 50, 250 and 500 µg/ml ( $p < 0.05$ ) of GO. Late apoptosis (**Figure 4.2C**) and necrosis (**Figure 4.2D**) measurements were consistent for A549 cells. Interestingly, in SKMES-1 cells, 250 and 500 µg/ml of GO significantly induced late apoptosis while necrotic cells were detected at concentrations of 50-500 µg/ml. **Figure 4.2E** shows the representative FACS images and analysis of one experiment. GO induced apoptosis and necrosis at concentrations higher than 50 µg/ml in both cell lines. However, the percentage count of apoptotic cells remained higher compared to necrosis, suggesting that GO may not cause significant damage to the cell membrane allowing only annexin V to bind to PS on cell surface membrane. This indicates that cell death observed at higher concentrations of GO is probably due to apoptosis rather than necrosis.

For the toxicity exposures undertaken, GO has been shown to be less toxic than other forms of graphene such as reduced graphene oxide, we recently reported for similar cell lines [29]. However GO has proven to be more toxic than graphene quantum dots as reported by Zhu et al where it was demonstrated that dots have little toxicity to

MG63 (80 ~ 90% of cell viability at low dose) [41]. This may be due to the fact that such dots are smaller than GO, and hence cause less damage to the cell membrane. GO has been proven to have less toxic effects on cellular viability, oxidative stress, and cell death compared to reduced GO because of two dimensional thin sheets, functional groups and surface charge which facilitate its improved cellular uptake [42]. Oxidative stress is thought to be one of the key factors leading to graphene toxicology, reducing the viability of cells and hindering uptake of essential proteins and nutrients [43]. We also investigated the relationships between concentration of GO and cell death rate, so as to determine the most biocompatible concentrations. For this purpose, we used a Gaussian process (GP) to model the relationships and readily incorporate the uncertainties in measurements to produce a Bayesian posterior predictive distribution [29]. Interestingly, the model for A549 cells indicates that concentrations below 200  $\mu\text{g/ml}$  are likely to have better biocompatibility than higher concentrations. In contrast, in the model for SKMES-1 cells, indicated that concentrations between 250 and 500  $\mu\text{g/ml}$  are likely to yield lower cell death. These predictions match with the experimental results. (The details of this model and modelling results are presented in **SI note 2** and **SI Figure 4.8**).

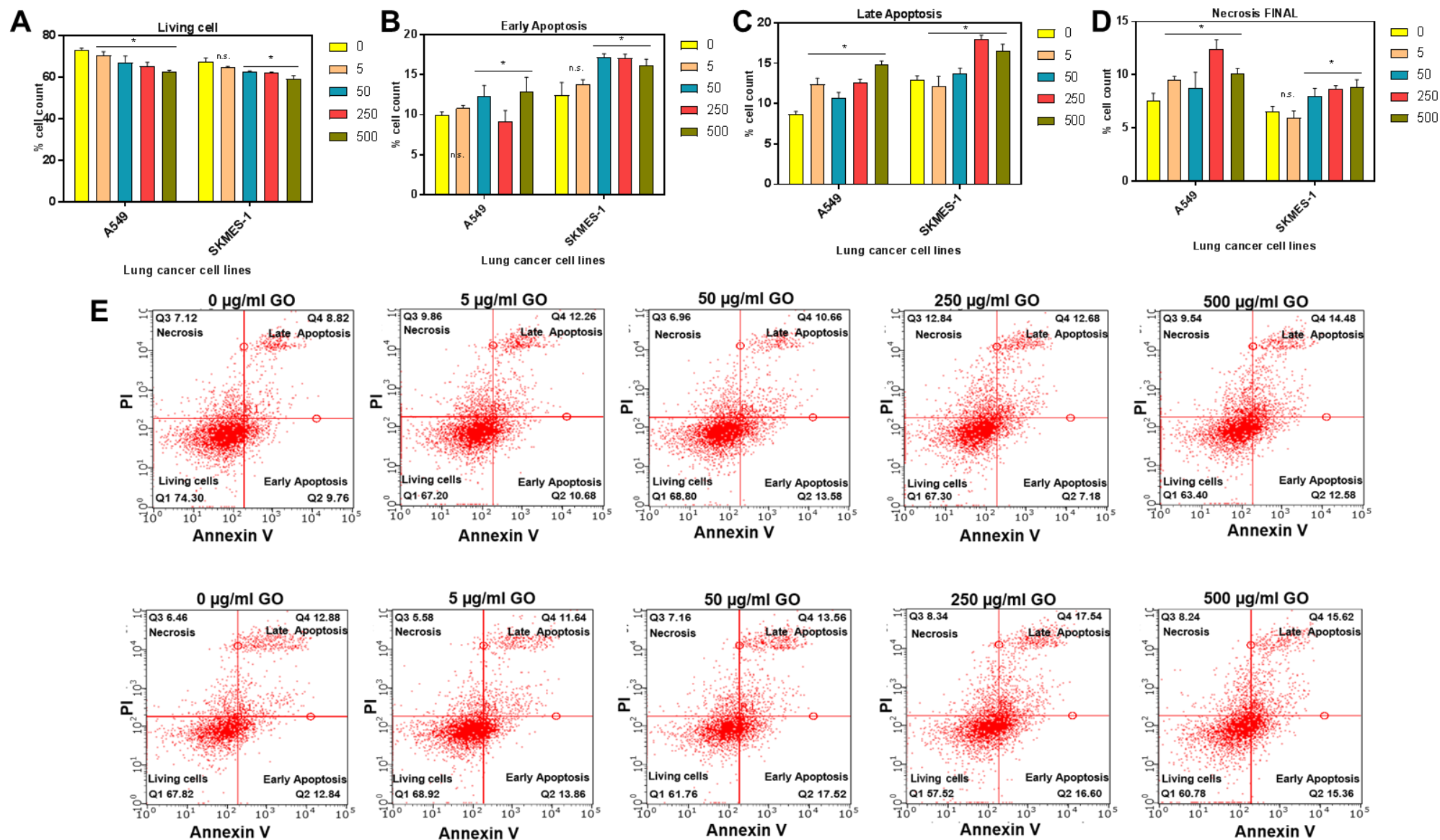


**Figure 4.2: The percentage of living and dying A549 and SKMES-1 lung carcinoma cells before and after graphene oxide treatment. (A-D)** The percentage of dead, living, early-stage apoptotic, and late-stage apoptotic cells in response to different concentrations of graphene oxide (GO). Flow cytometry for A549 and SKMES-1 lung carcinoma cells stained with annexin V (apoptosis) and propidium iodide (PI; late apoptosis and necrosis) following 24 h of treatment with varying concentrations of GO (0–500 µg/ml). **(A)** Percentage of living cells **(B)** early apoptosis **(C)** necrosis, **(D)** late apoptosis (flow cytometry) in response to rGO. Data are represented as mean ± SD, n.s., \*p < 0.05 vs control (0 µg/ml). **(E)** The effect of graphene oxide on cell apoptosis (early and late) and necrosis as quantified by flow cytometry using Annexin V and PI. (Upper panel) A549 and (lower panel) SKMES-1 lung carcinoma cells. The binding of AnnV and PI to the cells was measured by flow cytometry using Guava 3.1.1 software. Experiments were performed and interpreted as follows: cells that were Annexin V<sup>-ve</sup>/PI<sup>-ve</sup> (lower left quadrant) were considered as living cells, AnnV<sup>+ve</sup>/PI<sup>-ve</sup> cells (lower right quadrant) as early apoptotic cells, AnnV<sup>+ve</sup>/PI<sup>+ve</sup> (upper right quadrant) cells as late apoptotic cells, and AnnV<sup>-ve</sup>/PI<sup>+ve</sup> (upper left quadrant) as necrotic cells.

### 4.3.2 Basic characterization of enzymes

The proteolytic activity of CathD was investigated using a specific fluorogenic substrate (1 $\mu$ M pepstatin A) over a range of two pHs 3.6 and 7 while the proteolytic activity of CathL was investigated using a specific fluorogenic substrate ZVA (5 $\mu$ M) over a range of two pHs 5 and 7. It is evident that CathD is mostly active at its physiological pH (3.6). As pH was increased to 7, fluorescence signals were observed to be reduced (**Figure 4.3 A**). The result suggests that CathD is not active at pHs higher than its optimum and CathD is active as a mitogenic factor in non-proteolytic manner when used in the cell culture media. Fluorescence signals from the substrate hydrolysis did not rise significantly from their control. This suggests that pepstatin A is active and efficiently blocks CathD-mediated proteolysis. On the other hand, CathL is mostly active at its physiological pH 5 (**Figure 4.3 B**). Fluorescence signals remain almost two times higher than the control at pH 7 (pH of the cell culture media). The data suggested that CathL is proteolytically active at pHs above the physiological optimum level. CathL-mediated ZVA proteolysis were inhibited by 10 $\mu$ M FY-CHO. This suggests that FY-CHO is an efficient inhibitor of CathL's proteolytic activity and that CathL is a proteolysis-independent mitogenic factor in cell media.

The representative FTIR spectra of CathD and CathL are given in **Figure 4.3C** for the spectral range (3200–500  $\text{cm}^{-1}$ ). The most prominent band assignments of the CathD at 1100, 1243, 1280, 1413, 1713, and 2050-2150 are C-O stretch, CH wagging, C-O stretch, Carboxylate ion ( $\text{COO}^-$ ) symmetry,  $\text{C}=\text{O}$  stretch carboxylic acid and C-H alkyl stretch respectively [44,45]. The most prominent band assignments of CathL at 1100, 1243, 1280, 1413, 1713, and 2050-2150  $\text{cm}^{-1}$  are C-O stretch, CH wagging, C-O stretch, carboxylate ion ( $\text{COO}^-$ ) symmetry,  $\text{C}=\text{O}$  stretch carboxylic acid and C—H alkyl stretch respectively [44-46]. These bands were not observed in control experiments without CathD/CathL and substrate agents (data not shown). The regions with the widest ranges and their corresponding spectral signatures have been given in **SI Table 4.1**. The representative Raman spectra of CathD and CathL are given in **Figure 4.3 D** for the spectral range (2500–500  $\text{cm}^{-1}$ ). The most prominent band assignments of the CathD are 2243, 2024 and 1603  $\text{cm}^{-1}$  while assignments of CathL are 2024 and 1603  $\text{cm}^{-1}$ . The strong peak at 1608  $\text{cm}^{-1}$  corresponds to the known bands for the Fmoc group as reported earlier [47]. The Raman bands at 2024 and 2243

$\text{cm}^{-1}$  could be assigned to the  $\text{C}\equiv\text{C}$  stretching vibration, which was present in the propargyl group [47]. The surface free energy and its polar and dispersive parts were calculated to investigate the binding capacity and weight of electrostatic and/or van der Waals interactions between GO and the enzymes. The binding capacity of GO, CathD and CathL were calculated using the contact angle method and their respective contact angles have been shown in **Figure 4.3 E**. The surface free energies, polar and dispersive parts of GO, CathD and CathL are shown in **Figure 4.3 F**. CathD has the highest total surface energy of 77.4 mN/m, although GO, CathD and CathL have similar trends of surface energies of total and their respective parts because of the similar amount and weight of functional groups. As a result, the use of GO as an adsorbent could allow enzymes to be adsorbed and substituted to improve the binding of CathD/CathL with GO. It could also allow the rearrangement of the binding pocket in response to the substitutions. As a result of this process, it appears that the amino substitution at edge positions of GO ought to result in a more tightly binding ligand. (See set of “snapshots” in **Figure 4.3 G**).



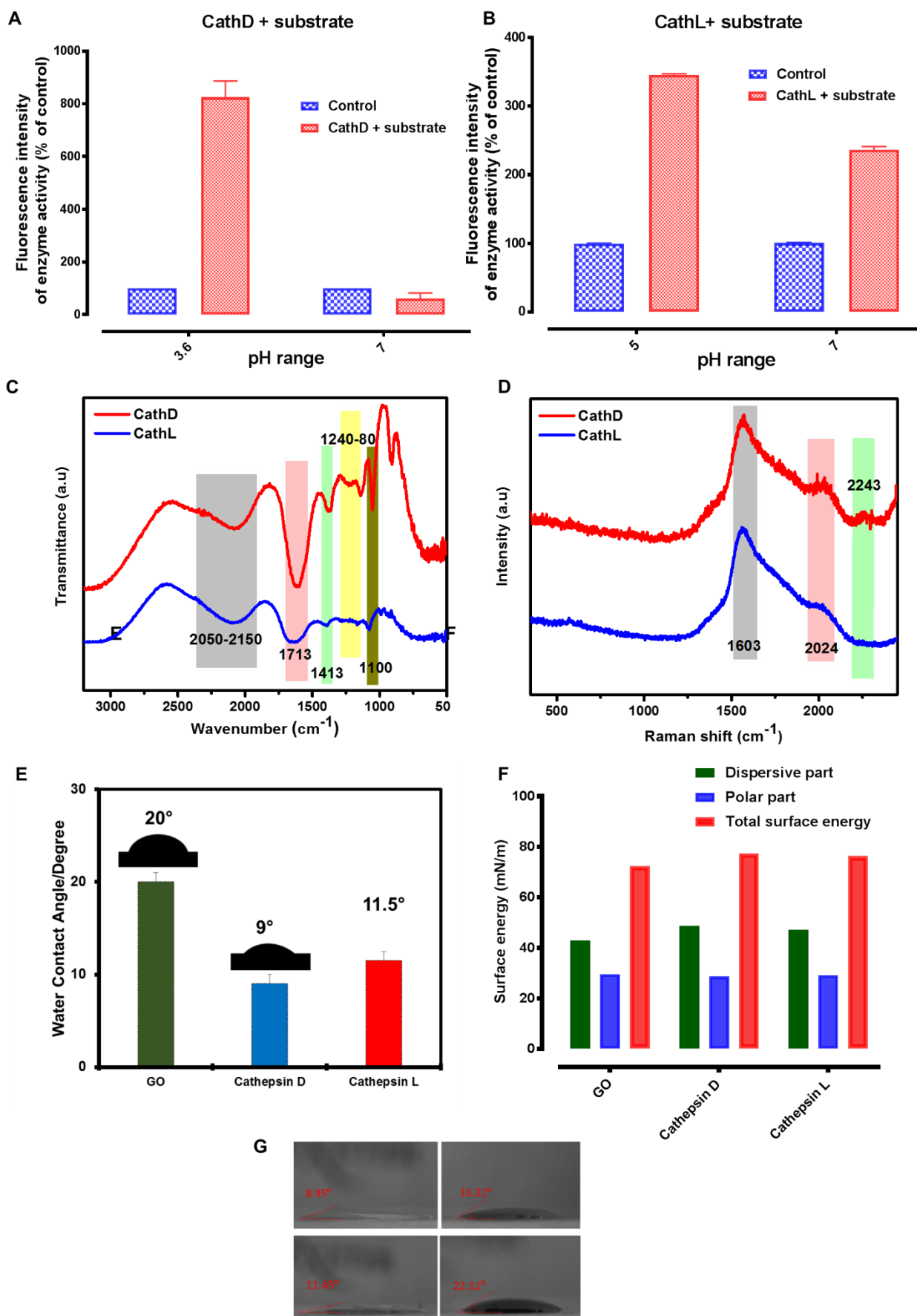


**Figure 4.3:** Characterization of cathepsin D (CathD) and cathepsin L (CathL). **(A)**

CathD is highly active at pH 4 (optimum) and inactive at pH 7 and above. A specific fluorogenic substrate (10 $\mu$ M) was incubated with CathD (50ng/ml) in 96 well plates at different pHs ranging from 3 to 7.6 as shown. Fluorescence signals were measured using plate reader at Ex/Em: 320/393. Control wells contained pH buffer and substrate. The data is represented as percentage of control. **(B)** CathL is highly active in ionic buffer. A specific fluorogenic substrate ZVA (5  $\mu$ M) was incubated with CathL (50ng/ml) in 96 well plates at different pH ranging from 3 to 7.6 as shown. Fluorescence signals were measured using a plate reader at Ex/Em: 365/440. Control wells contained pH buffer and substrate. The data are presented as percentage of control. **(C)** FTIR of CathD and CathL. **(D)** Raman spectra of CathD and CathL shows bands at 1602 and 2024  $\text{cm}^{-1}$ . **(E)** Water contact angle profile of GO, CathD and CathL gives the values of 20°, 9° and 11.5°. **(F)** Surface energy profile of GO, CathD and CathL. **(G)** Representative images and quantification of wettability, as measured by water and diiodomethane contact angles of GO, CathD and CathL. A digital camera was used to record the images and their contact angles were calculated by PolyPro software package.

#### 4.3.3 Enzyme interaction with GO

Batch adsorption studies were conducted to measure the adsorption properties of CathD and CathL on GO. **Figure 4.5** shows that an increase in adsorption capacity occurred for both enzymes over a 20 min time period, reaching a maximum capacity of above 90%. The capacity was found to be slightly greater for higher concentrations of GO with both kinetic models showing a good agreement with the experimental data (**Figure 4.6 A and B**). **Figure 4.4** shows absorbance variations at different concentrations of GO (0, 50, 500 and 1000  $\mu\text{g/ml}$ ) exposed to CathD and CathL over different time scales (0-20 mins). The decrease in absorbance signals of CathD and CathL at pH of 3.6 and 5, respectively revealed the adsorbed amount of CathD and CathL to GO. With increase of time and concentration, CathD and CathL were almost fully adsorbed onto the GO surface. CathD and CathL adsorption was pH dependent, with the highest concentration of GO, which demonstrated highest adsorbed amounts at more acidic pHs (3.6 and 5). For pH 3.6, the amount of CathD adsorbed increased from 50 to 1000  $\mu\text{g/ml}$  over a time scale of 0 to 20 mins. It is evident that adsorption capacity of 1000  $\mu\text{g/ml}$  of GO is above 90 % after 20 mins. CathL adsorption on the GO surface followed a similar pattern in pH of 5 and 1000  $\mu\text{g/ml}$  concentration of GO attained the highest value of efficiency after 20 min.

Adsorption kinetics are useful to investigate the adsorption mechanism and adsorption rate. In this study, we have used an intraparticle diffusion model which has clearly shown three linear segments to explain the adsorption stages: the first stage is attributed to the instantaneous adsorption onto the GO's surface; the second to intraparticle diffusion; and the third to the final equilibrium stage for which the intraparticle diffusion started to slow down because of the extremely low adsorbate concentration left in the solution. **Figure 4.6 A-B** show that none of the intraparticle diffusion plots passed through the origin, which showed that the intraparticle diffusion was part of the adsorption but was not the only rate-controlling step and indicates the effect of film diffusion (boundary layer diffusion) on the adsorption of CathD and CathL. (The intraparticle diffusion constant values are shown in **SI Table 4.2**). Gaussian process regression models for CathD and CathL relating independent variables (time and concentrations) to the dependent variable of adsorption are shown in **Figure 4.5 (C-F)**. In **Figure 4.5 C and E**, the mean predictions for CathD and CathL are depicted respectively and the uncertainty in these predictions has been shown in **Figure 4.5 D and F**. The mean predictions for CathD indicate that promising (lower) absorption can be achieved with a concentration around 100  $\mu\text{g/ml}$  when it is active for 15 to 20 min. The models also revealed that concentrations greater than 900  $\mu\text{g/ml}$  which is active for about 18 min could also be promising. Additionally, the uncertainty in the model is relatively low in these areas. **Figure 4.5 E and F** shows similar trends CathL.

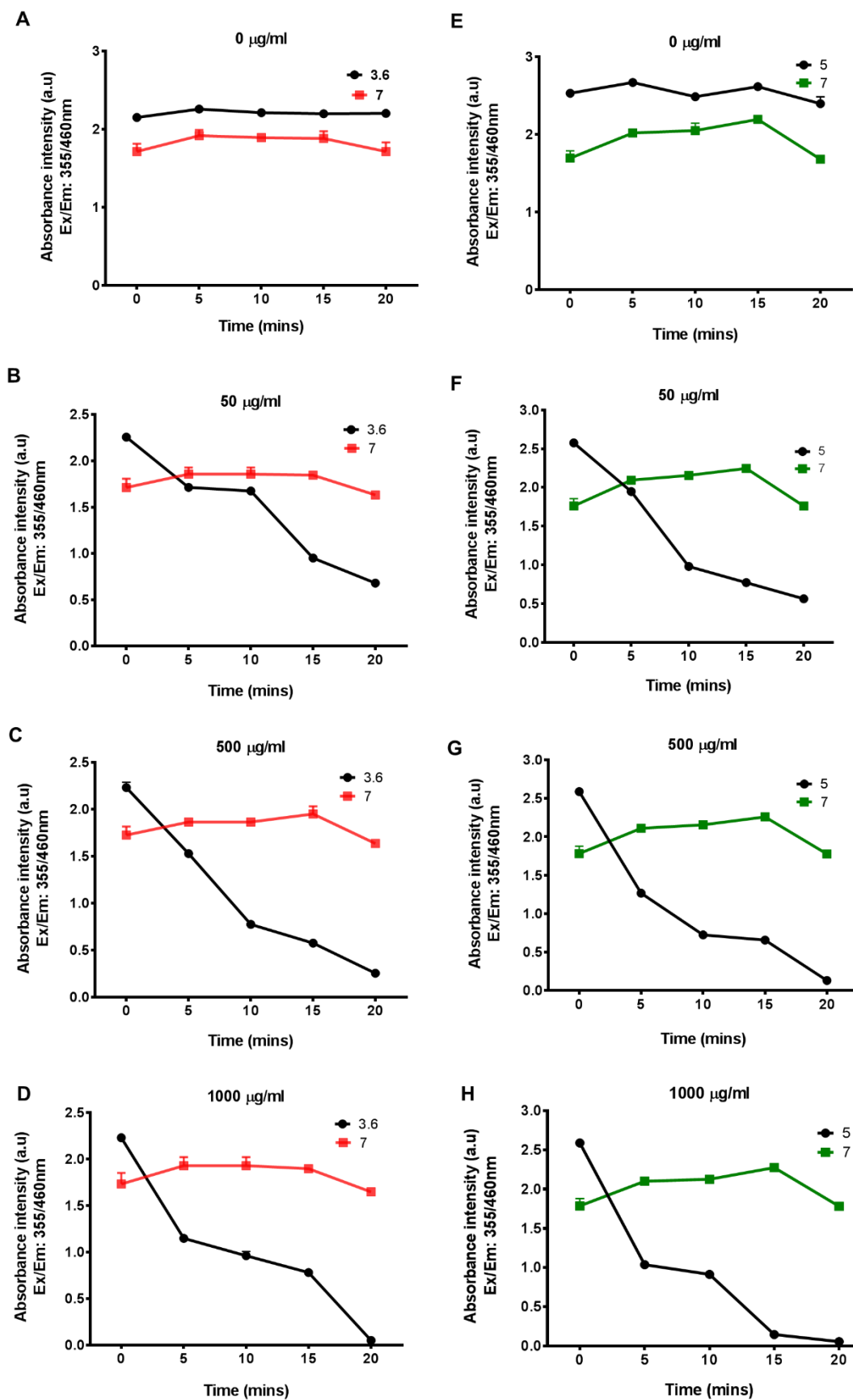


**Figure 4.4:** Effect of different concentrations of GO on CathD and CathL activities. Absorbance of CathD (A-D) and CathL (E-H) by GO at different concentrations (50,

500, and 1000  $\mu\text{g/ml}$ ) incubated in 96 well plates at different time-points (2, 5, 10, 15, and 20mins) Absorbance signals were determined using plate reader at Ex/Em: 355/460nm.

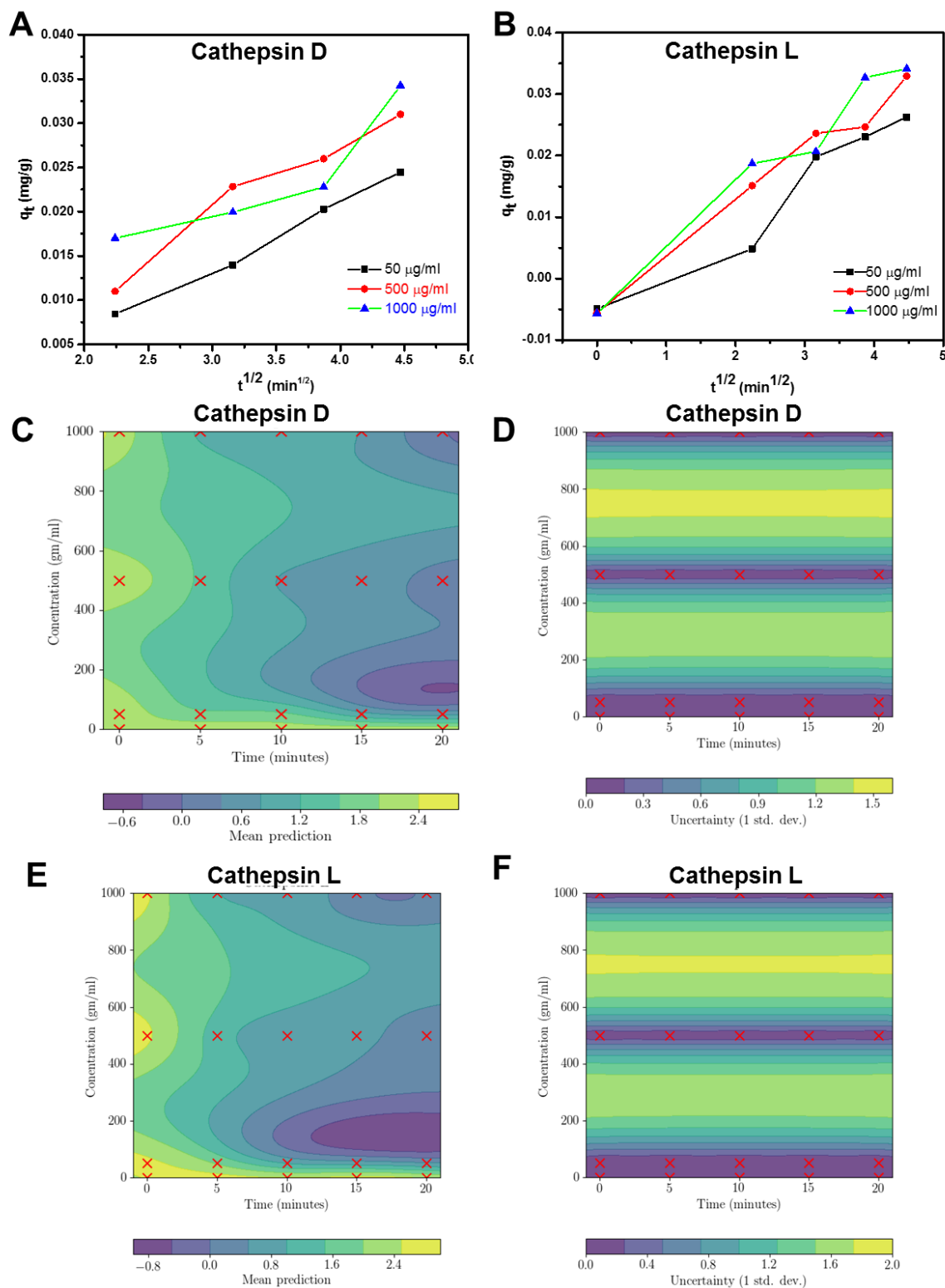


**Figure 4.5: (A-B)** Kinetic models fitting to the data for CathD and CathL using piecewise linear regression analysis of the adsorption experiments of (A) CathD and

(B) CathL on GO. **(C-F)** Gaussian process regression models to find prediction and uncertainty in CathD (C, D) and CathL (E, F) relating independent variables, (time and concentration), with dependent variable (absorption). In C and E, the mean predictions are depicted and the uncertainty in predictions is shown in D and F.

**Supplementary Figure 4.9** illustrates normalized fluorescence intensities of different concentrations of GO (0, 50, 500 and 1000  $\mu\text{g/ml}$ ) exposed to CathD and CathL over different time scales (0-20 min). The ability of both CathD and L to enzymatically cleave a fluorescent GO is reduced at increasing concentrations of GO (0, 50, 500 and 1000  $\mu\text{g/ml}$ ). GO dose dependently increase the catalytic activity of CathD and CathL at both pH tested. A slight difference in emission spectra also occurs, suggesting that lowering the pH to more acidic values triggers an increased solvent exposure of non-polar sites in the enzymes. Fluorescence loss was observed in the case of CathL at pH 7 due to the reversible nature of CathL inhibition. No significant difference in fluorescence could be due to uptake of enzymes induced by GO. This uptake allows localization of internalized GO under different pH conditions [48, 49]. This could be attributed to the large size of GO which blocks fluorescence signals. This suggests that the CathD and CathL were adsorbed onto the surface of GO via physiochemical interaction and hence block the emission of fluorescence signals from the GO. CathD and CathL bonding speeded up with increasing the concentration of GO. This behaviour could indicate that both the enzymes and GO surface had to adapt their structures to form a stable interface. At high enzyme coverage of the GO surface, one could also envisage that rearrangements of protein molecules already bonded to the GO were required to make room for an incoming protein molecule. This crowding effect would contribute significantly to the self-fluorescence properties of GO. Understanding the respective effects of these factors to allow the design and uptake of pro-tumourigenic and pro-metastatic enzymes released in extracellular matrix from malignant tumors will be the focus of further studies.

FTIR and Raman spectroscopic findings can be used to monitor the macromolecular movements and vibrational/rotational states of specific chemical groupings which bind target biomolecules with high specificity during the formation of the nano-bio-interface of CathD- and CathL-GO. **Figure 4.7(A-B)** shows FTIR spectra of GO linked to CathD

and CathL at the concentrations of 50, 500 and 1000  $\mu\text{g/ml}$  of GO after 20 mins. The FTIR spectrum of CathD-linked GO exhibited a variety of CathD and CathL absorption features such as C=O ( $\nu_{\text{C=O}}$  at  $1714\text{ cm}^{-1}$ ), and the peak of the C–N stretch mode ( $\nu_{\text{C=N}}$  at  $1100\text{ cm}^{-1}$ ) in all the concentration represents the CH stretching and NH bending. The spectra of CathD after interaction with 500 and 1000  $\mu\text{g/ml}$  GO (**Figure 4.6 A**) showed the characteristic peak of alkoxy group at  $980\text{ cm}^{-1}$  which arose from the C=O functional groups of GO and CathD. The peaks at  $1413\text{ cm}^{-1}$  ascribed to NH bending and CN stretching also confirmed the existence of CathD and CathL. These results confirmed that CathD and CathL have been successfully covalently bonded onto the surface of GO. **Figure 4.7(C-D)** shows Raman spectra of CathD and CathL-linked GO. In the spectra of 500 and 1000  $\mu\text{g/ml}$  concentrations of GO, the amide-I vibration at  $1590\text{ cm}^{-1}$  arose mainly from the  $\nu_{\text{C=O}}$  stretching vibration. The band in the range of  $2020\text{--}2250\text{ cm}^{-1}$  was caused by the C-H<sub>3</sub> and C-H<sub>2</sub> deformation vibrations from the side chains of different amino acids. The amide-III was the combination of the N-H bending and C-C stretching vibration in the region  $1200\text{--}1340\text{ cm}^{-1}$  [30, 31]. Slight shifts can be observed between the two Raman spectra of GO and CathD and CathL adsorbed on GO. In the spectrum of GO (**SI Figure 4.2**) there were two typical peaks at ca.  $1355\text{ cm}^{-1}$  and  $1580\text{ cm}^{-1}$ . The bands at  $1600\text{--}1620\text{ cm}^{-1}$  can be assigned to the C=O stretching of carboxylate and C-H<sub>2</sub> deformation vibration. In the Raman spectra of GO and CathD/CathL- GO, the prominent amide band at  $1600\text{--}1620\text{ cm}^{-1}$  of Cathepsins was shifted to  $1590\text{ cm}^{-1}$  at the CathD/CathL-GO interface. Based on these facts, it could be inferred that the CathD and CathL interacted with GO through its amide bonds. However, the amide bonds might not be the only force that bonded CathD and CathL to GO. Both Cathepsins have a deep bonding pocket with the binding groups identified by FTIR, at the bottom which provides the space and electrostatic attractions.

The functional groups existing at the surface of GO readily make its surface passivated covered with inert molecules, which increases surface hydrophilicity and subsequently enhances the bonding strength of these nanostructures [32]. Several site-specific variants of GO have made an attempt to alter the surface-inactivation of ‘wild-type’ enzymes. The extent of this change and mechanistic insight of protein interaction with surfaces have been probed by water contact angle (WCA) measurements and surface

energy (**Figure 4.6E-F**). The CathD and CathL displayed higher binding activity towards GO, as demonstrated by the WCA values. Upon CathD and CathL interaction, the WCA profiles of GO shifted to higher values, suggesting that a good level of surface hydrophilicity was achieved (**Figure 4.6F**). The effect was more pronounced for the higher concentrations, whose average WCA value increased by 8.5 and 15.02 for CathD and CathL, respectively. The changes in diiodomethane contact angle (**Figure 4.6F**) revealed the surface energy profile, which is quantitatively shown in **Figure 4.6G-H**. The binding free energies of GO to CathD and CathL are shown in **Figure 4.6G-H**. When one group is replaced with an amino group, the intermolecular vdW and electrostatic interactions become more favorable, while more desolvation penalty is paid. The total free energy is improved due to the charge distribution of nano-bio-interface substituent changed completely after introducing the amino group and carboxyl bond network to the ring, the conformation of the whole ligand changed accordingly. However, the polar penalties upon binding of these two proteins to GO was decreased. As a result of this process, it appears that the amino and carboxyl substitutions at the interface position ought to result in a more tightly binding ligand.

Overall, the results have addressed a couple of key features related to the surface interaction of GO substrates with CathD and CathL: (i) the effect of the functional groups existing on the surface of GO and CathD/CathL; (ii) hydrophobicity driven by the adsorption of CathD/CathL onto the GO surface to form a nano-bio-interface. (The WCA of CathD and CathL is shown in **Figure 4.3**). Furthermore, the rise in total and dispersive surface energy caused by the CathD/L-GO interaction revealed that differences in functional group content, conformational flexibility, and shape and distinct bonding affinities released a higher free surface energy. Higher concentrations of GO readily covered the surface of the CathD/CathL to initiate the formation of a protein 'soft' corona, while lower concentrations with lower yield of functional changes took over to form a corona. The low polar and high dispersion parts (**Figure 4.6 G-H**) of the surface energy revealed that the polar and nonpolar side-chains of CathD/CathL facilitate conformational changes in the CathD/CathL structure and which in turn leads to high adsorption capacity of CathD/CathL into GO.



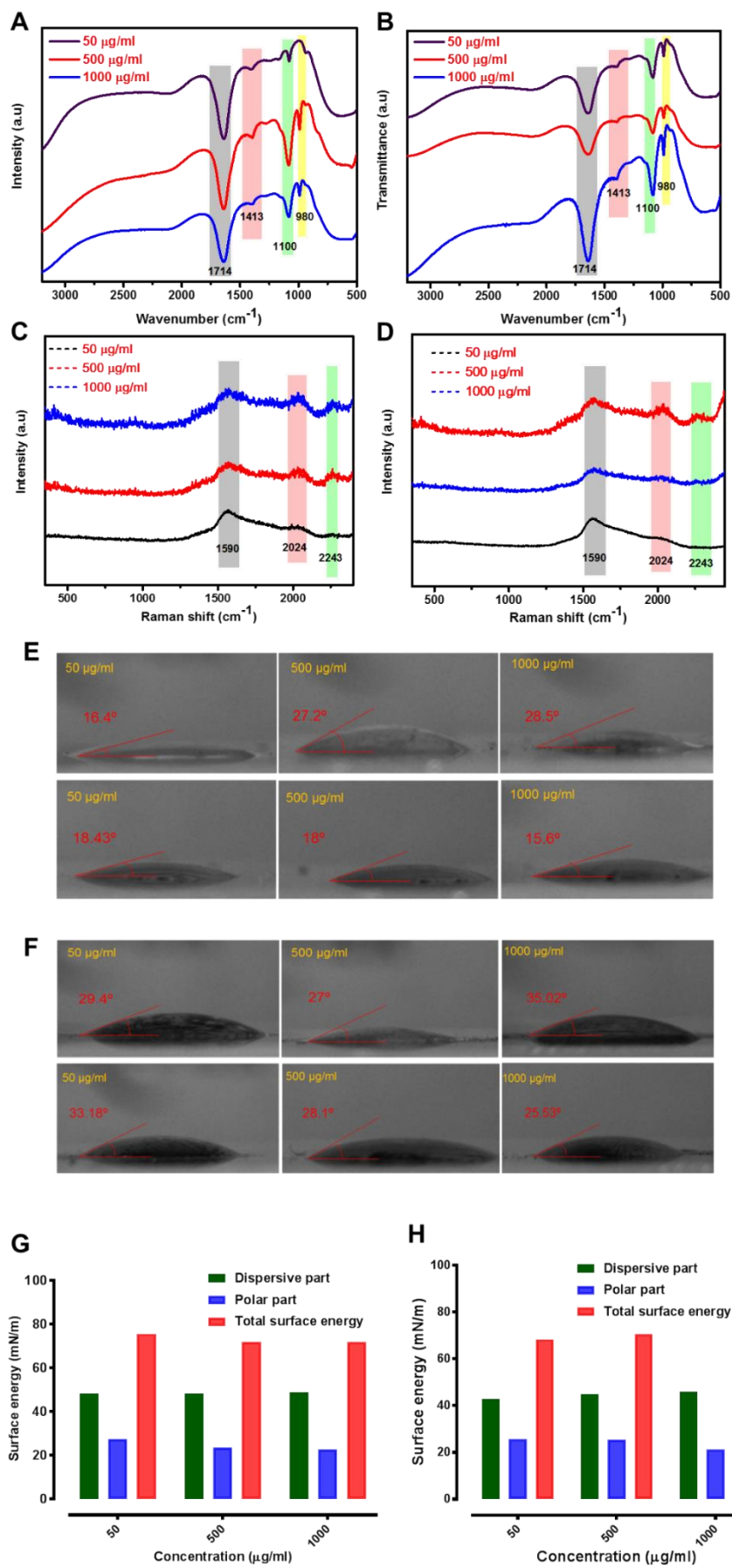


**Figure 4.6:** (A-B) FT-IR spectra of CathD/CathL-linked graphene oxide (GO) at 50, 500, and 1000  $\mu\text{g/ml}$  concentrations of GO. (C-D) Raman spectra of CathD/CathL-linked GO at 50, 500, and 1000  $\mu\text{g/ml}$  GO concentrations (E-F) Contact angle profiles of CathD/CathL-linked GO interfaces at 50, 500 and 1000  $\mu\text{g/ml}$  concentrations of GO. Diiodomethane contact angle was measured to calculate the surface energy of enzymes, GO and their interfaces. (G-H) Surface energy profile of GO- CathD/CathL interfaces which have three segments of total surface energy, dispersive surface energy and polar surface energy of 50, 500 and 1000  $\mu\text{g/ml}$  concentration of GO treated with CathD and CathL.

#### 4.4 Discussion

The complexities of cancer entail the innovation of treatment modalities that are capable of clearing out the pro-tumourigenic enzyme by developing a novel platform based on biocompatible adsorbents. The currently available mainstream treatment options have resulted in improved survival and quality of life, although ovarian and breast cancers remain progressive diseases. Thus, there is an ever growing need for the development of alternative approaches. Conventional biological drug therapies have limitations due to inherent risk of abnormality and unwanted side effects on normal tissues/cells that adversely affect the efficacy and safety of the treatment. An emerging paradigm in cancer therapy suggests that adsorption of these enzymes in the local tumour environment can be compromised by using porous adsorbents. Enzyme-targeted therapy holds great promise for this by addressing the mechanisms of their clearance and treatment escape. In this study, we developed GO that breaks down and uptakes such enzymes which promote increased invasiveness and metastasis. The surface charge, surface area, chemical reactivity and electronic characteristics of GO were used to target these enzymes with sustained release of its active functional groups, free radical and porous sites for entrapment of CathD and CathL. The inhibition of CathD and CathL was observed at specific pH values which supports metastasis also verified by enzyme activity using specific substrates. The analysis of the released CathD and CathL libraries are carried out using a wide variety of analytical tools such as FTIR, Raman, WCA and surface energy profiles (see **Figures 4.2 and 4.6**), thus offering a greatly accelerated identification process and

much higher throughput compared with conventional tools to analyse nanoparticle interactions with proteins. In this manner, the characterization of the studied enzymes for their binding and bioactivity is carried out to better understand their structural and functional behaviours.

The current approach of enzyme targeting offers a number of important advantages. First, it allows the facile tagging of cathepsins with very high transformation/removal efficiencies using GO, which significantly increases the chances of identifying biomolecular fractions. Second, the clinical safety of this approach would further benefit from using a GO system that is already used in clinical trials to introduce drug/gene carrier vehicles. Finally, and very importantly, our approach is highly versatile and can be applied broadly for the discovery of therapeutic rescuers of disease-associated proteins. Here, we have used it to target two prominent ovarian and breast cancer-associated enzymes. The two-dimensional and adsorbing nature of GO could reduce the likelihood of abundance of these enzymes to induce tumor cell invasion and metastasis, and thereby maximize its broad applicability. Furthermore, the GO not only allows for robust interaction with enzymes but also enables the compact packaging of the GO within dissolvable capsules, facilitating non-invasive oral administration to track these proteins, which could be used as a diagnostic tool. Despite the obvious advantages presented by enzyme-targeted therapy (compared with the blunt instruments of chemotherapy, radiation and surgery), the cost-effectiveness involved in producing GO is another advantage for implementing this material as a standard-of-care in the treatment of cancer. Currently, clinical-scale manufacturing of GO requires a variety of elaborate protocols to modify, deliver and selectively accumulate and administrate into the living systems. Future work will address cell based and pre-clinical metastatic disease models and will potentially involve further developments to incorporate targeted and achievable delivery of GO to the tumor sites with sufficient selectivity to facilitate the removal of disseminated enzymes. New drug delivery systems are needed to facilitate such combinations that may deliver adsorbent, and further studies are warranted to investigate the long-term impacts on cure rate, survival and potentiation of this therapy regimens.

## 4.5 Conclusions

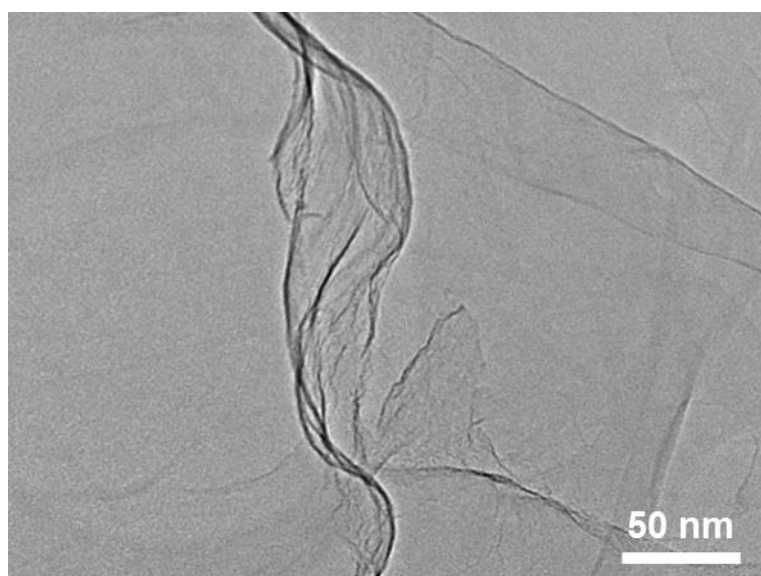
In summary, this chapter represents a straightforward and highly adaptable strategy for the rapid and facile removal of pro-metastasis enzymes that effectively rescue the disease. GO with its variable zeta potential, variety of functional groups and very large (and in principle fully accessible) surface area, is an extremely promising candidate for the adsorption of such enzymes. Results show that this material is compatible with cells. In addition, the adsorbent preparation is based on abundantly available and cost-effective graphite as main precursor. GO nanostructures are easy to manufacture and are stable, which simplifies long-term storage and correspondingly reduces the cost. Thus, if implemented in the clinic as a new form of active enzyme therapy, this technology could provide a practical, low-cost and broadly applicable way to treat cancer.

## 4.5 Supplementary information

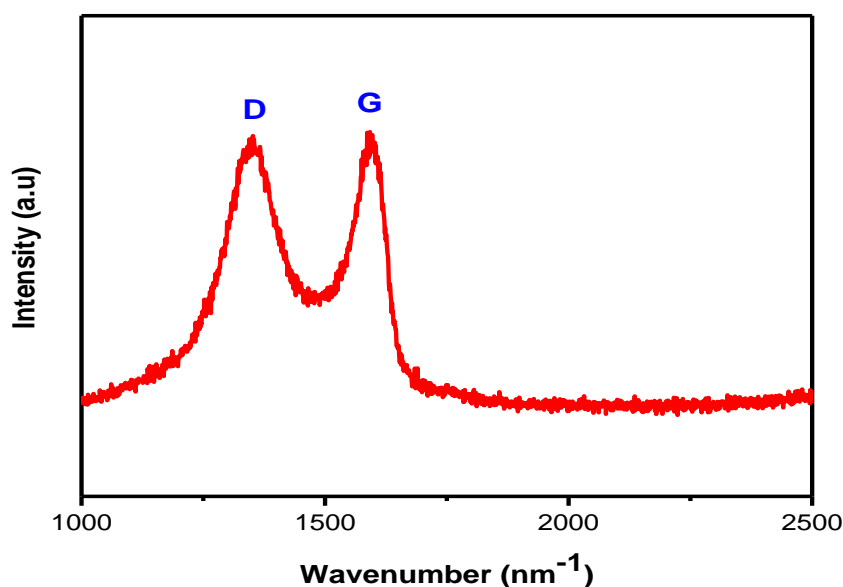
**Supplementary note 1:** We first characterized graphene oxide (GO) with a wide range of characterization tools such as Fourier-transform infrared spectroscopy (FTIR), Raman spectroscopy, transmission electron microscopy (TEM), scanning electron microscopy (SEM), Zeta potential analyser,, X-ray diffraction (XRD) and Brunauer–Emmett–Teller (BET) surface area method.

The surface area of the GO as measured by the N<sub>2</sub> absorption Brunauer–Emmett–Teller (BET) method is 25 m<sup>2</sup>/g having a pore volume of 0.07 cm<sup>3</sup>/g (**SI Figure 4.3**). However, it is still lower than the theoretical specific surface area for completely exfoliated and isolated graphene sheets (~2,620 m<sup>2</sup>/g), potentially because it measures the outer surface of GO grains. The nitrogen molecules are inaccessible to the interlayer and interlamellar spaces of GO and as a result acid-base processes in aqueous GO dispersions take place on much greater surfaces. According to the Ruess model, graphite oxide consists of wrinkled carbon sheets composed of trans-linked cyclohexane, and the fourth valencies of the carbon atoms are bound to axial OH-groups and ether oxygen atoms in 1,3-positions. As a result, this geometrical network, functional groups existing at the edges and basal planes of GO sheets, degree of exfoliation and dispersion, and surface chemistry of GO hinders nitrogen

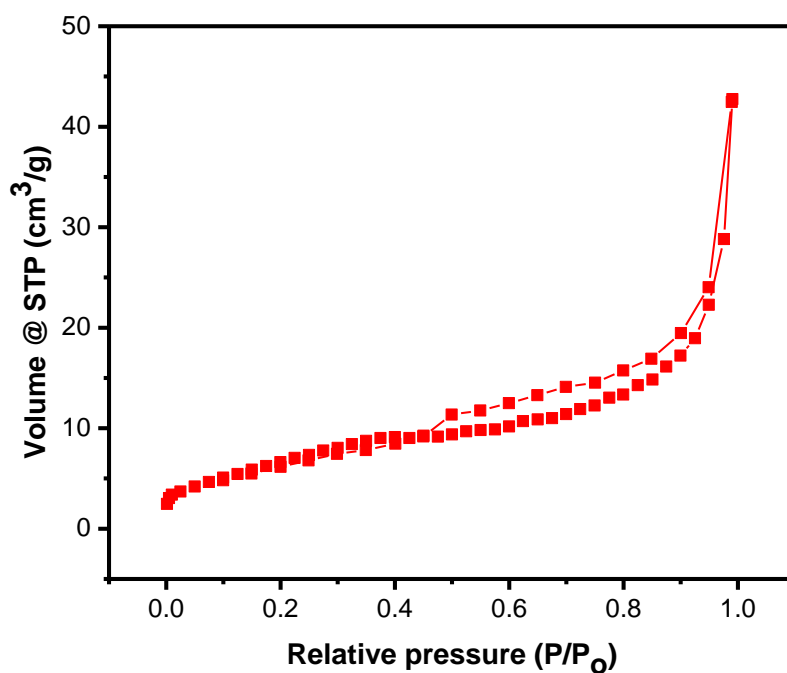
access/adsorption to inner surfaces of GO, which is generally opened up upon exfoliation. The hydrophilic oxygen-containing functional groups provide GO sheets with a good dispersibility in water. The GO obtained shows good water solubility (**SI Figure 4.6**) and exhibits ultraviolet-visible (UV/Vis) absorption spectra of the GO at absorption peak at 232 nm, which is attributed to  $\pi$ - $\pi^*$  transition of the C=C bonds.



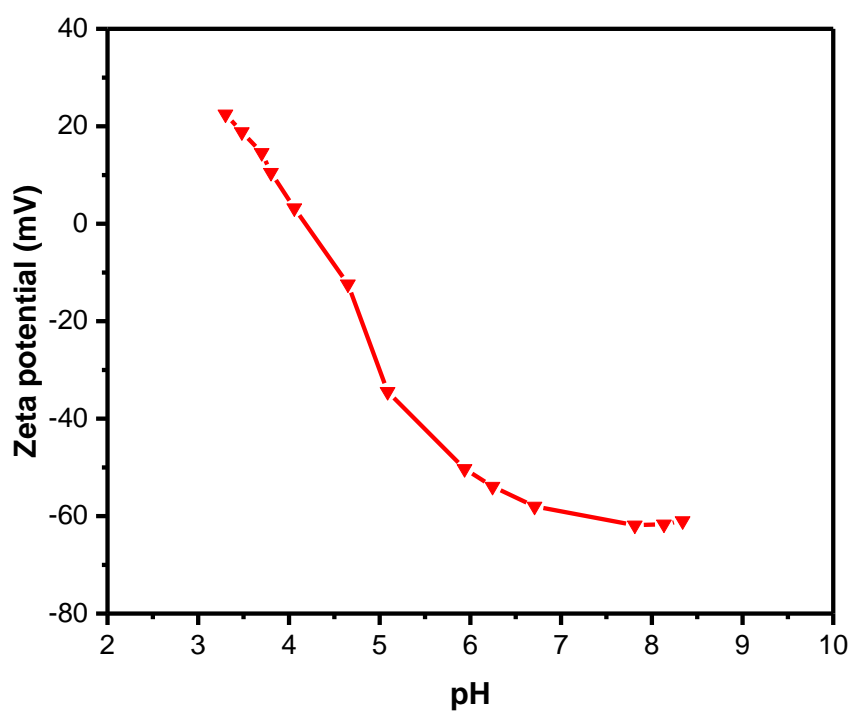
**SI Figure 4.1:** Transmission electron microscopy image of graphene oxide.



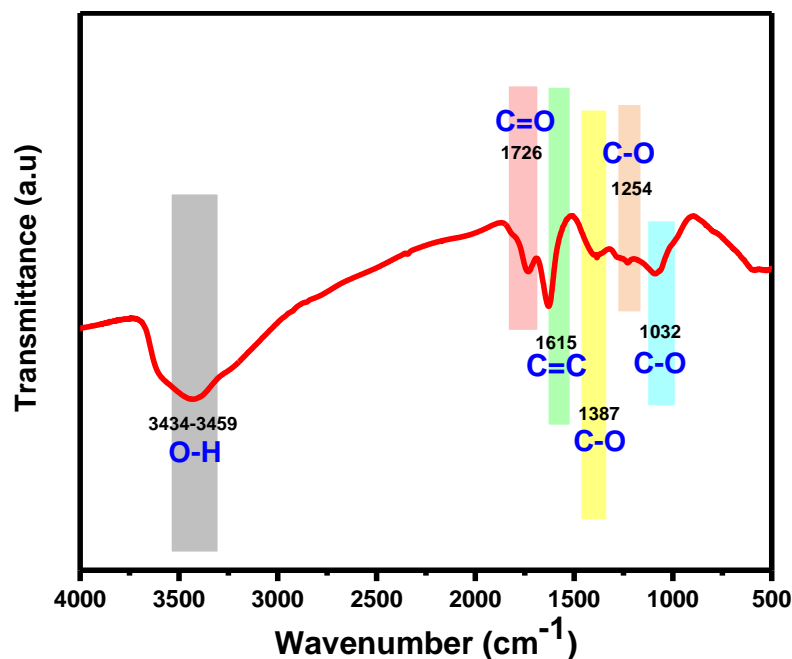
**SI Figure 4.2:** Raman spectrum of the graphene oxide sample shows intense D (1358  $\text{cm}^{-1}$ ) and G peaks (1595  $\text{cm}^{-1}$ ) of defects and the in-plane stretching motion of pairs of  $\text{sp}^2$  atoms, respectively.



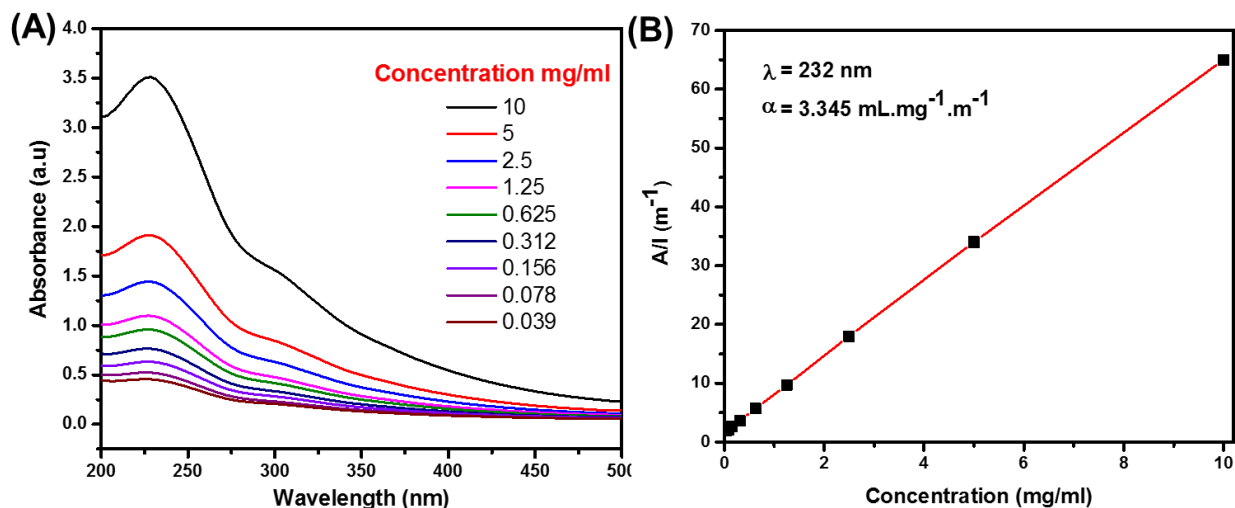
**SI Figure 4.3:** BET surface area of graphene oxide measured by nitrogen sorption isotherms measured at  $-196\text{ }^\circ\text{C}$ . The BET surface area value obtained for this sample using the BET method is  $25\text{ m}^2/\text{g}$ .



**SI Figure 4.4:** Representative zeta potential of graphene oxide over a range of different pH values.

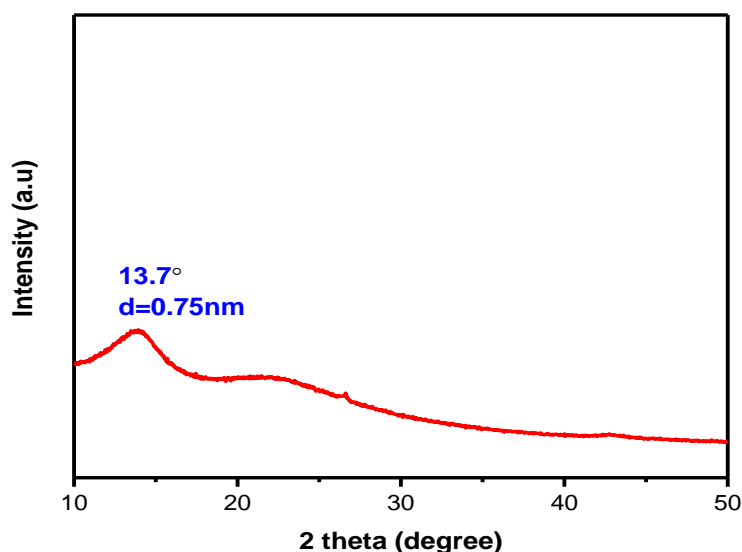


**SI Figure 4.5:** Fourier transformer infrared (FTIR) spectrum of graphene oxide shows vibrations of functional groups of C–O–C ( $\sim 1000 \text{ cm}^{-1}$ ), C–O ( $1230 \text{ cm}^{-1}$ ), C=C ( $\sim 1620 \text{ cm}^{-1}$ ), C=O ( $1740\text{--}1720 \text{ cm}^{-1}$ ) bonds and O–H ( $3600\text{--}3300 \text{ cm}^{-1}$ ).



**SI Figure 4.6: (A)** UV/Vis absorption spectra of graphene oxide solutions with different concentrations (from 0.039–10 mg/ml) show the main peak around 232 nm. **(B)** The plot of the absorbance ( $\lambda_{\text{ex}} = 232 \text{ nm}$ ) divided by the cell length, versus the concentration, given by the Lambert–Beer law ( $A = \alpha/C$ ), which determined the absorption coefficient ( $\alpha$ ) related to the absorbance per unit path length  $A/l$ . This linear

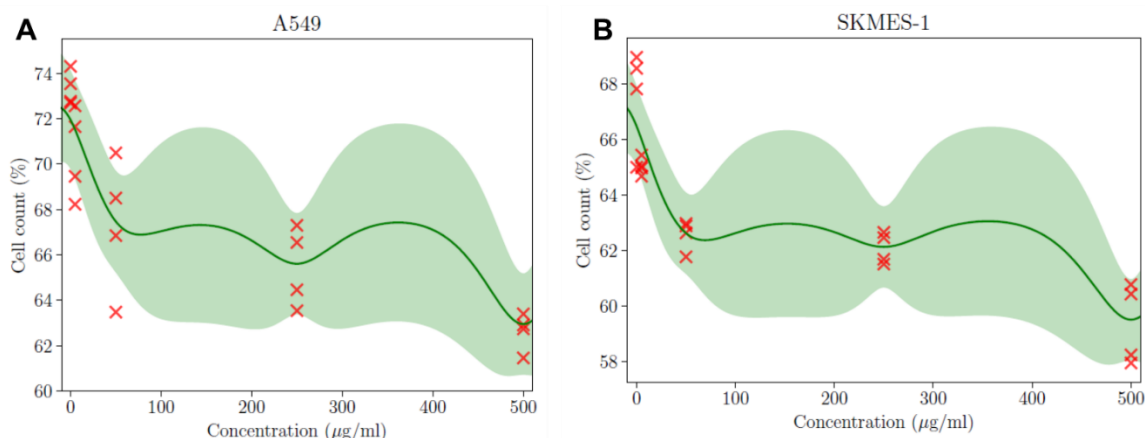
relationship fits well with the Lambert-Beer Law, indicating the good water solubility of the GO product.



**SI Figure 4.7:** XRD pattern recorded for graphene oxide shows a (001) peak at  $2\theta$  of  $13.7^\circ$ .

**Supplementary note 2: Regression model analysis of cell viability:** The resulting predictive distributions from the trained GP models for A549 and SKMES-1 cells are shown in **SI Figure 4.8**. The models not only capture the measurement noises, but also indicate how much confidence may be derived from the predictions through the associated standard deviation. Most interestingly, GP models can predict cell-specific toxicity levels of concentrations. As such, we may exploit this knowledge to run further experiments to find out optimal levels of concentrations. This approach is better known as Bayesian optimisation: a sequential design method that may locate near-optimal solutions with limited number of time consuming and computationally expensive experiments.





**SI Figure 4.8:** Gaussian process (GP) regression models for cell survival rates of A549 (*left*) and SKMES-1 (*right*) cells interacted with various concentrations of reduced Graphene Oxide (rGO). The green solid lines show the mean GP prediction, while the light green areas around the mean show the uncertainty (one standard deviation) in prediction. The models are trained with the data indicated by the red crosses.

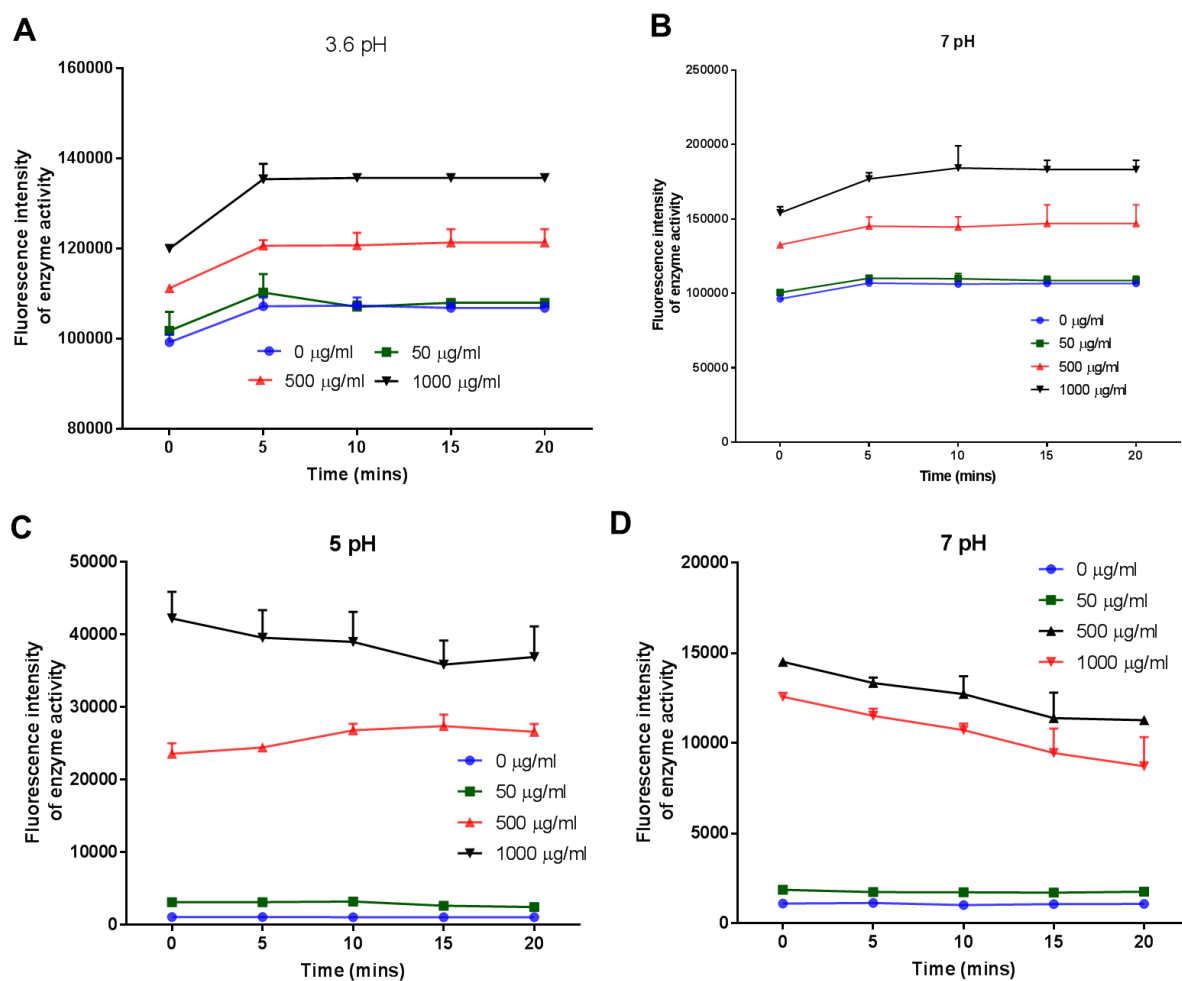
**Supplementary Note 3:** Different ranges of pHs were prepared to investigate the proteolytic activities of CathD and CathL. 21.01 g of citric acid was mixed to 1 ltr distilled water and 28.40 g of Na<sub>2</sub>HPO<sub>4</sub> in 1 ltr distilled water. Citric acid monohydrate and Na<sub>2</sub>HPO<sub>4</sub> pH buffer solutions were prepared ranging: 3.6, 5, and 7. Final volume of each pH buffer was 50 ml containing freshly prepared 1 mM DTT for CathL. Final volume of each pH buffer was 50 ml containing 0.005% Tween 20 (2.5 μl, sigma) for CathL.

**SI Table 4.1:** Characteristic IR bands of the protein linkages.

Approximate frequency (cm <sup>-1</sup> )	Vibrational modes	References
1610-1695	CO stretching  <b>C O:</b> Amide I (C O stretching mode of proteins)	[50]
1480-1575	NH bending and CN stretching  <b>CH<sub>2</sub>:</b> Asymmetric CH <sub>3</sub> bending and CH <sub>2</sub> scissoring <b>C N H:</b> Absorption of amide II, predominately $\beta$ -sheet; an N H bending attached to a C N stretching modes, C N H bending or/and C N stretching vibrational modes.	[50-54]
1220-1320	CH stretching and NH bending,  <b>C N H:</b> ( $\nu$ (CN), $\delta$ (NH) amide III, $\alpha$ -helix collagen, tryptophan; and PO <sub>2</sub> – asymmetric phosphate stretching associated with the phosphodiester groups of nucleic acids. <b>C N H:</b> Symmetric stretch: Amide III and CH <sub>3</sub> /CH <sub>2</sub> twisting	[50-54]
625-765	OCN bending, mixed with other vibrational modes of amide II and III	[53, 55]
640-800	Out-of-plane NH bending	[53, 55]
535-605	Out-of-plane CO bending	[53, 55]

**SI Table 4.2:** Kinetic parameters obtained for CathD and CathL for GO using intraparticle diffusion model

Adsorbent	Enzyme	Y	R <sup>2</sup>
GO (50 $\mu$ g/ml)	CathD	0.0087 $\pm$ 0.0071	0.9592
	CathL	0.0094 $\pm$ 0.0138	0.9068
GO (500 $\mu$ g/ml)	CathD	0.0073 $\pm$ 0.0084	0.9939
	CathL	0.0073 $\pm$ 0.0011	0.9323
GO (1000 $\mu$ g/ml)	CathD	0.0071 $\pm$ 0.0008	0.8094
	CathL	0.0078 $\pm$ 0.0002	0.8741



**SI Figure 4.9:** Effect of different concentrations of GO on CathD and CathL fluorescence activities. GO at different concentrations (50, 500, and 1000  $\mu\text{g/ml}$ ) were incubated with CathD(A, B) and CathL (C, D) in 96 well plates at different time-points (2, 5, 10, 15, and 20 min) as shown. Data (symbols) are shown together with guides to the eye (connecting lines). Fluorescence signals were determined using plate reader at Ex/Em: 355/460nm.

## References:

- [1] Michailidou, K., Hall, P., Gonzalez-Neira, A., Ghoussaini, M., Dennis, J., Milne, R. L., & Wang, Q. (2013). Large-scale genotyping identifies 41 new loci associated with breast cancer risk. *Nat. Genet.* 45(4), 353-361.
- [2] Eccles, S. A., Aboagye, E. O., Ali, S., Anderson, A. S., Armes, J., Berditchevski, F., & Bundred, N. J. (2013). Critical research gaps and translational priorities for the successful prevention and treatment of breast cancer. *Breast Cancer Res.* 15(5), 1-37.
- [3] Van Dam, G. M., Themelis, G., Crane, L. M., Harlaar, N. J., Pleijhuis, R. G., Kelder, W., & Bart, J. (2011). Intraoperative tumor-specific fluorescence imaging in ovarian cancer by folate receptor- $\alpha$  targeting: first in-human results. *Nat. Med.* 17(10), 1315-1319.
- [4] Aas, T., Børresen, A. L., Geisler, S., Smith-Sørensen, B., Johnsen, H., Varhaug, J. E., & Lønning, P. E. (1996). Specific P53 mutations are associated with de novo resistance to doxorubicin in breast cancer patients. *Nat. Med.* 2(7), 811-814.
- [5] Doufekas, K., & Olaitan, A. (2014). Clinical epidemiology of epithelial ovarian cancer in the UK. *Int. J. Women's Heal.* 6, 537-545.
- [6] Estrella, V., Chen, T., Lloyd, M., Wojtkowiak, J., Cornnell, H. H., Ibrahim-Hashim, A., & Johnson, J. (2013). Acidity generated by the tumor microenvironment drives local invasion. *Cancer Res.* 73(5), 1524-1535.
- [7] Trédan, O., Galmarini, C. M., Patel, K., & Tannock, I. F. (2007). Drug resistance and the solid tumor microenvironment. *J. Nat. Cancer Inst.* 99(19), 1441-1454.
- [8] Liotta, L. A., & Kohn, E. C. (2001). The microenvironment of the tumour–host interface. *Nature* 411(6835), 375-379.
- [9] Coussens, L. M., Fingleton, B., & Matrisian, L. M. (2002). Matrix metalloproteinase inhibitors and cancer—trials and tribulations. *Science* 295(5564), 2387-2392.
- [10] Alberti, S., Mateju, D., Mediani, L., & Carra, S. (2017). Granulostasis: protein quality control of RNP granules. *Front Mol. Neurosci.* 10, 1-14.
- [11] Berchem, G., Glondou, M., Gleizes, M., Brouillet, J. P., Vignon, F., Garcia, M., & Liaudet-Coopman, E. (2002). Cathepsin-D affects multiple tumor progression steps in vivo: proliferation, angiogenesis and apoptosis. *Oncogene* 21(38), 5951-5955.
- [12] Sudhan, D. R., Rabaglino, M. B., Wood, C. E., & Siemann, D. W. (2016). Cathepsin L in tumor angiogenesis and its therapeutic intervention by the small molecule inhibitor KGP94. *Clinic. Exper. Metast.* 33(5), 461-473.
- [13] Pranjol, M. Z. I., Gutowski, N., Hannemann, M., & Whatmore, J. (2015). The potential role of the proteases cathepsin D and cathepsin L in the progression and metastasis of epithelial ovarian cancer. *Biomolecules* 5(4), 3260-3279.
- [14] Winiarski, B. K., Wolanska, K. I., Rai, S., Ahmed, T., Acheson, N., Gutowski, N. J., & Whatmore, J. L. (2013). Epithelial ovarian cancer-induced angiogenic phenotype of human omental microvascular endothelial cells may occur independently of VEGF signaling. *Transl Oncol.* 6, 703-14.
- [15] Winiarski, B.K., Wolanska, K.I., Rai, S., Ahmed T., Acheson N., Gutowski N.J., Whatmore, J.L., (2013) Epithelial ovarian cancer-induced angiogenic phenotype of

human omental microvascular endothelial cells may occur independently of VEGF signaling *Transl. Oncol.* 6, 703-714

[16] Löscher, A., Schindl, M., Kohlberger, P., Lahodny, J., Breiteneker, G., Horvat, R., & Birner, P. (2004). Cathepsin D in ovarian cancer: prognostic value and correlation with p53 expression and microvessel density. *Gynecol. Oncol.* 92(2), 545-552.

[17] Westley, B. R. & May, F. E. 1996. Cathepsin D and breast cancer. *Eur. J. Cancer*, 32A, 15-24.

[18] Pranjoli, M. Z. I., Gutowski, N. J., Hannemann, M., & Whatmore, J. L. (2017). Cathepsin D non-proteolytically induces proliferation and migration in human omental microvascular endothelial cell via activation of the ERK1/2 and PI3K/AKT pathways. *Biochim. et Biophys. Acta-Mol. Cell Res.* 1865(1), 25-33.

[19] Johansson, A. C., Steen, H., Öllinger, K., & Roberg, K. (2003). Cathepsin D mediates cytochrome c release and caspase activation in human fibroblast apoptosis induced by staurosporine. *Cell Death Differ.* 10(11), 1253-1259.

[20] Sui, H., Shi, C., Yan, Z., & Wu, M. (2016). Overexpression of Cathepsin L is associated with chemoresistance and invasion of epithelial ovarian cancer. *Oncotarget* 7(29), 45995-46001.

[21] Levičar, N., Dewey, R. A., Daley, E., Bates, T. E., Davies, D., Kos, J., & Lah, T. T. (2003). Selective suppression of cathepsin L by antisense cDNA impairs human brain tumor cell invasion in vitro and promotes apoptosis. *Cancer Gene Therapy* 10(2), 141-151.

[22] Hare, J. I., Lammers, T., Ashford, M. B., Puri, S., Storm, G., & Barry, S. T. (2017). Challenges and strategies in anti-cancer nanomedicine development: An industry perspective. *Adv. Drug Deliver. Rev.* 108, 25-38.

[23] Liu, J. H., Yang, S. T., Wang, H., Chang, Y., Cao, A., & Liu, Y. (2012). Effect of size and dose on the biodistribution of graphene oxide in mice. *Nanomedicine*, 7(12), 1801-1812.

[24] Liu, Z., Robinson, J. T., Sun, X., & Dai, H. (2008). PEGylated nanographene oxide for delivery of water-insoluble cancer drugs. *J. Amer. Chem. Soc.* 130(33), 10876-10877.

[25] Hu, W., Peng, C., Lv, M., Li, X., Zhang, Y., Chen, N., & Huang, Q. (2011). Protein corona-mediated mitigation of cytotoxicity of graphene oxide. *ACS Nano*, 5(5), 3693-3700.

[26] Lin, L., Wu, H., Green, S. J., Crompton, J., Zhang, S., & Horsell, D. W. (2016). Formation of tunable graphene oxide coating with high adhesion. *Phys. Chem. Chem. Phys.* 18(7), 5086-5090.

[27] Lin, L., and Zhang, S. (2012). Effective solvothermal deoxidization of graphene oxide using solid sulphur as a reducing agent. *J. Mater. Chem.* 22.29, 14385-14393.

[28] Lin, L., Zheng, X., Zhang, S., & Allwood, D. A. (2014). Surface energy engineering in the solvothermal deoxidation of graphene oxide. *Adv. Mater. Interf.* 1 (3) 1300078-1300082.

- [29] Tabish, T. A., Pranjol, M. Z. I., Hayat, H., Rahat, A. A., Abdullah, T. M., Whatmore, J. L., & Zhang, S. (2017). In vitro toxic effects of reduced graphene oxide nanosheets on lung cancer cells. *Nanotechnology*, 28(50), 504001-504005.
- [30] Rasmussen, C. E., & Williams, C. K. (2006). Gaussian processes for machine learning (Vol. 1). Cambridge: MIT press.
- [31] Fowkes, F. M., (1964) 'Attractive Forces at Interfaces', *Industrial and Engineering Chemistry* **56**, 40.
- [32] Malana, M. A., Qureshi, R. B., & Ashiq, M. N. (2011) Adsorption studies of arsenic on nano aluminium doped manganese copper ferrite polymer (MA, VA, AA) composite: kinetics and mechanism. *Chem. Eng. J.* 172, 721-727.
- [33]. Alkan, M., Demirbaş, Ö., Celikcapa, S., & Doğan, M. (2004) Sorption of acid red 57 from aqueous solution onto sepiolite. *J. Hazard. Mater.* 116, 135-145.
- [34]. Altenor S., Carene B., Emmanuel E., Lambert J., Ehrhardt J. J. et al. (2009) Adsorption studies of methylene blue and phenol onto vetiver roots activated carbon prepared by chemical activation. *J. Hazard. Mater.* 165, 1029-1039.
- [35]. Qi L., and Xu Z. (2004) Lead sorption from aqueous solutions on chitosan nanoparticles. *Colloids and Surfaces A: Physicochemical and Engineering Aspects* 251: 183-190.
- [36] Chen, W., Yan, L., & Bangal, P. R. (2010). Chemical reduction of graphene oxide to graphene by sulfur-containing compounds. *J. Phys. Chem. C* 114(47), 19885-19890.
- [37] Szabó, T., Tombácz, E., Illés, E., & Dékány, I. (2006). Enhanced acidity and pH-dependent surface charge characterization of successively oxidized graphite oxides. *Carbon*, 44(3), 537-545.
- [38] Peng, C., Chen, B., Qin, Y., Yang, S., Li, C., Zuo, Y., & Yang, J. (2012). Facile ultrasonic synthesis of CoO quantum dot/graphene nanosheet composites with high lithium storage capacity. *ACS Nano*, 6(2), 1074-1081.
- [39] Szabó, T., Berkesi, O., Forgó, P., Josepovits, K., Sanakis, Y., Petridis, D., & Dékány, I. (2006). Evolution of surface functional groups in a series of progressively oxidized graphite oxides. *Chem. Mater.* 18(11), 2740-2749.
- [40] Marcano, D. C., Kosynkin, D. V., Berlin, J. M., Sinitskii, A., Sun, Z., Slesarev, A., & Tour, J. M. (2010). Improved synthesis of graphene oxide. *ACS Nano* 4 (8), 4806–4814
- [41] Zhu, S., Zhang, J., Qiao, C., Tang, S., Li, Y., Yuan, W., & Gao, H. (2011). Strongly green-photoluminescent graphene quantum dots for bioimaging applications. *Chem. Commun.* 47(24), 6858-6860.
- [42] Akhavan, Omid, and Elham Ghaderi. Toxicity of graphene and graphene oxide nanowalls against bacteria. *ACS Nano* 4.10 (2010): 5731-5736.
- [43] Montagner, A., Bosi, S., Tenori, E., Bidussi, M., Alshatwi, A. A., Tretiach, M., & Syrgiannis, Z. (2016). Ecotoxicological effects of graphene-based materials. *2D Materials* 4(1), 012001-012010.
- [44] Morhardt, C., Ketterer, B., Heißler, S., & Franzreb, M. (2014). Direct quantification of immobilized enzymes by means of FTIR ATR spectroscopy—a process analytics tool

for biotransformations applying non-porous magnetic enzyme carriers. *J. Mol. Catal. B Enzym.* 107, 55-63.

[45] Rehman, S., Movasaghi, Z., Darr, J. A., & Rehman, I. U. (2010). Fourier transform infrared spectroscopic analysis of breast cancer tissues; identifying differences between normal breast, invasive ductal carcinoma, and ductal carcinoma in situ of the breast. *Appl. Spectro. Rev.* 45(5), 355-368.

[46] Movasaghi, Z., Rehman, S., & Ur Rehman, D. I. (2008). Fourier transform infrared (FTIR) spectroscopy of biological tissues. *Appl. Spectro. Rev.* 43(2), 134-179.

[47] Sahoo, J. K., Sirimuthu, N. M., Canning, A., Zelzer, M., Graham, D., & Ulijn, R. V. (2016). Analysis of enzyme-responsive peptide surfaces by Raman spectroscopy. *Chem. Commun.* 52(25), 4698-4701.

[48] Sée, V., Free, P., Cesbron, Y., Nativo, P., Shaheen, U., Rigden, D. J., & Brust, M. (2009). Cathepsin L digestion of nanobioconjugates upon endocytosis. *ACS Nano*, 3(9), 2461-2468.

[49] Berciaud, S.; Cognet, L.; Blab, G. A.; Lounis, B. (2004) Photothermal Heterodyne Imaging of Individual Non-fluorescent Nanoclusters and Nanocrystals, *Phys. Rev. Lett.* 93, 257402-257411.

[50] Rehman, S., Movasaghi, Z., Darr, J. A., & Rehman, I. U. (2010). Fourier transform infrared spectroscopic analysis of breast cancer tissues; identifying differences between normal breast, invasive ductal carcinoma, and ductal carcinoma in situ of the breast. *Appl. Spectro. Rev.* 45(5), 355-368.

[51] Staniszevska, E., Malek, K., & Baranska, M. (2014). Rapid approach to analyze biochemical variation in rat organs by ATR FTIR spectroscopy. *Spectrochim. Acta-A. Mol. Biomol. Spectro.* 118, 981-986.

[52] Kumar, S., & Barth, A. (2010). Following enzyme activity with infrared spectroscopy. *Sensors*, 10(4), 2626-2637.

[53] Morhardt, C., Ketterer, B., Heißler, S., & Franzreb, M. (2014). Direct quantification of immobilized enzymes by means of FTIR ATR spectroscopy—a process analytics tool for biotransformations applying non-porous magnetic enzyme carriers. *J. Mol. Catal. B Enzym.* 107, 55-63.

[54] Barth, A. (2007). Infrared spectroscopy of proteins. *Biochimica et Biophysica Acta (BBA)-Bioenergetics*, 1767(9), 1073-1101.

[55] Movasaghi, Z., Rehman, S., & ur Rehman, D. I. (2008). Fourier transform infrared (FTIR) spectroscopy of biological tissues. *Appl. Spectro. Rev.* 43(2), 134-179.

## Chapter 5

# ***In Vitro* Toxic Effects of Reduced Graphene Oxide Nanosheets on Lung Cancer Cells**

---

The intriguing properties of reduced graphene oxide (rGO) have paved the way for a number of potential biomedical applications such as drug delivery, tissue engineering, gene delivery and bio-sensing. Over the last decade, there have been escalating concerns regarding the possible toxic effects, behaviour and fate of rGO in living systems and environments. This chapter reports on integrative chemical-biological interactions of rGO with lung cancer cells, i.e. A549 and SKMES-1, to determine its potential toxicological impacts on them, as a function of its concentration. Cell viability, early and late apoptosis and necrosis were measured to determine oxidative stress potential, and induction of apoptosis for the first time by comparing two lung cancer cells. We also showed the general trend between cell death rates and concentrations for different cell types using a Gaussian process regression model. At low concentrations, rGO was shown to significantly produce late apoptosis and necrosis rather than early apoptotic events, suggesting that it was able to disintegrate the cellular membranes in a dose dependent manner. For the toxicity exposures undertaken, late apoptosis and necrosis occurred, which was most likely resultant from limited bioavailability of unmodified rGO in lung cancer cells.

### **5.1 Introduction**

The potential applications of graphene are rapidly expanding with a global industry estimated to be worth more than 1790.7 Million USD by 2020, which is reflective of its wide range of application domains including, electronics, supercapacitors, energy storage and medicine [1, 2]. The development of real-world applications of graphene is fuelled by its unique and superior properties such as high electron mobility, high mechanical strength and high specific surface area [3]. Although some effort has been made to investigate the biosafety profile of graphene, a significant lack of viable data



on biocompatibility hinders the precise forecast of the potential of graphene to solve real-world clinical problems.

Pristine graphene, graphene oxide and reduced graphene oxide (rGO) have been investigated as potentially hazardous materials when used in healthcare because they could exert acute toxic effects on a wide range of living organisms including human cells, Gram-positive and Gram-negative bacteria, viruses, and plants, eukaryotic mammalian and *in vivo* animal models [4,5]. Current knowledge on their toxicological implications indicates the demand for further systematic investigations including a detailed basic physicochemical characterisation of the graphene-based materials exploited in each case. It has been demonstrated that graphene nanostructures cause harmful cellular effects when they enter the body, as they can pass through physiological barriers, encounter immune systems and trigger normal cellular responses and significantly enhance toxic potential in living systems [6]. Single and few-layered graphene having sharp edges may infiltrate cell membranes resulting in membrane damage and leakage of cytoplasmic substances. DNA damage, cell cycle arrest and oxidative stresses inside the cell are the main cytotoxicity responses to GO and rGO when they are exposed to different cell lines, which are likely due to the generation of reactive oxygen species, and deregulation of antioxidant genes [7]. The biocompatibility of graphene varies from their counterparts owing to their size, shape, lateral dimensions, high specific surface area and surface chemistry [8]. Most of the studies to date have focused mainly on the toxicity induced by pristine graphene and GO but the biocompatibility of rGO has not been fully understood. Recently, rGO has been evaluated for biological applications, for example, as drug delivery carriers, diagnostic sensors, biomarkers and antimicrobial agents [9]. However, it has been shown to cause several adverse effects *in vitro* including reactive oxygen species formation, cell apoptosis, inflammatory cytokine, loss of membrane integrity, membrane distress induced by direct contact with sharp edges of rGO, and inflammatory cell infiltration [10]. Recent studies also have shown that rGO is likely to be toxic and could integrate cell membranes and induce programmed cell death in a dose-dependent manner, particularly in concentrations higher than 50 µg/L [11-13]. In order to address these issues and to improve the bioavailability of rGO, it is essential to investigate its implications on the safety of living systems and develop a better

understanding of toxicological mechanisms, which would facilitate the existing methods for rGO preparation (with minimal toxicity for safer biomedical applications).

The current study is motivated by the requirements for a better understanding of the mechanisms and *in vitro* efficacy of graphene-induced degradation of cells. The *in vitro* toxicity of rGO against two lung cancer cells, A549 and SKMES-1, has been assessed and compared for the first time without premodification of rGO. We conducted the cell viability tests and measured the implications of early and late apoptosis and necrosis pathways to investigate the oxidative stress potential, and induction of apoptosis. We also showed the general trend between cell death rates and concentrations for cancer cells using a Gaussian process regression model. Our results demonstrated that a low concentration of rGO significantly produced late apoptosis and necrosis rather than early apoptotic events, though rGO was still able to disintegrate the cellular membranes in a dose dependent manner. Given the evolving field of graphene-based nanomedicine, our findings regarding the toxicity of graphene presented in this chapter using *in vitro* models would play a significant role in paving a new way to future biomedical applications of graphene.

## 5.2 Materials and methods

### 5.2.1 Synthesis and characterization

The method of preparing exfoliated graphene oxide (GO) flakes is the same as described in the previous chapter (**section 4.2.1**) using the Modified Hummers method [14]. The resultant GO was dispersed in water under stirring to the concentration of 0.25 mg mL<sup>-1</sup>. 75 mL GO (0.25 mg/mL) was mixed with 1.5 mL hydrazine (35 wt%) under magnetic stirring in a flask heated (in an oil bath) to 100 °C. The resultant rGO powder was then washed with distilled water for further characterization. Transmission electron microscope (TEM), X-ray diffraction (XRD) analysis, Fourier-transform infrared (FTIR) spectra, Raman spectra and zeta potential measurements of rGO samples were carried out in the same manner as described in chapter 4 (**section 4.2.1**).

### 5.2.2 Cell viability

The methods used for the preparation of seed cultures, preparation of suspensions for seeding, techniques for cell viability and flow cytometry have been described in chapter 4 (**section 4.2.2**). Cells were treated with or without 5, 50, 250, 500 and 1000  $\mu\text{g/ml}$  of rGO for 24 h.

### 5.2.3 Regression model

The relationships between concentration of rGO and cell death rate were investigated to determine the most appropriate concentration levels for therapeutic purposes [15]. The details of this method were given in chapter 4 (**section 4.2.3**).

## 5.3 Results and discussion

As well-known, reduction of GO in an aqueous suspension results in agglomerated graphene nanosheets [16]. Similarly to that reported previously [17,18], as-prepared rGO nanosheets from the present work also exhibited typical wrinkled and scrolled structures (**Figure 5.1 a, b**). They consisted of a few-layers (typically 6–8 layers), and had an average thickness of 1.5 nm, as revealed by HRTEM (**Figure 5.1b**). XRD (**Figure 5.2 A**) further shows a diffraction peak at  $26.40^\circ$  ( $2\theta$ ) corresponding to the (002) lattice plane of rGO with interlayer spacing of 3.37 Å, indicating the formation of  $\text{sp}^2$  network of carbon [19]. As shown in **Figure 5.2B**, rGO exhibited a D band at  $1358\text{ cm}^{-1}$  and a G band at  $1595\text{ cm}^{-1}$ , showing a series of defects and the in-plane stretching motion of pairs of  $\text{sp}^2$  atoms, respectively [20]. FTIR peak at  $3434\text{ cm}^{-1}$  was assigned to the O–H stretching vibration (**Figure 5.2C**). The weak peaks at  $1622\text{ cm}^{-1}$ ,  $1399\text{ cm}^{-1}$ ,  $1240\text{ cm}^{-1}$ , and  $1071\text{ cm}^{-1}$  arose from C=C stretching vibration, O–H deformation, C=O (epoxy) stretching vibration, and C=O (alkoxy) stretching, respectively, implying that the original functional groups were largely removed [21]. Zeta potential is a key parameter in the evaluation of stability of colloidal dispersions and prediction of the mobility/reaction of nanoparticles inside the cells [17]. Nanomaterials are generally considered to be fairly stable in a solution if the corresponding zeta potential is sufficiently high (more positive and negative than +30 mV and –30 mV respectively) [22]. As depicted in **Figure 5.2D**, as-prepared rGO

nanosheets showed a maximal zeta potential of  $-49.2$  mV at pH 12, which was resulted from the reduction of different functional groups existing on the surface of the original GO.

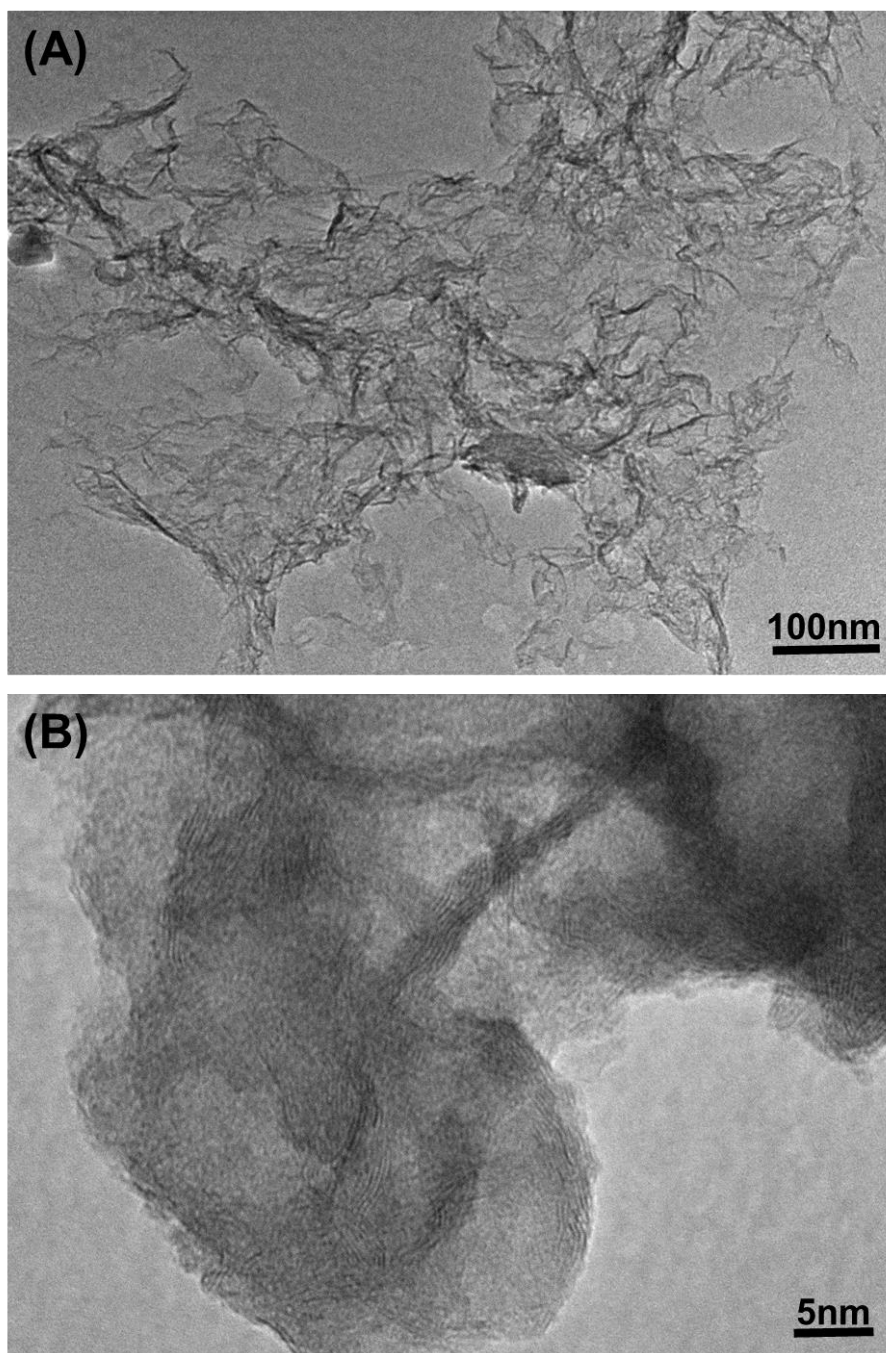


**Figure 5.1:** (A)- TEM and (B) HRTEM images of as-prepared exfoliated rGO sheets.

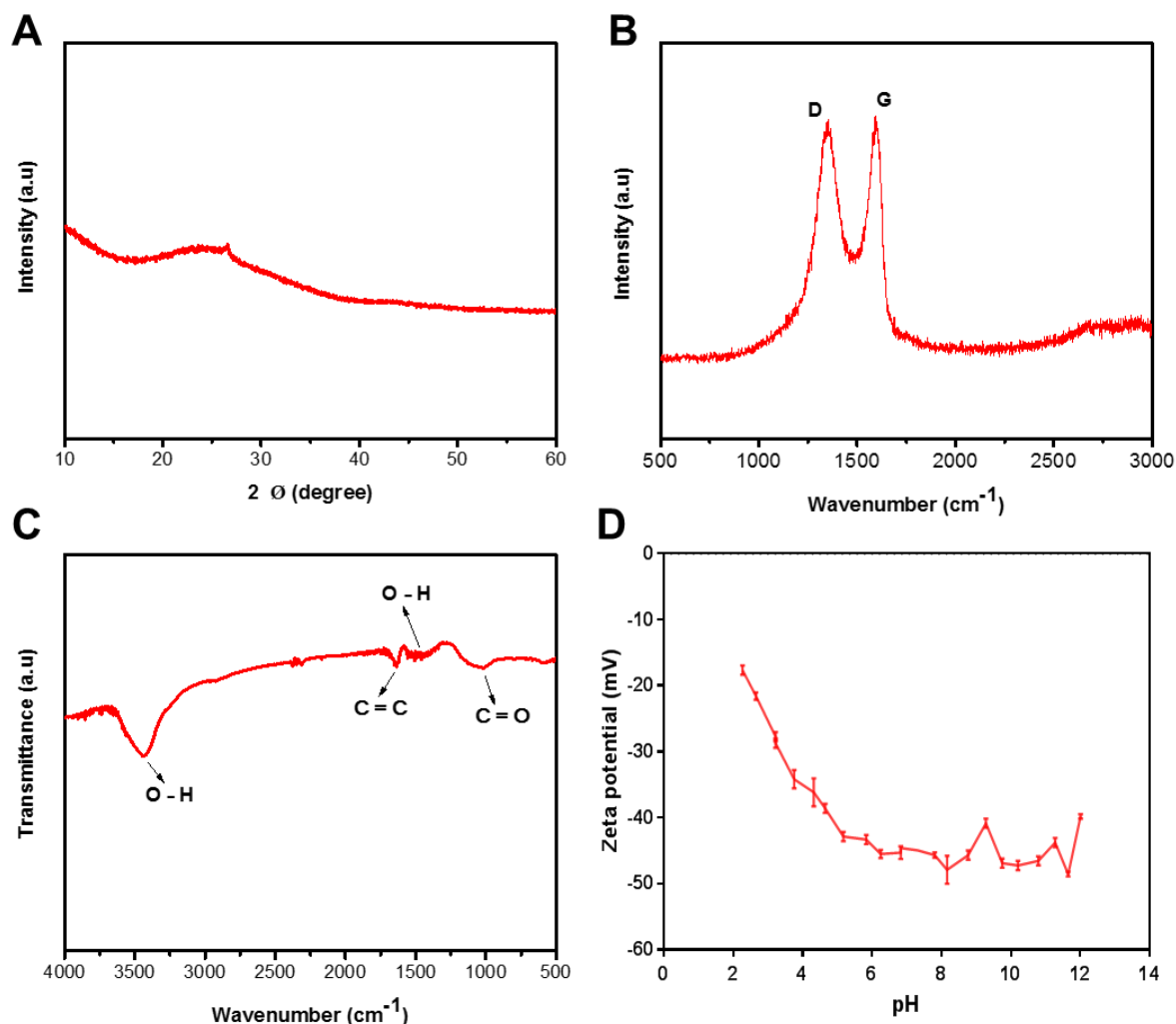


**Figure 5.2:** (A)- XRD pattern, (B)- Raman spectrum, (C) FTIR spectrum, and (D) Zeta potential-pH curve of as-prepared rGO.

As demonstrated in Fig. 3A, after 24-h exposure to rGO, the cell viability in the case of A549 cells decreased by virtue of increasing the concentration of rGO from 5 to 1000  $\mu\text{g/ml}$ . For example, the percentage of living cells was reduced to 70, 50 and 40% at concentrations 5, 50 and 250  $\mu\text{g/ml}$  respectively, compared to the controls (0  $\mu\text{g/ml}$ , ~90%). However, in SKMES-1 cells, rGO-induced toxicity was reduced significantly at a concentration of 50  $\mu\text{g/ml}$  or above. Cell viability was reduced to 70, 60, 42 and 42% at concentrations of 50, 250, 500 and 1000  $\mu\text{g/ml}$ , respectively, compared to the controls (0  $\mu\text{g/ml}$ , ~80%). Cells undergoing early apoptosis significantly increased when treated with 50  $\mu\text{g/ml}$  in a dose dependent manner up to 500  $\mu\text{g/ml}$  (both in A549 and SKMES-1 cells) (**Figure 5.3B**). A dose-dependent increase in late apoptosis

(Figure 5.3C) and necrosis (Figure 5.3D) was also observed in both cell lines, where rGO demonstrated a greater toxic effect on A549 cells compared to SKMES-1 cells.

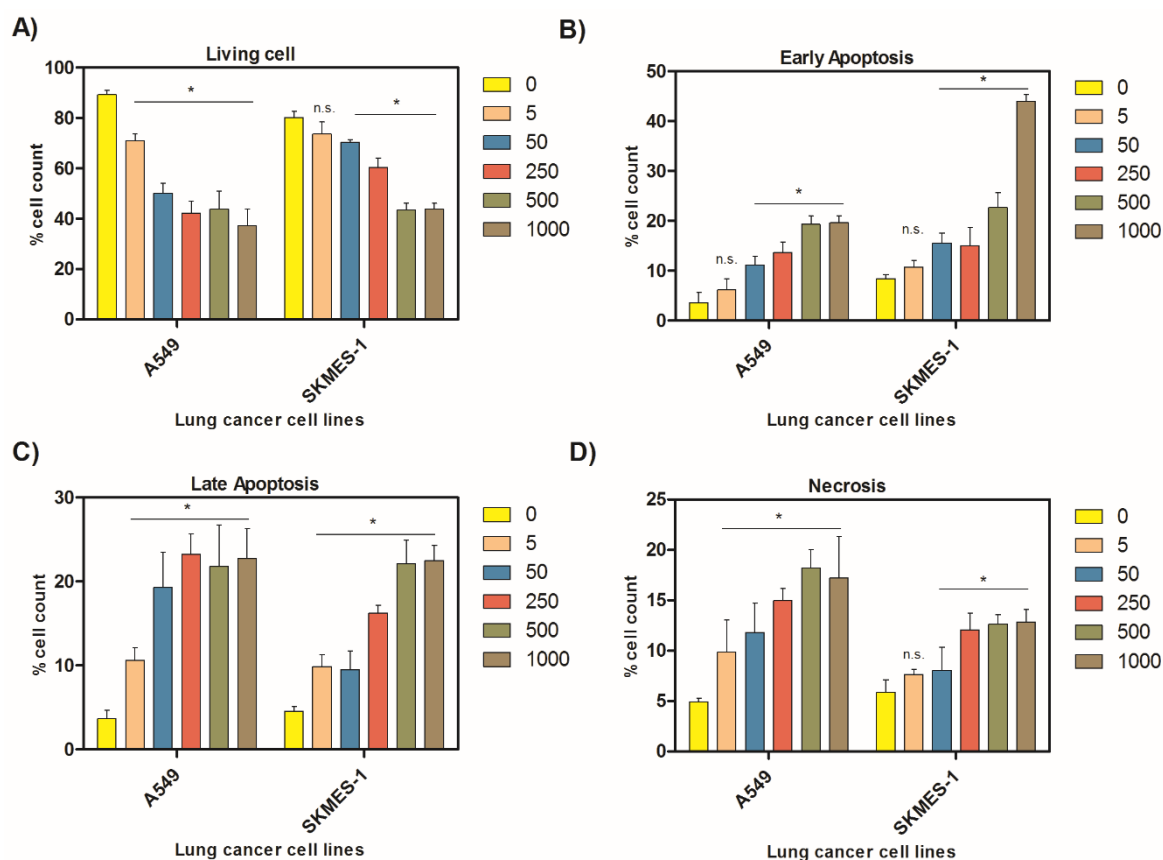


**Figure 5.3.** Bar graphs quantifying the percentage of dead, living, early-stage apoptotic, and late-stage apoptotic cells in response to different concentrations of reduced graphene oxide (rGO). Flow cytometry for A549 and SKMES-1 lung carcinoma cells stained with annexin V (apoptosis) and propidium iodide (PI; late apoptosis and necrosis) following 24 h of treatment with various concentrations of rGO (0–1000 µg/ml). **(A)** graphic representation of percentage of living cells **(B)** early apoptosis **(C)** necrosis, **(D)** late apoptosis (flow cytometry) in response to rGO. Data were represented as mean  $\pm$  SD, n.s., \* $p < 0.05$  vs control (0 µg/ml).

The resulting predictive distributions from the trained GP models for A549 and SKMES-1 cells are shown in Figure 5.4. The models not only capture the measurement noises, but also indicate how much confidence may be derived from the predictions through the associated standard deviation. Interestingly, the model for A549 cells indicates that concentrations below 200 µg/ml are likely to be better than higher concentrations. In contrast, the model for SKMES-1 cells, concentrations between 600 and 800 are likely

to yield lower cell death. These predictions match with the experimental results presented in **Figure 5.3**.

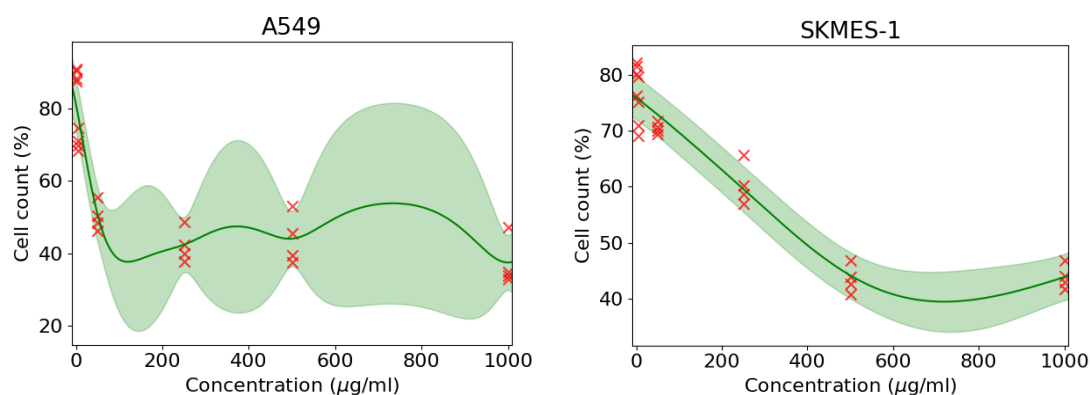


**Figure 5.4.** Gaussian process (GP) regression models for cell survival rates of A549 (*left*) and SKMES-1 (*right*) cells interacted with various concentrations of reduced Graphene Oxide (rGO). The green solid lines show the mean GP prediction, while the light green areas around the mean show the uncertainty (one standard deviation) in prediction. The models are trained with the data indicated by the red crosses.

Most interestingly, GP models can predict cell-specific toxicity levels of concentrations. As such, we may exploit this knowledge to run further experiments to find out optimal levels of concentrations. This approach is better known as Bayesian optimisation: a sequential design method that may locate near-optimal solutions with limited number of time consuming and computationally expensive experiments [23].

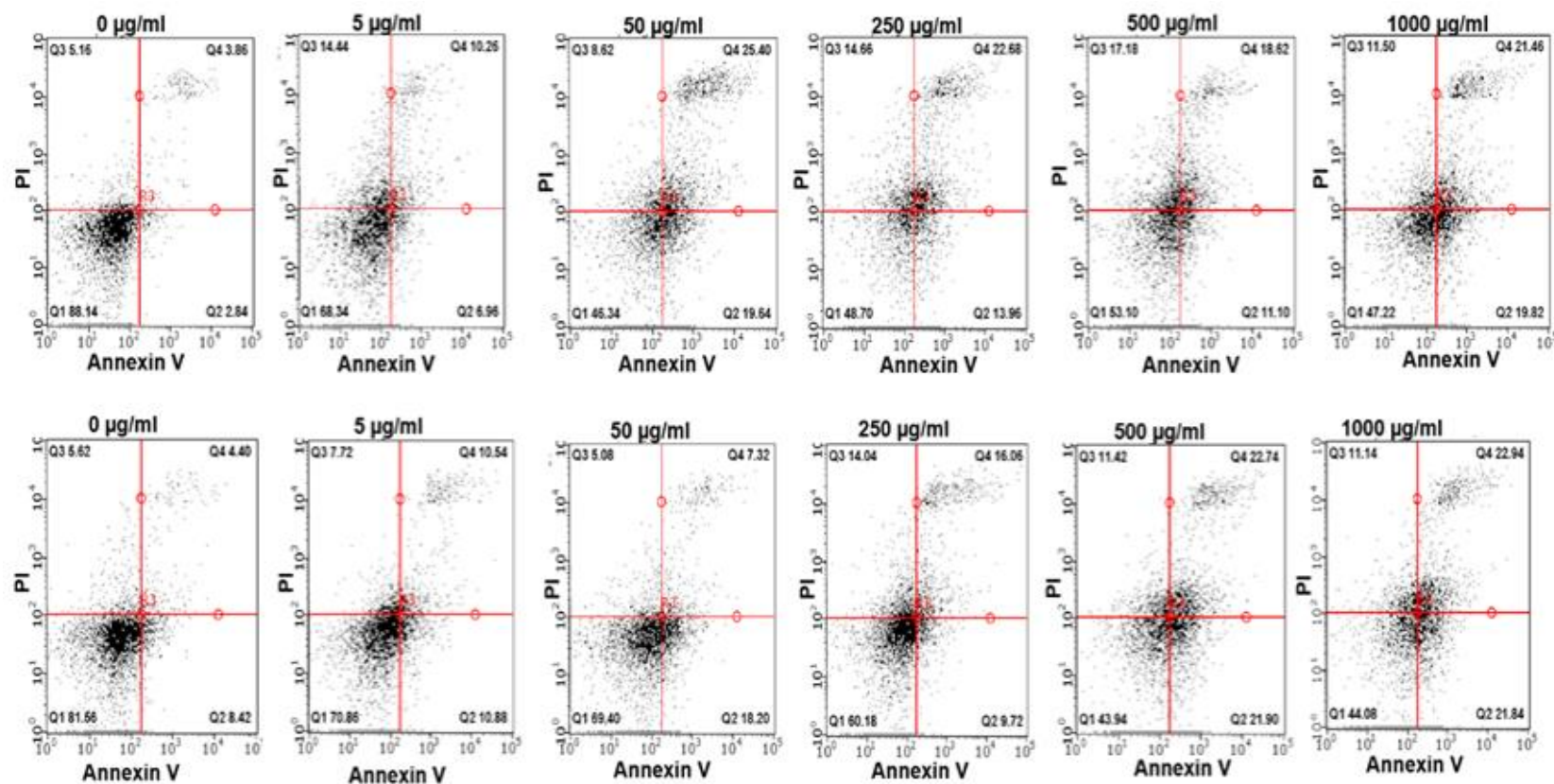


**Figure 5.5:** Representative FACS images and analysis of one experiment. Data were presented as percentage of the cell population. Cell viability of A549 (upper panel) and SKMES-1 (lower panel) at selected concentrations. Experiments were performed and interpreted as follows: Annexin V<sup>-ve</sup>/PI<sup>-ve</sup> cells (lower left quadrant), AnnV<sup>+ve</sup>/PI<sup>-ve</sup> cells (lower right quadrant), AnnV<sup>+ve</sup>/PI<sup>+ve</sup> (upper right quadrant) and AnnV<sup>-ve</sup>/PI<sup>+ve</sup> (upper left quadrant) were considered as living, early apoptotic, late apoptotic, and necrotic cells respectively.



Cell viability, early and late apoptosis and necrosis were also measured under similar conditions to those mentioned above. Early apoptosis is typically defined by an increase in phosphatidylserine (PS) expression on an intact cell membrane (detected by annexin V). In late apoptosis, however the membrane loses its integrity allowing PI into the cell and flags these cells as late apoptotic/necrotic. This study showed that rGO induced apoptosis and necrosis above the concentration of 5  $\mu\text{g/ml}$  in A549 and above the concentration of 50  $\mu\text{g/ml}$  in SKMES-1 cell lines (**Figure 5.5**). Even at lower concentrations, rGO was shown to significantly produce late apoptosis and necrosis, suggesting that rGO was able to disintegrate cellular membranes (PI staining) at lower concentrations. Interestingly, the effect was more pronounced in A549 cells compared to SKMES-1 cells upon exposure of rGO. Kumar et al [11] recently reported the high toxicity of rGO on A549 cancer cells arising from its reduced lateral size, and showed alteration of mitochondrial homeostasis upon rGO exposure. Hu et al. [10] found that rGO caused a dose-dependent decrease in A549 cell viability to 47% (20 mg/mL) and 15% (85 mg/mL). Toxicity screening of engineered nanomaterials is always accomplished in concentration-dependent manner to develop safety profile and risk management strategies for their real-world applications. In the case of graphene, low concentrations are generally not toxic in mammalian cells but high concentrations play a role in plasma membrane internalization and induction of programmed cell death [24]. Liao et al. [25] reported toxicity of graphene sheets in dose-dependent manner which showed chronic hemolysis activity to suspended erythrocytes owing to its good electrostatic interactions with the erythrocyte membrane. Also high concentrations of graphene sheets (200  $\mu\text{g/ml}$ ) produced higher reactive oxygen species in human skin fibroblast cells than low concentrations (3.125  $\mu\text{g/ml}$ ) of graphene sheets due to their strong interaction and binding to the cell surface. Comparable results were reported in A549 cell line [10, 11] suggesting that higher concentrations of graphene sheets damage membrane integrity and block the localization of sheets with cell barriers and produce high yield of reactive oxygen species. rGO has pronounced effects on cellular viability, oxidative stress, and cell death compared to GO because of its sharp edges, functional groups, surface charge and nanosheets which facilitate its improved cellular uptake [26]. The combined effect of early and late apoptosis and necrosis events produced by rGO implies a threat to clinical utility of rGO. rGO induced toxicity potentially causes the poor delivery of essential nutrients to cancer cells by blocking

the immune tolerance of the host cells to recruit blood vessel factories for their survival. Oxidative stress is one of the key paradigms leading to graphene toxicology that reduces the viability of cells and also hinders the uptake of essential proteins and nutrients into cells [12, 27]. Production and abolition of reactive oxygen species are well-adjusted inside the cells, and altering the balance could induce lipid peroxidation, dysfunction of mitochondria, and apoptosis and necrosis [28]. The toxic transformation of graphene, irrespective of the specific structure/assembly of graphene used, relies on its bioaccumulation, the structural and chemical morphology of graphene as well as the generation of reactive oxygen species in both dark and photo toxicity environments [29]. The excessive reactive oxygen species generation may induce the mitochondrial membrane damage from lipid peroxidation, DNA damage and apoptosis (at low dose) [30]. The generation of reactive oxygen species to induce oxidative stresses is considered to be a leading cause of toxicity for graphene nanocomposites [28]. Furthermore, the rGO revealed necrosis was more profound and prevalent at high doses, which is likely due to gene deregulation and encoding, demolition phase of apoptosis process, whereas, apoptosis events induced by low dose of rGO might be triggered due to death-receptor mediated pathways and mitochondrial-driven intrinsic pathways [31]. Furthermore, based on the existing literature work and this chapter, it is revealed that cellular membrane distress, oxidative stresses and direct contact of the sharp edges with the cells are considered to be majorly responsible for the toxicity of rGO. Direct contact of sharp edges and lateral dimensions of rGO may induce genotoxic lesions and genomic instability through their interactions with the DNA sequence and structure in target cells [32]. In addition, the presence of impurities and toxic chemicals during the fabrication of graphene nanocomposites may have adverse effects on their bioavailability to living systems. Diversity in size, shape, surface chemistry, lateral dimensions and fabrication routes of rGO make it impossible to establish clearly the comparison of biological and toxicological impacts of rGO between different studies. As different preparation methods produce different quantities of functional groups and free radicals on the surface of rGO, this subsequently induces oxidative stresses. Therefore, terminology, nomenclature and preparation methods need to be reconciled and standardized to validate analytical methods for measuring toxicology impacts, bio distribution and physicochemical characteristics of rGO in living systems. With the rapid growth and expansion of the graphene market, it is necessary

to assess the risk management strategies related to the fabrication processes and clinical settings which can potentially minimise the environmental and clinical risks of graphene. Furthermore, an important benefit of graphene over other nano-assemblies is that its physiochemical properties such as hydrophobicity/hydrophilicity, surface charge, size, and surface area could be tuned by adjusting synthesis conditions. Moreover, a variety of post-preparation methods may be introduced to graphene sheets targeting the efficient reduction of graphene oxide. Surface functionalization, reduction strategies, doping, and introduction of biocompatible coatings are another promising and intriguing window of opportunity to improve the bioavailability of rGO to living systems. This is of a particular importance in relation to bio-persistence and long-term toxicity of this material, since there is a lack of long term *in vivo* monitoring in this area.

The results from this study confirmed that rGO poses higher biological risks than GO and other derivatives of graphene. In order to improve the bioavailability of rGO, several significant challenges remain to be addressed such as translating its toxicological mechanisms and preparation of safer and modified rGO sheets. Further toxicological studies should take into consideration the facile preparation of the sample such as the intermixing of debris from sample impurities, residues of strong acids and reducing agents, which may profoundly revise and improve the surface features of rGO. Further *in vivo* investigations are also required to trace the bioavailability of rGO and to clarify the clinical effects of this ‘miracle material’.

## 5.4 Conclusions

This chapter describes the *in vitro* toxic effects of rGO on lung cancer cells (A549 and SKMES-1) as a function of its concentration. The results indicated that rGO caused significant late apoptosis and necrosis rather than early apoptotic event at lower concentrations, suggesting that rGO was able to disintegrate the cellular membranes in a dose dependent toxicity manner. For the toxicity exposures undertaken, late apoptosis and necrosis occurred, which was likely resultant from the limited bioavailability of unmodified rGO in lung cancer cells.

## References

- [1] Graphene market size global forecast  
<http://www.marketsandmarkets.com/PressReleases/graphene-electronics.asp> and  
<http://www.marketsandmarkets.com/PressReleases/graphene.asp>
- [2] Santos, C. M., Mangadlao, J., Ahmed, F., Leon, A., Advincula, R. C., & Rodrigues, D. F. (2012). Graphene nanocomposite for biomedical applications: fabrication, antimicrobial and cytotoxic investigations. *Nanotechnology*, 23(39), 395101-395111.
- [3] Nguyen, B. H., & Nguyen, V. H. (2016). Promising applications of graphene and graphene-based nanostructures. *Adv. Nat. Sc. Nanosci. Nanotechnol.* 7(2), 023002-023017.
- [4] Ou, L., Song, B., Liang, H., Liu, J., Feng, X., Deng, B., & Shao, L. (2016). Toxicity of graphene-family nanoparticles: a general review of the origins and mechanisms. *Part. Fibre Toxicol.* 13(1), 1-24.
- [5] Liu, S., Zeng, T. H., Hofmann, M., Burcombe, E., Wei, J., Jiang, R., & Chen, Y. (2011). Antibacterial activity of graphite, graphite oxide, graphene oxide, and reduced graphene oxide: membrane and oxidative stress. *ACS Nano*, 5(9), 6971-6980.
- [6] Sasidharan, A., Panchakarla, L. S., Chandran, P., Menon, D., Nair, S., Rao, C. N. R., & Koyakutty, M. (2011). Differential nano-bio interactions and toxicity effects of pristine versus functionalized graphene. *Nanoscale*, 3(6), 2461-2464.
- [7] Syama, S., Aby, C. P., Maekawa, T., Sakthikumar, D., & Mohanan, P. V. (2017). Nano-bio compatibility of PEGylated reduced graphene oxide on mesenchymal stem cells. *2D Materials*, 4(2), 025066-025081.
- [8] Tabish, T. A., Chabi, S., Ali, M., Xia, Y., Jabeen, F., & Zhang, S. (2017). Tracing the bioavailability of three-dimensional graphene foam in biological tissues. *Materials*, 10(4), 336-349.
- [9] Zhang, X., Nan, X., Shi, W., Sun, Y., Su, H., He, Y., & Ge, D. (2017). Polydopamine-functionalized nanographene oxide: a versatile nanocarrier for chemotherapy and photothermal therapy. *Nanotechnology*, 28(295102), 295102-295112.
- [10] Hu, W., Peng, C., Luo, W., Lv, M., Li, X., Li, D., & Fan, C. (2010). Graphene-based antibacterial paper. *ACS Nano*, 4(7), 4317-4323.
- [11] Mittal, S., Kumar, V., Dhiman, N., Chauhan, L. K. S., Pasricha, R., & Pandey, A. K. (2016). Physico-chemical properties based differential toxicity of graphene oxide/reduced graphene oxide in human lung cells mediated through oxidative stress. *Sci. Rep.* 6, 1-15.
- [12] Volkov, Y., McIntyre, J., & Prina-Mello, A. (2017). Graphene toxicity as a double-edged sword of risks and exploitable opportunities: a critical analysis of the most recent trends and developments. *2D Materials*, 4(2), 022001.
- [13] Seabra, A. B., Paula, A. J., de Lima, R., Alves, O. L., & Durán, N. (2014). Nanotoxicity of graphene and graphene oxide. *Chem. Res. Toxicol.* 27(2), 159-168.
- [14] Lin, L., Zheng, X., Zhang, S., & Allwood, D. A. (2014). Surface energy engineering in the solvothermal deoxidation of graphene oxide. *Adv. Mater. Interf.* 1(3).
- [15] Rasmussen, C. E., & Williams, C. K. (2006). Gaussian processes for machine learning (Vol. 1). Cambridge: MIT press.
- [16] Li, D., Müller, M. B., Gilje, S., Kaner, R. B., & Wallace, G. G. (2008). Processable aqueous dispersions of graphene nanosheets. *Nat. Nanotechnol.* 3(2), 101-105.
- [17] Lee, S., Bong, S., Ha, J., Kwak, M., Park, S. K., & Piao, Y. (2015). Electrochemical deposition of bismuth on activated graphene-nafion composite for anodic stripping voltammetric determination of trace heavy metals. *Sens. Actuat. B Chem.* 215, 62-69.

- [18] Pham, V. H., Pham, H. D., Dang, T. T., Hur, S. H., Kim, E. J., Kong, B. S., & Chung, J. S. (2012). Chemical reduction of an aqueous suspension of graphene oxide by nascent hydrogen. *J. Mater. Chem.* 22(21), 10530-10536.
- [19] Sykam, N., & Rao, G. M. (2017). Room temperature synthesis of reduced graphene oxide nanosheets as anode material for supercapacitors. *Mater. Lett.* 204, 169-172.
- [20] Díez-Betriu, X., Álvarez-García, S., Botas, C., Álvarez, P., Sánchez-Marcos, J., Prieto, C., & de Andrés, A. (2013). Raman spectroscopy for the study of reduction mechanisms and optimization of conductivity in graphene oxide thin films. *J. Mater. Chem. C* 1(41), 6905-6912.
- [21] Ren, P. G., Yan, D. X., Ji, X., Chen, T., & Li, Z. M. (2010). Temperature dependence of graphene oxide reduced by hydrazine hydrate. *Nanotechnology*, 22(5), 055705.
- [22] Konkana, B., & Vasudevan, S. (2012). Understanding aqueous dispersibility of graphene oxide and reduced graphene oxide through p K a measurements. *J. Phys. Chem. Lett.* 3(7), 867-872.
- [23] Shahriari, B., Swersky, K., Wang, Z., Adams, R. P., & de Freitas, N. (2016). Taking the human out of the loop: A review of bayesian optimization. *Proc. IEEE*, 104(1), 148-175.
- [24] Zhang, B., Wei, P., Zhou, Z., & Wei, T. (2016). Interactions of graphene with mammalian cells: Molecular mechanisms and biomedical insights. *Adv. Drug Deliv. Rev.* 105, 145-162.
- [25] Liao, K. H., Lin, Y. S., Macosko, C. W., & Haynes, C. L. (2011). Cytotoxicity of graphene oxide and graphene in human erythrocytes and skin fibroblasts. *ACS Appl. Mater. Interf.* 3(7), 2607-2615.
- [26] O. Akhavan, & E. Ghaderi, (2010), Toxicity of graphene and graphene oxide nanowalls against bacteria, *ACS Nano*, 4(10), 5731-5736.
- [27] Montagner, A., Bosi, S., Tenori, E., Bidussi, M., Alshatwi, A. A., Tretiach, M., & Syrgiannis, Z. (2016). Ecotoxicological effects of graphene-based materials. *2D Materials*, 4(1), 012001-012010.
- [28] Palmieri, V., Lauriola, M. C., Ciasca, G., Conti, C., De Spirito, M., & Papi, M. (2017). The graphene oxide contradictory effects against human pathogens. *Nanotechnology*, 28(15), 152001.
- [29] De Marchi, L., Pretti, C., Gabriel, B., Marques, P. A., Freitas, R., & Neto, V. (2018). An overview of graphene materials: Properties, applications and toxicity on aquatic environments. *Sci. Total Environ.* 631, 1440-1456.
- [30] Lopez, E., Arce, C., Oset-Gasque, M. J., Canadas, S., & Gonzalez, M. P. (2006). Cadmium induces reactive oxygen species generation and lipid peroxidation in cortical neurons in culture. *Free Radical Bio. Med.* 40(6), 940-951.
- [31] Wojtoniszak, M., Chen, X., Kalenczuk, R. J., Wajda, A., Łapczuk, J., Kurzewski, M., & Borowiak-Palen, E. (2012). Synthesis, dispersion, and cytocompatibility of graphene oxide and reduced graphene oxide. *Colloids and Surfaces B* 89, 79-85.
- [32] Akhavan, O., Ghaderi, E., & Akhavan, A. (2012). Size-dependent genotoxicity of graphene nanoplatelets in human stem cells. *Biomaterials* 33(32), 8017-8025.

## Chapter 6

# Investigation into the Toxic Effects of Graphene Nanopores on Lung Cancer Cells and Biological Tissues

---

As an inexpensive monolayer archetypal member of carbon family, graphene has triggered a new 'gold rush' in nanotechnology for achieving unique properties that were not available in many traditional materials. Owing to these unique features, graphene-related materials are finding new uses in nanomedicine and synthetic biology in addition to their diverse applications in electronics, optoelectronics, photonics and environmental clean-up. The increased production of graphene nanostructures and increased likelihood of exposures to these substances in environmental and occupational settings has raised concerns about adverse health outcomes. In particular, the biological effects of these materials needs to be assessed to ensure risk free, sustainable development of graphene for widespread applications. In this chapter, for the first time, we study the *in vitro* and *in vivo* interactions of a relatively new derivative of graphene, graphene nanopores (GNPs) in mammalian systems, to systematically elucidate the possible mechanism of their toxicity over time. This study shows that GNPs induce early apoptosis in both SKMES-1 and A549 lung cancer cells, however, late apoptosis is only induced at concentrations higher than 250 µg/ml, suggesting that, although GNPs at lower concentrations induces upregulation of phosphatidylserine on cell surface membrane (i.e. early apoptotic event), it does not significantly disintegrate the cell membrane. In this chapter, we also show that rats intraperitoneally injected with GNPs suffer sub-chronic toxicity in a period of 27 days when tested at single and multiple doses of GNPs (5 and 15 mg/kg) as evidenced by blood biochemistry, organo-somatic index, liver and kidney enzymes functions analysis, oxidative stress biomarkers and histological examinations. *In vivo* toxicity results reveal that GPNs mainly accumulate in the liver and lungs after intravenous administration and can be gradually cleared through kidney. In sum, our results show that GNPs are likely to have a low bioavailability in SKMES-1 and A549 lung cancer cells in rats. Nevertheless, this must be considered against the context of a wider lack

of knowledge regarding the bioavailability, fate and behaviour of this type of new porous frameworks of graphene in natural systems. Therefore, a more long-term GNPs exposure regime more realistic to real-life environmental consequences is needed to fully determine the transport capacities of GNPs in living systems.

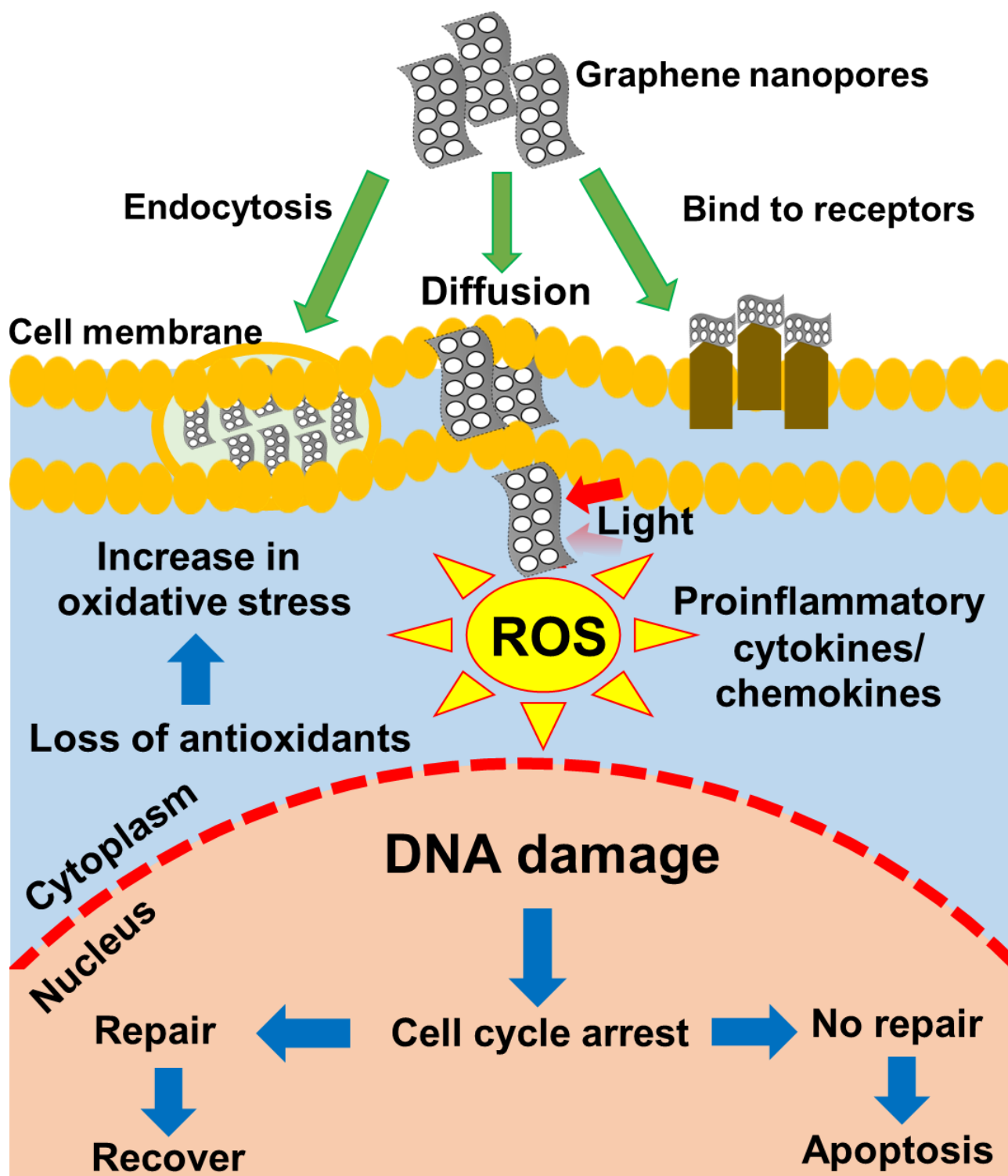
## **6.1 Introduction**

Graphene has become a 'superstar' in nanomedicine with applications to help improve diagnostics, therapeutics, and genetic risk factors, owing to their multifaceted properties such as small size, large surface area-to-volume ratio, quantum size effects, and unique physicochemical properties [1-3]. One important advantage of graphene-based materials is their ability to effectively cross biological barriers such as the blood brain barrier highlighting their potential as a drug delivery vehicle for anticancer therapeutic agents. In particular, the combined enhanced permeability and retention effect would facilitate their accumulation in tumors, releasing the therapeutic levels of drugs into the target cells with the reduced side effects [4]. Typically, graphene quantum dots have many properties far superior to conventional quantum dots such as photoluminescence, low toxicity and interplay between size and optical features which have been utilised as diagnostic imaging tools as well as photodynamic/photothermal therapy [5]. Similar use of three-dimensional graphene foam for stem cell therapy of stroke and its bioconjugates in regenerative medicine has been described in recent literature [6]. Recently, graphene nanopores (GNPs) have also been used for DNA sequencing [7-9] and water treatment [10,11] and GNPs have provided unique porous frameworks [12]. One drawback of the use of GNPs is that very few synthesis techniques are available. However, techniques such as electron beam irradiation, ion bombardment, doping, templating, chemical etching, chemical vapour deposition and other chemical methods have been utilised for their preparation [9, 13-16]. The drawbacks of these methods are the low production yield and the problems associated with their separation/purification. To address this omission, we have demonstrated a novel and facile approach to GNPs synthesis via thermal treatment of reduced graphene oxide without using any catalyst and template-based approach [17].

GNP, a thin, flexible material with excellent electrical addressability and robust mechanical properties is promising for label-free protein detection, DNA sequencing and high throughput wastewater based-micropollutant decontamination [7-11]. The high specific surface area and nanoporous framework allows direct sensing and sequencing of atomic-scale biomolecules. In recent years, cellular internalization and trans-barrier transport of micro/mesoporous graphene nanosheets have been the subject of major development in nanobiotechnology. It is evident that nanoscale materials with diameter less than 100 nm can enter cells, while nanoparticles smaller than 40 nm in diameter can reach the cellular nuclei. Particles with diameters below 35 nm are able to reach the brain by passing through the blood–brain barrier [18], while larger nanoparticles are excluded which in turn reduces the delivery of theranostic nanoparticles [19]. A better understanding of the physiochemical properties of graphene, the interaction between graphene and cells, and possible toxicity mechanism is of critical importance to outline potential biomedical applications of these materials. The proposed mechanism of GNPs toxicity is depicted in **Figure 1**. The widespread use of graphene- based materials and their potential toxic effects are likely to exacerbate several health concerns [20, 21]. Most laboratory experiments investigating the potential applications of GNPs in life sciences have not considered the toxicity associated with GNPs in their testing regimes. Recently, however, a few studies have examined the *in vitro* and *in vivo* toxic implications of three dimensional graphene foam to investigate the bioavailability and subsequent toxicity potential [22, 23]. The pre-clinical risks, and adverse effects of GNPs exposure and approaches to minimize their health hazards still remains undefined. However, inhalation of graphene structures is believed to be a risk for cardiorespiratory disease. For example, graphene nanoplatelets can be transported deep within the distal regions of lungs and trigger a chronic inflammation in the respiratory tract [24]. It is generally thought that the placenta, lung, gastrointestinal tract and skin act as major barriers for many nanostructures entry into living organisms [25]. Indeed, a recent study on mice demonstrated that intratracheally delivered few-layered graphene was mainly retained in the lung with 47 % remaining after 4 weeks, resulting in dose-dependent acute lung injury and pulmonary edema [26]. An *in vitro* study of the effects of graphene and graphene oxide on human skin HaCaT keratinocytes demonstrated that oxidized graphene was the most cytotoxic, inducing mitochondrial and plasma-membrane



damages, suggesting low cytotoxic effects at the skin level [27]. Reduced graphene oxide is more toxic than graphene oxide as evident by many studies reported recently which is primarily due to its sharp edges and structural morphology [28, 29]. In contrast to the typically soluble nanoparticles examined in conventional toxicology investigations, graphene nanostructures have different shapes and surface areas, and which in turn can significantly influence their diffusion, dispersion, aggregation and agglomeration in plasma. Importantly, these “tunable” characteristics of graphene account for the varying toxic outcomes on the tissues. *In vivo* toxicity testing of graphene, at post-mortem histological examinations of liver alterations have revealed hypertrophy of hepatocytes, necrosis and inflammatory cell infiltration in liver and kidney tissues [30]. The level of organ functions and oxidative stress have been reported to affect the fate, transport and toxicity of graphene in organs but there is currently a lack of consistency in this regard [30]. Liver enzyme functions can be used to reveal the biodistribution, metabolism, and excretion patterns of graphene. Similarly, investigation of oxidative stress indicators, is a commonly acknowledged mechanism adopted to investigate cellular injuries in mammals. Antioxidants act as a defence system to reinstate the cellular redox balance, when oxidative stress are generated as a result of excess production of reactive oxygen species. Disruption of this critical balance in the presence of excessive reactive oxygen species triggers the activation and promotion of pro-inflammatory cascade, cytokine and chemokine which in turn causes mitochondrial release of proapoptotic factors potentially leading to cell death. Since hepatocytes are key targets for reactive oxygen species damage and therefore liver function and biomarkers of oxidative stresses should be investigated with great care. Clearly, *in vitro* and *in vivo* investigations into the toxicity of graphene nanostructures is becoming increasingly important. In response to this, the present study investigates the toxic effects of GNPs on lung cancer cells (SKMES-1 and A549) *in vitro* and rat *in vivo*, specifically, biochemical, serum enzyme analyses, complete blood count as well as histological analysis have been used in this chapter.



**Scheme 6.1:** Scheme of the potential mechanisms of action of graphene nanopores (GNPs). When graphene reach the exterior membrane of a cell, they interact with the plasma membrane or extra- cellular matrix and enter the cell, mainly through diffusion, endocytosis and/or binding to receptors. The potential toxic effects of graphene mainly depends on its physicochemical characteristics, nature of its interaction with cell and

its accumulation in specific organs. Upon interaction with light, graphene can generate reactive oxygen species, which in turn can cause oxidative stress, loss in cell functionality, proinflammatory response and mitochondrial damage. Uptake of graphene into the nucleus may cause DNA-strand breaks and induction of gene expression via the activation of transcription factors, cell death and genotoxicity.

## **6.2 Materials and methods**

### **6.2.1 Synthesis of graphene nanopores**

The method of preparing exfoliated graphene oxide (GO) flakes and reduced GO is the same as described in chapters 4 and 5 (**sections 4.2.1 and 5.2.1**) using the Modified Hummers method. The resultant rGO was allowed to settle, washed with distilled water and filtered until the supernatant became clear. To obtain porous nanosheets, the filtered product was oven-dried in vacuum overnight and then thermally treated at 200 °C in Ar for 12 h under a slow ramp rate of 3 °C min<sup>-1</sup>. Transmission electron microscope (TEM), X-ray diffraction (XRD) analysis, UV–Vis absorbance, Fourier-transform infrared (FTIR) spectra, Raman spectra and zeta potential measurements of GNP samples were carried out in the same manner as described in chapter 4 (**section 4.2.1**). Microstructures of GNPs, graphite flakes and GO samples were taken on a Philips XL-30 scanning electronic microscope (SEM) under high vacuum conditions with accelerating voltage 20 kV and the samples were mounted onto carbon sticky tape. Nitrogen gas sorption analysis was conducted using a Quantachrome Autosorb-iQ gas sorptometer. Prior to the sorption measurements, sample was heated at 200 °C under vacuum conditions for 3 h. Surface area was calculated by using Brunauer–Emmett–Teller (BET) theory method. The total pore volume ( $V_t$ ) was measured from the amount of adsorbed nitrogen (at  $P/P_0 = ca. 0.99$ ).

### **6.2.2 Cell viability**

The methods used for the preparation of seed cultures and preparation of suspensions for seeding have been described in chapter 4 (**section 4.2.2**). Cells were treated for

24 h with and without various concentrations of GNPs (5, 50, 250, 500 and 1000 µg/ml) in culture medium and cells cultured without GNPs were taken as control.

### **6.2.3 Regression model analysis**

The relationships between concentration of rGO and cell death rate were investigated to determine the most appropriate concentration levels for therapeutic purposes [31]. The details of this method were given in chapter 4 (**section 4.2.3**).

### **6.2.4 Cell apoptosis and necrosis**

Cell apoptosis and necrosis were examined using flow cytometry as previously described in chapter 4 (**section 4.2.2**). Data were expressed as % cell count  $\pm$  SD and analysed by Mann Whitney.  $P < 0.05$  was considered statistically significant.

### **6.2.5 Animals**

All animal experiments were performed in compliance with the institutional ethics committee regulations and guidelines on animal welfare (Animal Care and Use Program Guidelines of Government College University), and approved by Government College University, Faisalabad, Pakistan. Sprague-Dawley adult male rats (average age of 6-7 weeks, 230-250 g weight) were obtained from the animal house of Government College University, Faisalabad, housed in groups in ventilated cages under standard lighting conditions and natural day/night cycle after approval from the ethical committee of the institution. They were given free access to water and food and the surrounding humidity and temperature ( $25\text{ }^{\circ}\text{C} \pm 2\text{ }^{\circ}\text{C}$ ) was controlled. After a period of acclimatization for 7 days, the animals of similar mean initial body weights were randomly divided into five groups,  $n=8$  per group. The body weights of the control group and all the experimental groups were observed and recorded weekly to note weekly changes in body weights. The body weight and behaviour were recorded every day after the first exposure. Organo-somatic index was calculated by the following formula:  $(\text{Weight of the organ (g)}/\text{Total body weight (g)}) \times 100$ . A control group was fed by usual water and food, while the other group was treated with various doses of GNPs (5

mg/kg, 15 mg/kg single and multiple doses) intraperitoneal injections for 27 days. The treatment continued on alternate days for a period of 27 days. Animal exposure schedule was also schematically represented in **Supplementary information Figure 6.1**. At the end of the experimental period, animals were fastened overnight, anaesthetized the next day, by administering ketamine hydrochloride (30 mg/kg body weight) and sacrificed. Blood samples were collected at the start of the experiment and after 27 days of the treatment, from the marginal ear vein, and used for the analysis of complete blood count (CBC), selected serum biochemical parameters, haematology, liver function tests and oxidative stress enzymes.

### **6.2.6 Complete blood count (CBC) and clinical biochemistry panel analysis**

Hematological parameters: Red blood cell count (RBC); Lymphocytosis (LYM); Lymphocytosis (LYM %); mid-range absolute count (MID); total % of granulocytes GRA; Hemoglobin (HBGL); mean corpuscular haemoglobin (MCH); Mean corpuscular hemoglobin concentration (MCHC); Mean corpuscular volume (MCV); hematocrit (HCT); Red cell distribution width (RDW); Platelet count (PLT); mean platelet component (MPC); large platelet concentration ration (LPCR); and White blood cell count (WBC), were analysed in blood samples by using Hitachi 902 automatic analyser (Japan) using a haematology autoanalyser. Blood samples (of approximately 7 ml) were collected into heparinised tubes and centrifuged at low speed of 2000×g for 5-10 min to separate plasma. The vital organs were collected, weighed immersed in fixative sera for further process of histology and for evaluation of enzyme activities, antioxidants and biomarkers.

### **6.2.7 Liver and kidney function analysis**

To evaluate the liver function, the activities of alanine aminotransaminase (ALT), aspartate aminotransferase (AST) and alkaline phosphatase (ALP) and to assess the activities of kidney function, the activities of creatinine was measured. Concentration of these enzymes were determined using marketed reagent kits (CHEMELEX, S.A Pol. Ind, Barcelona, Spain) and autoanalyser system (Hitachi Ltd., Tokyo, Japan) following the IFCC method [32].

### **6.2.8 Histological analysis**

The harvested heart, liver, kidney, brain, small intestine and testis were fixed with 4% paraformaldehyde for 5 h and then dehydrated and processed for histology. 6  $\mu$ m sections were cut from paraffin blocks using a Reichert microtome and stained with eosin (cytoplasm staining). The stained slides were examined by light microscopy through a 20X and 40X objective lens. A histological analysis of vital organs was performed to determine the toxic effects and the degradation of GNPs to inducing tissue damage or any histopathologic changes.

### **6.2.9 Oxidative stress biomarkers**

The activities of biomarkers of oxidative stress, i.e. catalase activity, superoxide dismutase activity, glutathione-S-transferase activity and lipid peroxidation, were measured. To determine these parameters in the liver, the liver was separated and washed in standard ice-cold isotonic saline solution. Then, the tissues were homogenized in 0.1 M Tris-HCl buffer solution at 4 °C following by the centrifugation (10,000 rpm for 15 min at 4 °C) and the supernatant was stored at -20 °C for the evaluations of enzyme activities. This procedure was followed by previously reported method [33]. The activity of lipid peroxidation was evaluated by quantifying the malondialdehyde (MDA), following by the thiobarbituric acid reactive substance (TBARS) method. This procedure was followed by previously reported method [34]. The concentration of MDA TBA compound was evaluated by using a spectrophotometer at 532 nm using blank as control. The reduced glutathione (GSH) was estimated according to the method described in ref [35]; catalase [36]; and hydroperoxide [37].

### **6.2.10 Statistical analysis**

The results was statistically analysed in GraphPad Prism 5.04 to investigate the impacts of GNPs injected groups for complete blood count parameters, body weight, liver and kidney function tests, and oxidative stress biomarkers, as compared to

control.  $P < 0.05$  was considered as statistically significant. Data were presented as the mean  $\pm$  standard deviation (SD).

## 6.3 Results

### 6.3.1 Basic characterization

Figure 1 shows basic characterization of as-prepared GNPs. Scanning electron micrographs enable the visualization of wrinkles and corrugations in the graphene sheets, and induce the formation of nano-sized channels or pores on the surface (**Figure 6.1a**). As seen in **Figure 6.1a**, the GNPS had an irregular, folded structure with sheets entangled with each other. This is further seen in the high-resolution transmission electron micrographs shown in **Figure 6.1(b)**. To further clarify the growth process of the GNPs structure, the raw material and intermediate product were investigated by XRD, FTIR and Raman spectroscopy. A comparison of the XRD patterns of graphite flakes, GO and GNPs reveals that the (002) peak of GNPs was broadened and had a markedly reduced intensity, indicating that they were composed of single-layer graphene sheets (**Figure 6.1 c**). The introduction of pores on graphene sheets resulted in a change of the D/G Raman peak intensity ratio (**Figure 6.1 d**) [38, 39]. For graphene-based materials, the Raman G-peak (ca.  $1590\text{ cm}^{-1}$ ) corresponded to the  $\text{sp}^2$ -hybridized hexagonal lattice of carbon atoms, and the D-peak (ca.  $1350\text{ cm}^{-1}$ ) was indicative of  $\text{sp}^3$ -hybridized carbon atoms in the lattice structure, which was categorised as defects on the edges of the graphene. In addition, the coexistence of D-peak revealed the  $\text{sp}^2$  hybridized carbon atoms which were slightly reduced as a result of oxidation. However, as indicated in **Figure 6.1d**, as-prepared GNPs had a higher D/G intensity ratio than graphite and GO, correlating to the reduction in the average size of the  $\text{sp}^2$  domains after the reduction of exfoliated GO. The increased amount of  $\text{sp}^3$ -hybridized carbon atoms indicated the activation of nanosheets for the formation of pores and edges in the nanosheets [40, 41]. The FTIR peak of GO was centred at about  $1615\text{ cm}^{-1}$ , which was shifted to the absorption peak of a carbonyl group at about  $1730\text{ cm}^{-1}$  for PG, indicating that the thermal treatment of rGO left more edged carbon atoms in the form of oxygen containing groups (**Figure 6.1 e**). To further analyse and quantify the pore structure, nitrogen adsorption–desorption isotherms for

the GNPs sample were determined. **Figure 6.1f** shows the isotherms and Barrett–Joyner–Halenda pore size distributions of PG. According to the IUPAC classification, the nitrogen adsorption–desorption isotherm curves of these samples exhibited a type IV with a H3 hysteresis loop, which is a characteristic feature of mesopores [42]. Furthermore, the adsorption segment of the nitrogen isotherms at  $P/P_0$  displayed a steady increase, suggesting the formation of large mesopores and small macropores with the average pore size in the GNPS calculated as 3–5 nm.



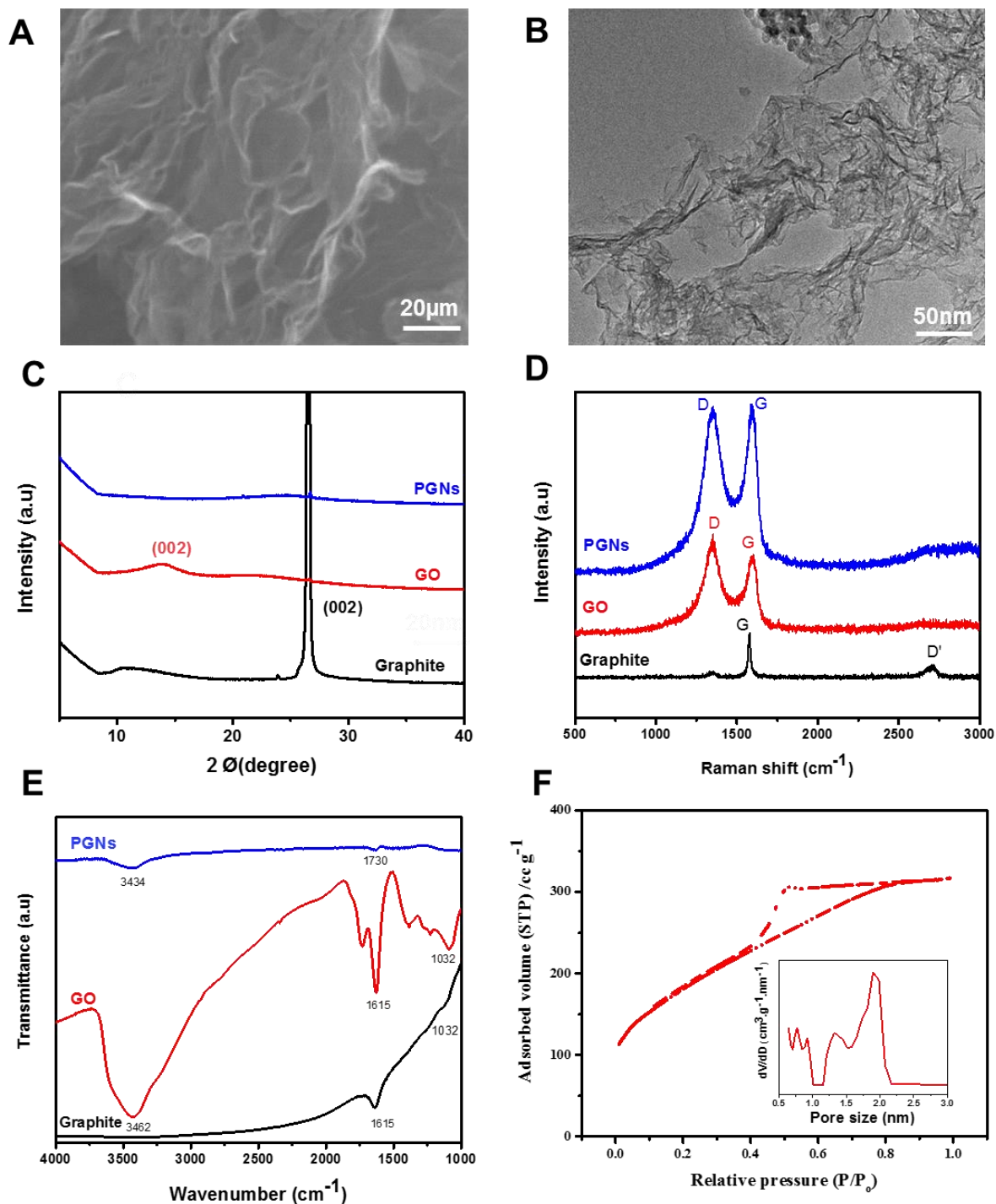


**Figure 6.1: Basic characterization of as-prepared GNPs.** (a) Low-magnification SEM images of as-prepared GNPs. (b) TEM images of a representative GNPS showing holes in the nanosheet. (c) X-ray diffraction, (d) Raman spectroscopy, and (e) Fourier transform Infrared spectroscopy of graphite flakes (black), GO (red) and GNPS (blue). (f) Measurement of specific surface area. The pore size distribution of GNPS

was calculated using Barrett–Joyner–Halenda method presented in Figure f as an inset at 77 K, pore size 1-4 nm.

### 6.3.2 *In Vitro* toxic effects of GNPs on lung cancer cells

**Figure 2A** demonstrates that after 24-h exposure to GNPs, the cell viability of A549 cells exhibited a significant dose-dependent reduction from 50 to 500  $\mu\text{g/ml}$ . For example, reduction in the percentage living cell were 52.8%, 42.5% and 33.2% at concentrations 50, 250 and 500  $\mu\text{g/ml}$  respectively, compared to control (0  $\mu\text{g/ml}$ , ~80%). A similar observation was made in SKMES-1 cells where GNPs concentrations 50 and above induced significant reduction of living cells. However, the reduction was not dose dependent (Figure 2A). For example, at 50, 250 and 500  $\mu\text{g/ml}$  of GNPs, percentage count for living cells were 50.8%, 46.5% and 47.4% respectively, compared to control (0  $\mu\text{g/ml}$ , 70%). Early apoptosis showed a significant increase in signals from 5  $\mu\text{g/ml}$  in a dose dependent manner up to 500  $\mu\text{g/ml}$  both in A549 and SKMES-1 cells (**Figure 6.2B**). A dose-dependent increase in late apoptotic (**Figure 6.2C**) and necrotic cells (**Figure 6.2D**) was also observed in A549 cell line, although no significant increase in necrosis was observed in the SKMES-1 cell line. The resulting predictive distributions from the GP models for A549 and SKMES-1 cells are shown in **Figure 6.2 (E & F)**. The models not only capture the measurement noises, but also indicate how much confidence may be derived from the predictions through the associated standard deviation. Interestingly, the model for both cells indicate that concentrations above 50  $\mu\text{g/ml}$  are likely to be toxic than lower concentration, which yields lower cell death. These predictions match with the experimental results presented in **figure 6.2 (A-D)**.

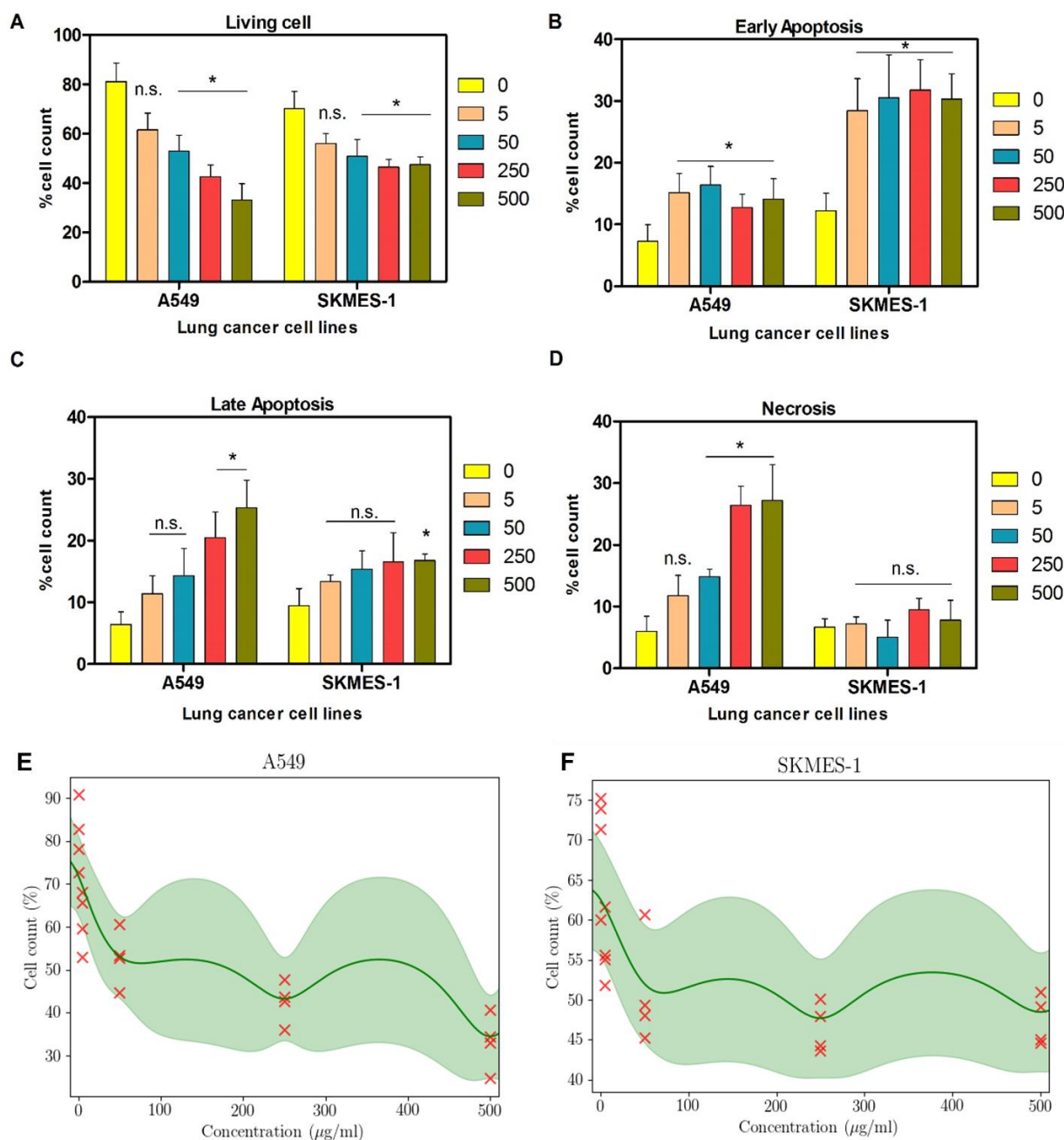


**Figure 6.2.** Bar graph quantifying the percentage of dead, living, early-stage apoptotic, and late-stage apoptotic cells in response to different concentrations of graphene nanopores (GNPS). Flow cytometry analysis of A549 and SKMES-1 lung carcinoma cells stained with annexin V (apoptosis) and propidium iodide (PI; late apoptosis and necrosis) following 24 h of treatment with varying concentrations of GNPs (0–500  $\mu\text{g/ml}$ ). **(A)** graphic representation of percentage of living cells **(B)** early apoptosis **(C)** late apoptosis, **(D)** necrosis (flow cytometry) in response to GNPS. Data are represented as mean  $\pm$  SD, n.s., \* $p < 0.05$  vs control (0  $\mu\text{g/ml}$ ). n.s. denotes not significant. **(E-F)** Gaussian process (GP) regression models for cell survival rates of

A549 (E) and SKMES-1 (F) cells interacted with various concentrations of GNPs. The green solid lines show the mean GP prediction, while the light green areas around the mean show the uncertainty (one standard deviation) in prediction. The models are trained with the data indicated by the red crosses.

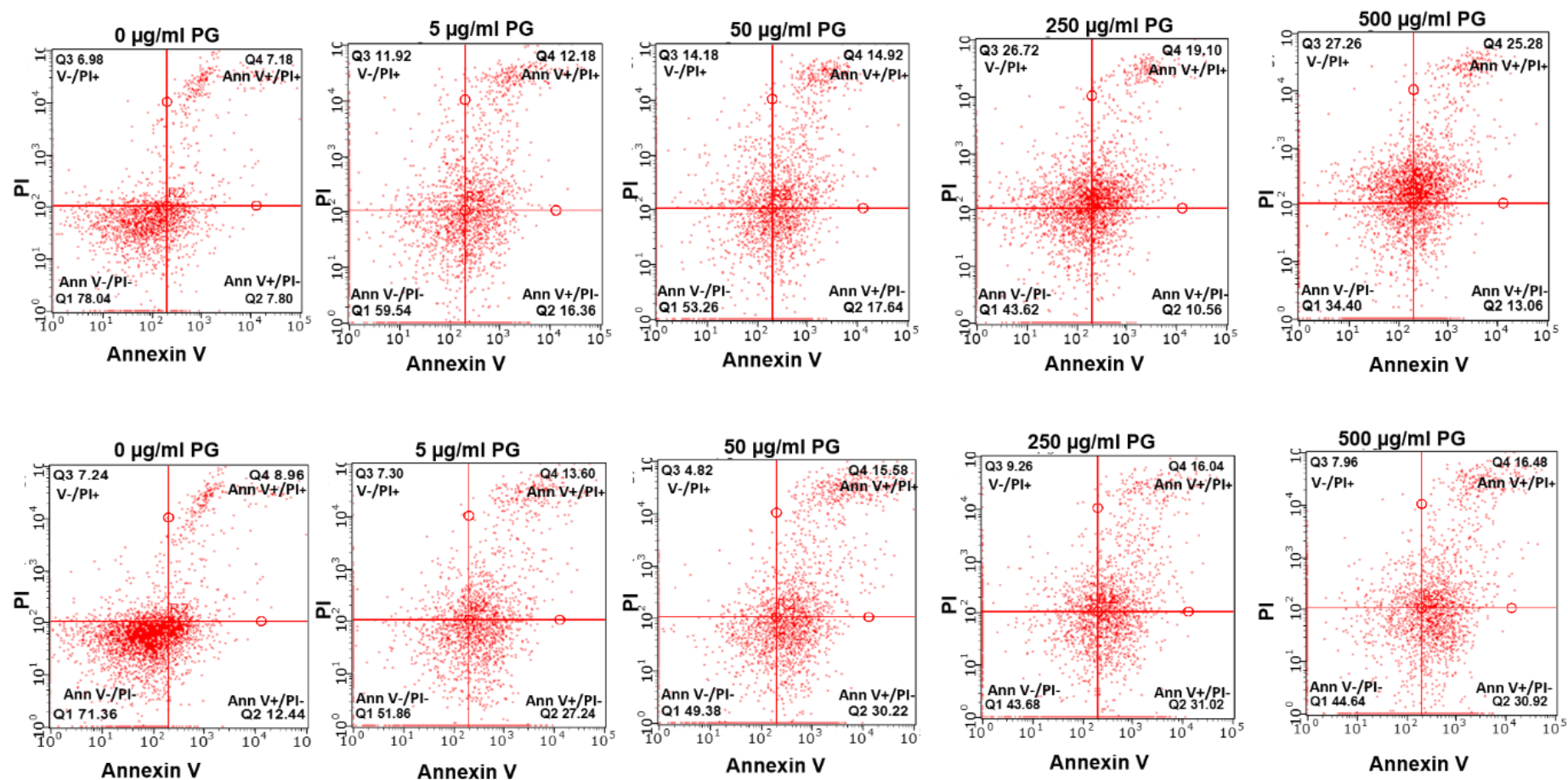


**Figure 6.3:** Representation of FACS images and analysis of one experiment. Data are presented as percentage of the cell population. Cell viability of A549 (upper panel) and SKMES-1 (lower panel) at selected concentrations. Experiments were performed and interpreted as follows: Annexin V<sup>-ve</sup>/PI<sup>-ve</sup> cells (lower left quadrant), AnnV<sup>+ve</sup>/PI<sup>-ve</sup> cells (lower right quadrant), AnnV<sup>+ve</sup>/PI<sup>+ve</sup> (upper right quadrant) and AnnV<sup>-ve</sup>/PI<sup>+ve</sup> (upper left quadrant) were considered as living, early apoptotic, late apoptotic, and necrotic cells.

### 6.3.3 Effects of GNPs on body and relative organ weights

*In vivo* toxicity of GNPs was assessed in rats following 27-day repeated dose intraperitoneal injections. GNPs treatment did not affect the body weight of the treated rats during the 27-days exposure period for treatment with 5 mg/kg body weight either once or multiple doses (**Figure 6.4**). No significant decrease in body weight was observed in rats administered GNPs up to 5 mg/kg. Rats in the high repeated dose group (15 mg/kg body weight) showed lower body weights after 27 days (**Figure 6.4**) compared to the control group. The analysis showed that rats did not differ statistically significantly in the dose–response for body weight (apart from high repeated dose). Organo-somatic indices demonstrated that organ weight did not change by the treatment of GNPs, compared to the control, supporting its low toxicity (**Supplementary information Figure 6.2**).

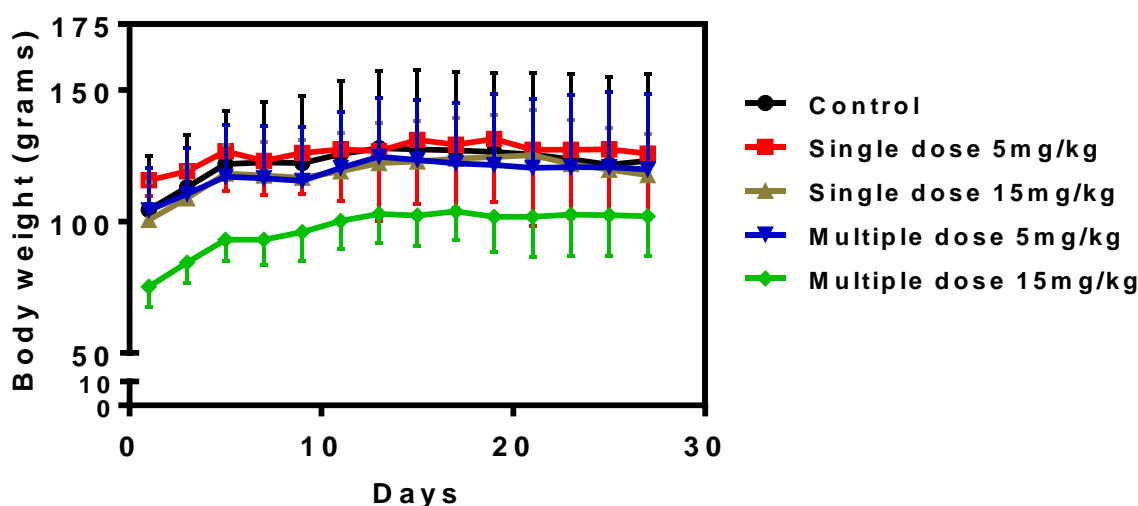


**Figure 6.4:** Daily body weight (g) of control groups and treated groups exposed to GNPs along with intraperitoneal injection of rats for 27 days.

### 6.3.4 Effects of GNPs on complete blood count in the rat

To examine the *in vivo* cytotoxicity of GNPs, we performed a complete blood count (CBC), liver and kidney function enzymes, biomarkers of oxidative stress and histological study of vital organs of control and treated rats in a dose-dependent manner (14 doses spread over a 27 day period of either 5 or 15 mg/kg body weight). Toxic effect of GNPs on CBC was observed (**Figure 6.5 a-o**) although there was a

slight (6%) reduction in platelet numbers in the 15 mg/kg group (**Figure 6.5 K**), although the proportion of lymphocytes remained stable (**Figure 6.5 B**) and total white cell count was unaffected (**Figure 6.5 N**).

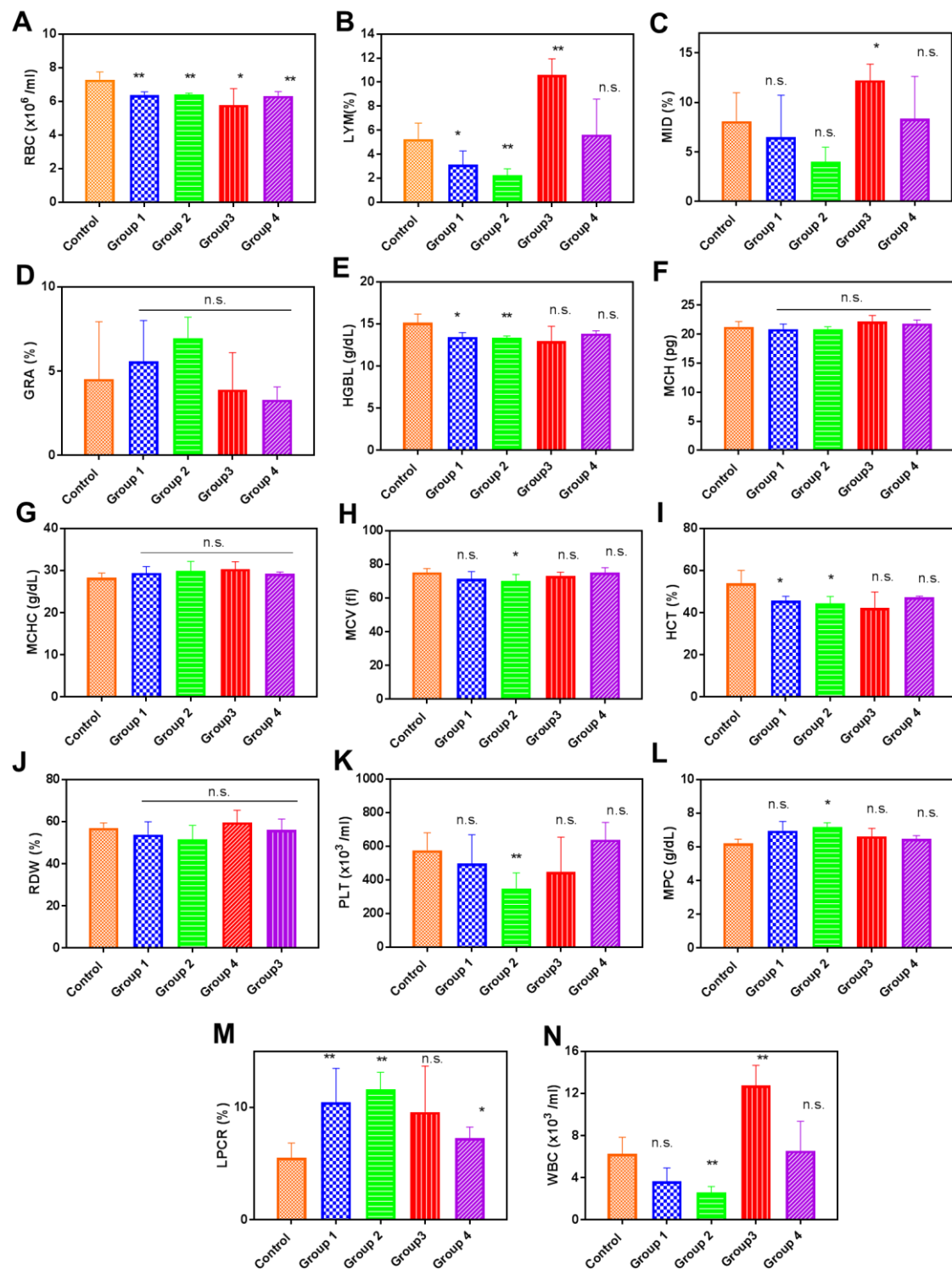


**Figure 6.5:** (A-N) Complete blood count in rats after 27 days of GNPs administration. Rats (n=8 per group) were intraperitoneally injected with single doses of 5 mg/kg body



weight (group 1), 15 mg/kg body weight (group 2) and multiple doses of 5 mg/kg body weight (group 3) and 15 mg/kg body weight (group 4). Results are presented as mean  $\pm$  standard deviation (SD), for: A) Red blood cell count (RBC); B) Lymphocytosis (LYM %); C) mid-range absolute count (MID); D) total % of granulocytes GRA; E) Hemoglobin (HBGL); F) mean corpuscular haemoglobin (MCH); G) Mean corpuscular hemoglobin concentration (MCHC); H) Mean corpuscular volume (MCV); I) hematocrit (HCT); J) Red cell distribution width (RDW); K) Platelet count (PLT); L) mean platelet component (MPC); M) large platelet concentration ratio (LPCR); and N) White blood cell count (WBC). Data are represented as mean  $\pm$  SD., \* $p < 0.05$ , \*\* $p < 0.01$ , \*\*\* $p < 0.001$  vs control. n.s. denotes not significant.

### 6.3.5 Liver and kidney function analysis

In general minor alterations were observed in liver and kidney functions (**Figure 6.6**) i.e, the results showed that activities of ALT, AST, ALP and creatinine enzymes increased in all groups. This increase in comparison to the control group in the second, third and fourth groups, is significant from the statistical point ( $p < 0.05$ ). The increased ALP, ALT and AST are indicative for liver damage. Liver function tests such as ALT, AST and ALP were carried out to study liver damage of GNPs treated groups as compared to control. After 27 days of exposure, the activities of ALT, AST and ALP were increased significantly in 15 mg/kg of GNPs repeated doses, while at the highest dose (15 mg/kg) of GNPs, the activity of kidney enzyme creatinine gradually decreased. The single low and high doses (5 and 15 mg/kg body weight of rats) were least effective in ameliorating the alterations in the concentrations of the creatinine induced, while the repeated dose (5 and 15 mg/kg body weight of rats) showed significant ameliorative effects on the blood levels of creatinine.



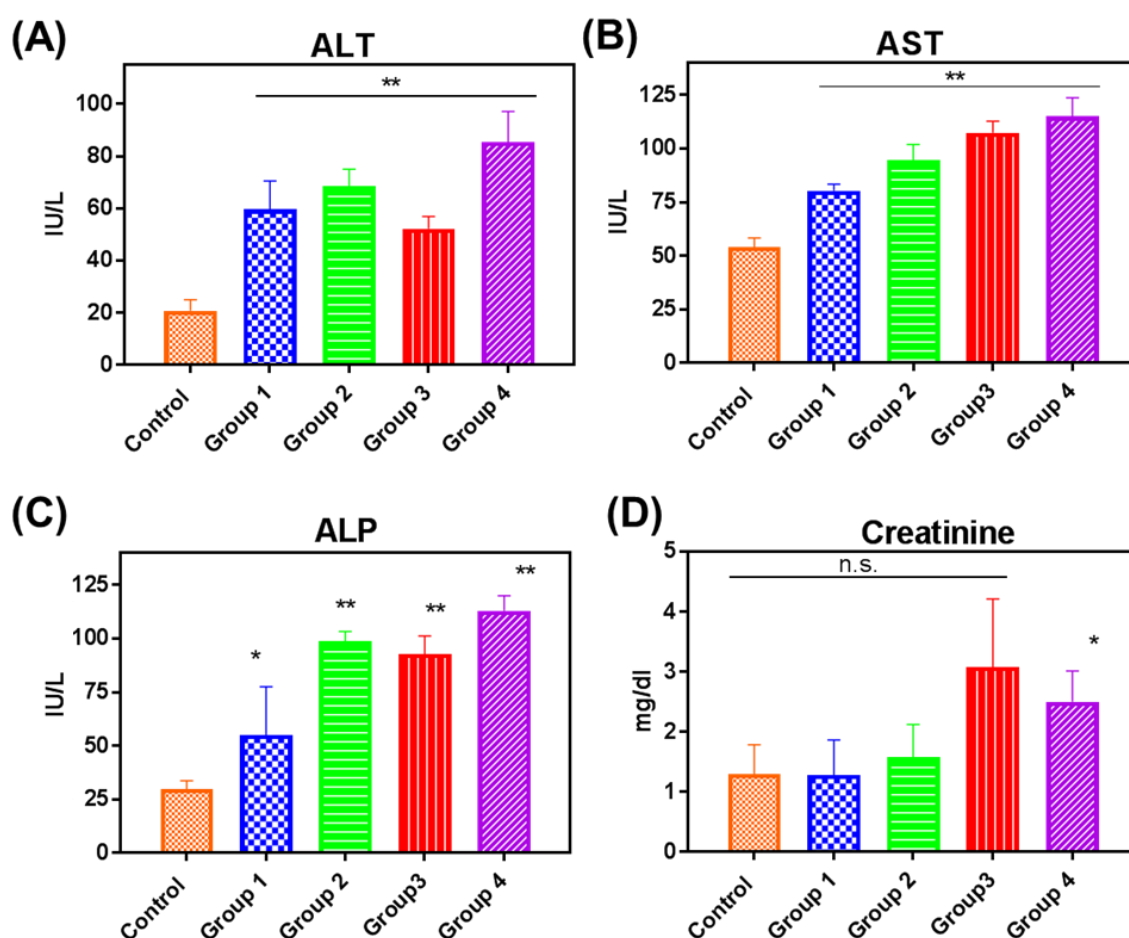


**Figure 6.6:** Liver and kidney enzyme functions results in rats after 27 day post GNPs administration. Rats (n=8 per group) were intraperitoneally injected with single doses of 5 mg/kg body weight (group 1), 15 mg/kg body weight (group 2) and multiple doses of 5 mg/kg body weight (group 3) and 15 mg/kg body weight (group 4). Values are expressed as mean  $\pm$  standard deviation, for: A) Alanine transaminase (ALT), B) Aspartate transaminase (AST), C) alkaline phosphatase (ALP) and D) Creatinine. Data are represented as mean  $\pm$  SD., \* $p < 0.05$ , \*\* $p < 0.01$ , \*\*\* $p < 0.001$  vs control. n.s. denotes not significant.

### 6.3.6 Histopathological changes

A comprehensive post mortem histological study was then performed to assess any tissue interactions with GNPs. Sections of heart, kidney, liver, small intestine, brain and testis were examined for histopathological changes 27 days after GNPs administration (at single and multiple doses of 5 and 15 mg/kg of body weight of rats).

The histology photographs of the liver, kidney, heart and small intestine tissues were shown in **Figure 6.7 and 6.8**. GNPs for 27 days showed significant pathological changes, vacuolation, dilation of central vein and haemorrhage, vacuolation and dilation of central vein, damage of vacuolation, haemorrhage and degeneration of central vein, dilation of epithelial lining and hydropic degeneration edema in liver tissues. Kidney tissues of treated group showed acute vacuolization, dilation of epithelial lining, vacuolation and nucleus degeneration, nucleus damage, necrosis and epithelial degeneration. Heart showed the chemodectoma, toxic myocarditis, reddish brown atrophy; yellowish brown pigments lipofuscin, the lipofuscin granules as remnants of cell organelles and cytoplasmic material. Brain showed effects of carcinoma, oligodendrocytoma small thin walled blood vessel and cryptococcosis. Testicular tissue of treated groups showed spermatogenesis and vacuolation, dilation of germinal layer, degeneration of secondary spermatocytes, damage in germinal layer, vacuolation and low process of spermatogenesis. The lung showed damage of vacuolation, degeneration of central vein, inflammation, hemorrhage, d-shaped cells structure, hemosiderophages and lesion. The multiple-dose of GNPs exposed to rats induced histopathological changes that indicates the accumulation of GNPs in the liver. The histopathological alterations of these organs at 14 days in the rats were shown in **Supplementary information Figures 6.3 and 6.4**. All the rats were in normal condition at end of experiment. No clinical abnormality or death was observed in the treated rats.

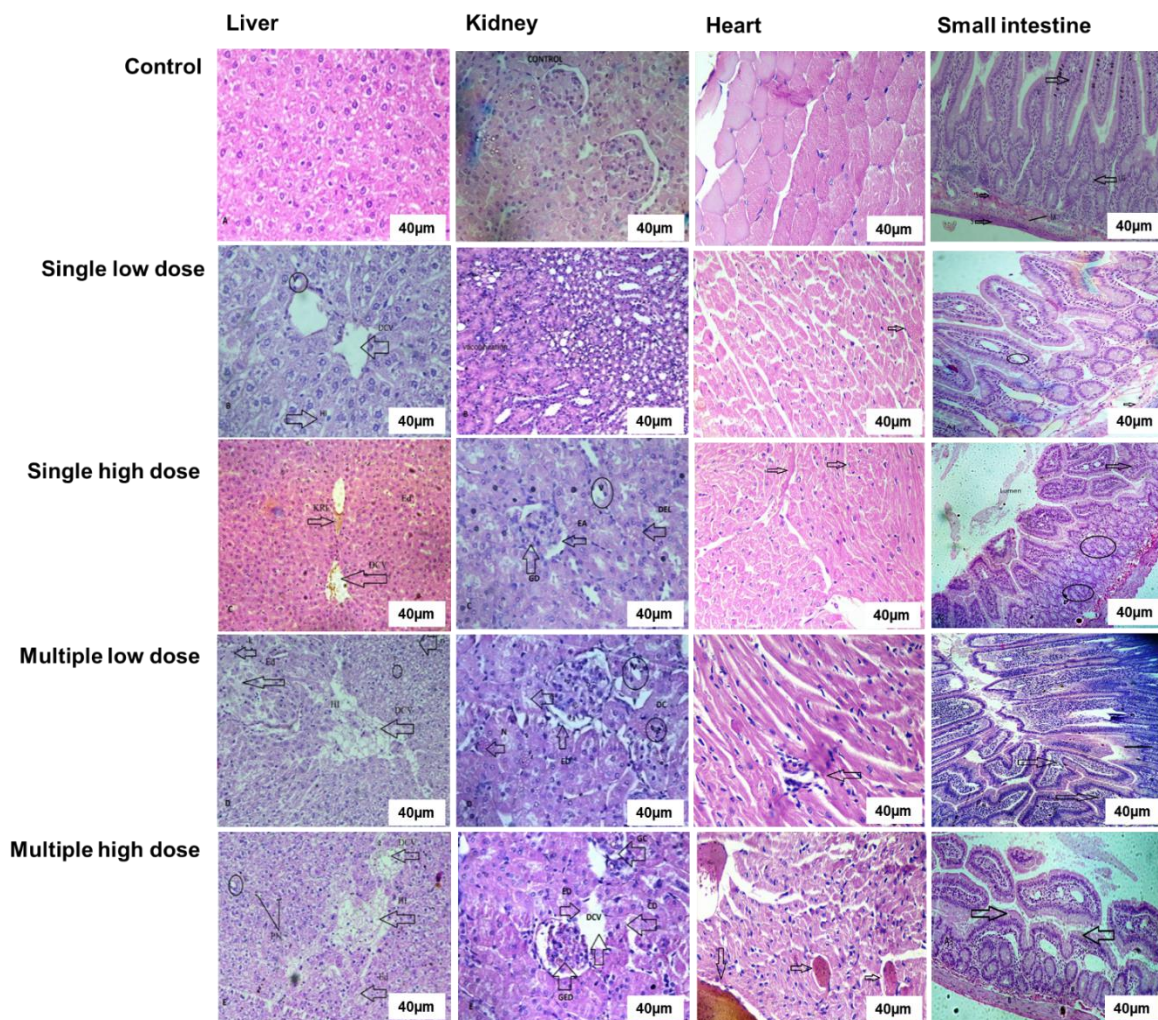


**Figure 6.7:** Representative histopathological changes of the liver, kidney, heart and small intestine of the GNPs-exposed and control rats in the haemotoxyline-eosin (H&E) stained sections. The doses of GNPs were 5 and 15 mg/kg for the single-dose exposure and 5 and 15 mg/kg (every other day, in total fourteen injections) for the multiple-dose exposure. Control group liver showed normal histology while single low dose group (5 mg/kg) showed vacuolation (circle), dilation of central vein (DCV indicated by arrow) and haemorrhage (H indicated by arrow). Single high dose group (15 mg/kg) showed haemorrhage (H), vacuolation (V) and dilation of central vein (DCV) and Karyolysis (K). Multiple low dose group (5 mg/kg) showed the high frequency of vacuolation (circle), haemorrhage (H) and degeneration of central vein (DCV), Nuclear damage (N), Karyolysis (K) and epithelial damage (ED). Multiple high dose group (15 mg/kg) in rats caused destructive effects on liver haemorrhage (H), massive vacuolation (circle), complete dilation of epithelial lining (ED), dilation of central vein (DCV indicated by arrow) and hydropic degenerative edema (HDE). Kidney tissues of control group showed normal histology, single low dose group showed acute vacuolization (arrow) and single high dose group caused dilation of epithelial lining (DEL), vacuolation (circle) and nuclear damage (ND). Kidney tissues of group treated with multiple low dose group showed nucleus degeneration (ND), vacuolation (circle),

while high dose group showed acute necrosis (N), epithelial degeneration (E) and vacuolization (V). Control group heart showed normal histology of heart muscle tissues and single low dose treated group showed the chemodectoma, an ovoid mass, the tumors were enclosed in a fibrous capsule. Single high dose group indicated toxic myocarditis, in this heart muscle fibers showed varying degree of damage, ranging from loss of striation to complete necrosis and fragmentation, whereas multiple low dose group caused acute rheumatism heart, which is the collection of pleomorphic histocytes with large basophilic nuclei which having prominent nucleolus that give the cell an 'owl-eye' appearance. While rats treated with multiple high dose group showed reddish brown atrophy; yellowish brown pigments lipofuscin tends to accumulate in many tissues, the lipofuscin granules are remnants of cell organelles and cytoplasmic material. When the parenchymal cells of an organ have atrophied because of increase age or presence of wasting diseases it causes the condition of brown atrophy. Histology of control group small intestine showed the normal cell of serosa (s), muscular layer (M), sub mucosa ('S), intestinal glands (I.G) and villus (V) and single low dose treated group showed the damage of submucosa and muscular layer (arrow) and enlargement of lacteal (circle). Single high dose treated group showed reduction in villi length (thin arrow), distortion of lamina propria (thick arrow), and intestinal crypts destruction (circle). Multiple low dose treated group indicated moderate villus atrophy (big arrows) and crypt hyperplasia (small arrow) and multiple high dose group showed total distortion of villi and villus atrophy flat mucosa and no visible microvilli (arrows).



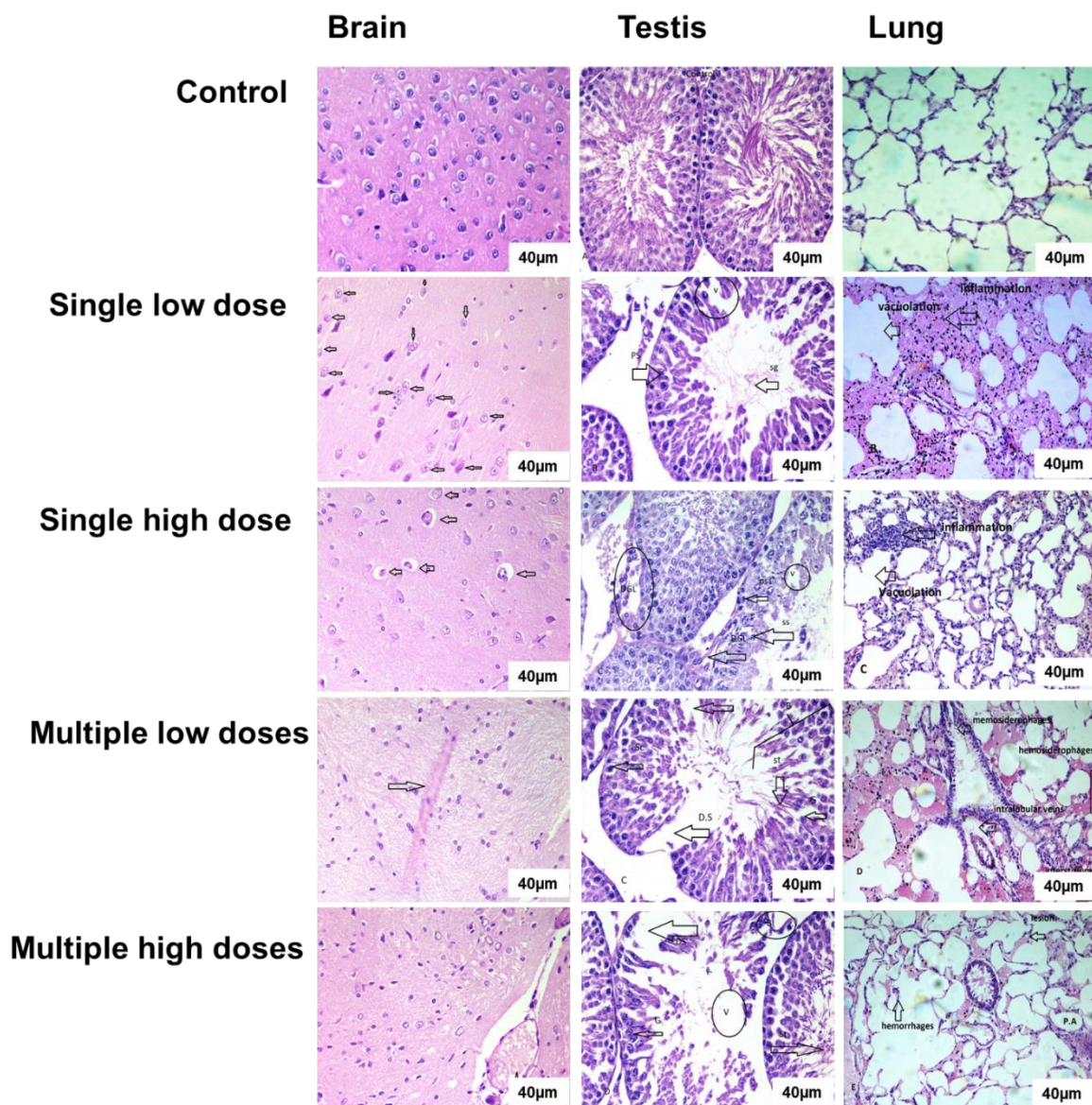


**Figure 6. 8:** Representative histopathological changes of the brain, testis and lung of the GNPs-exposed and control rats in haematoxylin-eosin (H&E) stained sections after 27 days. The doses of GNPs were 5 and 15 mg/kg for the single-dose treatment and 5 and 15 mg/kg (every other day, in total fourteen injections) for the multiple-dose treatments. Control group brain showed normal cells, while rat treated with a single dose (5 mg/kg body weight) exhibited reduced motor neurons and the degenerated sparse neurons (thin arrows). The single high dose treated group exhibited tumors (arrow) and cords of tumor. Rat treated with multiple dose (5 mg/kg body weight) suffered oligodendrocytoma with numerous small thin walled blood vessels (arrow). Rats treated with the multiple high dose group exhibited cryptococcosis and a flask shaped depression (arrow). Testicular tissue of the control group of rats exhibited normal histology. Rats treated with a single dose (5 mg/kg body weight) showed spermatogenesis (thin arrow), vacuolation (circle) and primary spermatids (thick arrow). The single high dose treated group showed the dilation of germinal layer (circle), degeneration of secondary spermatocytes (thick large arrow), production of primary spermatids (small arrow), and vacuolation (circle). Rats treated with the multiple low dose group showed dilation of the germinal layer (circle), the degeneration

of secondary spermatocytes (thick large arrow), the production of primary spermatids (small arrow), and the vacuolation (circle). The multiple high dose treated group showed vacuolation (circle), damaged basement membrane (B), damaged primary spermatocytes (DS shown by large arrow) and damaged sertoli (st). Control group lung showed normal cells, while rat treated with a single dose (5 mg/kg body weight) exhibited damages of vacuolation, degeneration of central vein and acute inflammation. The single high dose treated group showed damage of vacuolation, hemorrhage and hemosidophroages. Rat treated with multiple dose (5 mg/kg body weight) showed damage of vacuolation, vein and artery damages, disruption, hemorrhage and d-shaped cells structure and hemosidophroages. Rats treated with the multiple high dose group showed damage of vacuolation, vein and artery damage, hemorrhage, d-shaped cells structure, hemosidophroages and lesion.

### 6.3.7 Biomarkers of oxidative stress

The oxidative stress induced by GNPs exposures in the vital organs was evaluated to disclose the potential toxic effects. However, as shown in **Figure 6.9**, the MDA activity in the liver of rat treated with low single and multiple dose (5 mg/kg body weight of rat) remained unaffected among the treatments. Hence, there was no obvious oxidative damage observed in the liver in response to the low dose. The activities of GSH inflated after 27 days of both single and multiple doses exposures. Catalase activity (CAT) is the crucial enzyme in antioxidant defence systems which transform the species  $H_2O_2$  to water and oxygen [43]. As prepared GNPs triggered a reduction in the CAT activity in treatments whereas a notable reduction was seen at the dose of high multiple dose group. Results indicated that under stress, the CAT activity was reduced. MDA and GSH activities were assessed by the difference of optical density of the compound at 365 nm.

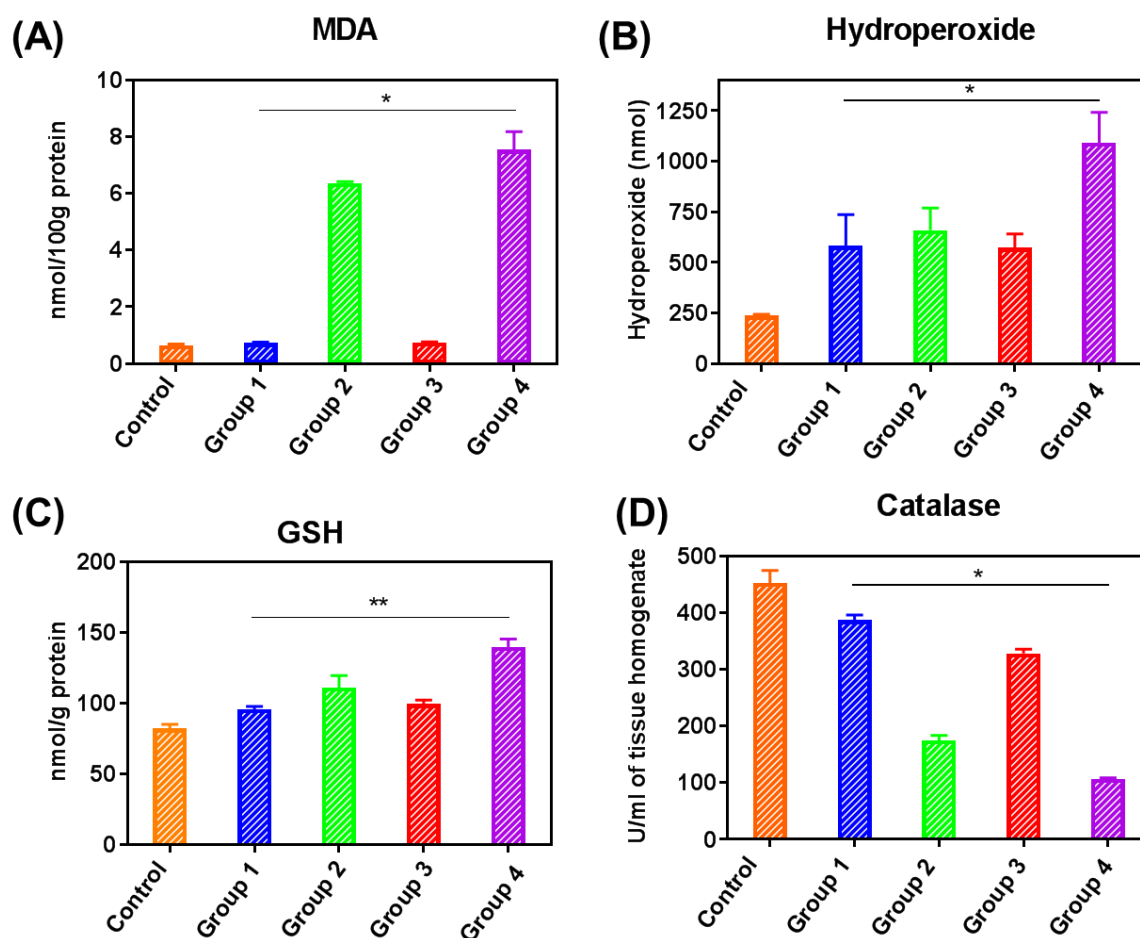


**Figure 6.9:** Biomarkers of oxidative stress results in rats after 27 days of GNPs administration. Rats (n=8 per group) were intraperitoneally injected with single doses of 5 mg/kg body weight (group 1), 15 mg/kg body weight (group 2) and multiple doses of 5 mg/kg body weight (group 3) and 15 mg/kg body weight (group 4). Values are expressed as mean  $\pm$  standard deviation, for: A) MDA, B) hydroperoxide, C) GSH, and D) catalase. Data are represented as mean  $\pm$  SD., \*p<0.05, \*\*p<0.01 vs control.

## 6.4 Discussion

Since the isolation of graphene in 2004, research has been conducted to elucidate the potential toxic effects of graphene exposure in *in vitro* and *in vivo* environments. Much research has been carried out on pristine graphene, graphene oxide, reduced graphene oxide, graphene quantum dots, and graphene nanoribbons and has showed that these single or few-layered structures are capable of inducing adverse effects in the cell lines and animal models [44]. These early investigations initiated a whole raft

of pre-clinical toxicity studies on graphene nanostructures designed to inform the potential use of these structures in clinical settings. The results of these studies suggest that graphene nanostructures such as graphene oxide and reduced graphene oxide, have the capacity to induce toxicity to mammals both as a function of their chemistry by inducing oxidative stress and lipid peroxidation, and as a result of their aggregation causing physical blockages [45]. Indeed, 3D porous graphene frameworks have shown various effects from acute lethally to sub lethal toxic effects including histological, and oxidative stress responses. However, GNPs, one of the most prominently used derivatives of graphene, e.g. used in DNA sequencing, drug delivery cargos and water treatment have not been investigated for their potential toxicity [46].

GNPs have different properties from their bulk counterparts based on their size, surface area and porosity. In terms of toxicity a size related increased surface area can lead to an enhanced dissolution of materials and thus lead to the release of potentially toxic ions and increase in toxic sites. Additionally due to small pore and sheet sizes, graphene nanopores might retain in many cells and organs compared to larger structures. Many studies have shown a size-dependent increase in toxicity as a function of particle size decrease as well as more specific size dependent generation in reactive oxygen species [47]. Although, size is an obvious initial determinant of graphene toxicity, many other factors have important contributions to make. Surface charge, stability and aggregation behaviour of graphene nanopores within various exposure environments, are determined both by the physiochemical properties of the surrounding media and the properties of GNPs themselves. A variety of parameters relating to the physiochemical features of GNPs have been shown to influence their toxicity. Their parameters are poorly understood with many studies producing contradictory results, making predicting effects difficult. Graphene nanostructures can cross either para-cellularly or transcellularly, and can travel within circulatory system and to subsequently accumulate within tissues and organs [48]. These nanostructures, depending on their composition and physiochemical properties can produce severe damages to cells by inducing oxidative stresses [49]. An understanding of the toxicity mechanism is vital to attaining a more uniform understanding and comparison of observed effects. Here we investigated *in vitro* and *in vivo* toxic effects of GNPs. Our data indicate that GNPs have acute toxicity in SKMES-1 and A549 lung cancer cells cultured *in vitro*. Due to poor solubility and superhydrophobicity, GNPs aggregate, non-



specifically bind to proteins on cell surface membrane and disintegrate membrane integrity, and thus measuring cellular membrane integrity is an effective way to detect cell toxicity [50]. However, PI enters the cell that has lost its membrane integrity, and subsequently flags the cell as late apoptotic/necrotic. This chapter shows that GNPs induce early apoptosis in all cells, however, late apoptosis is only induced at concentrations higher than 250 µg/ml, suggesting that although GNPs at lower concentrations induce upregulation of phosphatidylserine on cell surface membrane (i.e. early apoptotic event), and they do not significantly disintegrate the cell membrane. Also, none of the GNPs concentrations were found to induce necrosis in SKMES-1 cells, although concentration higher than 50µg/ml significant induced necrosis in A549 cells. This is probably due to the different proteome profile and morphologies of the two cell lines. Also, generation of reactive oxygen species in response to graphene induces oxidative stress which is considered to be the leading cause of cellular toxicity. Thus, a number of factors can be involved in the induction of cellular toxicity by GNPs and therefore, testing toxicity in animal models is comprehensive and more physiologically relevant. Hence, we investigated effect of GNPs at different concentrations in rats, particularly examining toxicity in key organs such as liver, kidney, heart, small intestine, brain and testis.

Body weight and organ indices are generally considered as significant toxicity parameters to investigate the acute exposure of foreign materials in animals [51]. In this study, the first sign of toxicity recorded for the rats given intraperitoneal injection of GNPs was an observed decrease in body weight. GNPs also induced histopathological changes in small intestine, liver and kidney. The increased levels of AST, ALT, AMP and decreased levels of creatinine observed after 27 days are indicators of toxicity that appear in the rats receiving both single and multiple doses of GNPs, compared to control groups. Severe organ damage can generally increase the activities of ALT and AST and enhanced activities of both are observed when disease processes affect liver cell integrity. Importantly, increased serum ALT activity reflects specific hepatocellular injury. Some of the histopathological alterations associated to these injuries were also evident in liver, where GNPs induced in dose- and time-dependent histological alterations of the liver tissues, including congestion, prominent vasodilatation. Histopathological changes in the liver at 27 days was higher than that

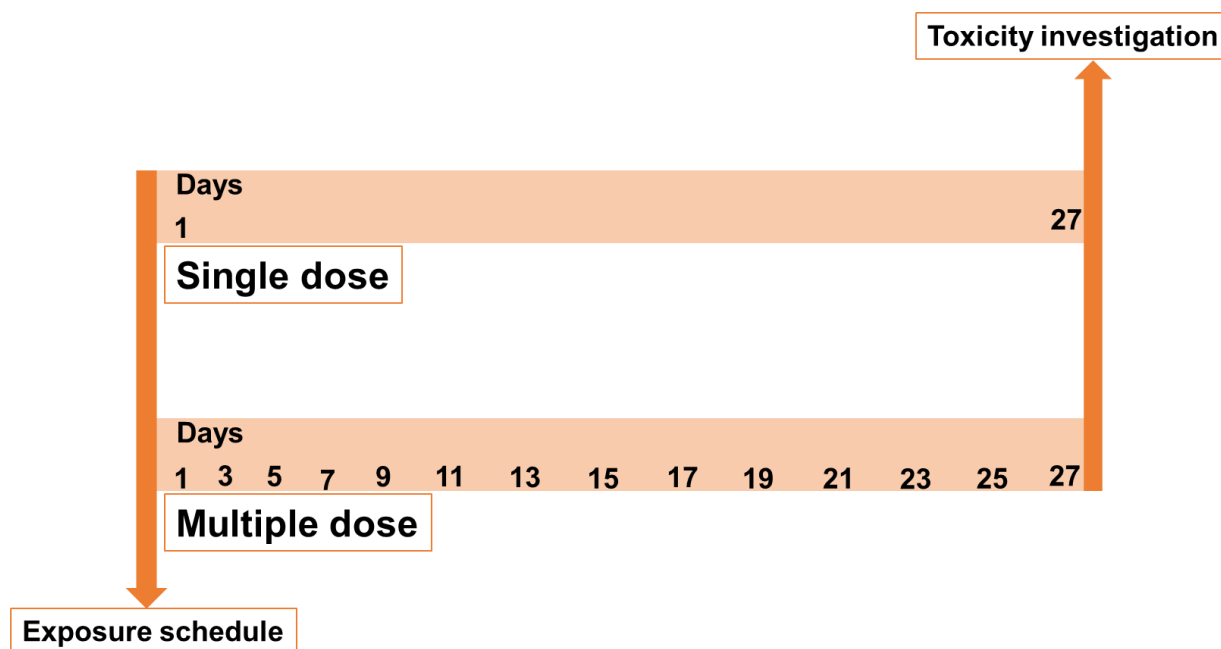
of rats sacrificed at 14 days following both single and multiple doses of GNPs. Nevertheless, GNPs treatment groups also revealed GNPs accumulation in the lung, compared to their control groups. The impact of GNPs in these organs could be due to agglomerated states of GNPs which is dependent on physiochemical synthesis process of GNPs. Furthermore, GNPs accumulated in Kupffer cells did not induce any inflammatory response. Similarly, GNPs are not involved in the inflammatory responses in lymph nodes. Minor inflammatory responses can be observed in other organs particularly in the lung which shows isolated areas with a granulomatous inflammation. Interestingly, GNPs did not induce any significant histopathological variations in the kidney compared to their control groups, which suggests their rapid clearance from the renal tissues. Our data support previous studies that have demonstrated the accumulation of graphene nanosheets in the liver, lung, kidneys, and spleen after intraperitoneal, intravenous, or dermal administration [52]. After inhalation exposure in rats, graphene has been found to accumulate in the lung, leading to phagocytosis [24]. In this chapter, the acute intraperitoneal exposure of GNPs at 15 mg/Kg for 27 days leads to significant liver damage. This was evident by the elevated ALT and ALP serum levels and pathological alterations in the liver. Increased levels of MDA, GSH and hydroperoxidase were observed in the liver of GNPs-treated rats. Interestingly, decreased levels of CAT were also found in the liver, suggesting that GNPs reduced the activity of this endogenous antioxidant enzyme, contributing to oxidative stress and hepatocyte damage. This study suggests that more studies are needed to determine the relatively long-term toxicity of porous graphene frameworks via variety of administration routes to detect any possible serious side effects from such materials.

## 6.5 Conclusions

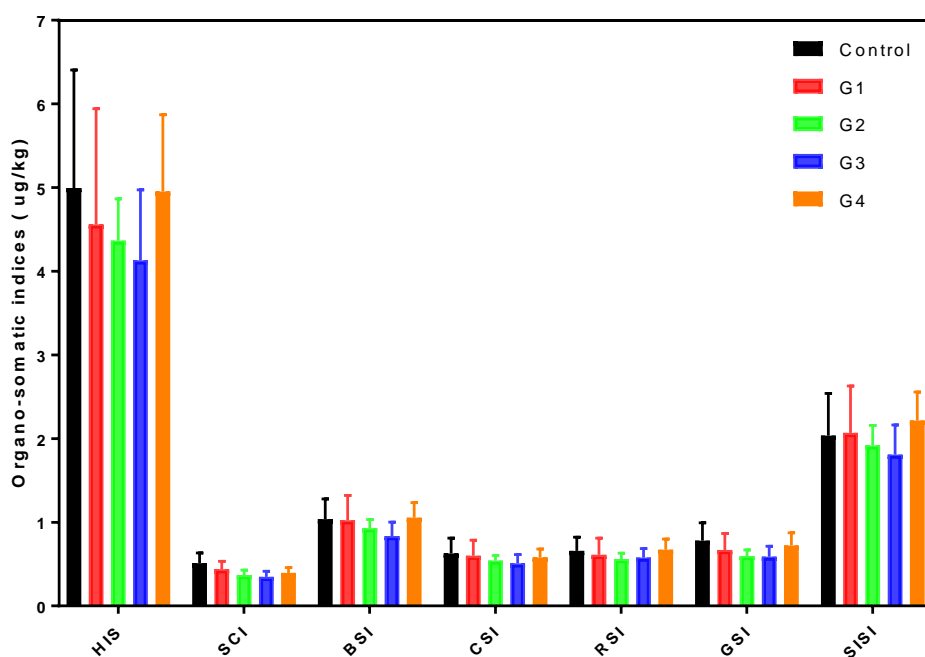
This chapter was aimed to assess the *in vitro* and *in vivo* interactions of relatively new derivative of graphene, graphene nanopores (GNPs) in mammalian systems, for the first time and to elucidate the possible mechanism of their toxicity. *In vitro* results show that GNPs induce early apoptosis in both SKMES-1 and A549 lung cancer cells, however, late apoptosis is only induced at concentrations higher than 250 µg/ml,

suggesting that, although GNPs at lower concentrations induce upregulation of phosphatidylserine on cell surface membrane (i.e. early apoptotic event), it does not significantly disintegrate the cell membrane. Subsequent, *in vivo* studies indicated damage in the main organs of rats (liver, kidney, lungs, heart, brain and testis) but the possible fast clearance of GNPs through kidney. We also showed that GNPs can induce oxidative stress in the liver. Blood markers remained within normal ranges following treatment. Our results show that changes in liver and kidney functions of these treatments can be minimal. GNPs cause sub-acute toxicity at our tested dose (5 and 15 mg/kg) to the treated rat in a period of 27 days as evidenced by blood biochemistry, liver and kidney enzymes functions, oxidative stress biomarkers and histological examinations. We for the first time investigated the *in vitro* and *in vivo* toxic effects of any porous graphene nanostructure and found the time and dose dependent toxicity of GNPs in lung cancer cell lines and rat. These findings will help elucidate how GNPs induces time-course toxicity that may facilitate the modified and biocompatible development of porous graphene-based systems for industrial applications. Therefore, long-term, high dose, and careful selection of administration route using different animal models are crucial before seeking any clinical application of this 'wonder material'.

## 6.6 Supplementary information

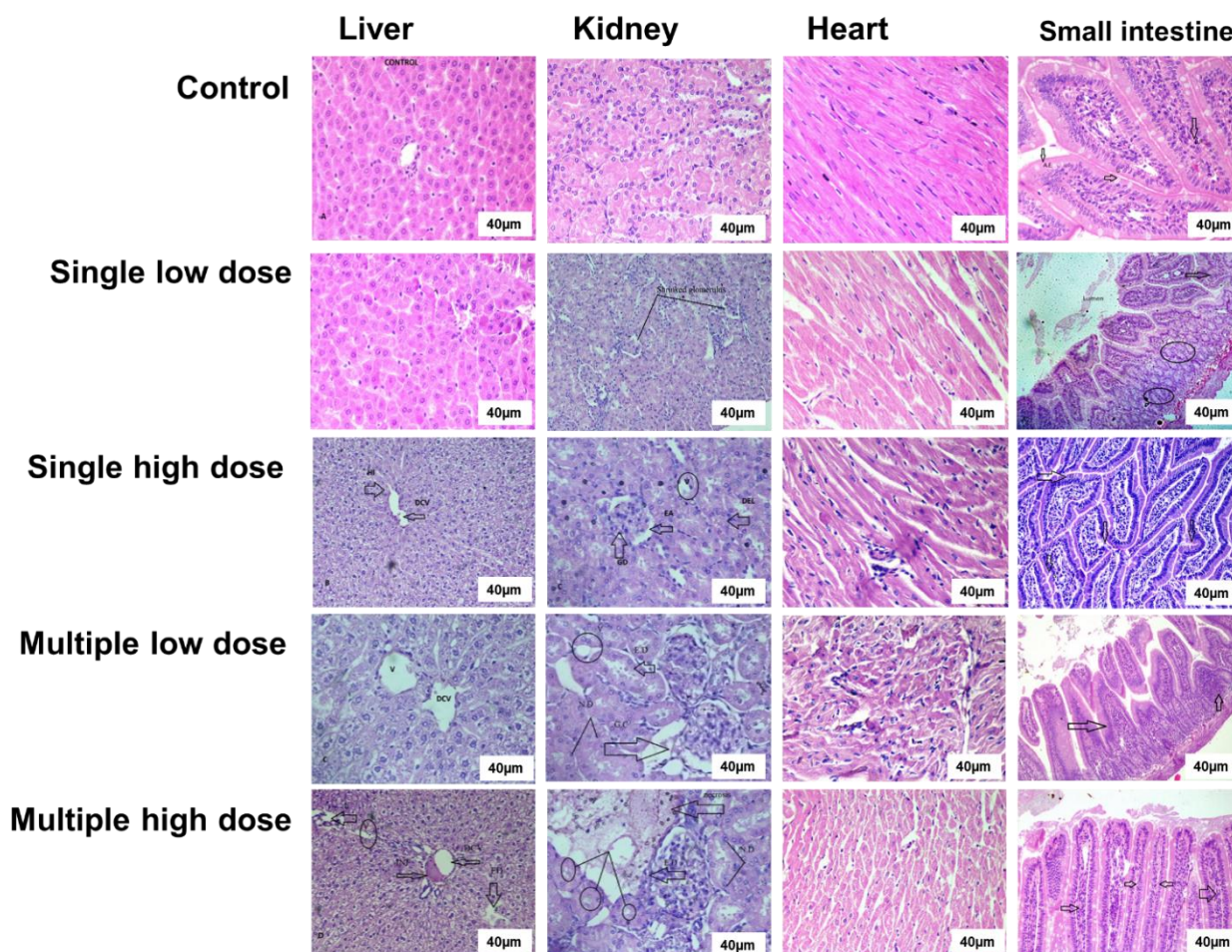


**SI Figure 6.1:** Exposure schedule of graphene nanopores (GNPs) administration in rats. Rats were intraperitoneally injected with GNPs in a period of 27 days to test at single and multiple doses of GNPs (5 and 15 mg/kg) to analyse blood biochemistry, organo-somatic index, liver and kidney enzymes functions analysis, oxidative stress biomarkers and histological examinations. All of these testing has been carried out at day 27.



**SI Figure 6.2:** Organosomatic indices of organs in different groups of rats at 14 days after intravenous administration. All treated groups showed statistically no significant differences from the control group.

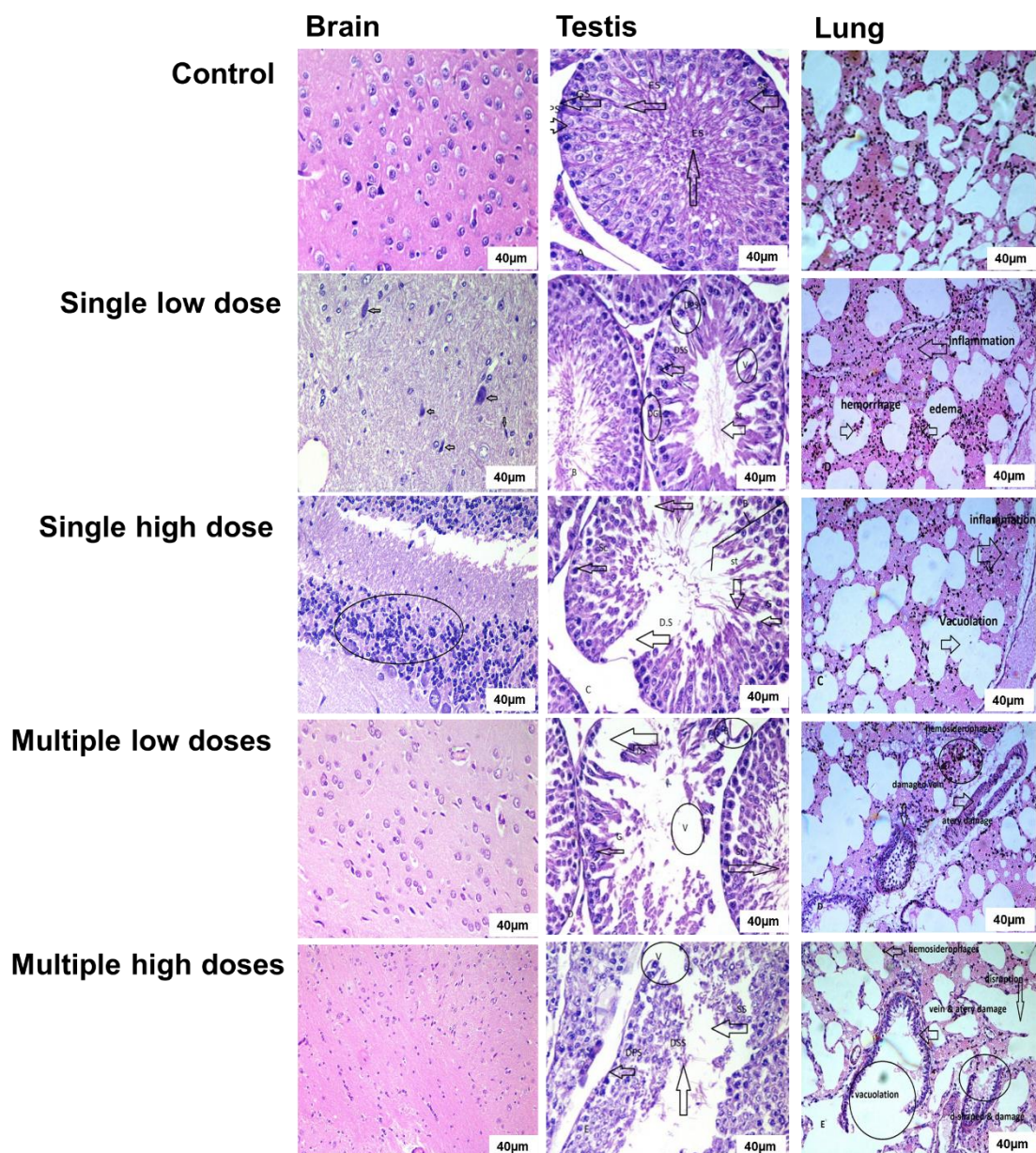
HSI = Hepato-somatic Index  
 GSI = Gonado-somatic Index  
 SSI = Spleeno-somatic Index  
 CSI = Cardio-somatic Index  
 RSI = Renato-somatic Index  
 SISI = Small Intestino somatic Index



**SI Figure 6.3:** Representative histopathological changes of the liver, kidney, heart and small intestine of the GNPs-exposed and control rat in the haematoxyline-eosin (H&E) section. The doses of GNPs were 5 and 15 mg/kg for the single-dose exposure and 5 and 15 mg/kg (every other day, in total fourteen injections) for the multiple-dose exposure. Control group liver showed normal histology while single low dose treated group showed vacuolation, dilation of central vein and haemorrhage. A group treated with single high dose showed the damage and the healing process while a group treated with multiple low dose caused liver injury alongwith vacuolation, hemorrhage, dilation and epithelial damage. Multiple high dose treated group showed considerable destruction of epithelial lining, vacuolation, karyolysis degeneration of central vein, dilation of blood sinusoid and neutrophilic and lymphocytic infiltration. Control group showed normal histology section of kidney while group treated with single low dose showed shrunken and d-shaped glomerulus. A group treated with single high dose indicated glomerulus constriction, nucleus distortion, epithelial degeneration and vacuolization. Multiple low dose group showed epithelial degeneration and d-shaped glomerulus. Multiple high dose treated group induced necrosis, nucleus distortion, epithelial lining degeneration and vacuolization. Control group of heart tissue showed normal histology of heart muscle tissues and single low dose treated group showed the chemodectoma. Single high dose group indicated toxic myocarditis. Whereas

multiple low dose group caused acute rheumatism heart, which was the collection of pleomorphic histocytes with large basophilic nuclei. Multiple high dose treated group showed reddish brown atrophy; yellowish brown pigments lipofuscin. Histology of control group of small intestine showed the normal goblet cell at epithelial of the villus, absorptive epithelial and lamina propria. Single low dose group showed the damage of sub mucosa and muscular layer (arrow) and enlargement of lacteal (circle) and single high dose group showed puncture goblet cell (  $\Rightarrow$  G) at epithelial of the villus, absorptive epithelial and lamina propria. Multiple low dose treated group indicated the destructive and distorted villus (left side arrow) and ruptured crypts and intestinal glands (right side arrow) and multiple high dose group indicated the complete shrinking of lamina propria and lacteal (small arrows) and showed mild or to some extent no shrinking of lamina propria (big arrows).





**SI Figure 6.4:** Representative histopathological changes of the brain, testis and lung of the GNPs-exposed and control rat in the haematoxyline-eosin (H&E) section after 14 days. The doses of GNPs were 5 and 15 mg/kg for the single-dose exposure and 5 and 15 mg/kg (every other day, in total seven injections) for the multiple-dose exposure. Control group showing normal histology of brain tissue of rats. Rats treated with single low dose (5mg/kg body weight) causes astrocytoma, brain shows the cells are pleomorphic, with wide variation in the size and shape of their nuclei which are also deeply basophilic. Rats treated with single high dose (15mg/kg body weight) causes hemangioblastoma; the pleomorphism of the nuclei of the closely packed large cells. Rats treated with multiple low dose (5mg/kg body weight) causes meningioma, a meningioma may invade the overlaying skull bone and cause it to thicken. The tumor cells have uniform ovoid vesicular nuclei and abundant eosinophilic cytoplasm which is vacuolated in some cell. There is no pleomorphism of nuclei and no mitosis in tis



tissue. Rats treated with multiple high dose (15mg/kg body weight) causes meningioma, which are lobulated tumors attached to the dura. A control group of testis shows the normal histology. Rats treated with single low dose showed vacuolation, less number of primary, secondary spermatocytes, damage in germinal layer. Rats treated with single high dose showed degeneration of germinal layer, damage in primary and secondary germ cells. Rats treated with multiple low dose showed that vacuolation, spermatogenesis completely stopped. Rats treated with multiple high dose showed massive damage in complete germ cell d-shaped completely destruction in spermatogenesis. Control group brain showed normal cells, while rat treated with a single dose (5 mg/kg body weight) exhibited showed damage of vacuolation, vein and artery damage, disruption, hemorrhage and edema. The single high dose treated group showed damage of vacuolation, vein and artery damage and inflammation. Rat treated with multiple dose (5 mg/kg body weight) showed damage of vacuolation, vein and artery damage, hemorrhage and hemosidophroages. Rats treated with the multiple high dose group showed damage of vacuolation, vein and artery damage, hemorrhage and d-shaped cells structure and hemosidophroages.

## References

- [1] Kostarelos, K., & Novoselov, K. S. (2014). Graphene devices for life. *Nat. Nanotechnol.* 9(10), 744-745.
- [2] Kostarelos, K., & Novoselov, K. S. (2014). Exploring the interface of graphene and biology. *Science* 344(6181), 261-263.
- [3] Ferrari, A. C., Bonaccorso, F., Fal'Ko, V., Novoselov, K. S., Roche, S., Bøggild, P., & Garrido, J. A. (2015). Science and technology roadmap for graphene, related two-dimensional crystals, and hybrid systems. *Nanoscale* 7(11), 4598-4810.
- [4] Bitounis, D., Ali-Boucetta, H., Hong, B. H., Min, D. H., & Kostarelos, K. (2013). Prospects and challenges of graphene in biomedical applications. *Adv. Mater.* 25(16), 2258-2268.
- [5] Tabish, T. A., Zhang, S., & Winyard, P. G. (2018). Developing the next generation of graphene-based platforms for cancer therapeutics: The potential role of reactive oxygen species. *Redox Biol.* 15, 34-40.
- [6] Li, N., Zhang, Q., Gao, S., Song, Q., Huang, R., Wang, L., & Cheng, G. (2013). Three-dimensional graphene foam as a biocompatible and conductive scaffold for neural stem cells. *Sci. Rep.* 3, 1604.
- [7] Schneider, G. F., & Dekker, C. (2012). DNA sequencing with nanopores. *Nat. Biotechnol.* 30(4), 326-328.
- [8] Schneider, G. F., Kowalczyk, S. W., Calado, V. E., Pandraud, G., Zandbergen, H. W., Vandersypen, L. M., & Dekker, C. (2010). DNA translocation through graphene nanopores. *Nano Lett.* 10(8), 3163-3167.

- [9] Merchant, C. A., Healy, K., Wanunu, M., Ray, V., Peterman, N., Bartel, J., & Drndic, M. (2010). DNA translocation through graphene nanopores. *Nano Lett.* 10(8), 2915-2921.
- [10] Surwade, S. P., Smirnov, S. N., Vlassiouk, I. V., Unocic, R. R., Veith, G. M., Dai, S., & Mahurin, S. M. (2015). Water desalination using nanoporous single-layer graphene. *Nat. Nanotechnol.* 10(5), 459-464.
- [11] Cohen-Tanugi, D., & Grossman, J. C. (2012). Water desalination across nanoporous graphene. *Nano Lett.* 12(7), 3602-3608.
- [12] Garaj, S., Hubbard, W., Reina, A., Kong, J., Branton, D., & Golovchenko, J. A. (2010). Graphene as a subnanometre trans-electrode membrane. *Nature*, 467(7312), 190-193.
- [13] Lin, Z., Waller, G. H., Liu, Y., Liu, M., & Wong, C. P. (2013). Simple preparation of nanoporous few-layer nitrogen-doped graphene for use as an efficient electrocatalyst for oxygen reduction and oxygen evolution reactions. *Carbon*, 53, 130-136.
- [14] Yuan, W., Chen, J., & Shi, G. (2014). Nanoporous graphene materials. *Mater. Today* 17(2), 77-85.
- [15] Reyntjens, S., & Puers, R. (2001). A review of focused ion beam applications in microsystem technology. *J Micromech. Microeng.* 11(4), 287-300.
- [16] Yuan, W., Chen, J., & Shi, G. (2014). Nanoporous graphene materials. *Mater. Today* 17(2), 77-85.
- [17] Tabish T. A., Memon F. A., Gomez D. E., Horsell D. W., & Zhang S., A facile synthesis of porous graphene for efficient water and wastewater treatment, *Sci. Rep.* 8, 1817-1833.
- [18] Oberdörster, G., Oberdörster, E., & Oberdörster, J. (2005). Nanotoxicology: an emerging discipline evolving from studies of ultrafine particles. *Environ. Heal. Perspec.* 113(7), 823-839.
- [19] Elsabahy, M., & Wooley, K. L. (2012). Design of polymeric nanoparticles for biomedical delivery applications. *Chem. Soc. Rev.* 41(7), 2545-2561.
- [20] Perreault, F., De Faria, A. F., & Elimelech, M. (2015). Environmental applications of graphene-based nanomaterials. *Chem. Soc. Rev.* 44(16), 5861-5896.
- [21] Bussy, C., Ali-Boucetta, H., & Kostarelos, K. (2012). Safety considerations for graphene: lessons learnt from carbon nanotubes. *Accounts Chem. Res.* 46(3), 692-701.
- [22] Zhang, B., Ni, H., Chen, R., Zhang, T., Li, X., Zhan, W., & Xu, Y. (2016). Cytotoxicity effects of three-dimensional graphene in NIH-3T3 fibroblasts. *RSC Adv.* 6(51), 45093-45102.
- [23] Tabish, T. A., Chabi, S., Ali, M., Xia, Y., Jabeen, F., & Zhang, S. (2017). Tracing the Bioavailability of Three-Dimensional Graphene Foam in Biological Tissues. *Materials* 10(4), 1-17.
- [24] Schinwald, A., Murphy, F. A., Jones, A., MacNee, W., & Donaldson, K. (2012). Graphene-based nanoplatelets: a new risk to the respiratory system as a consequence of their unusual aerodynamic properties. *ACS Nano* 6(1), 736-746.

- [25] Sharifi, S., Behzadi, S., Laurent, S., Forrest, M. L., Stroeve, P., & Mahmoudi, M. (2012). Toxicity of nanomaterials. *Chem. Soc. Rev.* 41(6), 2323-2343.
- [26] Mao, L., Hu, M., Pan, B., Xie, Y., & Petersen, E. J. (2015). Biodistribution and toxicity of radio-labeled few layer graphene in mice after intratracheal instillation. *Parti. Fibre Toxicol.* 13(1), 7-19.
- [27] Pelin, M., Fusco, L., León, V., Martín, C., Criado, A., Sosa, S., & Prato, M. (2017). Differential cytotoxic effects of graphene and graphene oxide on skin keratinocytes. *Sci. Rep.* 7, 40572-40584.
- [28] Wojtoniszak, M., Chen, X., Kalenczuk, R. J., Wajda, A., Łapczuk, J., Kurzewski, M., & Borowiak-Palen, E. (2012). Synthesis, dispersion, and cytocompatibility of graphene oxide and reduced graphene oxide. *Colloids Surface B* 89, 79-85.
- [29] Tabish, T. A., Pranjol, M. Z. I., Hayat, H., Rahat, A. A., Abdullah, T. M., Whatmore, J. L., & Zhang, S. (2017). In vitro toxic effects of reduced graphene oxide nanosheets on lung cancer cells. *Nanotechnology*, 28(50), 504001-504010.
- [30] Ma, Y., Shen, H., Tu, X., & Zhang, Z. (2014). Assessing in vivo toxicity of graphene materials: current methods and future outlook. *Nanomedicine*, 9(10), 1565-1580.
- [31] Rasmussen C E and Williams C K, (2006) Gaussian Processes for Machine Learning vol 1 (Cambridge: MIT Press)
- [32] Lefrere, B., Servonnet, A., Ceppa, F., Dorandeu, F., & Delacour, H. (2017). Use of IFCC guidelines to verify acetylcholinesterase reference interval in adults determined with ChE check mobile testing system. *Clinical Chem. Lab. Med.* 55(11), 268-270.
- [33] Dkhil, M. A., Zrieq, R., Al-Quraishy, S., & Abdel Moneim, A. E. (2016). Selenium Nanoparticles Attenuate Oxidative Stress and Testicular Damage in Streptozotocin-Induced Diabetic Rats. *Molecules*, 21(11), 1517-1529.
- [34] Genet S, Kale RK, Baquer NZ (2002) Alterations in antioxidant enzymes and oxidative damage in experimental diabetic rat tissues: effect of vanadate and fenugreek (*Trigonella foenum graecum*). *Mol. Cell Biochem.* 236(1–2):7–12.
- [35] Jollow, D. J., Mitchell, J. R., Zampaglione, N. A., & Gillette, J. R. (1974). Bromobenzene-induced liver necrosis. Protective role of glutathione and evidence for 3, 4-bromobenzene oxide as the hepatotoxic metabolite. *Pharmacology*, 11(3), 151-169.
- [36] Aebi, H. (1984). [13] Catalase in vitro. *Methods in enzymology*, 105, 121-126.
- [37] Patlolla, A. K., Hackett, D., & Tchounwou, P. B. (2015). Silver nanoparticle-induced oxidative stress-dependent toxicity in Sprague-Dawley rats. *Mol. Cell. Biochem.* 399(1-2), 257-268.
- [38] Ferrari, A. C., Meyer, J. C., Scardaci, V., Casiraghi, C., Lazzeri, M., Mauri, F., ... & Geim, A. K. (2006). Raman spectrum of graphene and graphene layers. *Phys. Rev. Lett.* 97(18), 187401-187405.
- [39] Kosynkin, D. V., Higginbotham, A. L., Sinitskii, A., Lomeda, J. R., Dimiev, A., Price, B. K., & Tour, J. M. (2009). Longitudinal unzipping of carbon nanotubes to form graphene nanoribbons. *Nature* 458(7240), 872-876.

- [40] Guo, H. L., Wang, X. F., Qian, Q. Y., Wang, F. B., & Xia, X. H. (2009). A green approach to the synthesis of graphene nanosheets. *ACS Nano* 3(9), 2653-2659.
- [41] Zhang, J., Li, C., Peng, Z., Liu, Y., Zhang, J., Liu, Z., & Li, D. (2017). 3D free-standing nitrogen-doped reduced graphene oxide aerogel as anode material for sodium ion batteries with enhanced sodium storage. *Sci. Rep.* 7(1), 4886-4892.
- [42] Jiang, D., Chen, L., Zhu, J., Chen, M., Shi, W., & Xie, J. (2013). Novel p–n heterojunction photocatalyst constructed by porous graphite-like C<sub>3</sub>N<sub>4</sub> and nanostructured BiOI: facile synthesis and enhanced photocatalytic activity. *Dalt. Trans.* 42(44), 15726-15734.
- [43] Zhang, F. Q., Wang, Y. S., Lou, Z. P., & Dong, J. D. (2007). Effect of heavy metal stress on antioxidative enzymes and lipid peroxidation in leaves and roots of two mangrove plant seedlings (*Kandelia candel* and *Bruguiera gymnorhiza*). *Chemosphere* 67(1), 44-50.
- [44] Volkov, Y., McIntyre, J., & Prina-Mello, A. (2017). Graphene toxicity as a double-edged sword of risks and exploitable opportunities: a critical analysis of the most recent trends and developments. *2D Materials* 4(2), 022001-022011.
- [45] Santos, C. M., Mangadlao, J., Ahmed, F., Leon, A., Advincula, R. C., & Rodrigues, D. F. (2012). Graphene nanocomposite for biomedical applications: fabrication, antimicrobial and cytotoxic investigations. *Nanotechnology* 23(39), 395101-395106.
- [46] Bussy, C., Jasim, D., Lozano, N., Terry, D., & Kostarelos, K. (2015). The current graphene safety landscape—a literature mining exercise. *Nanoscale* 7(15), 6432-6435.
- [47] Montagner, A., Bosi, S., Tenori, E., Bidussi, M., Alshatwi, A. A., Tretiach, M., & Syrgiannis, Z. (2016). Ecotoxicological effects of graphene-based materials. *2D Materials* 4(1), 012001-012010.
- [48] Bae, Y. H., & Park, K. (2011). Targeted drug delivery to tumors: myths, reality and possibility. *J. Controlled Release* 153(3), 198-216.
- [49] Muzi, L., Mouchet, F., Cadarsi, S., Janowska, I., Russier, J., Ménard-Moyon, C., & Pinelli, E. (2016). Examining the impact of multi-layer graphene using cellular and amphibian models. *2D Materials* 3(2), 025009-025018.
- [50] Liu, S., Zeng, T. H., Hofmann, M., Burcombe, E., Wei, J., Jiang, R., & Chen, Y. (2011). Antibacterial activity of graphite, graphite oxide, graphene oxide, and reduced graphene oxide: membrane and oxidative stress. *ACS nano*, 5(9), 6971-6980.
- [51] Reagan-Shaw, S., Nihal, M., & Ahmad, N. (2008). Dose translation from animal to human studies revisited. *The FASEB J.* 22(3), 659-661.
- [52] Guo, X., & Mei, N. (2014). Assessment of the toxic potential of graphene family nanomaterials. *J Food Drug Anal.* 22(1), 105-115.

## Chapter 7

# Influence of Luminescent Graphene Quantum Dots on Trypsin Activity

---

Protein-graphene interactions have the potential to play a pivotal role in the future directions of nanomedicine. These interactions lead to the diverse processes such as generation of protein coronas, nano-bio-interfaces, particle wrapping and biocatalytic processes that could determine the ultimate fate of graphene nanocomposites in biological systems. However, such interactions and their effects on the bioavailability of graphene have not yet been widely appreciated, despite the fact that this is the primary surface in contact with cells. This chapter reports on the integrative physiochemical interaction between trypsin and graphene quantum dots (GQDs) to determine their potential biological identity in enzyme engineering. This interaction was measured by a wide range of analytical methods. Definitive binding and modulation of trypsin-GQDs was demonstrated for the first time by use of vibrational spectroscopy and wetting transparency, which revealed that trypsin was absorbed on GQDs' surface through its cationic and hydrophilic residues. Our finding suggested that trypsin's active sites were stabilized and protected by the GQDs, which was likely to be responsible for the high bioavailability of GQDs in enzymes. Our work demonstrated the efficacy of GQDs as an enzyme modulator with high specificity, and their great application potential in enzyme engineering as well as enzyme-based therapies.

### 7.1 Introduction

The regulation of enzyme activity plays diverse roles in catalytic activity adjustments and modulation of cellular events such as signal transduction, DNA replication, metabolism, gene expression, immune responses, metastasis, and metabolism [1, 2]. Various types of enzyme dysfunction cause a wide variety of human diseases and disorders associated with inborn errors of metabolism and specific mutations within the enzymes [3-5]. The regulation of enzyme function provides a promising direction for

the development of therapeutic interventions [6]. Hence, regulation of enzyme activity and stability have attracted a great deal of attention. Recently, luminescent quantum dots (QDs) have emerged as a promising system for enzyme modulation [7]. These QDs have several advantages over conventional regulators: for instance, they can enter cells easily, and have unique luminescent features, surface charge, hydrophilicity, and geometry and surface properties for the binding of enzymes [8, 9]. Recent developments in graphene nanocomposites indicate promising new pathways to control the binding and activation of protein structure and cell behaviour [10]. Several derivatives of graphene, such as graphene oxide, reduced graphene oxide and pristine graphene, have been reported to show their interactions and influences on enzymes activities [10-12]. In the past few years, graphene oxide with different functionalization and modifications has been extensively investigated to understand its interaction with proteins [10-15]. The electrostatic bonding and  $\pi$ - $\pi$  stacking interactions and covalent/non-covalent bonding are considered to be the major mechanisms of graphene-protein interactions. Graphene-biomolecule interactions have been shown to underpin clinical diagnostic tools for cancer biomarker detection, which demonstrate that graphene based enzyme modulators are becoming an increasingly relevant alternative to traditional techniques [10].

Graphene quantum dots (GQDs) have widely been explored in biological applications but their interaction with enzymes has not. They are photoluminescent nanoparticles with excellent optical characteristics, unique physiochemical properties, excellent photo stability and minimal toxicity [16, 17]. These characteristic features make them an ideal system for biomedical applications, including drug delivery systems, diagnosis and therapy, bio-imaging and sensing [18]. Their interactions with biomolecules form the basis of a variety of clinical and real world applications. For this field to evolve, we need to understand the dynamic forces, surface chemistry and the biophysiochemical nature of both components that shape these interactions. Chemical or electrostatic attachment of enzymes to GQDs could enhance the rate of nano-bio-interface formation and/or cause an enzyme to denature. GQD-induced changes in biomolecular behaviour and morphology would help us to better understand the bioavailability and implications of GQDs on human health and the environment.

As a biologically relevant target enzyme we selected trypsin, which is a pancreatic serine protease involved in the digestive systems of food proteins and number of

important biological activities. Trypsin is a medium-sized globular protein with applications in, e.g., wound healing machineries, in washing agent involved in many biotechnology activities. The bonding forms a nano–bio-interface that defines the role of the QD and can induce damage in the interacting trypsin. Features of the QD that contribute to the formation of the interface in a biological environment are surface charge, electronic states, size, shape, functional groups, free radicals, surface roughness and wetting properties. Features of trypsin that may influence its interaction with the QD are size, ionic strength, temperature, surface hydrophobicity, surface charge, sequence and conformation. The trypsin-QD interactive profile may lead to dynamic changes in the living system. The interface can form when trypsin moves towards QDs. As a result, QDs can also induce potential changes to trypsin such as function and conformation as a result of surface energy release. We define how the interaction modifies the nano-bio-interface and probe the trypsin activity over a range of GQDs concentrations (25, 50, 75, 100, 125 and 150  $\mu\text{g/ml}$ ). The changes in surface and physiochemical properties as a result of enzymatic interaction of graphene are also unknown. Therefore, we utilised Raman spectroscopy, Fourier transform infrared spectroscopy (FTIR) and wettability tests to investigate the chemical, structural and surface hydrophilicity/hydrophobicity changes encountered by GQDs towards the stability of trypsin. Different levels of inherent surface oxygen containing functional groups of GQDs were found to be the reason behind the tuning of trypsin's specific activity. A fluorogenic substrate for trypsin was used to carry out control experiments of trypsin activity.

## **7.2 Materials and methods**

### **7.2.1 Synthesis and basic characterization of GQDs**

GQDs were prepared by tuning the carbonization degree of citric acid (CA) as previously reported [19]. In a typical procedure, 2 g CA was put into a 5 ml beaker and heated to 200 °C using a heating mantle. About 5 min later, the CA was liquated. Subsequently, the colour of the liquid changed from colourless to pale yellow, and then orange in 30 min, implying the formation of GQDs. The resultant orange liquid was added dropwise into 100 ml of 10 mg/ml NaOH solution, under vigorous stirring. After neutralization to pH 7.0 with NaOH, an aqueous suspension of GQD was obtained.

Transmission electron microscope (TEM), X-ray diffraction (XRD) analysis, Fourier-transform infrared (FTIR) spectra, Raman spectra and zeta potential measurements of GQD samples were carried out in the same manner as described in chapter 4 (**section 4.2.1**). The photoluminescence (PL) features were obtained by using an Edinburgh Instruments Spectrofluorometer FS5 at 350 nm of excitation wavelength. The wettability of GQDs was determined using a contact angle goniometer. A digital camera was used to record the images and the contact angle was calculated (using PolyPro). The surface of the sample was prepared for wetting by gently drop casting it onto a glass slide. The surface energy was determined by measuring the contact angle of a 10  $\mu$ l drop of diiodomethane (DIO) on the surface. The equations used in the surface energy calculations are given in the chapter 4 (**section 4.2.4**).

## 7.2.2 Trypsin proteolytic activity on substrates and GQDs

A fluorogenic substrate, Boc-Gln-Ala-Arg-AMC ( $k_{cat}/K_m=2.0 \times 10^7 \text{ M}^{-1}\text{sec}^{-1}$ ;  $K_m=6.0 \mu\text{M}$ ) at different concentrations (0, 0.1, 0.25, 0.5 and  $1 \mu\text{M}$ ) was used to examine trypsin-mediated enzymatic activity at 37 °C at various time-points (2, 5, 10, 15, 30 and 60 mins). The trypsin (trypsin-EDTA solution 1X) was purchased from sigma-Aldrich, Dorset United Kingdom and used without further purifications. The substrate stock solution was prepared in DMSO and was further diluted. The test wells within a black opaque 96 well plate (Greiner Bio-one) contained 1% trypsin and various concentrations of the substrate: controls were 1% (V/V) trypsin + distilled water and substrate (v/v) only in distilled water. Plates were read at the aforementioned time points of incubation at room temperature. Plates were read at Ex/Em: 355/450nm and the data normalised to the control (and represented as a percentage of this control). The fluorescence intensity of the substrate hydrolysis was detected kinetically using a SpectraMax plate reader. The same procedure was repeated ( $n=4$ ) with GQDs at various concentrations (0, 25, 50, 75, 100, 125 and  $150 \mu\text{g/ml}$ ). The control wells contained GQDs only (dispersed in distilled water). Statistical analysis was performed between the concentration of GQDs/substrate and trypsin by unpaired Student's t-test (using GraphPad Prism). Results were presented as mean  $\pm$  s.d. unless otherwise indicated. Values of  $p < 0.05$  were considered significant. FTIR, Raman spectroscopy, water contact angle and DIO contact angles were measured in the similar way as described in Section 7.2.1.



## 7.3 Results and discussion

### 7.3.1 Basic characterization

TEM was used to observe the microstructure of GQDs (**Supplementary Figure 7.1**). Dark spots shown in **SI Figure 7.1(A)** were GQDs which had regular diameter, circular shape and were not aggregated. TEM image shows a relatively identical size distribution between 5 and 10 nm. As shown in **Supplementary Figure 7.1(B)**, an absorption peaks centered at 1637 and 3402  $\text{cm}^{-1}$  revealed C=C and O-H bonding appeared in the FTIR spectrum. The absorptions at 1255 and 1078  $\text{cm}^{-1}$  indicated the existence of C-H and C-O, respectively. Furthermore, the GQDs exhibited stretching vibrations of C-H at 2950 and  $<1350 \text{ cm}^{-1}$ , suggesting that the GQDs contained some partially carbonized CA [20]. As shown in **Supplementary Figure 7.1(C)** the Raman spectrum of GQDs exhibited a D band at 1355  $\text{cm}^{-1}$  and a G band at 1580  $\text{cm}^{-1}$ , which are related to a series of structure defects and the in-plane bond-stretching motion of the pairs of  $\text{sp}^2$  atoms, respectively [21]. PL spectra of GQDs was almost excitation-independent, with the maximum excitation and emission wavelengths at 365 and 455 nm, respectively (**Supplementary Figure 7.1D**). PL spectra of GQDs at the excitation wavelengths of 340, 350, 360, 370 and 380 nm are shown in **Supplementary Figure 7.2**. **Figure 7.1** shows that the GQDs had good water solubility (**Figure 7.1A**) and droplets of water on the surface (**Figure 7.1C**) exhibited a typical water contact angle (WCA) of  $14^\circ$  indicating a strongly hydrophilic nature. The water wettability data were combined with wettability measurements of diiodomethane (**Figure 7.1D**) to determine the surface energy (see Supplementary Note 1 in the SI). A dispersive surface energy of 36.5 mN/m and polar surface energy of 35.7 mN/m led to a total surface energy of 72.2 mN/m.

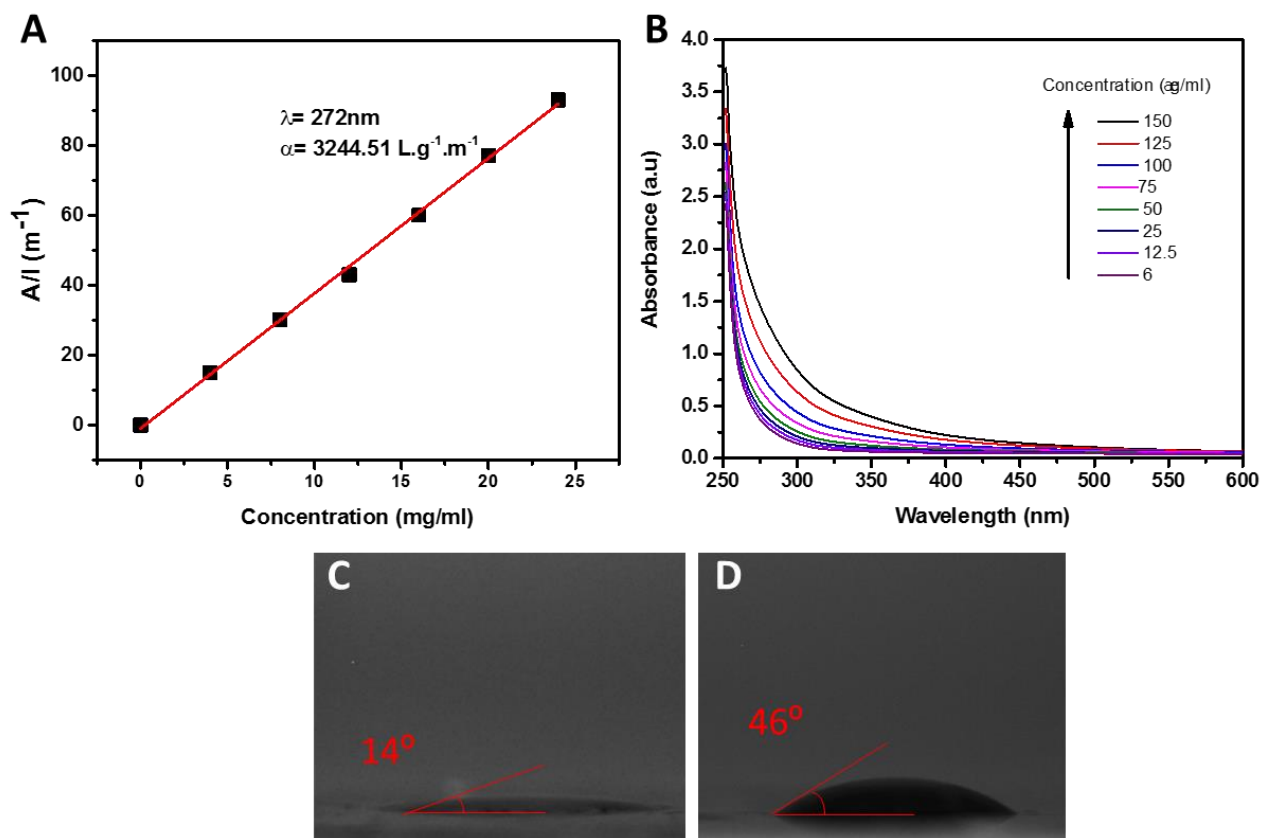


**Figure 7.1:** Water solubility, wetting transparency and surface energy of GQDs. (A) The absorbance ( $\lambda_{\text{ex}} = 275 \text{ nm}$ ) as a function of concentration. The experimental data (symbols) are well described by the Lambert-Beer Law (line), which indicates good water solubility of the prepared GQDs. (B) UV/Vis absorption spectra of GQD having concentrations of 150, 125, 100, 75, 50, 25, 12.5 and 6  $\mu\text{g/ml}$  indicate band around 260 nm. (C) Photograph of a 10  $\mu\text{l}$  drop of water on the GQDs, showing a water contact angle of  $14^\circ$ . (D) Photograph of a 10  $\mu\text{l}$  drop of diiodomethane on the GQDs with a contact angle of  $46^\circ$ .

### 7.3.2 Trypsin activity with substrate and GQDs

Fluorogenic substrate concentration and trypsin activity assays were conducted in order to determine the substrate breakdown and activity. **Figure 7.2** shows that the highest concentration of substrate (1  $\mu\text{M}$ ) had the highest enzyme activity. In trypsin-substrate interaction, highest concentration of substrate was also active over different time points (**Figure 7.2e**). **Figure 7.2e** shows the increase in enzymatic activity over the varying concentration of substrate.

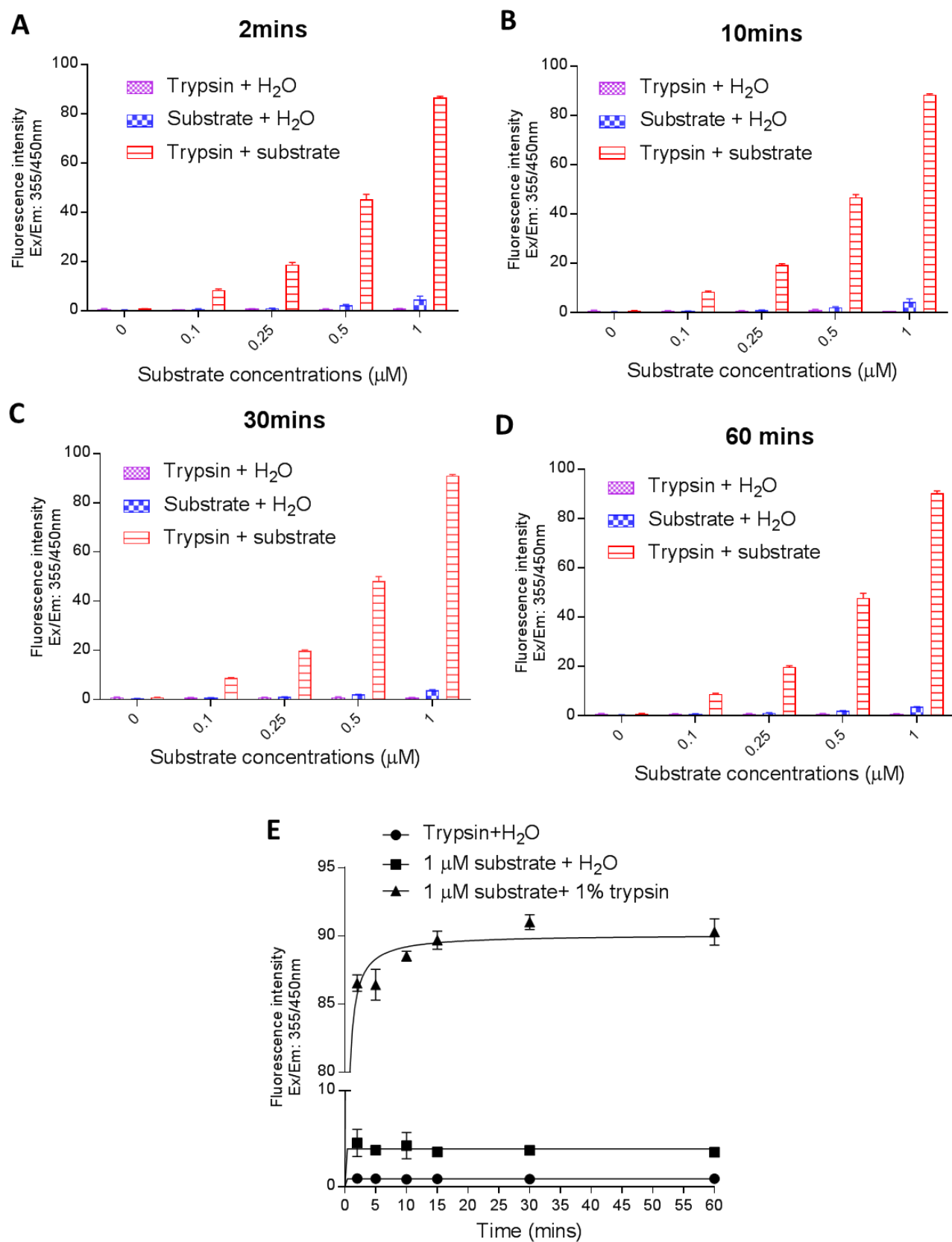


**Figure 7.2:** Fluorescence intensity of trypsin, substrate and trypsin+substrate as a function of time and substrate concentration. Fluorogenic substrate, Boc-Gln-Ala-Arg-

AMC at different concentrations (0, 0.1, 0.25, 0.5, 1  $\mu$ M) was incubated with 1 % trypsin in 96 well plates at different time-points (2, 10, 30 and 60 mins). (A-D) Different concentration of substrate over different time-points compared to only trypsin and substrate. (E) Highest concentration of substrate compared to substrate and trypsin only. Fluorescence signals were measured using plate reader at Ex/Em: 355/450nm. Control wells contained H<sub>2</sub>O+substrate and H<sub>2</sub>O+trypsin.

**Figure 7.3** shows normalized fluorescence intensities at different concentrations of GQDs (25, 50, 75, 100, 125 and 150  $\mu$ g/ml) exposed to trypsin over different time scales (0-60 mins). Trypsin was active at all the concentrations of GQDs but most active at 150  $\mu$ g/ml. As the concentration was decreased from 150 to 25  $\mu$ g/ml, the fluorescence signals reduced. This could suggest that the trypsin was adsorbed onto the surface of GQDs via physiochemical interaction and hence block the emission of fluorescence signals from the GQDs. Decreased fluorescence intensity is also relevant to increased trypsin quenching. This may be due to the fact that water molecules are surrounded between the enzyme and the hydrophilic GQDs surface, and hence, the adsorption-induced conformational reshuffles result in revealing trypsin to water molecules. Trypsin bonding speeded up with increasing the concentration of GQDs. This behaviour could indicated that both the trypsin and GQDs surface had to adapt their structures to form a stable interface. At high enzyme coverage of the GQDs surface, one could also envisage that rearrangements of protein molecules already bonded to the GQDs were required to make room for an incoming protein molecule. This crowding effect would contribute significantly to the self-fluorescence properties of GQDs.

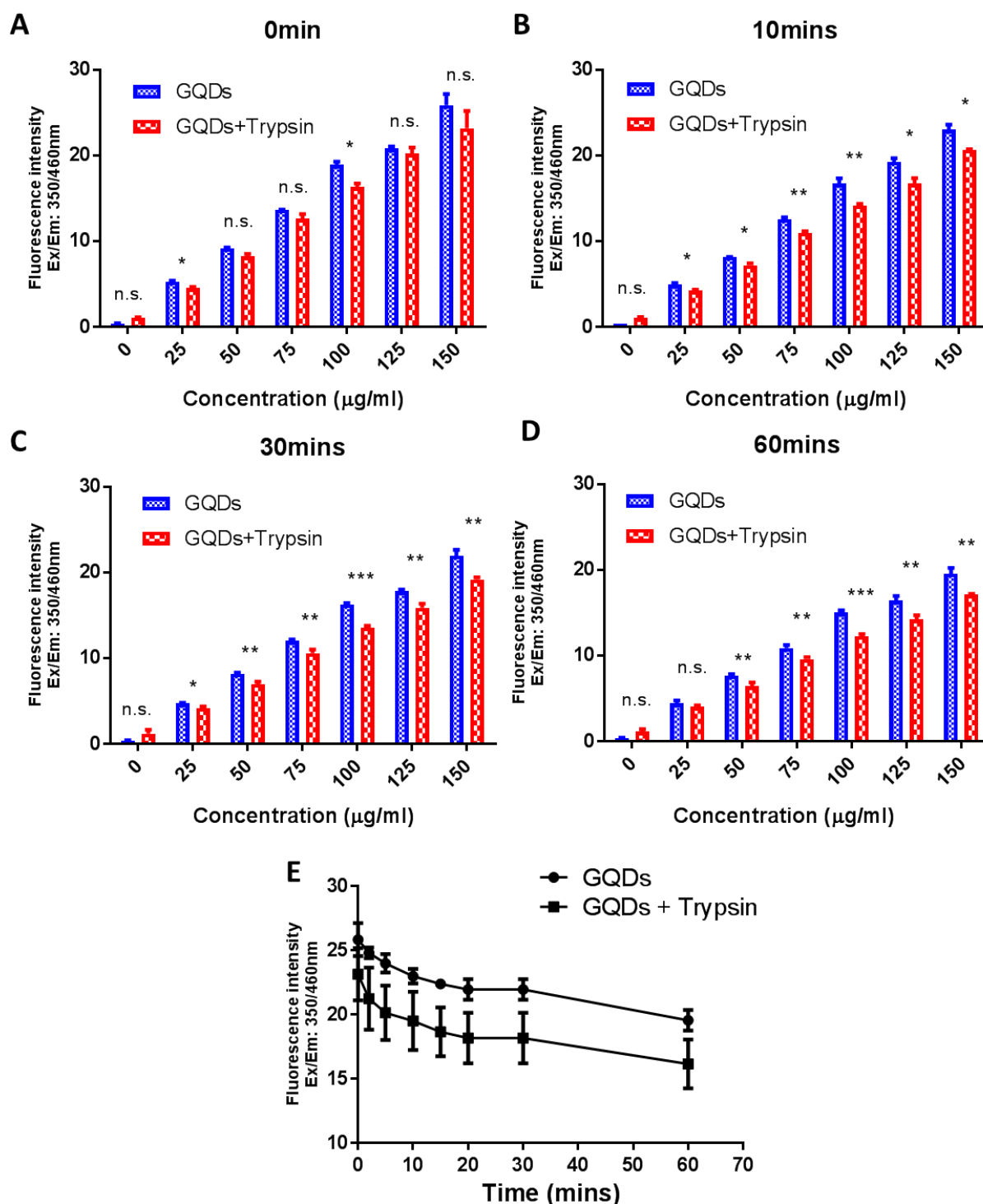


**Figure 7.3:** Effect of different concentrations of GQDs on trypsin activity. GQDs at different concentrations (150, 125, 100, 75, 50 and 25 µg/ml) were incubated with 1 % trypsin in 96 well plates at different time-points (2, 5, 10, 15, 30 and 60mins) as shown. (A-D) Comparison of different concentration of GQDs on trypsin activity over 0-60 mins. (E) Influence of the highest concentration of GQDs on trypsin activity compared to the case of GQDs only. Trypsin was highly active at 150 µg/ml concentration of GQDs and

slightly active at other concentrations. Fluorescence signals were determined using plate reader at Ex/Em: 355/460nm. Control wells contained H<sub>2</sub>O and GQDs, H<sub>2</sub>O and trypsin.

The nano-bio-interface resulting from the trypsin-GQDs interaction can be confirmed by FTIR. The changes/shifts in the functional groups of interfaces were identified by using FTIR. **Figure 7.4(a-f)** shows FTIR spectra of GQDs linked to trypsin at concentrations of 25, 50, 75, 10, 125 and 150 µg/ml of GQDs. The FTIR spectrum of 1% trypsin is given in **Supplementary Figure 7.3**. The FTIR spectra of trypsin-GQDs interfaces exhibited a variety of trypsin absorption features such as C=O ( $\nu_{\text{C=O}}$  at 1639 cm<sup>-1</sup>). In particular, the C–N stretching mode peak in 100 µg/ml concentration trypsin-linked GQDs appeared at 1366 cm<sup>-1</sup> ( $\nu_{\text{C–N}}$  receptor binding with an aromatic compound) [22]. The spectra of trypsin after interaction with 50 µg/ml GQDs (**Figure 7.4b**) showed not only the characteristic peaks of C=N at 1629 cm<sup>-1</sup>, which arose from the amino groups of trypsin and the aldehyde groups of GQDs, but also the characteristic bands of the GQDs, 1255 and 1637 cm<sup>-1</sup> (C–N, stretching vibration), and 1078 cm<sup>-1</sup> (C–O–C, antisymmetric vibrations) (**Figure 7.4c**). The peaks at 1102 cm<sup>-1</sup> assigned to the stretching vibration of O–H and C–O–C confirmed the presence of GQDs. Furthermore, the peak appeared at 1736 cm<sup>-1</sup> (150 µg/ml, the highest concentration of GQDs), can be assigned to C=O which did not appear at other concentrations except 25 µg/ml. These spectra also showed the presence of C=O ( $\nu_{\text{C=O}}$  at 1736 cm<sup>-1</sup>), C=C ( $\nu_{\text{C=C}}$  at 1629 cm<sup>-1</sup>), and at 1228 /1055 cm<sup>-1</sup> in carboxyl, epoxy and alkoxy groups, respectively (**Figure 7.4f**). These results confirmed that trypsin had been successfully covalently bonded onto the surface of GQDs.

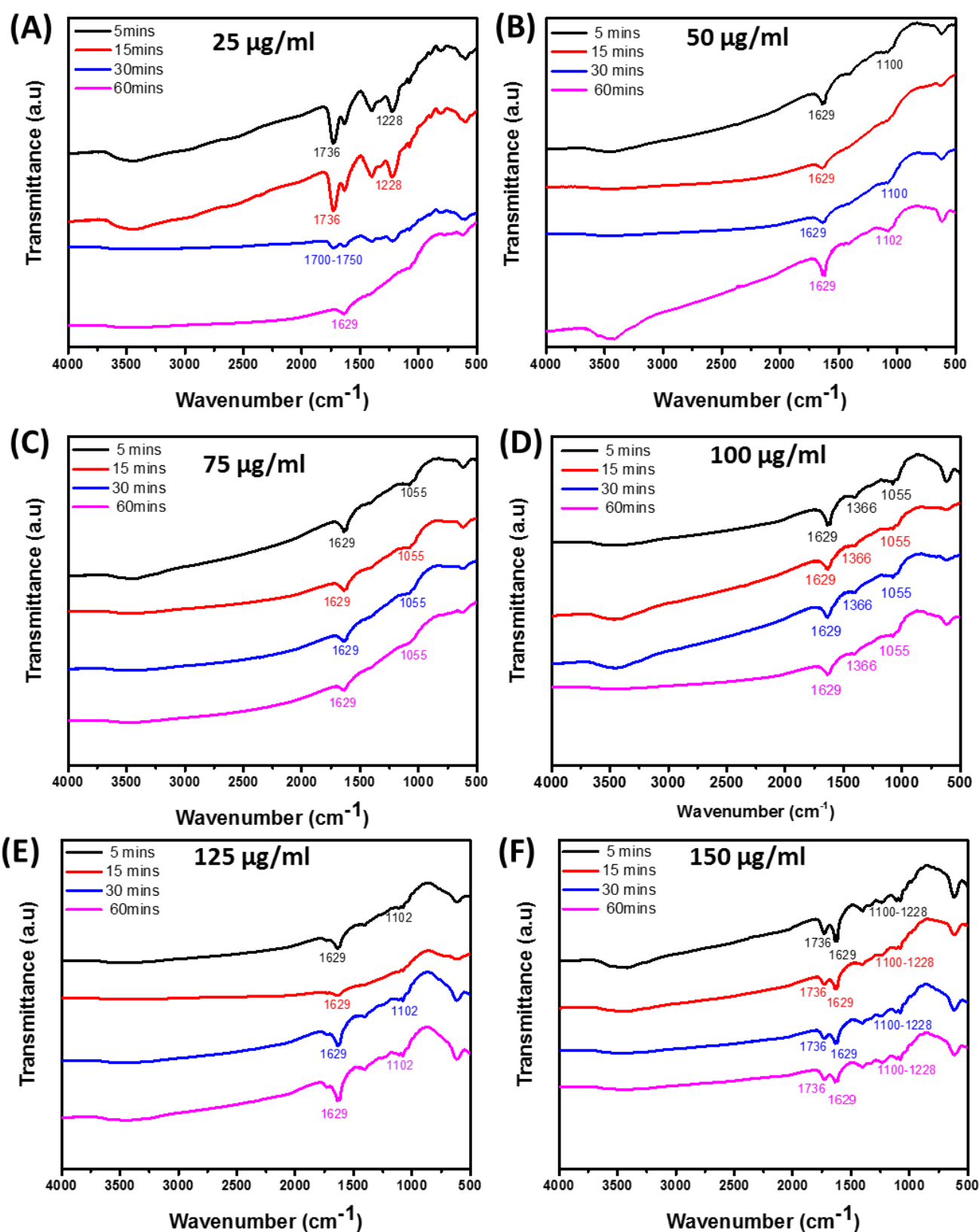


**Figure 7.4:** FT-IR spectra of trypsin-linked GQDs. (A) 25, (B) 50, (C) 75, (D) 100, (E) 125, and (F) 150  $\mu\text{g/ml}$  GQDs concentration.

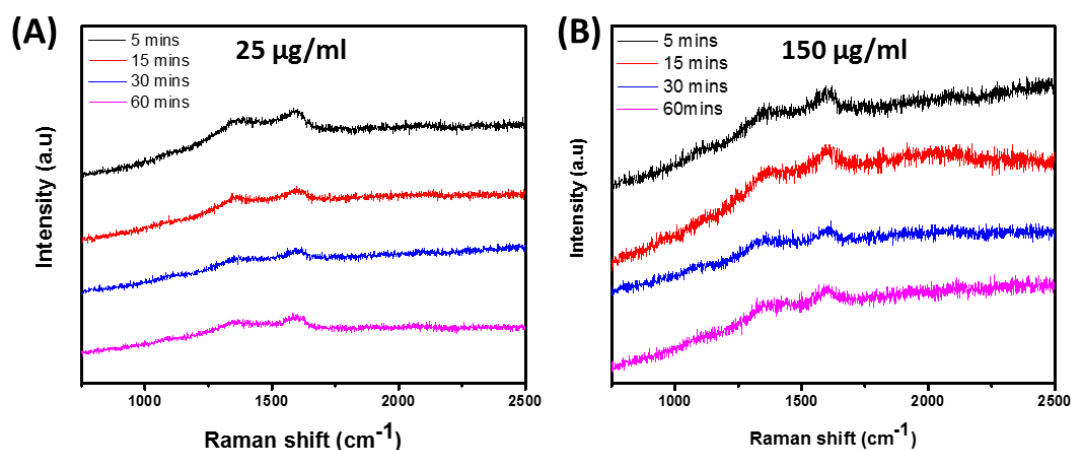


**Figure 7.5:** Raman spectra of trypsin-linked GQDs. (A) 25 and (B) 150 µg/ml.

**Figure 7.5** shows Raman spectra of trypsin-linked GQDs. In the spectra of 25 and 150 µg/ml concentrations of GQDs, the amide-I vibration at  $1625\text{ cm}^{-1}$  arose mainly from the  $\nu_{\text{C=O}}$  stretching vibration. The band in the range of  $1250\text{--}1340\text{ cm}^{-1}$  was caused by the  $\text{C-H}_3$  and  $\text{C-H}_2$  deformation vibrations from the side chains of different amino acids. The amide-III was the combination of the N-H bending and C-C stretching vibration in the region  $1200\text{--}1340\text{ cm}^{-1}$  [23, 24]. Slight shifts can be observed between the two Raman spectra of GQDs and trypsin adsorbed on GQDs. In the spectrum of GQDs (Fig S1e) there were two typical peaks appeared at ca.  $1355\text{ cm}^{-1}$  and  $1580\text{ cm}^{-1}$ . The bands at  $1600\text{--}1625\text{ cm}^{-1}$  and  $1250\text{--}1340\text{ cm}^{-1}$  can be assigned to the C=O stretching of carboxylate and  $\text{C-H}_2$  deformation vibration. After combining with GQDs, the strong amide band at  $1629\text{ cm}^{-1}$  in the FTIR spectrum of trypsin appeared and merged with the band of GQDs at  $1637\text{ cm}^{-1}$  (C=C group). Additionally, in the Raman spectra of GQDs and trypsin-GQDs, the prominent amide band at  $1580\text{ cm}^{-1}$  of GQDs was shifted to  $1625\text{ cm}^{-1}$  in trypsin-GQDs interface. Based on these facts, it could be inferred that the trypsin interacted with GQDs through its amide bonds. However, the amide bonds might not be the only force that bonded trypsin to GQDs. Trypsin has a deep bonding pocket with an aspartic acid at the bottom. This provides the space and electrostatic complementarity to specifically bond long basic side chains, such as lysine and arginine. These are positively charged amino acids and, therefore, could be conjugated to the negatively charged surface of the GQDs through the electrostatic interaction.



The functional groups of GQDs act as a passivating layer and contribute to the increased hydrophilicity. To evaluate the extent of surface modification induced by trypsin, WCA measurements were carried out on the samples before and after treatment and also at different time-points of trypsin-GQDs interaction (**Figure 6**). The trypsin displayed higher hydrolytic activity towards GQDs, as demonstrated by the decrease in the WCA values. The decrease in WCA confirmed that the reaction proceeded effectively. Upon trypsin interaction, the WCA of GQDs was moved to lower values of CAs, which indicates an increase in the surface hydrophilicity (**Figure 6a**). This effect was distinct and noticeable in the case of the higher concentrations, for which the average WCA value was decreased by about 30°. A decrease of 6.5° was recorded at 25 µg/ml. The decrease in DII contact angle (**Figure 7.6b**) revealed the surface energy profile, which is quantitatively shown in **Figure 7.7**. Overall, the results addressed a couple of key features related to the surface interaction of GQDs substrates with trypsin: (i) the effect of the functional groups existing on the surface of GQDs and trypsin; (ii) hydrophobicity driven by the adsorption of trypsin onto the GQDs surface to form a nano-bio-interface (the WCA of trypsin is shown in Supplementary Figure S4.). Furthermore, the rise in total and dispersive surface energy caused by the trypsin-GQDs interaction revealed that differences in functional group content, conformational flexibility, and shape and distinct bonding affinities released higher free surface energy. Higher concentrations of GQDs readily covered the surface of the trypsin to initiate the formation of a protein ‘soft’ corona, while lower concentrations with lower yield of functional changes took over to form a corona. Polar part of total surface energy enhanced dispersion of liquid on the surface, while the dispersion section improved the hydrophobic nature and consequently increased the CA profile (**Figure 7.7**). Low polar part (**Figure 7.7 c**) and high dispersion part (**Figure 7.7 d**) of surface energy exhibited different trends were evident because of the polar and nonpolar side-chains of trypsin facilitating conformational changes in the trypsin structure and consequently leading to high adsorption capacity of trypsin into GQDs. A recent study conducted by Gupta et al. showed the similar surface energy profile for carbon nanotubes [25].

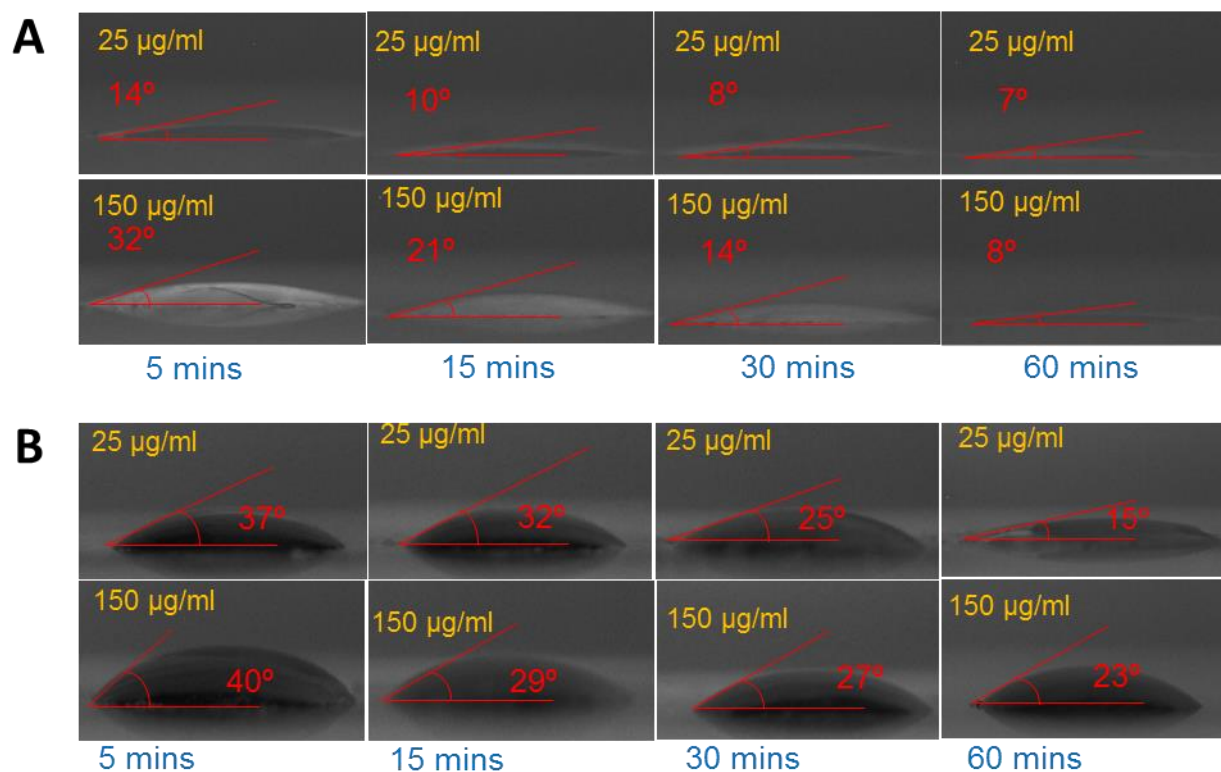


**Figure 7.6:** Contact angle profiles of trypsin-GQDs interfaces at 25 and 150  $\mu\text{g/ml}$  concentrations of GQDs. (A) water contact angle of interface from 5 to 60 mins. (B) DIIO contact angle of interface from 5 to 60 mins. DIIO contact was measured to calculate the surface energy of trypsin, GQDs and their interfaces.

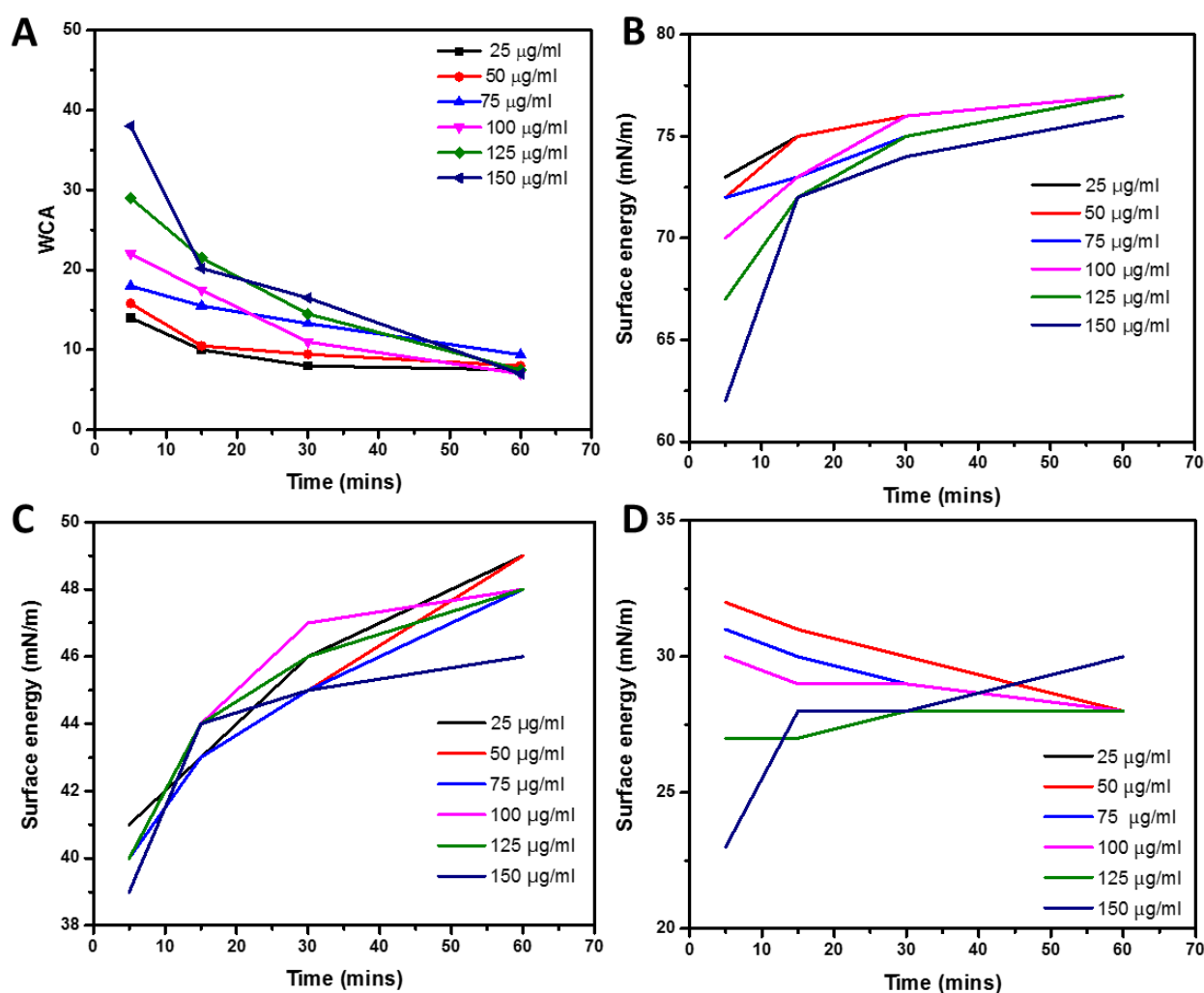


**Figure 7.7:** Water contact angle and surface energy profile of GQDs-trypsin interfaces from 0 to 60 mins. (A) water contact angle (B) total surface energy (C) dispersive surface energy and (D) polar surface energy of 25  $\mu\text{g/ml}$ , 50  $\mu\text{g/ml}$ , 75  $\mu\text{g/ml}$ , 100  $\mu\text{g/ml}$ , 125  $\mu\text{g/ml}$  and 150  $\mu\text{g/ml}$  concentration of GQDs treated with trypsin.

The entrapment of enzyme immobilization is generally carried out by ionic/covalent interaction, encapsulation and adsorption. The process of adsorption is considered to be a simple, effective and economical method for enzyme immobilization. Enzyme interactions with nanoparticles surfaces occur upon adsorption [24] and the adsorbed enzyme molecules in facilitating these interactions display the structure of the nanoparticle-enzyme interface. However, a key challenge in understanding the enzyme-nanoparticle interaction is to characterize the nano-bio-interfaces to analyse their bulk properties such as release of surface energy, functional changes in enzyme conformation, nature of bonding and change in wettability. The turn-over product of

interfacial homogeneity comes from the transfer, localization and distribution of proteins amide groups towards nanoparticles. In this regard, vibrational spectroscopic analytical methods can define the undergoing continuous changes as a result of bonding and interaction. The increased enzymatic activity of trypsin adsorbed on GQDs surface are ascribed to a definite adsorption conformation/arrangement where trypsin were adsorbed with their active site toward the surface of GQDs.

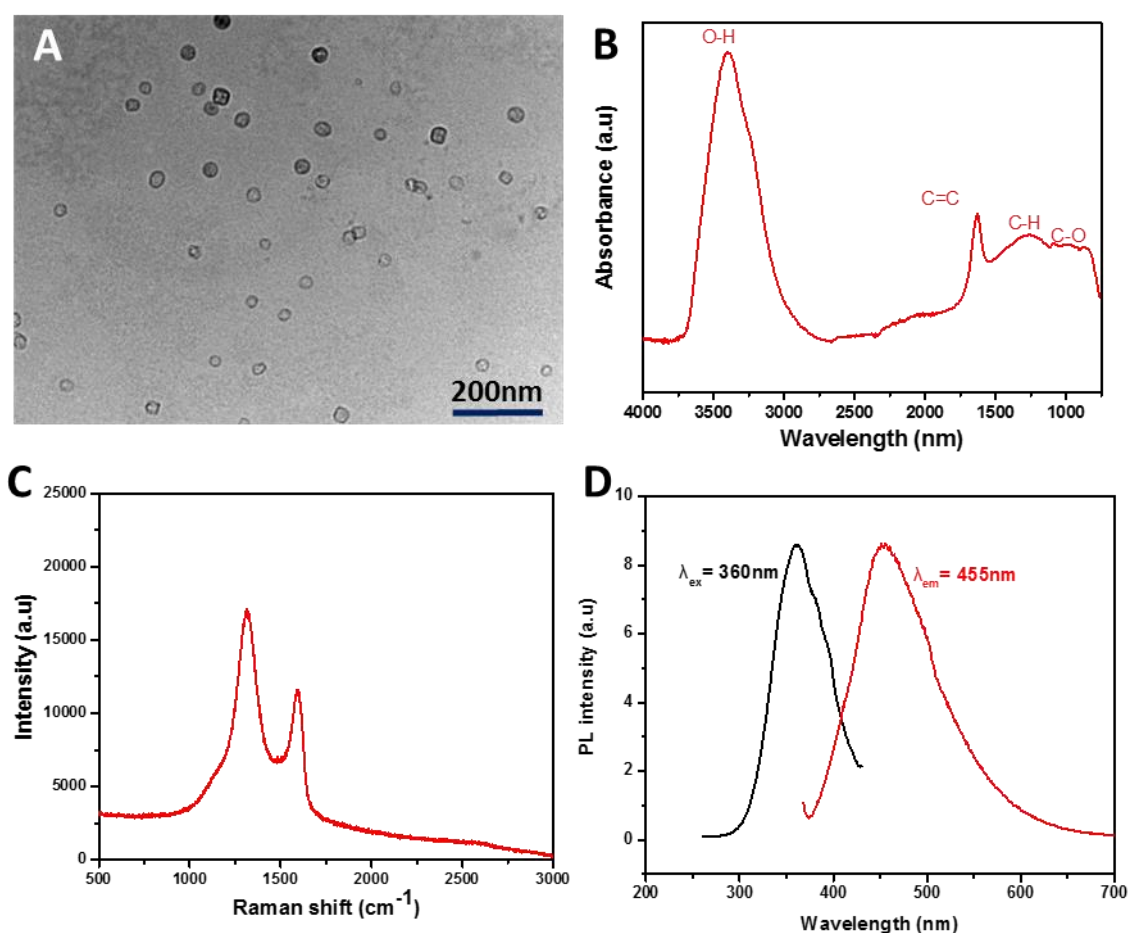
The changes identified by analytical methods in this study revealed the biosafety of GQDs. GQDs are biocompatible and more likely not to induce oxidative damage. The interaction between GQDs and trypsin is very important to reveal the influence of GQDs on enzyme activity. Vibrational spectroscopic methods and wetting transparencies have been utilised to characterize possible bonding between GQDs and trypsin. Electrostatic weak interactions may contribute to their interaction, and these weak interaction may change the conformation of trypsin which makes its activity decreased. This work highlighted that the interactions of graphene nanocomposites with enzymes were associated with their surface chemistry. The role of tunable surface chemistry of GQDs could be exploited in the modulation and regulation of essential processes involved in cell differentiation and proliferation where trypsin plays the main role to hydrolyze proteins into smaller peptides or even amino acids. Addition of GQDs to trypsin activity could specifically and selectively favour the biocatalyst reactions, such as to improve the the functional properties of trypsin such as solubility, viscosity, emulsifying features, foaming and gelling properties and to produce protein hydrolysates and bioactive peptides that are used in infant formulas. Immobilization of trypsin on GQDs demonstrated that GQDs are an ideal enzyme carrier. The high surface area of graphene allows significant loadings of trypsin, which results in a higher ionic-strength and stability of enzymes. Further work is required to investigate the stability and thermostability of other relevant enzymes and graphene nanocomposites with specifically tailored surface properties, with the aim to further the understanding of enzyme–graphene interactions at the molecular level.

## **7.4 Conclusions**

We systematically studied the interactions of GQDs with trypsin to elucidate the general fate of GQDs in biological systems. GQDs exhibited a strong bonding capacity owing to their surface charge and surface functionalities. They were highly

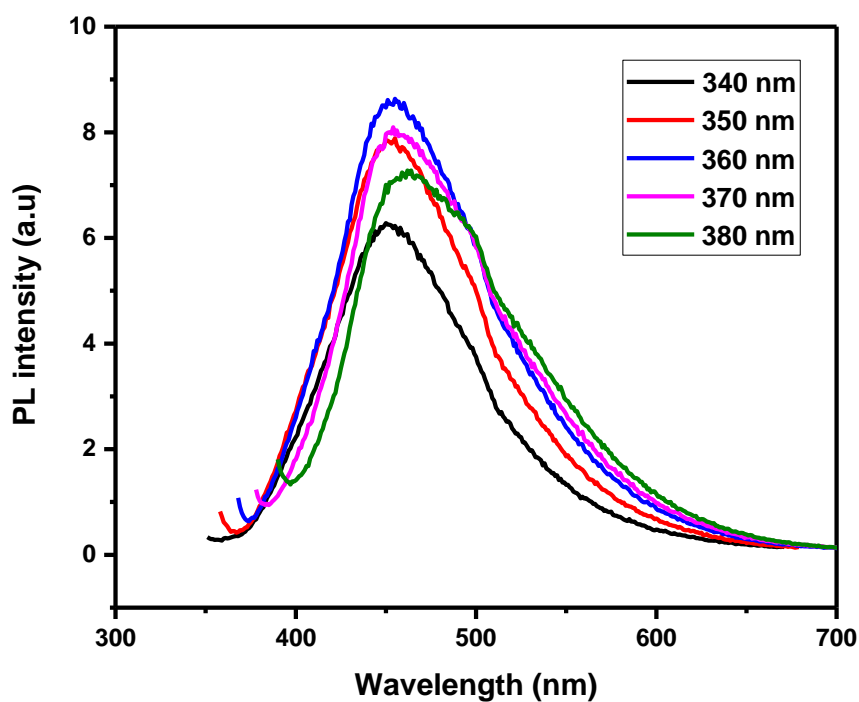
biocompatible, as demonstrated by the fact that the trypsin was adsorbed onto their surface via chemical interaction and hence blocking the emission of fluorescence signals from the graphene molecule. Furthermore, FTIR, Raman spectroscopy and wetting transparencies of GQDs-trypsin interfaces were performed to understand the role of surface chemistry in the enzyme-GQD interactions. Detailed investigation illustrated that the GQD-induced acceleration was concentration-dependent. The results indicated that GQDs are a potential substrate for efficient enzyme immobilization. The nano-bio-interface between adsorbing enzyme and GQDs surface could have potential applications in the development of biocompatible nanomaterials, nanomedicine and for enzyme separation and purification approaches.

### 7.5 Supplementary information:

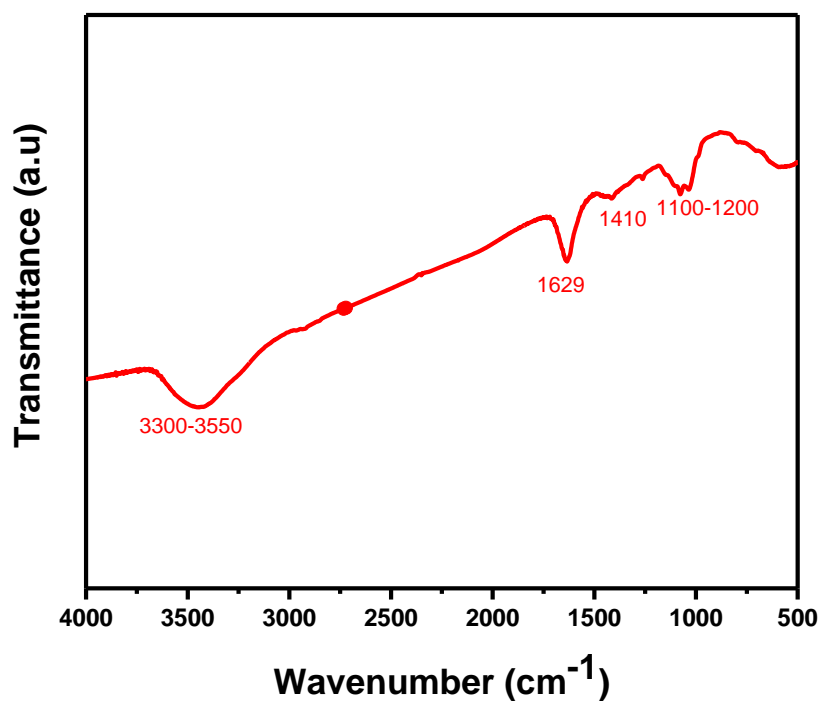


**SI Figure 7.1:** Basic characterization of GQDs. (A) Transmission electron microscopy image of GQDs showing their regular diameter, round shape and spatial distribution. Scale bar: 200 nm. (B) FTIR spectrum of the GQDs showing vibrations of different

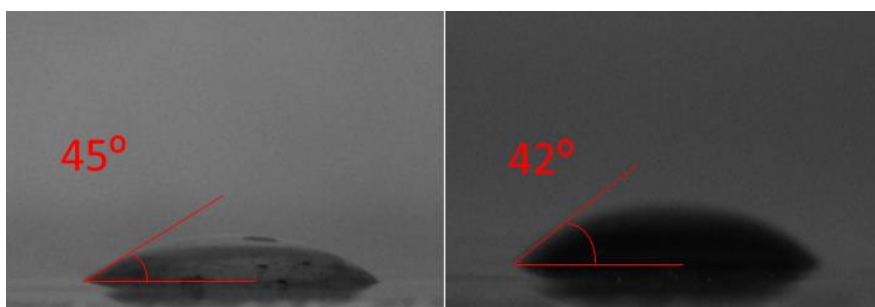
functional groups. (C) Raman spectrum of the GQDs showing the D ( $1355\text{cm}^{-1}$ ) and G peaks ( $1580\text{ cm}^{-1}$ ). (D) Photoluminescence spectrum of the GQDs.



**SI Figure 7.2:** Luminescence property and emission diagram of GQDs. PL spectra of GQDs at the excitation wavelength of 340, 350, 360, 370 and 380 nm. The strongest photoluminescence emission occurs at 460 nm.



**SI Figure 7.3: FTIR of 1% trypsin** showing vibrations of C=O at 1629 cm<sup>-1</sup>, stretching modes of O–H and C–O–C at 1100-1200 cm<sup>-1</sup>, and stretching vibration of C–H at 3300-3550 cm<sup>-1</sup> [26,27].



**SI Figure 7.4: Trypsin contact angle measurements** with water (left, 45°) and DIIO (right, 42°).

## References:

- [1] Reyes-Turcu, F. E., Ventii, K. H., & Wilkinson, K. D. (2009). Regulation and cellular roles of ubiquitin-specific deubiquitinating enzymes. *Annu. Rev. Biochem.* 78, 363-397.
- [2] Wang, M. S. (2017). Iron oxide magnetic nanoparticles combined with actein suppress non-small-cell lung cancer growth in a p53-dependent manner. *Int. J. Nanomed.*, 12, 7627-7651.
- [3] Williams, R. A., Mamotte, C. D., & Burnett, J. R. (2008). Phenylketonuria: an inborn error of phenylalanine metabolism. *Metabolism*, 12, 13-24.
- [4] DeBerardinis, R. J., & Thompson, C. B. (2012). Cellular metabolism and disease: what do metabolic outliers teach us? *Cell*, 148(6), 1132-1144.
- [5] Bruun, J., Larsen, T. B., Jølk, R. I., Eliassen, R., Holm, R., Gjetting, T., & Andresen, T. L. (2015). Investigation of enzyme-sensitive lipid nanoparticles for delivery of siRNA to blood–brain barrier and glioma cells. *Int. J. Nanomed.*, 10, 5995-6008.
- [6] Cabrera, I., Abasolo, I., Corchero, J. L., Elizondo, E., Gil, P. R., Moreno, E., & Rivas, M. (2016).  $\alpha$ -Galactosidase-A Loaded-Nanoliposomes with Enhanced Enzymatic Activity and Intracellular Penetration. *Adv. Healthc. Mater.* 5, 829-840.
- [7] Qiu, J., Zhang, R., Li, J., Sang, Y., Tang, W., Gil, P. R., & Liu, H. (2015). Fluorescent graphene quantum dots as traceable, pH-sensitive drug delivery systems. *Int. J. Nanomed.*, 10, 6709-6724.
- [8] Murthy, S. K. (2007). Nanoparticles in modern medicine: state of the art and future challenges. *Int. J. Nanomed.*, 2(2), 129-141.
- [9] Mahmoudi, M., Lynch, I., Ejtehadi, M. R., Monopoli, M. P., Bombelli, F. B., & Laurent, S. (2011). Protein–nanoparticle interactions: opportunities and challenges. *Chem. Rev.* 111(9), 5610-5637.
- [10] Piktel, E., Niemirowicz, K., Wątek, M., Wollny, T., Deptuła, P., & Bucki, R. (2016). Recent insights in nanotechnology-based drugs and formulations designed for effective anti-cancer therapy. *J. Nanobiotechnol.* 14, 39-48.
- [11] Jin, L., Yang, K., Yao, K., Zhang, S., Tao, H., Lee, S. T., & Peng, R. (2012). Functionalized graphene oxide in enzyme engineering: a selective modulator for enzyme activity and thermostability. *ACS Nano* 6(6), 4864-4875.
- [12] Hernández-Cancel, G., Suazo-Dávila, D., Ojeda-Cruzado, A. J., García-Torres, D., Cabrera, C. R., & Griebenow, K. (2015). Graphene oxide as a protein matrix: influence on protein biophysical properties. *J. nanobiotechnol.* 13, 70-92.
- [13] De, M., Chou, S. S., & Dravid, V. P. (2011). Graphene oxide as an enzyme inhibitor: modulation of activity of  $\alpha$ -chymotrypsin. *J. Amer. Chem. Soc.* 133(44), 17524-17527.
- [14] Zhu, Z., Wang, Y., Kang, Y., Zhang, H., Zhang, Z., Fei, Z., & Cao, J. (2017). Graphene oxide destabilizes myoglobin and alters its conformation. *Carbon*, 114, 449-456.
- [15] Huang, W., Hao, Q., Lei, W., Wu, L., & Xia, X. (2014). Polypyrrole-hemin-reduce graphene oxide: rapid synthesis and enhanced electrocatalytic activity towards the reduction of hydrogen peroxide. *Mater. Res. Express*, 1(4), 045601-045616.



- [16] Feng, L., Wu, L., & Qu, X. (2013). New horizons for diagnostics and therapeutic applications of graphene and graphene oxide. *Adv. Mater.*, 25, 168-186.
- [17] Habiba, K., Encarnacion-Rosado, J., Garcia-Pabon, K., Villalobos-Santos, J. C., Makarov, V. I., Avalos, J. A., ... & Morell, G. (2016). Improving cytotoxicity against cancer cells by chemo-photodynamic combined modalities using silver-graphene quantum dots nanocomposites. *Int. J. Nanomed.*, 11, 107-119.
- [18] T. A. Tabish and S. Zhang, "Graphene Quantum Dots: Syntheses, Properties, and Biological Applications", in: Saleem Hashmi (editor-in-chief). Reference Module in Materials Science and Materials Engineering, Oxford: Elsevier; 2016. pp. 1-21.
- [19] Dong, Y., Shao, J., Chen, C., Li, H., Wang, R., Chi, Y., & Chen, G. (2012). Blue luminescent graphene quantum dots and graphene oxide prepared by tuning the carbonization degree of citric acid. *Carbon* 50(12), 4738-4743.
- [20] Permatasari, A., Aimon, H., Iskandar, F., Ogi, T., & Okuyama, K. (2016). Role of C–N configurations in the photoluminescence of graphene quantum dots synthesized by a hydrothermal route. *Sci. Rep.* 6. 21042-21049.
- [21] Lin, L., & Zhang, S. (2012). Creating high yield water soluble luminescent graphene quantum dots via exfoliating and disintegrating carbon nanotubes and graphite flakes. *Chem. Commun.* 48(82), 10177-10179.
- [22] Xu, G., Chen, X., Hu, J., Yang, P., Yang, D., & Wei, L. (2012). Immobilization of trypsin on graphene oxide for microwave-assisted on-plate proteolysis combined with MALDI-MS analysis. *Analyst*, 137(12), 2757-2761.
- [23] Anderle, G., & Mendelsohn, R. (1987). Thermal denaturation of globular proteins. Fourier transform-infrared studies of the amide III spectral region. *Biophys. J.* 52(1), 69-74.
- [24] Lynch, I., & Dawson, K. A. (2008). Protein-nanoparticle interactions. *Nano Today* 3(1), 40-47.
- [25] Gupta, A., Tripathi, G., Basu, B., & Balani, K. (2012). Dependence of protein adsorption on wetting behavior of UHMWPE–HA–Al<sub>2</sub>O<sub>3</sub>–CNT hybrid biocomposites. *JOM* 64(4), 506-513.
- [26] Saha, B., Saikia, J., & Das, G. (2015). Correlating enzyme density, conformation and activity on nanoparticle surfaces in highly functional bio-nanocomposites. *Analyst* 140(2), 532-542.
- [27] Sun, J., Xu, B., Shi, Y., Yang, L., & Ma, H. L. (2017). Activity and Stability of Trypsin Immobilized onto Chitosan Magnetic Nanoparticles. *Adv. Mater. Sci. Eng.* 2017, 1-10.

## Chapter 8

# Tracing the Bioavailability of Three-Dimensional Graphene Foam in Biological Tissues

---

Graphene-based materials with a three-dimensional (3D) framework have been investigated for a variety of biomedical applications because of their 3D morphology, excellent physiochemical properties, volume stability, and their controllable degradation rate. Current knowledge on the toxicological implications and bioavailability of graphene foam (GF) has major uncertainties surrounding the fate and behavior of GF in exposed environments. Bioavailability, uptake, and cell attachment could have potential effects on the behavior of GF in living organisms, which has not yet been investigated. This chapter describes the toxicological effects on 3D GF on human glioblastoma U87 cell line and common carps. Our results showed that GF did not show any noticeable toxicity in U87 cell line and common carps, and the antioxidant enzymatic activities, biochemical and blood parameters persisted within the standard series. Histological imaging revealed that GF remained within liver and kidney macrophages for 7 days without showing obvious toxicity. Furthermore, fluorescence imaging revealed cell attachment which could play a pivotal role in regenerative medicine. An *in vitro* and *in vivo* studies also demonstrated a direct interaction between GF and biological systems, verifying its eco-friendly nature and high biocompatibility.

### 8.1 Introduction

Recent development of three-dimensional graphene foams (3D GF) provides an effective route to uniform dispersion of graphene in a composite matrix [1-3]. The effective and homogeneous distribution of graphene has been the focus of substantial investigations, with the most critical changes in morphology and porous architecture [4]. 3D GFs form a united and continuous network of graphene sheets, thus fulfilling the requirement of uniform distribution [5]. 3D GFs could be potentially used in a variety of areas, such as in energy storage [6], Li ion batteries [7], supercapacitors [8], electrochemical sensing [9], and tissue engineering (as stem cell scaffolds) [10] owing

to their high surface area (ranging from a few hundred to ca. 2000 m<sup>2</sup>/g) and hierarchical (macro/meso/micro pores) structure in combination with the intrinsic properties of two dimensional (2D) graphene. 3D GFs are economical to produce and highly scalable for commercial and industrial applications [11]. Recently, the biocompatibility of GF in living systems has become a great concern [11], although it shows great potential in stem cells and some other applications. Regardless of these applications, studies on the direct biological interaction of GF with living and aquatic system are not available. So far, only a few studies have exploited GF's porous morphology and architecture for neural and human mesenchymal stem cells, bioactive scaffolds and drug delivery system. Wang et al. used polycaprolactone-enriched GF (PCL/GF) as a promising scaffold for bone tissue engineering because of its excellent biomineralization rate and the presence of a hydroxyl group [12]. Nieto et al. fabricated a high strength biocompatible scaffold via forming a thin uniform PCL coating on GF using a dipping method [13]. Although these reports demonstrated *in vitro* applicability of GF in tissue engineering, the bioavailability and potential toxic effects of 3D GF in living models remains unclear. Assessing the potential impacts of GF on the human health is critical for the sustainable development of the graphene-industry. Bioavailability and uptake of GF to organisms are key determinants of toxicity, yet these features are useful and coherent modes of aquatic animals. This work addresses this omission by focusing on these important principles for GF.

In this chapter, GFs were probed as a biocompatible materials for cellular attachment. Common carps (*Cyprinus carpio*) are a remarkable class of species in freshwater environments and are commonly used as an *in vivo* model. Common carp is fundamentally an important aquatic species for toxicology of nanomaterials (NMs) [14]. Compared to laboratory fishes, common carps are stronger against contaminants mainly due to the variety of their interaction routes, multiple exposure routes into organisms, physicochemical characteristics of water, and diversity of aquatic environment [15]. These are generally considered the most appropriate model to evaluate the properties of toxins and their implications on a biological system. GFs were shown to maintain remarkable biocompatibility, low responsiveness to toxicity screening, and very small fluctuations in enzymatic patterns of common carp [15]. In the present work, we investigated the interactions of GF with U87 cell line and fish, to

investigate the cell attachment and its effects on antioxidant enzymatic activities (superoxide dismutase (SOD), catalase (CAT), and glutathione-S-transferase (GST)) in vital tissues such as the liver, kidney, and heart), biochemical features in the blood and histological alterations in the liver, kidney, and heart, when exposed for 7 days. These findings would help explore and develop novel and facile GF-based approaches for tissue engineering and regenerative medicine.

## **8.2 Materials and methods**

### **8.2.1. Fabrication and characterization of three-dimensional GF**

Graphene foams were prepared via a CVD route using styrene and a Ni foam template (supplied by Novamet, USA, with a 99% porosity and 1.6 mm thickness). Briefly, the Ni template was activated in a tube furnace at 1000 °C for 10 min under Ar flow of 180 mL/min and H<sub>2</sub> flow of 200 mL/min, followed by injecting the styrene carbon source into the furnace tube at a rate of 0.254 mL/h (controlled by a syringe pump (Razel Scientific Instrument, Inc. USA)), still under the same mixture gas flow for 1 h. Finally, the sample was cooled down naturally to room temperature under a reduced Ar flow of 50 mL/min. The 3D graphene networks were obtained by overnight etching of the original Ni template in 3 M HCl, and the final product was characterized by using a scanning electron microscope (SEM), transmission electron microscope (TEM), X-ray diffraction (XRD) analysis, Raman spectra of GF samples were recorded in the same manner as described in chapter 4 (**section 4.2.1**).

### **8.2.2 Cell viability and fluorescence imaging**

Human glioblastoma U87 cell line was purchased from the American Type Culture Collection (ATCC, USA) and were then cultured in Dulbecco's modified Eagle's medium (DMEM) which was supplemented with 10% fetal bovine serum (FBS) and 1% penicillin streptomycin. Cells were incubated at 37 °C under humidified air with 5% CO<sub>2</sub> for three days to achieve 80% confluence and were then trypsinized with trypsin and suspended in DMEM. Cells were also cultured on 3D GF attached at the bottom of 24-well plate for 28 days. The 3D GF sheet was 1 cm wide, 1 cm long, and 0.2 cm thick.

Alamar blue stock solution (0.1 mg/ml in phosphate buffered saline (PBS)) was diluted to 1:10 with DMEM serum-free medium. The solution was transferred to each well and then incubated under dark condition at 37 °C. The solution was dropped in 96-well plate to obtain the volume of 500 µl/well and was triplicated. Cytotoxicity was determined using AlamarBlue® cell viability assay (Thermofisher Scientific, Italy) following the guideline provided by manufacturer. Fluorescence ( $\lambda_{\text{ex}} = 540 \text{ nm}$ ;  $\lambda_{\text{em}} = 595 \text{ nm}$ ) was measured by using plate reader after 2 h of incubation at 37 °C. Experiments were repeated for 3 times and cell viability was presented as percentage of control cells. The cells were then washed with PBS and fixed with 4% paraformaldehyde for 15 min. A fluorescence microscope (Olympus MODEL BX51WIF) was employed for imaging assessment of cell attachment to 3D GF.

### 8.2.3 Procedure for *in vivo* toxicity

Common carp (*Cyprinus carpio*) ( $50 \pm 2 \text{ g}$  weight and  $29 \pm 0.9 \text{ cm}$  in length) was procured from the Fish Hatchery Satiana Road Faisalabad Punjab, Pakistan and held there for two weeks in a stock aquarium with flowing aerated dechlorinated tap water. Stock fishes were fed with commercial fish meal, and maintained in the stock aquarium at  $28 \pm 2 \text{ °C}$  and 12:12 light to dark period (after permission by the ethical committee of Government College University, Faisalabad, Pakistan). After 2 weeks acclimatization, fishes weighing around 50 g ( $n = 40$ ) were transferred into four aerated experimental glass aquaria (10 fishes/tank) and further acclimated for 48 h. They were randomly divided into four groups having the non-significant difference in weight. The first group was used as the control group (without GF treatment), and the other groups were exposed to either 5 (low dose), 10 (medium dose) or 15 (high dose)  $\text{mg}\cdot\text{L}^{-1}$  of sterile GF for 7 days. During the test period, the fishes were fed twice a day with artificial diet. Both blood and tissues (heart, kidney and liver) were collected after 24, 48, 96 h and 7 days of exposure for each treatment, randomly. Blood samples were collected through cardiac puncture by using 2 mL heparinized needle flushed with EDTA and transferred to a tube containing EDTA. The tissues were frozen at  $-4\text{°C}$  for further analysis. For histological analysis, heart, kidney and liver tissues with a diameter of 3–5 mm were fixed in sera (60% ethanol + 30% formalin + 10% acetic acid) for 3–4 h [18]. The fixed samples were

dehydrated at room temperature with ethanol and toluene series and embedded in paraffin. These paraffin embedded tissues were sectioned into thin slices of 4–5  $\mu\text{m}$  by using a microtome (SLEE Rotary Microtome CUT5062 by Nikon Instruments Europe), stretched in water and mounted on gelatin-coated marked glass slides. These sections were then stained with haematoxylin and eosin. The stained tissues were examined under an optical microscope (Nikon Eclipse 50i by Nikon Instruments Europe) fitted with a digital camera.

#### **8.2.4 Measurement of enzymatic activities and other biochemical parameters**

Liver, heart and kidney samples from the fishes were collected at different timescales after treatment, ice-covered, and kept separately at  $\sim 20^{\circ}\text{C}$ . These sections were washed with 0.15 mM KCl solution and normalized on ice with 50 mM phosphate buffer (pH 7.0). The suspension was sonicated and then centrifuged (at rate of  $10,000\times g$  at  $4^{\circ}\text{C}$  for 10 min). GST activity was measured using a GST Tag assay kit (Novagen, Germany). The reaction absorbance was monitored at 340 nm by using a UV spectrophotometer (Tecan Infinite F200, Austria). CAT activity was measured using the Abei method [19]. SOD activity was measured by using an SOD assay kit (Dojindo Laboratories, Kumamoto, Japan). Total protein concentration was calculated by using the Bradford method [20]. The biochemical parameters (total cholesterol (TCHO), alanine aminotransferase (GPT/ALT), albumin (ALB), alkaline phosphates (ALP), ammonia ( $\text{NH}_3$ ), glucose (GLU),  $\gamma$ -glutamyltransferase (GGT), glutamic oxaloacetic transaminase/aspartate aminotransferase (GOT/AST), blood urea nitrogen (BUN), creatinine (CRE), and total bilirubin (TBIL)) were examined in the current work. Statistical records were measured and analyzed using Excel software and plotted using the origin pro 2016 version. The differences between the samples and controls were assessed using one-way Anova. Data are presented as mean  $\pm$  SE ( $n = 3$ ).

### **8.3 Results and discussion**

GFs were fabricated via chemical vapor deposition (CVD) of graphene on a Ni foam template. The Ni scaffold assisted CVD process is an effective way to obtain larger

grains for better quality growth and to produce GF with a controlled morphology. The porosity, grain size, and surface smoothness of three-dimensional (3D) Ni foam with visible grain boundaries make it suitable for GF growth. As-prepared GFs were characterized by scanning electron microscopy (SEM). **Figure 8.1A, B** presented together SEM images of an as-prepared GF. SEM images revealed that the as-prepared GF had a porous interconnected 3D network. **Figure 8.1 C** showed a wrinkled piece of graphene foam. GFs were also characterized by Raman spectroscopy. As seen in **Figure 8.2a**, two strong peaks at  $1574\text{ cm}^{-1}$  (G) and at  $2720\text{ cm}^{-1}$  (2D) appeared. The position and intensity of the Raman peaks give valuable information about the defect level, the number of graphene layers or the  $\text{sp}^3$  hybrid phase. The G peak is the  $\text{E}_{2g}$  optical mode of graphite and this band arises from the C=C in-plane stretching vibration. Negligible effect of the D mode at  $\approx 1300\text{ cm}^{-1}$  indicates a perfect crystal structure of the foam, and a carbon monolithic-like structure [21–24]. As shown, the G peak (intensity:  $I_G$ ) is stronger than the 2D peak (intensity:  $I_{2D}$ ), suggesting the few layer feature of the GF ( $I_G/I_{2D} \sim 2.4$ ). In a single layered graphene,  $I_{2D}$  is greater than  $I_G$ , whereas in a bilayered graphene, both are almost equal. **Figure 8.2b** shows the XRD pattern of a powder sample prepared from as-prepared GF. The sharp peak at  $26.5^\circ$  ( $2\theta$ ) corresponds to the (002) plane of graphite, and the weak one at ca.  $55^\circ$  to the (004) plane.

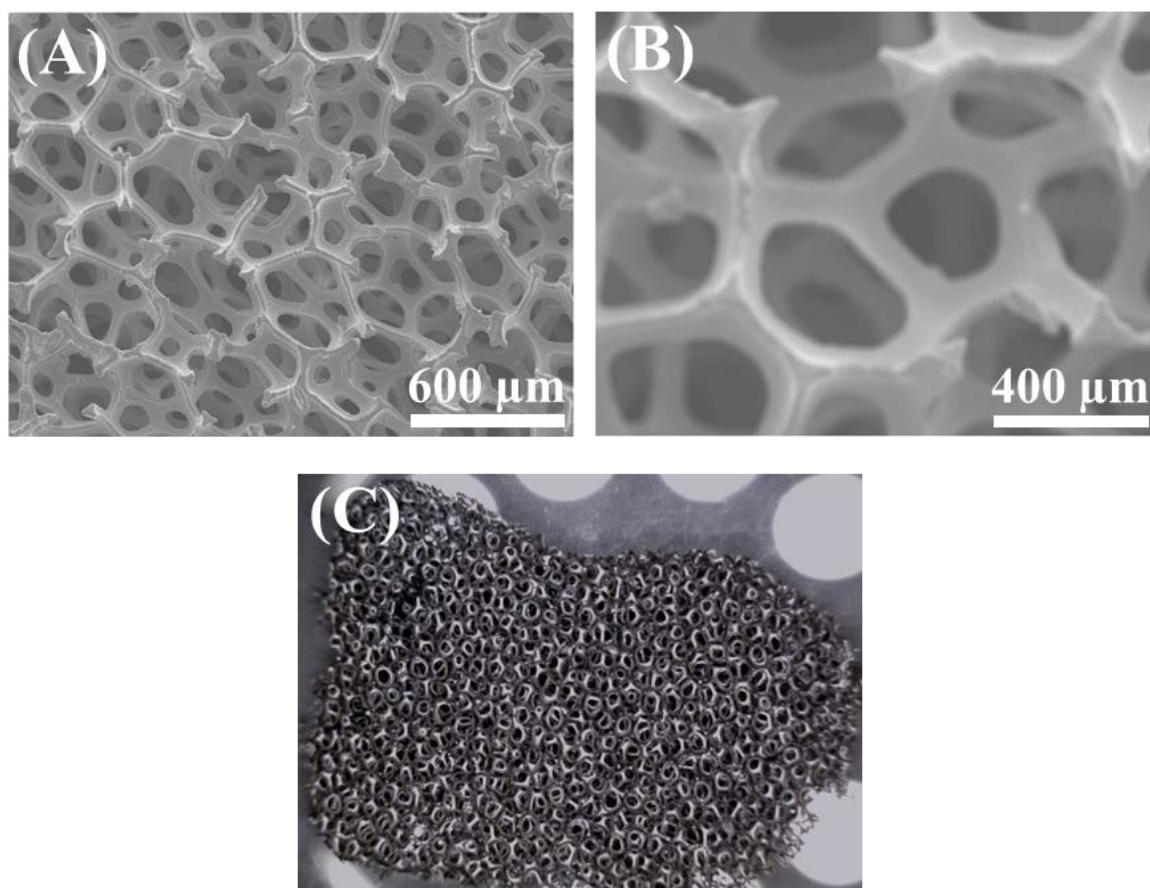


**Figure 8.1:** Basic characterization of as prepared graphene foam (GF) (A, B) Scanning electron microscopy (SEM) images of GF representing its porous network, (C) a photograph of a piece of GF.

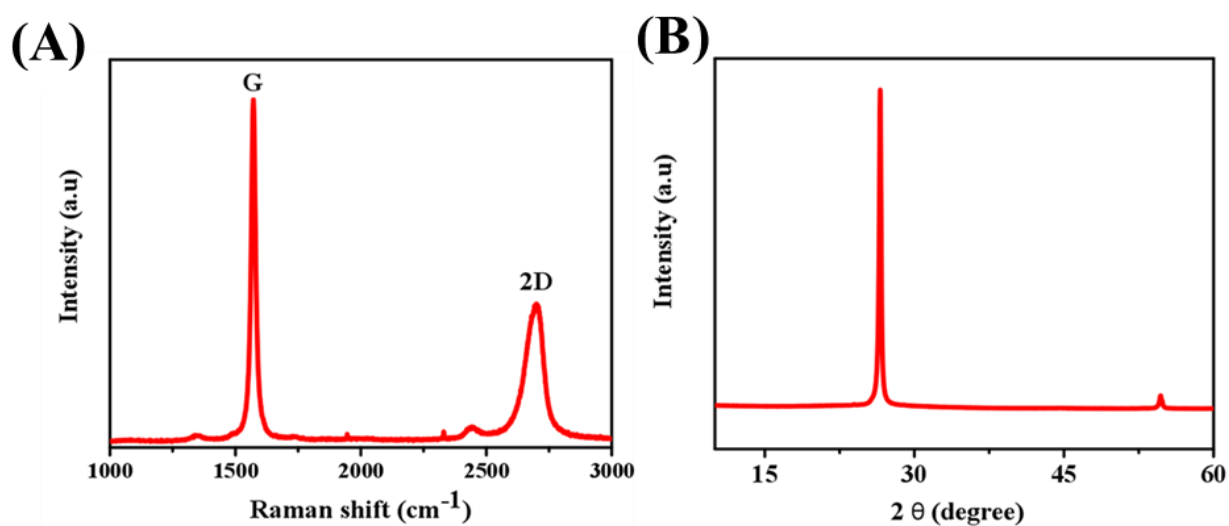


**Figure 8.2:** (A) Raman spectroscopy and (B) XRD of GF with Cu-Kα radiation ( $\lambda$  0.154 nm) operated at 40 kV and 40 mA.



As-prepared GFs were further investigated for toxicity and spontaneous morphological and histological changes in common carp. The cytotoxicity of the 3D GF has been shown by cell viability over 24 h. The cell population is significantly increasing using GF-based scaffold (**Figure 8.3 A**). Hence, GF has capability to attach and grow cells in 3D microenvironment. It is also evident that 3D GF has a good cytocompatibility in U87 cell line over a period of 28 days. Cell attachment was further investigated by SEM and fluorescence imaging which revealed cell adhesion and cell confluent on 3D GF after 21 days of seeding as shown in **Figure 8.3 (B-D)**. Cells shown in green exhibited their attachment in 3D scaffolds. Although, cell attachment was not uniform on GF, which was due to the porous network of scaffold. The results indicated cell maintenance in 3D culture, good cell viability and cell growth.

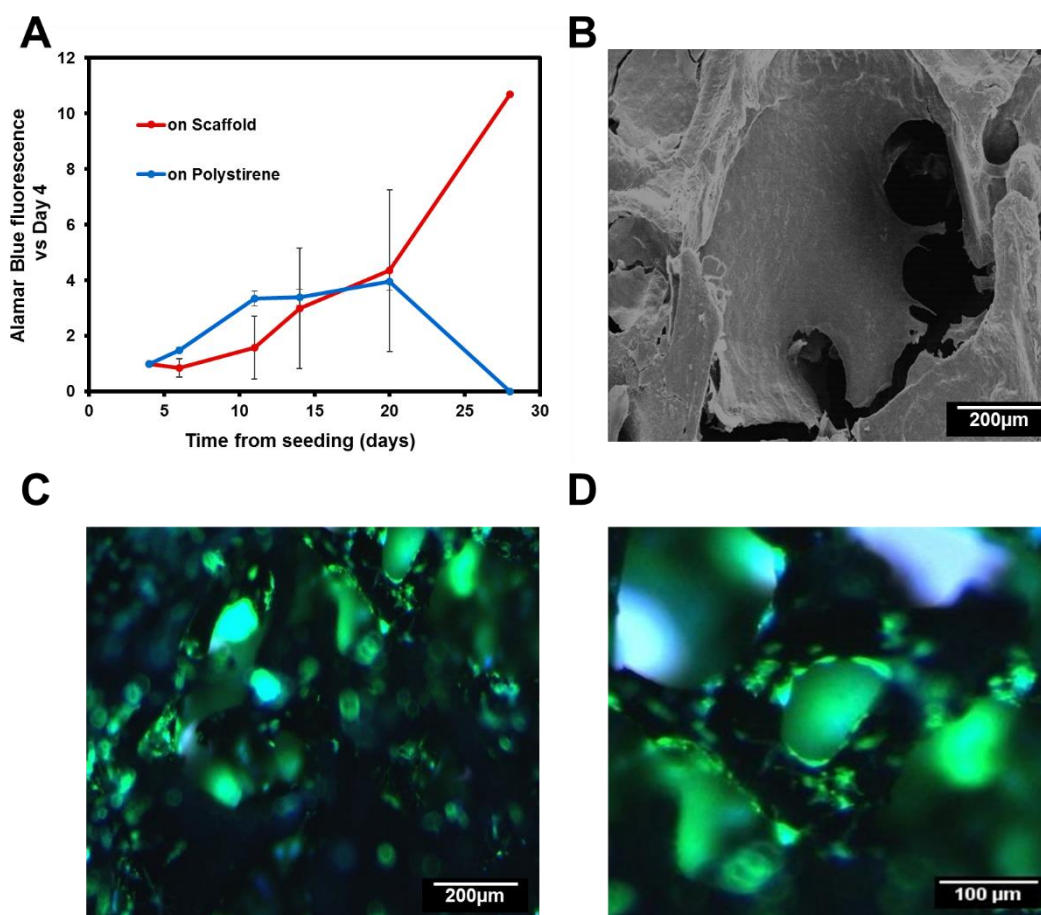


**Figure 8.3:** Cytotoxicity and fluorescence imaging of 3D graphene foam. (A) Alamar Blue™ cell viability assay test on U87 seeded on GF and polystyrene samples over 28 days, (B) SEM image of cells cultured on GF-based scaffold and (C-D) immunofluorescence image of U87 cells seeded on 3D GF for 21 days at magnifications of 200 and 100  $\mu\text{m}$ .

In this chapter, common carps were investigated for 7 days following treatments with low (5 mg/L), medium (10 mg/L) and high (15 mg/L) doses of GF. Animal models were distributed in four groups, three treated with low, medium, and high doses and one untreated as a control group,  $n = 8$  per group. The control and treated animals were then euthanized for histological analysis, biochemical parameters, enzymatic activities, and further studies. There were some additional animal models involved in this experiment, as a safe side of the experiment. Body weights were supervised and measured every 48 h and the variations were very close between treated and untreated groups (**SI Figure 8.1**), suggesting insignificant systemic effects. The eating, drinking, experimental conduct, grooming, urination, and neural changes were normal

throughout the 30 day study. No nausea was detected before and after the treatment of GF formulation.

The biochemical parameters of treated and control fishes were examined for any acute and appreciable marks of toxicity and their responses to GFs over 7 days. These features did not show any significant changes. **Figure 8.4 A, B** presents blood testing results of common carps exposed to GF in a dose-dependent manner after 7 days, including NH<sub>3</sub>: ammonia (μg/dL), GLU: glucose (mg/dL), TCHO: total cholesterol (mg/dL), ALP: alkaline phosphates (μ/L), GOT/AST: glutamic oxaloacetic transaminase/Aspartate Aminotransferase (μ/L), GPT/ALT: alanine aminotransferase (μ/L), GGT: v-glutamyltransferase (μ/L), ALB: albumin (d/dL), BUN: blood urea nitrogen (mg/dL), CRE: creatinine (mg/dL), and TBIL: total bilirubin (mg/dL). Data represent the average ± SD (*n* = 3). No statistically significant changes were observed between different groups in a dose dependent manner except the BUN. The assessment of the biochemical parameters revealed that a higher dose of GF likely had a toxic effect because of its strong hydrophobic interface with cell membranes [20], although GF exhibited an insignificant hemolytic effect (up to 75 μg/mL) and minor intensities of coagulation. However, graphene oxide (GO) and their other counterparts at 2 μg/mL provoked persistent and severe injury in lungs [25]. GF did not induce appreciable toxic effects in serum biochemical levels because of its different morphology, chemical structure, higher surface area, and porous architecture as compared to other graphene-based counterparts.

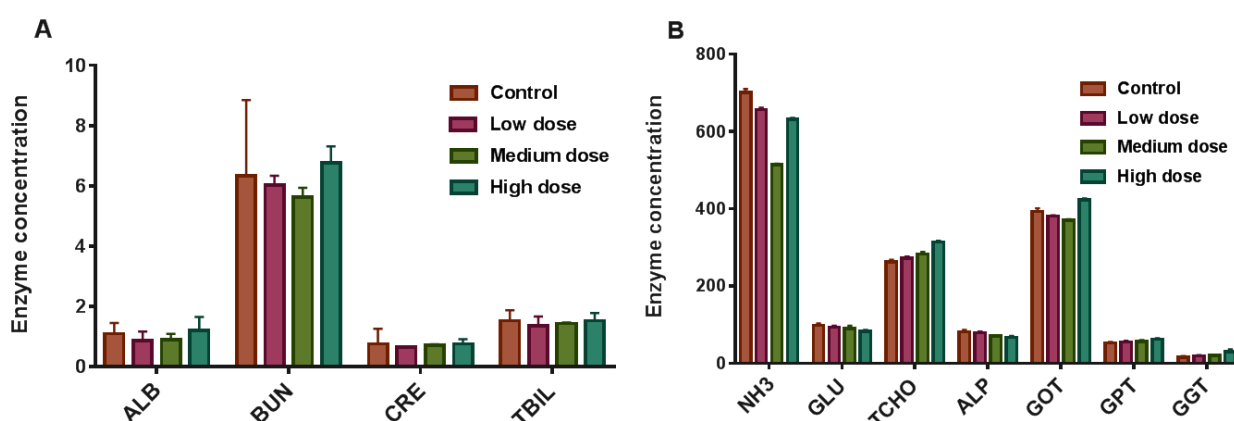


**Figure 8.4 (A,B):** Blood analysis of common carp exposed to GF as a function of dose level after 7 days. These results showed mean and standard deviations of ALB: albumin

(d/dL), BUN: blood urea nitrogen (mg/dL), CRE: creatinine (mg/dL), TBIL: total bilirubin (mg/dL) and B: NH<sub>3</sub>: ammonia (μg/dL), GLU: glucose (mg/dL), TCHO: total cholesterol (mg/dL), ALP: alkaline phosphates (μ/L), GOT/AST: glutamic oxaloacetic transaminase/Aspartate Aminotransferase (μ/L), GPT/ALT: alanine aminotransferase (μ/L) and GGT: γ-glutamyltransferase (μ/L). Data are presented as mean ± SE (*n* = 3).

Next, we studied antioxidant enzyme activities before carrying out the histological analysis on the vital organs. It should be noted that the antioxidant enzyme expressions and levels are accountable for the removal of chemically induced oxidative stresses in the immune and defensive mechanism of a living system. Antioxidants include several enzyme classes such as glutathione-S-transferase (GST), catalase (CAT), and superoxide dismutase (SOD). Irregular abnormalities in these enzymatic repairs reveal the level of oxidative damages and defense. Variations in oxidative lesions have also recently been found to be a main factor for tumor growth in the liver as a result of polluted environment [26]. Exposure of nanoparticles (NPs) induces the mitochondria damage (via) depletion of glutathione, an endogenous thiol (SH<sup>-</sup>) group, and stress proteins. These antioxidants and free radicals are mediators of tissue and cellular related injuries and diseases [27,28]. Also the increased bioaccumulation of NPs causes a steady rise of hepatic and renal antioxidant activities, affecting the mitochondrial respirational system [29]. Hence, there must be a balance between generation of oxidants and antioxidants and the level of lipid peroxidation in vital tissues of the carps. Environmental stress is also involved in the functions of aquatic organisms.

The antioxidant enzymatic activities (GST, CAT, and SOD) are presented in **Figures 5–7**. As shown, enzymatic activities generally showed variation in a dose-dependent manner. GST actions in the liver, kidney and heart were normal regardless of the GF exposure after 48 h (**Figure 8.5A**). While at a higher dose, GST declined more significantly in the kidney than in the liver and heart at 96 h, and it was prominent in the liver at a higher dose (**Figure 8.5B**). GST plays a catalytic role in conjugation of toxic and harmful metabolites. Higher levels of GST cause the activation of enzymes involved in glutathione (GSH) synthesis. GSH indicates amplified detoxification activities in the main organs of fish [30]. The decline in GST levels was an effect of the

overuse of enzymes to resist the oxidative stresses instigated by GF, eventually GSH concentration was increased in vital tissues. In this work, the common carp revealed a substantial increase in GST over a 24 h and a 7 day timescale, but oxidative stresses decreased with increasing the GST concentration. Therefore, a rise in GST concentration can also be used for the analysis of reduced GSH dependent metabolism changes involved in redox and detoxification processes.

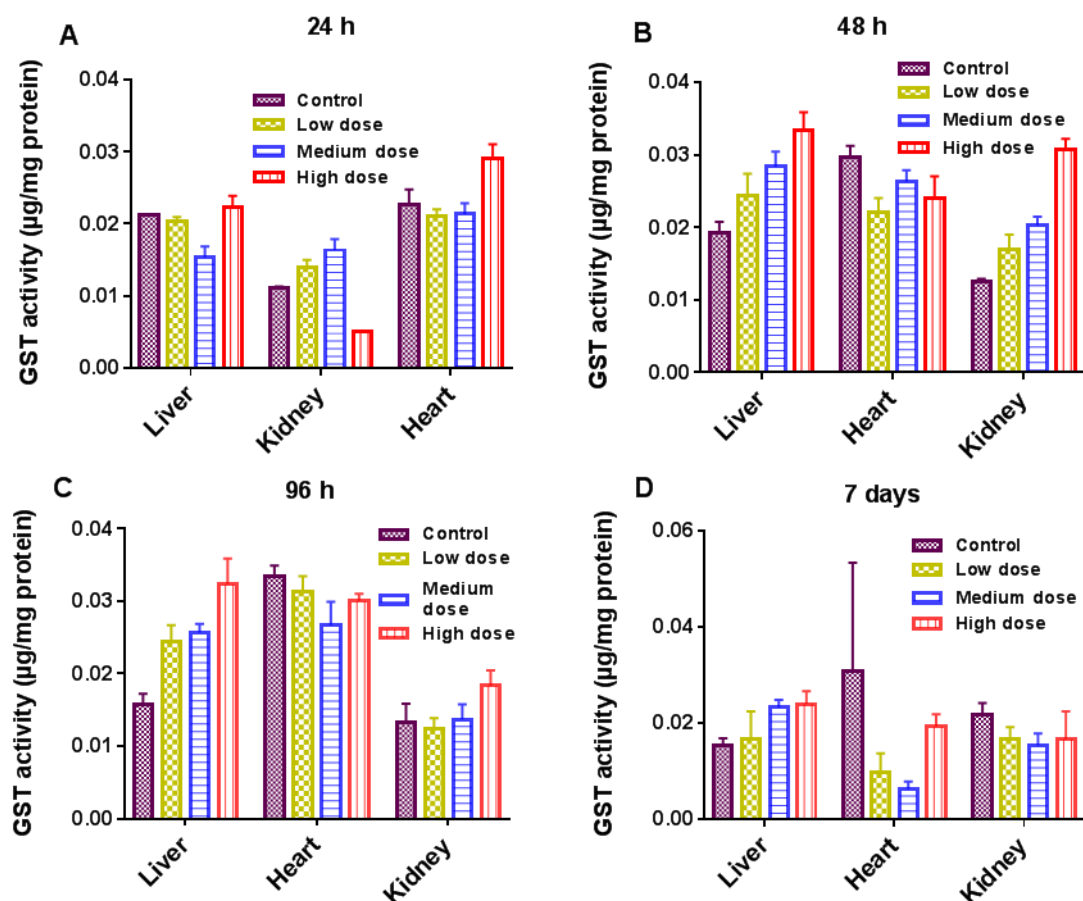


**Figure 8.5 (A–D):** Glutathione-S-transferase (GST) activity in different organs of the common carp exposed to various concentrations of GF for different times: (A) 24 h (B) 48 h (C) 96 h (D) 7 days. Data are presented as mean  $\pm$  SE ( $n = 3$ ).

The key role of CAT is to protect the cells from accumulations of  $H_2O_2$  by catalyzing its decomposition to  $H_2O$  and  $O_2$ , and to activate  $H_2O_2$  as a peroxidase [31]. Its levels were similar among the control and treated groups, except a slight change in the kidney tissues of the common carp at a 7 day timescale indicated a reduced activity to protect the cells against  $H_2O_2$  (Figure 8.6). It was reported that the enhanced SOD and CAT in the hepatocytes of the fish might be prompted by microcystin [32].

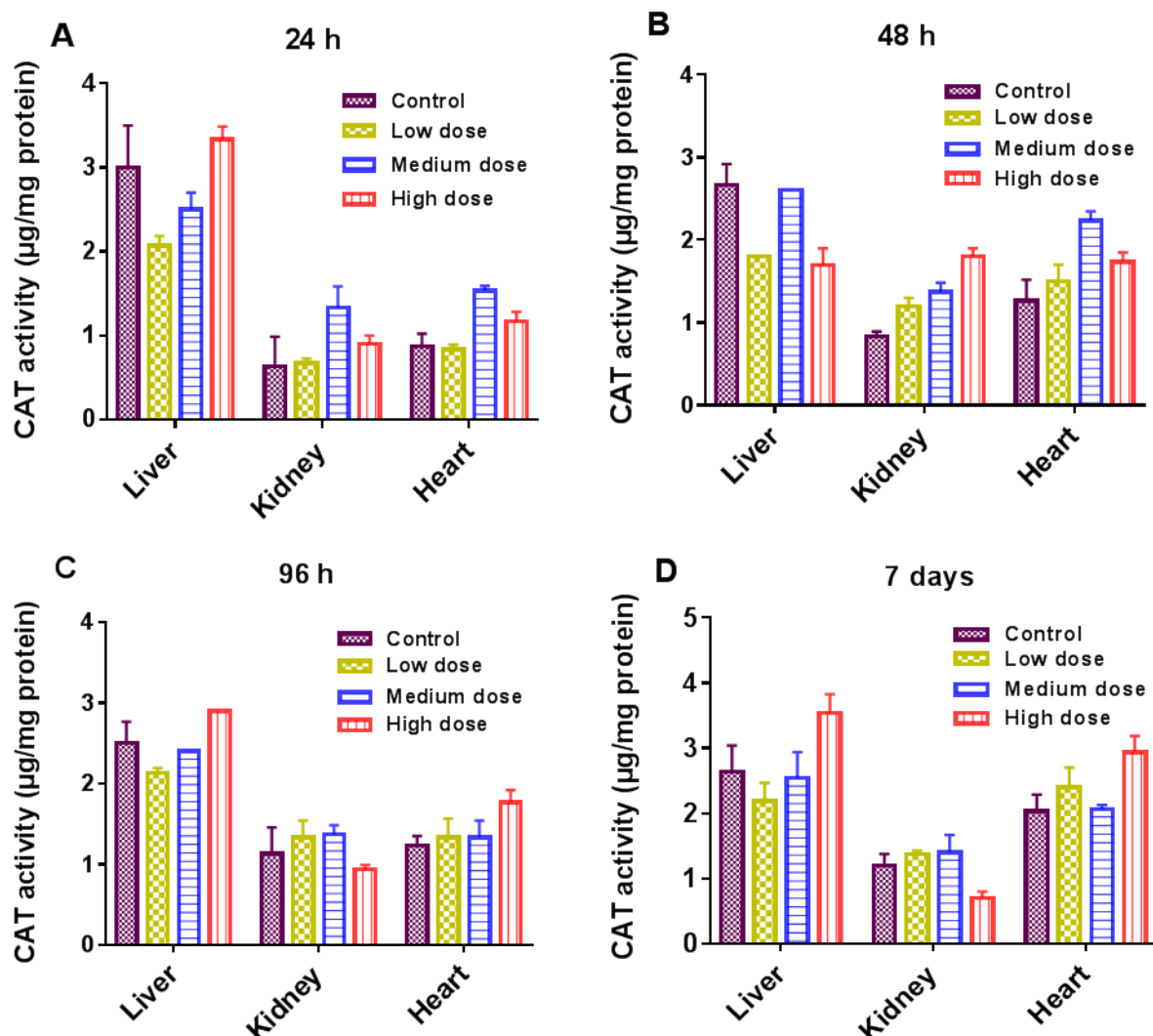


**Figure 8.6 (A–D):** catalase (CAT), activity in different organs of the common carp exposed to various concentrations of GF for different times: (A) 24 h (B) 48 h (C) 96 h (D) 7 days. Data are presented as mean  $\pm$  SE ( $n = 3$ ).

SOD levels were within the range observed for control and treated carps (**Figure 8.7**). SOD is a defensive free radical in enzyme systems that principally dismutase superoxide radicals [33]. This also reveals the greater requirement of proteins to protect the cells against the radicals. However, SOD activity was considerably lesser in the liver of fish exposed to high dose as compared to the liver in the control model (**Figure 8.7A**). The antioxidant resistance of the liver was affected at higher concentration, as evidenced by CAT and GST in the liver of carp exposed to a low

dose. Based on these results, we consider that GST and CAT were generated in appropriate capacities to neutralize the oxidative stress produced by GF. However, the relationships between GST, CAT, SOD and other antioxidant enzymes need to be established by further investigations.

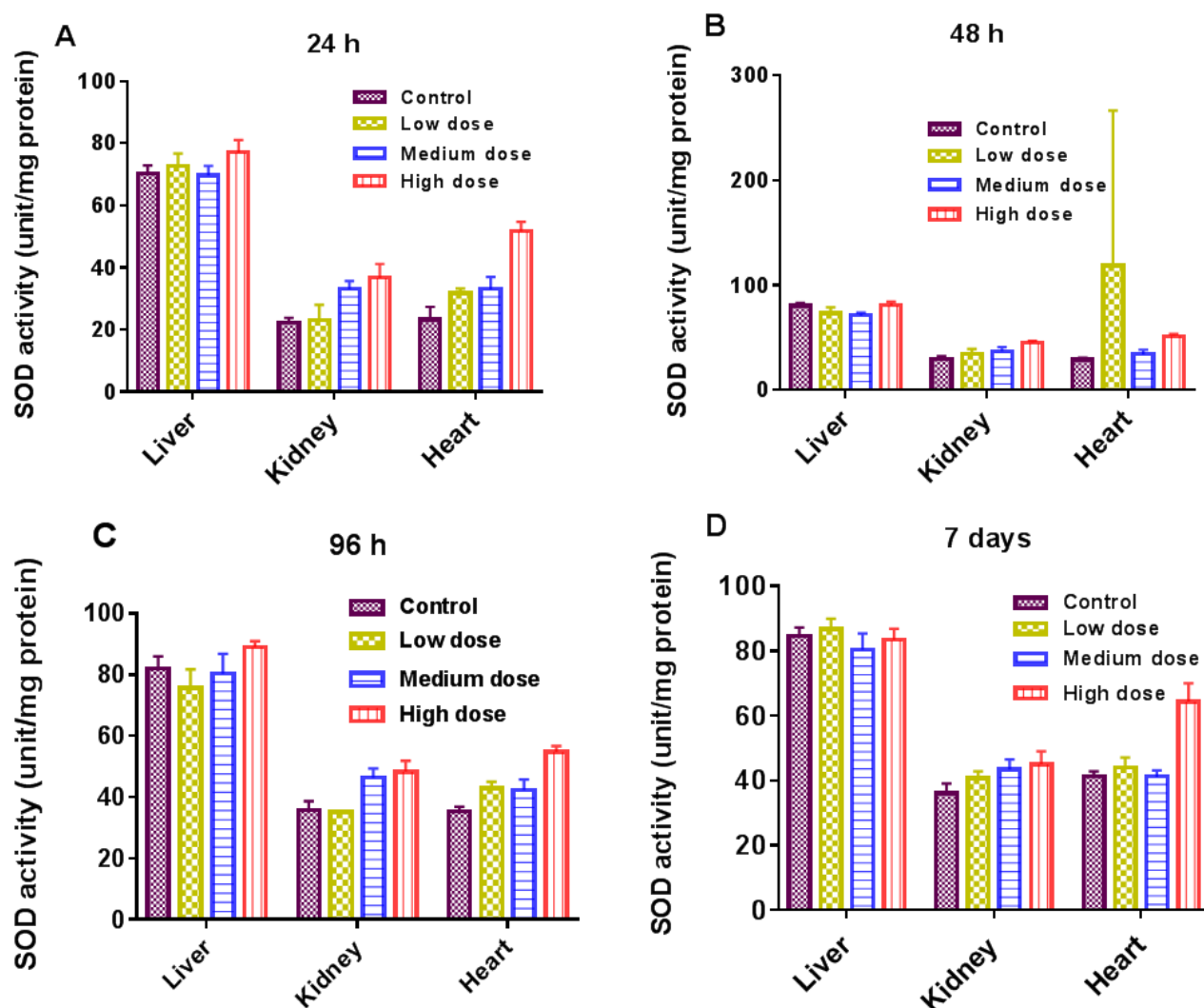


**Figure 8.7 (A–D):** Superoxide dismutase (SOD) activity in different organs of the common carp exposed to various concentrations of GF for different times: (A) 24 h (B) 48 h (C) 96 h (D) 7 days. Data are presented as mean  $\pm$  SE ( $n = 3$ ).

Histopathology of the heart, kidney, and liver of the common carp was also exploited and the results are shown in **Figure 8.8** (in a dose dependent manner). Less damage was revealed in the low dose groups, but more damage was perceived in the high dose groups. Heart tissues showed normal histology in the control and low dose treated

common carps (**Figure 8.8 A, B**), whereas brown atrophy (↗) was found in the fish heart treated with medium dose (**Figure 8.8 C**) due to the deposition of pale golden brown (↗) (lipofuscin) granules in the heart muscle fibers. Common carp treated with a high dose showed degeneration of muscle fibers (\*), vacuolization and thin fibers (**Figure 8.8 D**). Figure 8e–h show micrographs of the kidney of common carp treated with different doses of GF. Normal histology of the kidney was observed in the control and low dose treated groups (**Figure 8.8 E, F**). Atrophy and degeneration of glomerulus was found in the medium treated group (**Figure 8.8 G**). Necrosis and degeneration (ϕ) of kidney tubules was found in the high dose treated group (**Figure 8.8 H**). Normal histology of the fish liver was found in the control and low dose treated groups (**Figure 8.8 I, J**) while degeneration of hepatocytes (#), pyknosis, karyolysis, and karyorrhexis in nuclei of hepatocytes and degeneration of the central vein in the liver lobule of common carp were found in the medium dose treated groups. High levels of hepatocytes degeneration (λ), karyorrhexis, and haemorrhage were also found in liver lobule of fish treated with a high dose of GF (l). The respective histopathological alterations in these vital tissues of both control and treated groups (**Figure 8.8**) are given in **SI Table 8.1**. Histological alterations in these organs after 5 days of GF treatment are also shown in **SI Figure 8.2** and **SI Table 8.2**.



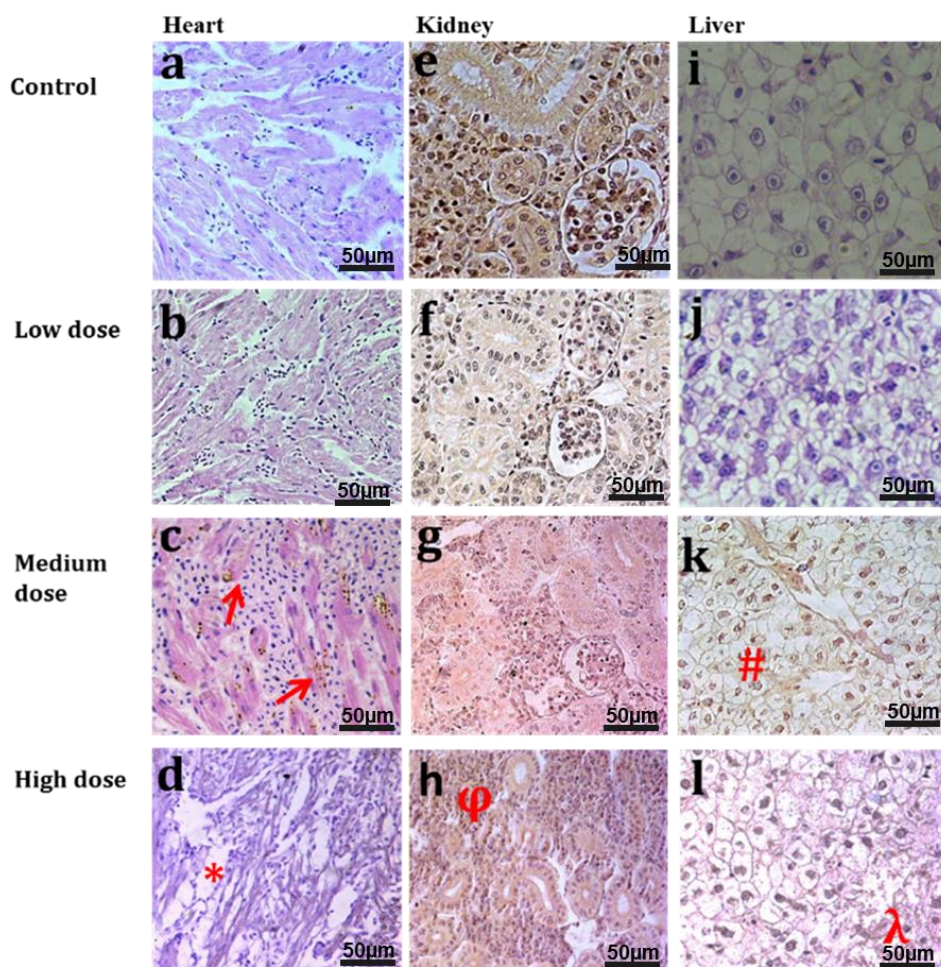


**Figure 8.8** H & E stained light micrographs of *Cyprinus carpio* (heart (a–d), kidney (e–h) and liver tissues (i–l)) treated with GF in a dose dependent manner. Figure 8a,b show normal histology of heart tissues, Figure 8c,d show histological alterations with deposition of lipofuscin granules (c) and degeneration/thinning of cardiac muscles (d) in high dose. **Figure 8e,f** show normal histology of kidney in the control and low dose treated groups while atrophy and constriction of glomerulus was found in the medium treated group (g). Necrosis and degeneration ( $\phi$ ) of kidney tubules was found in the high dose treated group (h). Normal histology of fish liver was found in the control and low dose treated groups (i,j) while degeneration of hepatocytes (#), pyknosis, karyolysis and karyorrhexis in nuclei of hepatocytes (k,l) and degeneration of central vein in liver lobule of *Cyprinus carpio* (k) were found in the medium and high dose treated groups.

No noticeable toxicity was found after breakdown of GF *in vivo* over a timescale of 7 days. However, the biodistribution and toxicokinetics in the cells and animal model investigation revealed remarkable biocompatibility with GF, which could offer a new avenue for potential real-world applications of GF. Common carp treated with a high dose of GF survived without any sign of toxicity. The enzymatic and anti-oxidant activities were used to define the ultimate fate of GF in living systems. All results from this work suggested that as-prepared GF had excellent biocompatibility on the timescale investigated. These could unveil the potential risk associated with their bioaccumulation. The relative infancy of NMs begs for animal model investigations to shed light on *in vivo* interactions of NMs before translation to humans. Importantly, it is necessary to assess long term toxicity in other animal models to better understand the mechanism of toxicity and compatibility of such materials before clinical applicability. Although such toxicological investigations indicated the less toxic effects in such animal models and were useful for research, it is really hard to relate these responses and effects to those in humans. A cross-species comparative approach can significantly improve the prediction of human responses to practical and realistic applications. However, long term toxicology studies are needed to using such materials in clinical settings.

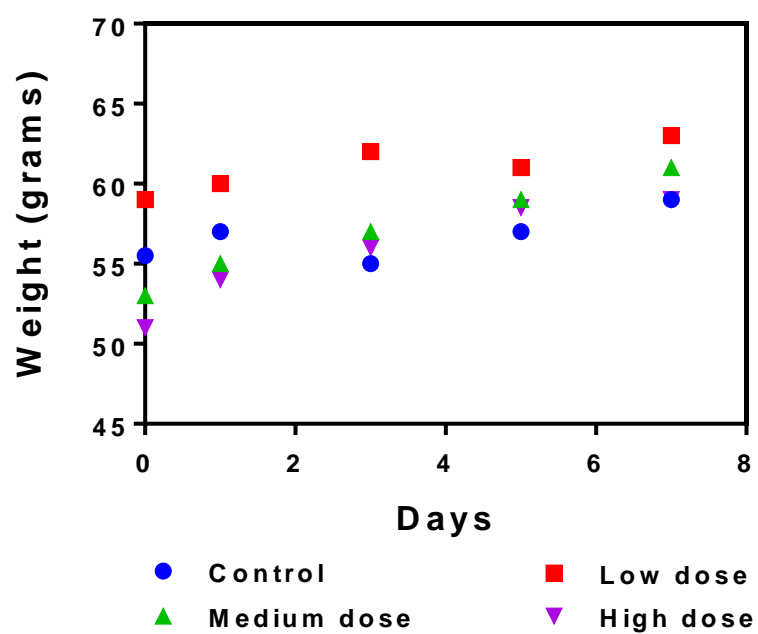
A large number of *in vivo* studies based on histology changes of vital organs exposed to graphene have been carried out before. A non-biodegradable feature of GFs as implanted scaffolds was demonstrated in rat exhibiting good biocompatibility [34]. GO administration in some other animal models, such as rat, caused prolonged toxicity and lung granuloma death [35]. In another study, GO administration was found to induce dose-dependent lung toxicity, granulomatous abrasions and injuries, and inflammatory cell penetration [36]. Higher concentrations of graphene, GO and rGO (reduced graphene oxide) were reported to be toxic. Fortunately, the results from the present study indicated that toxicity of GF was very minor. This is probably because of its different porous structure, chemical and physical morphology, and architecture, compared to those of its other graphene-based counterparts. Synthesis routes, size, surface charge, colloidal stability, surface chemistry, and water solubility affect *in vivo* nano-formulations. No noticeable differences were found in the *in vivo* toxicity of GF in this study. Additionally, GF appeared to be non-biodegradable even after 7 days of

treatment. Several factors might have contributed to the toxicity mechanism of GF, including the variety of exposure routes to living models, short or long term exposure periods, different chemiophysical properties, volume stability, and surface properties *in vivo*. To solve the real world clinical problems, these factors must be considered before evaluation of toxicology and bio-distribution of NPs. Hence, understanding the fundamentals of aquatic toxicology and bioavailability of GF would also provide insights into the validity of environmental fate and impacts of GF. Long term toxicological and biodegradability studies of GF rooted into the target tissue for regenerative engineering need to be carried out in the future.

## **8.4 Conclusions**

The present work deals with the systematic toxicity assessment of GF in U87 cell line and common carp. High dose administrations did not clue to critical or prolonged toxicity in fish, but some variations in blood cells were observed. In terms of biochemical and blood parameters testing, values remained within standard series resulting in no morphological and metabolism changes in fish model. Histopathology imaging revealed that GF remained within liver and kidney macrophages for 7 days without showing obvious sign of toxicity. Fluorescence imaging probed the cell attachment with 3D microenvironment of GF. The findings from this work provide insights into the diverse biological effects of GF and open new opportunity for their biomedical applications as an interface and scaffold material.

## 8.5 Supplementary information



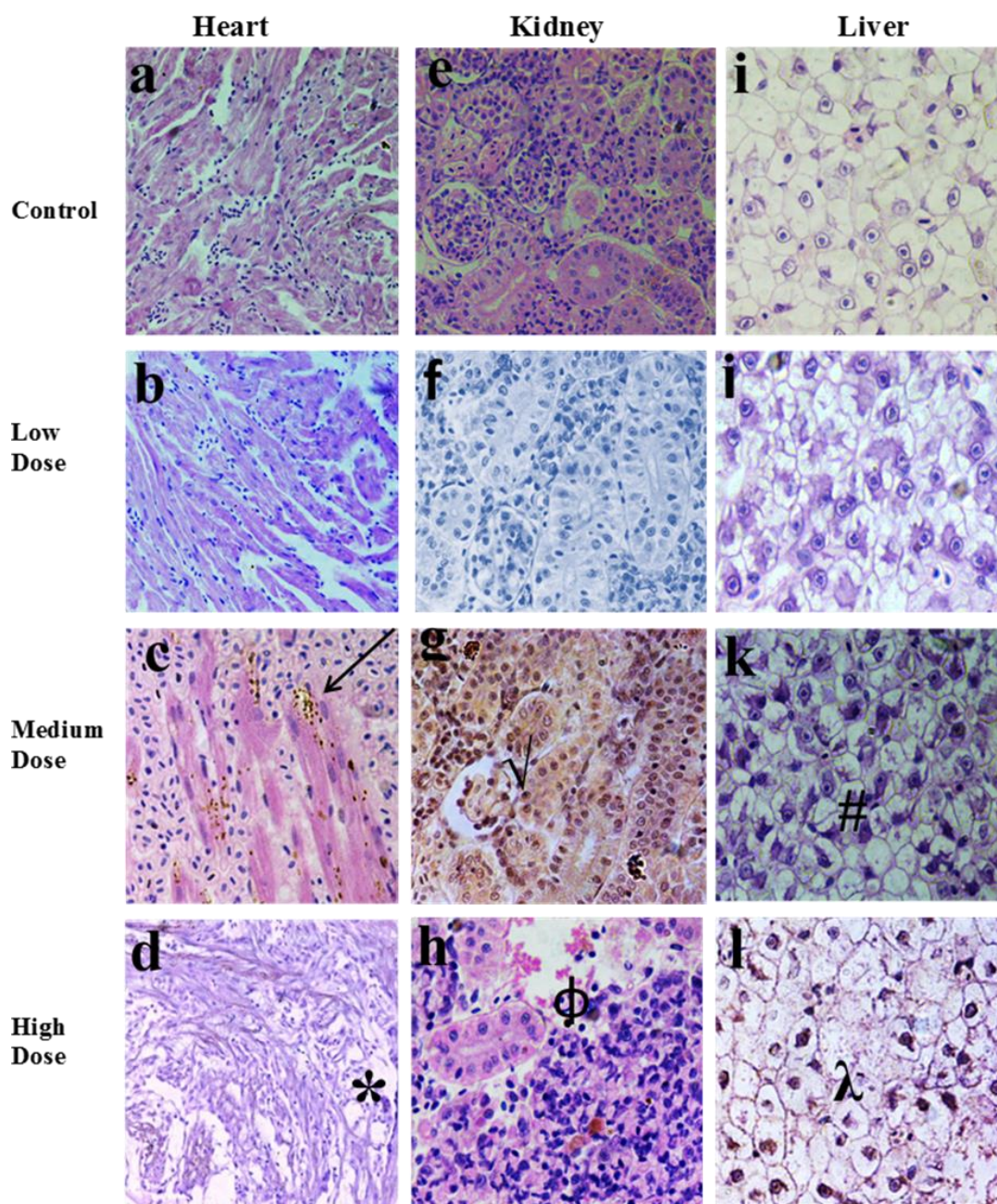
**SI Figure 8.1:** Mean and standard deviations of body weight of common carp treated with GF show no statistically substantial changes over a period of 7 days. Data are presented as mean  $\pm$  SE ( $n = 3$ ).

**SI Table 8.1:** Histological changes in fish after treatment with GF for 7 days. Histological changes were observed in both control and treated groups and indicated by + and – (where + means this is found in particular tissue, ++ means this is highly noted in particular tissue, and – means it is not found in the tissue).

Histological alteration	Control	Low dose	Medium dose	High dose
<b>Liver</b>				
Karyolitic nuclei in hepatocytes	-	-	+	++
Karyorrhexis nuclei in hepatocytes	-	-	+	++
Pyknosed nuclei in hepatocytes	- -	- -	+	++
Necrosis	- -	- -	+	++
Degeneration of central vein	-	-	+	++
Degeneration of hepatocytes	-	-	+	++
Inflammatory cells	-	-	+	++
Hemorrhage	-	-	-	++
<b>Renal tissue</b>				
Glomerulus shrinkage	-	-	+	++
Pyknosed nuclei	-	-	+	++
Congestion	-	-	+	++
Necrosis	-	-	+	+
Deposition of Lipofuscin granules	-	-	+	-
Haemorrhage	-	-	-	++
<b>Heart</b>				
Condensed pyknosed nuclei	-	-	-	-

Deposition of Lipofuscin granules	-	-	+	-
Thinning and degeneration of myofibrils	-	-	-	+
Haemorrhages	-	-	-	-





**SI Figure 8.3:** H & E stained light micrographs of *Cyprinus carpio* {heart (a-d), kidney (e-h) and liver tissues (i-l)} treated with GF in dose dependant manner after 5 days. Figures a-b, e-f and i-j show normal histology of heart, kidney and liver. Figures c-d, g-h and k-l show histological alterations in dose dependent manner in selected tissues. Details of histological alterations are given in Table S2. All the images were taken at 50µm scale bar.

**SI Table 8.2:** Histological findings in fish after treatment with GF for 5 days. Histological changes were observed in both control and treated groups and indicated by + and – (where + means this is found in particular tissue, ++ means this is highly noted in particular tissue, and – means it is not found in the tissue).

Histological alteration	Control	Low dose	Medium dose	High dose
<b>Liver</b>				
Karyolitic nuclei in hepatocytes	-	-	+	+
Karyorrhexis nuclei in hepatocytes	-	-	+	++
Pyknosed nuclei in hepatocytes	- -	- -	+	+
Necrosis	- -	- -	+	++
Degeneration of central vein	-	-	+	+
Degeneration of hepatocytes	-	-	+	++
Inflammatory cells	-	-	+	+
Hemorrhage	-	-	-	++
<b>Renal tissue</b>				
Glomerulus shrinkage	-	-	+	+
Pyknosed nuclei	-	-	+	++
Congestion	-	-	+	+
Necrosis	-	-	+	+
Deposition of Lipofuscin granules	-	-	+	-
Haemorrhage	-	-	-	++
<b>Heart</b>				



Condensed pyknotic nuclei	-	-	-	-
Deposition of Lipofuscin granules	-	-	+	-
Thinning and degeneration of myofibrils	-	-	-	+
Haemorrhages	-	-	-	-

## References

- [1] Nardecchia, S., Carriazo, D., Ferrer, M. L., Gutiérrez, M. C., & del Monte, F. (2013). Three dimensional macroporous architectures and aerogels built of carbon nanotubes and/or graphene: synthesis and applications. *Chem. Soc. Rev.*, 42(2), 794-830.
- [2] Chen, Z., Ren, W., Gao, L., Liu, B., Pei, S., & Cheng, H. M. (2011). Three-dimensional flexible and conductive interconnected graphene networks grown by chemical vapour deposition. *Nat. Mater.*, 10(6), 424-428.
- [3] Jiang, L., & Fan, Z. (2014). Design of advanced porous graphene materials: from graphene nanomesh to 3D architectures. *Nanoscale*, 6(4), 1922-1945.
- [4] Wu, Z. S., Sun, Y., Tan, Y. Z., Yang, S., Feng, X., & Müllen, K. (2012). Three-dimensional graphene-based macro-and mesoporous frameworks for high-performance electrochemical capacitive energy storage. *J. Chem. Soc.*, 134(48), 19532-19535.
- [5] Singh, E., Chen, Z., Houshmand, F., Ren, W., Peles, Y., Cheng, H. M., & Koratkar, N. (2013). Superhydrophobic graphene foams. *small*, 9(1), 75-80.
- [6] Zhang, X., Liu, D., Yang, L., Zhou, L., & You, T. (2015). Self-assembled three-dimensional graphene-based materials for dye adsorption and catalysis. *J. Mater. Chem. A* 3(18), 10031-10037.
- [7] Luo, J., Liu, J., Zeng, Z., Ng, C. F., Ma, L., Zhang, H., ... & Fan, H. J. (2013). Three-dimensional graphene foam supported Fe<sub>3</sub>O<sub>4</sub> lithium battery anodes with long cycle life and high rate capability. *Nano Lett.* 13(12), 6136-6143.
- [8] Patil, U., Lee, S. C., Kulkarni, S., Sohn, J. S., Nam, M. S., Han, S., & Jun, S. C. (2015). Nanostructured pseudocapacitive materials decorated 3D graphene foam electrodes for next generation supercapacitors. *Nanoscale*, 7(16), 6999-7021.
- [9] Dong, X., Ma, Y., Zhu, G., Huang, Y., Wang, J., Chan-Park, M. B., & Chen, P. (2012). Synthesis of graphene-carbon nanotube hybrid foam and its use as a novel three-dimensional electrode for electrochemical sensing. *J. Mater. Chem.* 22(33), 17044-17048.
- [10] Li, N., Zhang, Q., Gao, S., Song, Q., Huang, R., Wang, L., & Cheng, G. (2013). Three-dimensional graphene foam as a biocompatible and conductive scaffold for neural stem cells. *Sci. Rep.* 3, 1604-1609.
- [11] Shi, J. L., Wang, H. F., Zhu, X., Chen, C. M., Huang, X., Zhang, X. D., & Zhang, Q. (2016). The nanostructure preservation of 3D porous graphene: New insights into the graphitization and surface chemistry of non-stacked double-layer templated graphene after high-temperature treatment. *Carbon*, 103, 36-44.
- [12] Wang, J. K., Xiong, G. M., Zhu, M., Özyilmaz, B., Castro Neto, A. H., Tan, N. S., & Choong, C. (2015). Polymer-enriched 3D graphene foams for biomedical applications. *ACS Appl. Mater. Interfaces* 7(15), 8275-8283.
- [13] Nieto, A., Dua, R., Zhang, C., Boesl, B., Ramaswamy, S., & Agarwal, A. (2015). Three dimensional graphene foam/polymer hybrid as a high strength biocompatible scaffold. *Adv. Funct. Mater.* 25(25), 3916-3924.

- [14] Schultz, A. G., Boyle, D., Chamot, D., Ong, K. J., Wilkinson, K. J., McGeer, J. C., & Goss, G. G. (2014). Aquatic toxicity of manufactured nanomaterials: challenges and recommendations for future toxicity testing. *Environ. Chem.* 11(3), 207-226.
- [15] Köprücü, K., & Aydın, R. (2004). The toxic effects of pyrethroid deltamethrin on the common carp (*Cyprinus carpio* L.) embryos and larvae. *Pesti. Biochem. Phys.* 80(1), 47-53.
- [16] Chabi, S., Peng, C., Yang, Z., Xia, Y., & Zhu, Y. (2015). Three dimensional (3D) flexible graphene foam/polypyrrole composite: towards highly efficient supercapacitors. *RSC Adv.* 5(6), 3999-4008.
- [17] Chabi, S., Chang, H., Xia, Y., & Zhu, Y. (2016). From graphene to silicon carbide: ultrathin silicon carbide flakes. *Nanotechnology*, 27(7), 075602-075607.
- [18] Jabeen, F., & Chaudhry, A. S. (2011). Effects of cadmium chloride and sodium selenite alone or in combination on the liver of male Sprague–Dawley rats assessed by different assays. *Biol. Trace Elem Res.* 143(2), 1077-1090.
- [19] Lee, J. S. (2006). Effects of soy protein and genistein on blood glucose, antioxidant enzyme activities, and lipid profile in streptozotocin-induced diabetic rats. *Life Sci.* 79(16), 1578-1584.
- [20] Zor, T., & Selinger, Z. (1996). Linearization of the Bradford protein assay increases its sensitivity: theoretical and experimental studies. *Anal. Biochem.* 236(2), 302-308.
- [21] Yu, Q., Lian, J., Siriponglert, S., Li, H., Chen, Y. P., & Pei, S. S. (2008). Graphene segregated on Ni surfaces and transferred to insulators. *Appl. Phys. Lett.* 93(1), 113103-13110.
- [22] Paronyan, T. M., Thapa, A. K., Sherehiy, A., Jasinski, J. B., & Jangam, J. S. D. (2017). Incommensurate Graphene Foam as a High Capacity Lithium Intercalation Anode. *Sci. Rep.* 7, 39944-39954.
- [23] Ferrari, A. C., Meyer, J. C., Scardaci, V., Casiraghi, C., Lazzeri, M., Mauri, F., & Geim, A. K. (2006). Raman spectrum of graphene and graphene layers. *Phys. Rev. Lett.* 97(18), 187401-187405.
- [24] Janowska, I., Vigneron, F., Bégin, D., Ersen, O., Bernhardt, P., Romero, T., & Pham-Huu, C. (2012). Mechanical thinning to make few-layer graphene from pencil lead. *Carbon*, 50(8), 3106-3110.
- [25] Seabra, A. B., Paula, A. J., de Lima, R., Alves, O. L., & Durán, N. (2014). Nanotoxicity of graphene and graphene oxide. *Chem. Res. Toxicol.* 27(2), 159-168.
- [26] Reuter, S., Gupta, S. C., Chaturvedi, M. M., & Aggarwal, B. B. (2010). Oxidative stress, inflammation, and cancer: how are they linked?. *Free Radic. Biol. Med.* 49(11), 1603-1616.
- [27] Sanfeliu, C., Sebastià, J., & Kim, S. U. (2001). Methylmercury neurotoxicity in cultures of human neurons, astrocytes, neuroblastoma cells. *Neurotoxicology*, 22(3), 317-327.
- [28] AshaRani, P. V., Low Kah Mun, G., Hande, M. P., & Valiyaveetil, S. (2008). Cytotoxicity and genotoxicity of silver nanoparticles in human cells. *ACS Nano*, 3(2), 279-290.

- [29] Natarajan, V., Wilson, C. L., Hayward, S. L., & Kidambi, S. (2015). Titanium dioxide nanoparticles trigger loss of function and perturbation of mitochondrial dynamics in primary hepatocytes. *PLoS One*. 10(8), 1-19.
- [30] Li, Z. H., Zlabek, V., Velisek, J., Grabic, R., Machova, J., & Randak, T. (2009). Responses of antioxidant status and Na<sup>+</sup>–K<sup>+</sup>-ATPase activity in gill of rainbow trout, *Oncorhynchus mykiss*, chronically treated with carbamazepine. *Chemosphere* 77(11), 1476-1481.
- [31] Perendija, B. R., Despotović, S. G., Radovanović, T. B., Gavrić, J. P., Mitić, B. S. S., Pavlović, S. Z., & Saičić, Z. S. (2011). Biochemical and ultrastructural changes in the liver of European perch (*Perca fluviatilis* L.) in response to cyanobacterial bloom in the Gruža reservoir. *Arch. Biol. Sci.* 63(4), 979-989.
- [32] Kütter, M. T., Romano, L. A., Ventura-Lima, J., Tesser, M. B., & Monserrat, J. M. (2014). Antioxidant and toxicological effects elicited by alpha-lipoic acid in aquatic organisms. *Comp. Biochem. Physiol. C* 162, 70-76.
- [33] Jos, A., Pichardo, S., Prieto, A. I., Repetto, G., Vázquez, C. M., Moreno, I., & Cameán, A. M. (2005). Toxic cyanobacterial cells containing microcystins induce oxidative stress in exposed tilapia fish (*Oreochromis* sp.) under laboratory conditions. *Aquat. Toxicol.* 72(3), 261-271.
- [34] Zha, Y., Chai, R., Song, Q., Chen, L., Wang, X., Cheng, G., ... & Wang, M. (2016). Characterization and toxicological effects of three-dimensional graphene foams in rats in vivo. *J. Nanopart. Res.* 18(5), 122-131.
- [35] Liu, J. H., Wang, T., Wang, H., Gu, Y., Xu, Y., Tang, H., & Liu, Y. (2015). Biocompatibility of graphene oxide intravenously administrated in mice—effects of dose, size and exposure protocols. *Toxicol. Res.* 4(1), 83-91.
- [36] Patlolla, A. K., Randolph, J., Kumari, S. A., & Tchounwou, P. B. (2016). Toxicity evaluation of graphene oxide in kidneys of Sprague-Dawley rats. *Int. J. Environ. Pub. Health* 13(4), 380-394.

## Chapter 9

# Conclusions and Future Outlook

---

Although nanostructured graphene is physically tiny, it has a vast and growing impact on the economy. Nanostructured graphene could reap huge technological and economic advantages in nanomedicine. Nanomedicine, a multidisciplinary field that embraces biology, chemistry, physics and material sciences, is playing a key role in the treatment of human diseases such as cancer, neurological disorders and infectious diseases. The ‘war’ against cancer was declared in the early 1970s; there has been much research done on cancer diagnosis and treatment since then. More recently, considerable attention has been paid to developing graphene-based anticancer nanomedicine for the point-of-care management and treatment of these diseases. The leading payoff of nanomedicine lies in the realisation of nanostructured graphene-based therapeutic platforms to potentially deal with the prevention and cure of cancer. Although nanostructured graphene is already used as an anticancer medicine, there is still uncertainty on the biological effects and bioavailability of graphene to facilitate a non-toxic and sustainable advancement of this technology. This thesis focused on biological effects of graphene-based materials (graphene oxide (GO), reduced graphene oxide (rGO), graphene nanopores (GNPs), graphene quantum dots (GQDs) and 3D graphene foam (GF)) as anticancer nanomedicines. The work reported here was motivated by the pressing need to understand the occupational, health and safety aspects of graphene-based nanosystems that could overcome a number of barriers to clinical translations. Taken together, all of these experimental works lay a foundation for subsequent adaptation of these materials into biomedical practices.

### 9.1 Conclusions

The main achievements and key findings for the work carried out in each chapter of this thesis are summarised below:

1. **Chapter 4** presents a straightforward and highly adaptable strategy for the rapid and facile removal of pro-metastasis enzymes that effectively rescue the disease. GO,

with its variable zeta potential, variety of functional groups and very large (and in principle fully accessible) surface area, is an extremely promising candidate for the adsorption of such enzymes. Overexpression and secretion of the enzymes cathepsin D (CathD) and cathepsin L (CathL) is associated with metastasis in several human cancers. As a superfamily, extracellularly, these proteins may act within the tumor microenvironment to drive cancer progression, proliferation, invasion and metastasis. We have conducted research into the potential of anti-metastatic target therapy using GO to adsorb these pro-tumourigenic enzymes. Definitive binding and modulation of CathD/L with GO revealed that CathD/L were adsorbed onto the surface of GO through its cationic and hydrophilic residues indicating non-toxic effects on cells. GO nanostructures are easy to manufacture and are stable, which simplifies long-term storage and correspondingly reduces the cost. This work could provide a roadmap for the rational integration of CathD/L-targeting agents into clinical settings.

2. **Chapter 5** reports on integrative chemical-biological interactions of rGO with lung cancer cells, A549 and SKMES-1, to determine its potential toxicological impacts on them, as a function of its concentration. The *in vitro* toxicity of rGO against these two lung cancer cells has been assessed and compared for the first time without premodification of rGO. Cell viability, early and late apoptosis and necrosis were measured to determine oxidative stress potential and induction of apoptosis. The general trend was shown between cell death rates and concentrations for different cell types using a Gaussian process regression model. At low concentrations, rGO was shown to significantly produce late apoptosis and necrosis rather than early apoptotic events, suggesting that it was able to disintegrate the cellular membranes in a dose-dependent manner. Given the evolving field of graphene-based nanomedicine, our findings regarding the toxicity of graphene using *in vitro* models could play a significant role in paving a new way to future biomedical applications of rGO.

3. In **chapter 6**, a cost-effective and facile method for the preparation of a relatively new derivative of graphene, graphene nanopores (GNPs) was presented along with their *in vitro* and *in vivo* interactions in the mammalian and non-mammalian systems to systematically elucidate the possible mechanism of their toxicity over time. This study showed that GNPs induce early apoptosis in both SKMES-1 and A549 lung

cancer cells; however, late apoptosis is only induced at concentrations higher than 250 µg/ml, suggesting that, although GNPs at lower concentrations induces upregulation of phosphatidylserine on a cell surface membrane (*i.e.* early apoptotic event), it does not significantly disintegrate the cell membrane. Here, we also showed that rats intraperitoneally injected with GNPs exhibited acute toxicity in a period of 27 days when tested at single and multiple doses of GNPs (5 and 15 mg/kg) as evidenced by blood biochemistry, organo-somatic index, liver and kidney enzymes functions analysis, oxidative stress biomarkers and histological examinations. *In vivo* biodistribution results reveal that GPNs mainly accumulate in the liver and lungs after intravenous administration and can be gradually cleared through the kidney. Our results showed that GNPs are likely to have a low bioavailability in SKMES-1 and A546 lung cancer cells and in rats.

4. **Chapter 7** demonstrates the integrative physiochemical interaction between trypsin and GQDs to determine their potential biological identity in enzyme engineering. We selected trypsin, due to its role as a biologically relevant target enzyme; trypsin is a pancreatic serine protease involved in digestion of proteins as well as playing a role in other important biological activities. Trypsin is a medium-sized globular protein with applications in wound healing machineries, and in washing agents. The bonding forms a nano–bio-interface that defines the role of the QD and can induce damage in the interacting trypsin. GQDs exhibited a strong bonding capacity owing to their surface charge and surface functionalities. They were highly biocompatible, as demonstrated by the fact that the trypsin was adsorbed onto their surface via chemical interaction and hence blocking the emission of fluorescence signals from the graphene molecule. Different levels of inherent surface oxygen containing functional groups of GQDs were found to be the reason behind the tuning of trypsin’s specific activity. A fluorogenic substrate for trypsin was used to carry out control experiments of trypsin activity. Our findings suggested that trypsin’s active sites were stabilised and protected by the GQDs, which was likely to be responsible for the high bioavailability of GQDs in enzymes.

5. **Chapter 8** presents a cytotoxicity study on 3D GF in human glioblastoma U87 cell line and common carps, which was measured by antioxidant enzymatic activities,

biochemical and blood parameters, and histological alterations in key organs (kidney, liver, heart, and spleen). High dose administrations did not cause any acute toxicity in fish, but some variations in blood cells were observed. In terms of biochemical and blood parameters testing, values remained within standard series, resulting in no morphological or metabolism changes in the fish model. Histopathology imaging revealed that GF remained within liver and kidney macrophages for 7 days without showing obvious signs of toxicity. Additionally, fluorescence imaging of U87 cells seeded on GF-based scaffolds probed the cell attachment with 3D microenvironment of GF.

## 9.2 Future work

Based on these research findings, a number of future recommendations can be made to benefit the discipline of anticancer nanomedicine with respect to the research and development work required for the progression of this ‘miracle material’. The following future studies for each derivative of graphene discussed in this thesis should be taken into consideration to further validate the fate of graphene-based materials in nanomedicine:

### 9.2.1 Graphene-based anti-metastatic extracellular enzyme therapy

The findings presented in **Chapter 4** make a significant contribution towards the further development of anti-metastatic extracellular enzyme therapy.

- One aspect that is worth investigating in the future is the *in vivo* testing of GO for the adsorption and subsequent removal of pro-metastatic enzymes from living systems. However, the other adsorbents for selective targeting of extracellular enzymes could also be investigated for a range of enzymes.
- Further *in vitro* testing with enzyme suspensions and substrates, and using further cellular assays which explore potential mechanisms of other enzyme adsorption, could also be interesting to extend this novel therapy. Furthermore, testing the role of reactive oxygen species in adsorption and tuning the GO properties could give a wider insight into the interplay between *in vivo* activity–structure relationships.



- Importantly, tumors tend to survive under hypoxic conditions, which are characteristic features of tumor metastasis and drug resistance. Low oxygen environments could also be taken into account while using GO as an anticancer therapeutic agent. Design of hypoxia-activated modulators and reductants with graphene-based materials could help improve the anticancer efficacy of such nanomaterials-based therapies to target/leverage tumor hypoxia.

### 9.2.2 Bioavailability of reduced graphene oxide

Future studies are desirable to investigate the *in vivo* structure–activity relationships for rGO (**Chapter 5**), using different cell lines with differing lateral and sheet sizes of rGO or differing chemical modifications, and preparation to make it biocompatible and less toxic for biological applications.

- The release of untreated rGO to the animal models and their pro or antibacterial and inflammatory responses should be taken into consideration for the wellbeing of humans.
- Further studies must be conducted in this field to exploit the role of redox signalling. Chemical preparation of rGO involves exfoliation using sodium nitrate which can in turn release reactive nitrogen species in the cells. For example, the chemical exfoliation of GO is commonly carried out by using graphite flakes in  $\text{H}_2\text{SO}_4$  and  $\text{NaNO}_3$  to oxidise graphite flakes into graphite oxide. Oxidation by  $\text{HNO}_3$  may liberate gaseous  $\text{NO}_2$  and/or  $\text{N}_2\text{O}_4$ . The addition of  $\text{NaNO}_3$  increases the interlayer distance marginally with improved basal planes oxidation of graphite. As a result, graphite flakes are broken into the smallest possible sheets layer wise (e.g. single or few layers) with the maximal functionalisation on the basal plane. After the exfoliation of GO, hydrazine is the commonly used reducing agent to reduce the functional groups and to enhance surface area and porosity. As a result of using hydrazine, nitrogen tends to remain covalently bonded to the surface of graphene in the form of hydrazones, amines, aziridines and/or other analogous species. On this basis, it is important to quantify and analyse nitrogen-centred radicals present in graphene nanostructures. Elevated levels of reactive nitrogen species are involved in the

hyperactivation of cellular oxidases and mitochondrial dysfunction as a result of cell damage by inducing or repressing nitrosative stresses.

### 9.2.3 Role of reactive oxygen species in oxidative stress and toxicity of graphene nanopores

**Chapter 6** presented the sub chronic levels of toxicity in rats when it was intraperitoneally administrated.

- As part of future work, it will certainly be interesting to work on the role of reactive oxygen species in oxidative stress and *in vivo* toxicity by other routes of administration.
- Testing other organs of interest, such as the liver and lung, for potential toxicity can also be adapted to look at the biosafety profile of GNPs. These superhydrophobic GNPs nanosystems can also be used to store and release therapeutic levels of nitric oxide for the disruption of biofilms with chronic wounds.
- It is clearly evident that GNPs have a high specific surface area in which to store and release high amounts of nitrogen gas. A similar approach can be used for infectious diseases. Such wounds cannot be healed with antibiotics, hence these nanoporous systems could be a promising candidate for controlling wound biofilm infections.

### 9.2.4 Graphene quantum dots in enzyme engineering

The nano-bio-interface between the adsorbing enzymes and the GQDs surface could have potential applications in the development of biocompatible nanomaterials, nanomedicines, and for enzyme separation and purification approaches. It is clearly evident from our results presented in **Chapter 7** that GQDs-trypsin interaction has shown consistency, time efficiency and the capability to tag chemically.

- This work can be further extended to understand the kinetics of GQDs protein binding and affinities of GQDs for different proteins. Though we have shown that GQDs are able to bind to trypsin, the affinity and specificity for different proteins are unknown.

- Future studies can be directed towards understanding the dependence of size, charge, and amino acid composition of different proteins in GQDs-protein complex formation. However, a similar approach could be used to deliver high molecular drug within diseased cells. Exploring the potential biological applications of GQDs, such as drug delivery and imaging among many other applications.

### 9.2.5 3D graphene in regenerative medicine

It was demonstrated that development of biocompatible 3D GF-based scaffolds can be used for the attachment and growth of cells (**Chapter 8**).

- Regeneration of stem cell and non-stem cell cultures within 3D microenvironments of GF-based scaffolds could be exploited in animal models for their clinical settings, hence when tested in *in vivo* models this can potentially open a new route for the realisation of 3D GF in regenerative medicine.
- As part of future work, it will also be interesting to study other recently reported advanced functionalities of biodegradable GF for stem cell therapy.